ABSTRACT

Title of Dissertation: DESIGN AND CONSTRUCTION OF A THREE-NODE QUANTUM NETWORK

Allison Levin Carter
Doctor of Philosophy, 2021

Dissertation Directed by: Professor Christopher Monroe
Joint Quantum Institute,
University of Maryland Department of Physics

Quantum computers have wide-ranging potential applications, many of which will require thousands or even millions of quantum bits to be useful. Current state-of-the-art universal quantum computers, on the other hand, contain only several tens of qubits, and scaling to larger system sizes remains one of the primary challenges. Among current quantum computing platforms, trapped ions are a leading hardware option. One proposal for scaling such systems consists of a modular architecture.

The architecture consists of multiple nodes, each with an ion trap containing a communication qubit ($^{138}Ba^{+}$) and a memory qubit ($^{171}Yb^{+}$). The communication qubit is responsible for generating photons that link the remote nodes together via entanglement swapping while the memory qubits are used for storing information and performing local computations. We report progress towards demonstration of the remote entanglement of two barium ions. The creation of this link is a probabilistic process and fails much more often than it succeeds. The success rate does not impact the fidelity of the resulting entangled state but imposes significant

constraints on the utility of this protocol. We examine the current limitations on both the fidelity of the resulting entangled state and the success probability.

In addition to the two-node experiment, we have designed and built a new ion trap system that should yield much higher photon collection rates. This design represents a significant shift from previous systems because of the inclusion of optical elements inside the vacuum chamber and their resulting proximity to the ions. We incorporate two objective lenses with a numerical aperture of 0.8, each of which can collect twice as much light as the objectives used for the remote entanglement experiment. We present preliminary results characterizing the performance of this system and discuss how it could be incorporated into a three-node network, which has not yet been demonstrated using trapped ions.

DESIGN AND CONSTRUCTION OF A THREE-NODE QUANTUM NETWORK

by

Allison Levin Carter

Dissertation submitted to the Faculty of the Graduate School of the
University of Maryland, College Park in partial fulfillment
of the requirements for the degree of
Doctor of Philosophy
2021

Advisory Committee:
Professor Christopher Monroe, Chair/Advisor
Professor Alicia Kollár
Professor Norbert Linke
Professor Steven Rolston
Professor Ronald Walsworth

Acknowledgments

Throughout my time in graduate school, the support of numerous people has been instrumental to my success. First, I would like to thank my advisor, Chris Monroe, for the incredible research opportunity he has provided. Working in his group has allowed me to grow as a scientist under the guidance of many talented physicists and to begin developing my own ideas about interesting scientific directions. I have greatly appreciated his support along the way.

This work would not have happened without the many other people who contributed to this experiment and the support of the broader ion trapping community at UMD. When I first joined the ion-photon lab, I had the pleasure of working with our postdoc Marty Lichtman and graduate students Clay Crocker and Ksenia Sosnova. Marty was instrumental in getting me involved in important lab work immediately and ensuring that I had the necessary resources and support for pursuing my first projects in graduate school. Clay was very welcoming and I greatly enjoyed working with him to build a new lab. I worked most closely with Ksenia, and she taught me the vast majority of what I know about running our experiment and was incredibly patient as I became more involved with the key aspects of the lab and then as I transitioned from a junior to senior graduate student. I also am immensely grateful for her support as we struggled through numerous frustrations in the lab and her friendship in general.

More recently, George Toh joined the lab as a postdoc and Jameson O'Reilly and Sagnik Saha started as graduate students. Their contributions have been essential to obtaining the results reported in this thesis. George's leadership on the remote entanglement experiment has been important for our progress in recent months. Both Jameson and Sagnik have been extraordinary junior graduate students, and without their contributions, much of this work could not have happened especially on the new ion trap. Jameson has rapidly learned to assist with and lead important elements of the lab's work and contributed thoughtful insights about the future direction of the lab. Sagnik's diligent work has been essential in working out all of the details of very complicated technical systems, and his growth in the lab has been very impressive. I look forward to seeing their success going forward. During my time in this lab, we have also had three undergraduate students work with us– Hanna Ruth, Sophia Scarano, and Leeza Moldavchuk. I enjoyed working with them and appreciated their contributions to our work as well. One of the best aspects of this group has been the proximity to and chance to work with so many incredible people. I especially appreciate the support of Kristi Beck, Caroline Figgatt, Crystal Noel, Wen Lin Tan, and Kate Collins. Marko Cetina's scientific advice has also been crucial, especially for vacuum work, and without Drew Risinger's work on software development, we would not have been able to perform our remote entanglement experiment.

I also would not have gotten to this point without my undergraduate professors. They helped me both to develop the confidence I needed to consider going to graduate school and to obtain sufficient research experience to understand my inter-

ests and have some experimental background before I started my work at UMD. I want to thank my friends who have supported me during my time in graduate school as well. My parents also have been incredibly supportive, and I am so grateful to have always had them to turn to. My siblings and extended family have also been very supportive, and my brothers Luke and Finn in particular can always make any day better. Finally, to James, thank you so much for your support. The past couple of years have been filled with so many ups and downs, and I'm so thankful you've been with me through all of it.

Table of Contents

Acknowledgements ii

Table of Contents v

List of Tables viii

List of Figures ix

List of Abbreviations xii

Chapter 1: Introduction 1
- 1.1 Quantum Computing Background . . . 1
- 1.2 Trapped Ion Quantum Computers and Networks . . . 2
  - 1.2.1 Experimental Apparatus . . . 8
- 1.3 Thesis Outline . . . 9

Chapter 2: Theory of Trapped Ion-Laser Interactions 12
- 2.1 Doppler cooling . . . 12
- 2.2 Coherent Operations . . . 14
  - 2.2.1 Driving Ion Motion Using Coherent Operations . . . 24
- 2.3 Calculation of Dipole Matrix Elements . . . 26
  - 2.3.1 Dipole Matrix Elements for Atoms with $\mathbf{I} = 0$ . . . 27
  - 2.3.2 Dipole Matrix Elements of Atoms with Nonzero Nuclear Spin 30
- 2.4 Optical Bloch Equations for Barium . . . 31
  - 2.4.1 Three-Level System . . . 34
  - 2.4.2 Eight-Level System and Multiple Polarizations . . . 37

Chapter 3: Operations with Ytterbium and Barium Ions 42
- 3.1 $^{171}Yb^{+}$ Ions . . . 42
  - 3.1.1 Atomic Sources and Photoionization . . . 42
  - 3.1.2 Doppler cooling . . . 46
  - 3.1.3 State Initialization and Detection . . . 49
  - 3.1.4 Coherent Operations . . . 52
- 3.2 $^{138}Ba^{+}$ Ions . . . 54
  - 3.2.1 Atomic Sources and Photoionization . . . 54
  - 3.2.2 Doppler Cooling . . . 59
  - 3.2.3 State Preparation and Detection in the $6S_{1/2}$ Manifold . . . 62

3.2.4 State Preparation and Detection in the $5D_{3/2}$ Manifold 67
3.2.5 Coherent Operations in the $6S_{1/2}$ Manifold 74
3.2.6 Coherent Operations in the $5D_{3/2}$ Manifold 78

Chapter 4: RF Paul Traps 82
4.1 RF Paul Trap Theory 82
4.2 Trap Design and Simulations 87
4.2.1 Simulation Results 89
4.3 Trap Parameter Optimization and Measurement 92
4.3.1 Measurement of Trap Secular Frequencies 92
4.3.2 Micromotion Compensation 94
4.3.3 Application of a DC Radial Quadrupole 102

Chapter 5: Experimental Design and Testing 104
5.1 Imaging Systems for the First Two Traps 104
5.1.1 Alice Free Space Imaging Setup 105
5.1.2 Bob Free Space Imaging Setup 107
5.1.3 High Numerical Aperture Imaging System for Fiber Coupling 109
5.2 Design of an Ion Trap with In-Vacuum High Numerical Aperture Imaging 111
5.2.1 Imaging Systems Design 112
5.2.2 Vacuum Chamber Design 120
5.3 Testing of the Trap with In-Vacuum High Numerical Aperture Imaging 124
5.3.1 Optics Testing 124
5.3.2 Testing of Trap Properties 132

Chapter 6: Remote Entanglement of $^{138}Ba^{+}$ Ions 135
6.1 Generating Single Photons from $^{138}Ba^{+}$ 136
6.1.1 Double Excitations 140
6.2 Ion-Photon Entanglement 144
6.2.1 Ion-Photon Entanglement Fidelity and Sources of Error 147
6.3 Ion-Ion Entanglement 157
6.3.1 Hong-Ou-Mandel Effect 157
6.3.2 Bell State Measurements and Ion Entanglement 160
6.4 Experimental Procedure 164
6.4.1 Experimental Sequence 164
6.4.2 Experimental Control System 173
6.4.3 Entanglement Generation Rate 175
6.4.4 Sources of Fidelity Loss in Remote Entanglement 178
6.4.5 Beam Splitter and Fiber Errors 180

Chapter 7: Optics Considerations for Fiber Coupling Ion Light 188
7.1 Theoretical Calculations of Fiber Coupling Efficiencies 188
7.1.1 Waist Measurement and Mismatch 189
7.2 Experimental Characterization of Beam Aberrations 194

7.2.1 Defocus . . . 194
7.2.2 Zernike Polynomials for Describing Aberrations . . . 197
7.3 Adding Optics for Improving Fiber Coupling . . . 204

Chapter 8: Outlook 207
8.1 Deterministic State Readout of Barium Ions . . . 207
8.2 Two-Trap Entanglement Experiments . . . 210
8.2.1 Entanglement Distillation . . . 210
8.3 Protocols for Networks with More Than Two Traps . . . 211
8.3.1 Four Trap Protocol . . . 216
8.4 Other Ion Combinations for an Interspecies Quantum Network . . . 218
8.4.1 Motivation for a Different Ion Combination . . . 218
8.4.2 Use of $^{133}Ba^{+}$ as a Memory Qubit . . . 220

Appendix A: UHV Processing 229
A.1 Materials and Vacuum Pumping . . . 229
A.2 Cleaning Procedure . . . 231
A.3 Baking the Chamber . . . 233
A.4 Use of a Residual Gas Analyzer . . . 237

Bibliography 240

List of Tables

3.1 Summary of Yb operations laser requirements 51
3.2 Neutral barium transition wavelengths and branching ratios 56
3.3 Transitions in $^{138}Ba^{+}$ 59
3.4 Two-photon Rabi frequencies for $5D_{3/2}$ manifold Raman transitions . 79
3.5 Two-photon AC Stark shifts in the $5D_{3/2}$ manifold 80

5.1 Free space objective for Alice 106
5.2 Design parameters for the free space imaging aspheric lens on Bob . . 109
5.3 Bob free space imaging system design 110
5.4 Third Trap In-Vacuum Asphere Parameters 114
5.5 Third Trap Out-of-Vacuum Asphere Parameters 114
5.6 Parameters for Yb detection asphere 119
5.7 Loss of ion light through various pinhole sizes 129

6.1 High and low power Ba AOM control 170
6.2 Factors determining entanglement rate 177

List of Figures

1.1 Architecture for a modular quantum computer with photonic links . . 5
1.2 Pictures of the three vacuum chambers 9

2.1 Simple level scheme for Raman transitions 17
2.2 Simplified atomic structure of $^{138}Ba^{+}$ 36
2.3 Barium Clebsch-Gordan Coefficients 39

3.1 Atomic source oven 43
3.2 Yb neutral fluorescence 44
3.3 Atomic structure of Yb^{+} 47
3.4 Operations in Yb^{+} 52
3.5 Ba neutral atom energy levels 57
3.6 Ba Neutral Fluorescence 58
3.7 Ba^{+} Atomic Structure 60
3.8 State preparation and measurement in the $^{138}Ba^{+}$ $6S_{1/2}$ manifold . . 63
3.9 Ba $5D_{3/2}$ State Preparation and Measurement 68
3.10 Parameter optimization for state $5D_{3/2}$ pumping times 70
3.11 Raman transitions in the Ba S manifold 74
3.12 Clebsch-Gordan coefficients for transitions between the $6S_{1/2}$ and $6P_{3/2}$ manifolds. 75
3.13 $5D_{3/2} \leftrightarrow 6P_{3/2}$ transition strength coefficeints 77
3.14 Raman transitions in the $5D_{3/2}$ manifold in Ba 78

4.1 RF Paul ion trap geometries 83
4.2 Ion trajectories in an RF Paul trap 87
4.3 Four rod trap designs 89
4.4 Simulated potentials for a four rod trap with a square geometry . . . 90
4.5 Simulated potentials for a four rod trap with a rectangular geometry 91
4.6 Scattering rate plot in time for an ion with or without excess micromotion 97
4.7 Micromotion detection scheme experimental setup 100
4.8 Motional mode spectrum of ion with micromotion 101

5.1 Spot diagrams for the Alice free space objective 105
5.2 Cross section of the ray trace for the Bob 493 nm free space imaging system 108

5.3 Spot diagram for the Bob free space imaging system for 493 nm . . . 111
5.4 Spot diagram for 493 nm light through Alice and Bob fiber coupling objective . . . 112
5.5 Cross section of high NA asphere system for barium fluorescence collection . . . 113
5.6 Spot diagram for high NA asphere system . . . 115
5.7 CAD model of in-vacuum asphere mounting setup . . . 116
5.8 Trap mounting CAD model . . . 121
5.9 Laser beam delivery diagram for the third trap . . . 123
5.10 Third Trap Chamber CAD Model . . . 125
5.11 Image analysis of high-NA aspheres using artificial point source . . . 126
5.12 Ion images with high-NA aspheres . . . 127
5.13 Spot size analysis of the image of an ion through a high-NA asphere . 128
5.14 Setup for testing vacuum window birefringence . . . 130
5.15 Measurement of retardance on Cleo vacuum windows . . . 132
5.16 Dependence of micromotion in Cleo on bottom asphere position . . . 133

6.1 Ba single photon generation scheme . . . 137
6.2 Electronics for generating 650 nm pulses . . . 139
6.3 Error from double excitations . . . 141
6.4 Hanbury Brown Twiss setup for measuring $g^{(2)}(\tau)$ . . . 142
6.5 Results from $g^{(2)}$ experiment . . . 143
6.6 Experimental setup for ion-photon entanglement experiments . . . 144
6.7 Free space ion-photon entanglement data . . . 145
6.8 Coordinates for fiber coupling and polarization analysis . . . 147
6.9 Ion-photon entanglement data with fiber coupled light . . . 148
6.10 Plot of fidelity vs. light collection angle accounting for unequal numbers of H and V photons . . . 152
6.11 Free space ion-photon entanglement fidelity versus angle from the quantization axis . . . 153
6.12 Experimental setup for remote entanglement experiments . . . 161
6.13 Timing of optical control events in the remote entanglement fast loop 168
6.14 Fidelity with a polarization-dependent beam splitter . . . 182
6.15 Fidelity loss due to polarization-dependent loss before beam splitter . 183

7.1 Fiber coupling efficiency vs. fiber NA . . . 191
7.2 Ion image spot size analysis plot . . . 195
7.3 Spot diagram through focus with rectangular aperture . . . 196
7.4 Ion images showing effect of rectangular aperture . . . 197
7.5 Shack-Hartmann Wavefront Sensor . . . 201

8.1 Schematic for a three trap network . . . 211
8.2 Plot of mode participation for different mass ratios . . . 219
8.3 Mode participation in a 4 Yb-1 Ba chain . . . 220
8.4 Comparison of the atomic structures of $^{138}Ba^{+}$ and $^{133}Ba^{+}$ . . . 222

8.5 Operations with possible associated crosstalk 223
8.6 Crosstalk vs. beam waist in an all-barium network 225
8.7 Crosstalk from scattered photons in an all-barium quantum network . 227

A.1 RGA scans of partial pressure vs. mass 238

List of Abbreviations

AC	Alternating Current
AOM	Acousto-Optic Modulator
AMU	Atomic Mass Unit
APD	Avalanche Photodiode
AWG	Arbitrary Waveform Generator
CAD	Computer-Aided Design
CCD	Charge-Coupled Device
CDEM	Continuous-Dynode Electron Multiplier
CNOT	Controlled-Not
CPU	Central Processing Unit
CW	Continuous Wave
DC	Direct Current
DDS	Direct Digital Synthesizer
DI	Deionized
DMA	Direct Memory Access
EOM	Electro-Optic Modulator
FPGA	Field-Programmable Gate Array
GHZ	Greenberger–Horne–Zeilinger
H.C.	Hermitian Conjugate
HOM	Hong-Ou-Mandel
HWP	Half Wave Plate
IPA	Isopropyl Alcohol
ITO	Indium Tin Oxide
LOCC	Local Operations and Classical Communication
MS	Mølmer-Sørensen

NA	Numerical Aperture
NEG	Non-Evaporable Getter
NV	Nitrogen-Vacancy
PMT	Photo-Multiplier Tube
PSF	Point Spread Function
QCCD	Quantum Charge-Coupled Device
QWP	Quarter Wave Plate
RF	Radio Frequency
RGA	Residual Gas Analyzer
RMS	Root Mean Square
RTIO	Real Time Input/Output
RWA	Rotating Wave Approximation
SPAM	State Preparation and Measurement
TIG	Tungsten Inert Gas
TTL	Transistor-Transistor Logic
UHV	Ultra-High Vacuum
UPS	Uninterruptible Power Supply

Chapter 1: Introduction

1.1 Quantum Computing Background

Spurred on by a myriad of possible applications beginning with Shor's factoring algorithm [1], quantum computing has progressed dramatically in the last few decades. General proposals [2, 3] gave way to more specific implementations [4] and finally recent claims of quantum computers outperforming classical computers [5]. Quantum computing relies on two uniquely quantum properties: the ability to form superposition states and the correlations of the states of multiple quantum bits (qubits) beyond what is possible in a classical system. Intuitively, we can begin to understand the potential of a quantum computer by noting that for a system with N qubits, 2^N (complex) numbers are required to describe the full state of all of the qubits. Unlike this exponential growth, the amount of information that classical computers can store, grows linearly with the number of bits. Therefore, simulating quantum systems with classical computers rapidly becomes infeasible as the system size grows. To date, a system of 56 qubits has been simulated on a classical computer [6], but this simulation required several terabytes of classical data. To calculate the state of 400 qubits, a classical computer with more bits than the number of particles in the universe would be required.

As mentioned above, Shor's algorithm was one of the first practical uses of a quantum computer proposed, but others have followed. These applications include optimization problems [7], quantum chemistry [8], and simulations of more complicated quantum systems [9]. Several of these applications have been experimentally demonstrated on a small scale, such as in [10] and [11]. However, the full practical capabilities of quantum computers will likely require millions of qubits [12]. The largest current universal quantum computers, however, contain approximately 50 qubits at most. In part, this limitation is due to limited fidelities of quantum operations and the sensitivity of quantum systems to noise, but it is also partially a result of the difficulty of linking many qubits together.

1.2 Trapped Ion Quantum Computers and Networks

There has been progress toward building a quantum computer on many different quantum hardware platforms such as neutral and charged atoms, superconductors, NV centers in diamond, and others [13]. Trapped ions and superconductors are the two most advanced platforms, and each have their own advantages. Trapped ions have the longest coherence times [14], highest single-qubit [15] and two-qubit [16] gate fidelities (99.9999% and 99.92% respectively), and natural all-to-all connectivity. Superconductors, on the other hand, have much shorter gate times than trapped ions [17] and do not require lasers for control. While contributions using each platform have been made to the field, we focus on trapped ions in this thesis.

In small systems, trapped ions have been shown to have extremely high per-

formance in all operations. As stated above, they have the highest single-qubit and two-qubit gate fidelities along with the longest coherence times of any qubit yet demonstrated. Additionally, state preparation and readout with fidelities of $> 99.9\%$ have been achieved [15, 18]. As with many other quibt platforms, the main limitation of trapped ion systems to date is scaling beyond a few tens of qubits. If all of the ions are arranged in a single crystal, some of the motional modes will become increasingly close together in frequency as the chain length increases [19]. These modes are of central importance to entangling operations within a crystal, and this "spectral crowding" will require longer gate times to achieve the same fidelity. Gate times also increase in time proportional to $\sqrt{N}$ due to the increased total mass of the chain, where N is the number of ions in the chain [20]. Additionally, longer chains will result in faster heating of the ions, which will hurt the gate fidelities [21].

We can consider these successes and challenges in the framework of the DiVincenzo criteria, the first five of which are required for a universal quantum computer [22]:

1. The system must be scalable and consist of qubits whose properties are well understood.

2. It must be possible to prepare the qubits in a simple initial state.

3. The coherence time of the qubit must be much longer than the time to perform gates.

4. A universal gate set must be possible.

5. The state of each qubit can be independently measured.

6. Transferring information between stationary and flying qubits is possible (not required, but preferable).

7. If flying qubits are involved, it is important that they maintain their information as they propagate from one location to another.

The second through fourth criteria have clearly already been demonstrated, with the third satisfied, for example, by a combination of our native XX gates and single qubit rotations [23]. For the first criterion, the possibility of scaling is not fundamentally limited, but it is technically challenging. The qubit properties are very well understood, however. The sixth and seventh criteria are requirements for quantum communication, not computing, but they are related to the work we perform in this thesis.

One possible solution to the issue of scaling is the quantum charge-coupled device (QCCD) architecture proposed in [24] and demonstrated in [25]. This architecture requires an ion trap with multiple zones, each with a small ion crystal. The ions can be shuttled between zones to interact temporarily without suffering the negative consequences of adding more ions to a single chain. Utilizing this architecture, it will likely be possible to significantly increase the number of ions in a single trap, but there is substantial overhead involved with moving the ions. A single such trap also likely will not be able to contain millions of ions [26].

An alternative approach, as proposed in [20, 27], is the use of photons to connect multiple relatively small ion traps, each of which contains all the functionality

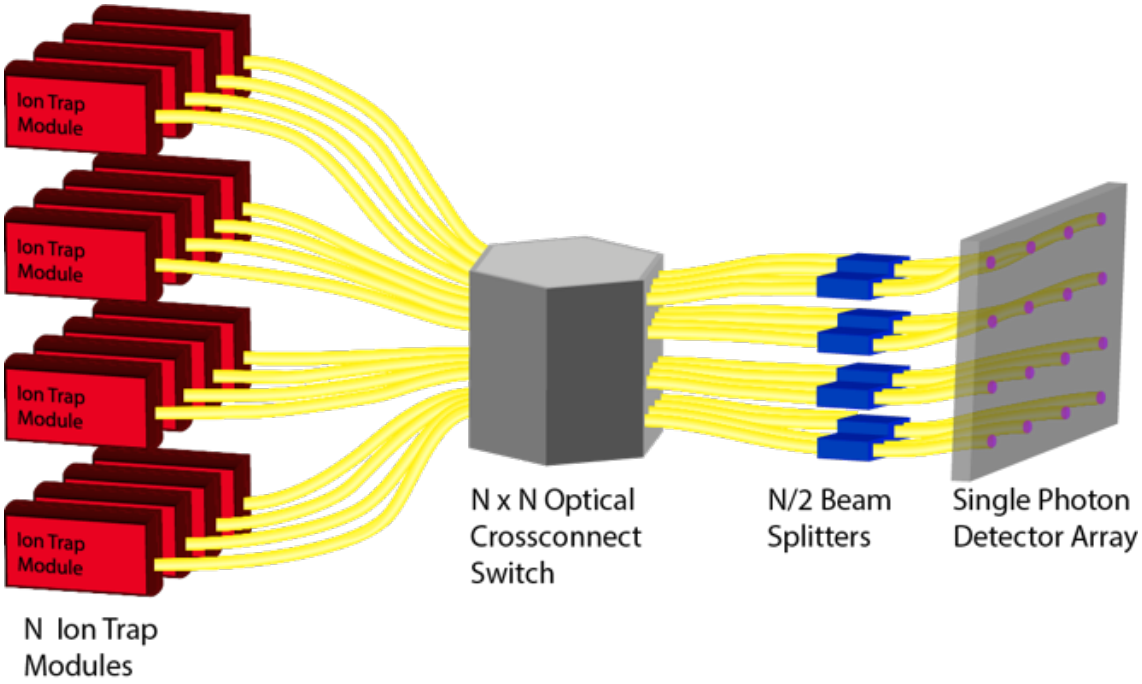

Figure 1.1: Architecture for a modular quantum computer with photonic links. The figure is from [27]. Photonic links connect many small ion traps through a reconfigurable optical switch so that any pair of traps may be connected. The switch is followed by beam splitters in which photons from each path will interfere to become entangled. The arrival of a photon on the detector array heralds entanglement.

of a universal quantum computer. A schematic of this modular quantum computing architecture is shown in Fig. 1.1. Ideally, each of the small ion trap modules would be identical and easily replicable. Each trap contains a communication qubit that generates photons carrying quantum information that can be used to link multiple traps remotely (see Chapter 6 for more details) and a memory qubit for storing information and performing local computations. For the photonic link, the photon qubit must be entangled with the communication qubit.

Photonic transmission is inherently lossy and as such may appear to be a poor link between ion traps. However, probabilistic entanglement generation is acceptable as long as we know when the entanglement attempt has been successful.

In our case, successful detection of two photons, one from each of two of the ion trap modules, on appropriate detectors will indicate that we have succeeded in generating entanglement between the modules. This approach is known as heralding and ensures the fidelity of our entanglement is not harmed due to photon loss. Probabilistic entanglement will, however, require many trials to succeed.

Since it is unlikely that remote entanglement generation will have either a higher rate or a higher fidelity than local operations, we want to be able to perform local computations as well. Additionally, one of the major advantages of ions is the fact that all ions in a trap can interact via their collective motion, which would not be the case for the photonic links [28]. Therefore, each ion trap module will also have some number of computational or memory qubits, which are used for performing local operations and storing memory. The photon generation protocol must not disturb this stored information. As a result, we find that it is essential to use different species of ions for the communication and memory qubits. In our case, we use $^{138}Ba^{+}$ as our communication qubit and $^{171}Yb^{+}$ as our memory qubit. The atomic structure of $^{171}Yb^{+}$ naturally yields long qubit coherence times. Barium ions, on the other hand, have the reddest photon emission on the primary transition to the ground state of any commonly trapped ion, which increases compatibility with fiber optic technology, and a fairly similar mass to ytterbium. This second factor is important for local entangling operations, as will be discussed in Chapter 8. The properties of these ions will be detailed in Chapter 3.

In this thesis, we demonstrate high-fidelity entanglement of a communication qubit with a photonic qubit. We also discuss progress toward demonstrating entan-

glement between two modules. Together, these two steps satisfy DiVincenzo's sixth and seventh criteria. Thus, this architecture serves not only as a quantum computer but also as a system capable of quantum communication. Quantum communication in and of itself has many applications since it is more secure than classical communication because quantum information cannot be copied without affecting the transmitted state [29]. Multiple protocols for quantum communication that are provably secure have been proposed [30, 31].

The main limitation with the modular architecture approach to scaling is the rates we can achieve for the remote entanglement generation. Recent work has demonstrated a large improvement in the achievable rates with Sr^+ as the communication qubit [32], and we anticipate rates that are not quite as high as those but much higher than the previous results from our group [33]. Nonetheless, the time to generate entanglement for both of these results will be approximately 10 ms. For comparison, the time that it takes to perform a local entangling gate is approximately 100 μs. Much of the work discussed in this thesis was devoted to improving those rates with a redesigned experimental system. In the new trap, we place the objectives inside the vacuum chamber and only 6 mm from the ion, enabling us to collect a much larger fraction of the light the ion releases.

So far, there has not been any demonstration of a trapped ion modular quantum computer with more than two nodes. Not only is moving to more than two nodes a critical element of demonstrating the true scalability of this architecture, but the scientific problems that can be explored with tripartite entanglement are also significantly broader than what is possible with two traps [34]. For example,

with three qubits, there are two classes of maximally entangled states–the GHZ and W states–with fundamentally different properties. Each of these states cannot be translated into the other with only local operations and classical communication (LOCC) [35]. With a three-node network, we could explore the properties of these states. Additionally, we could perform experiments with differing types of nonlocality such as the bilocal and triangle configurations [36].

We now have three fully functional ion traps in our lab and all of the building blocks necessary to link together the three traps. To our knowledge, the only demonstration of a three-node network with memories to date has utilized NV centers in diamond [37]. We hope to follow up on this result with a demonstration of a trapped ion network with three nodes in the near future.

1.2.1 Experimental Apparatus

As mentioned above, our lab contains three vacuum chambers, which can be linked together to form a quantum network. Throughout this work, we will refer to the first chamber as Alice, the second as Bob, and the third as Cleo. Alice and Bob have nearly identical designs with regards to the ion traps they contain and the lenses they use for collecting the photons for remote entanglement. Most importantly, the lenses used are out-of-vacuum multi-element objectives with a numerical aperture (NA) of 0.6. Cleo, on the other hand, contains in-vacuum aspheric lenses with an NA of 0.8, which should allow for significantly more light collection. The three vacuum chambers are shown in Fig. 1.2.

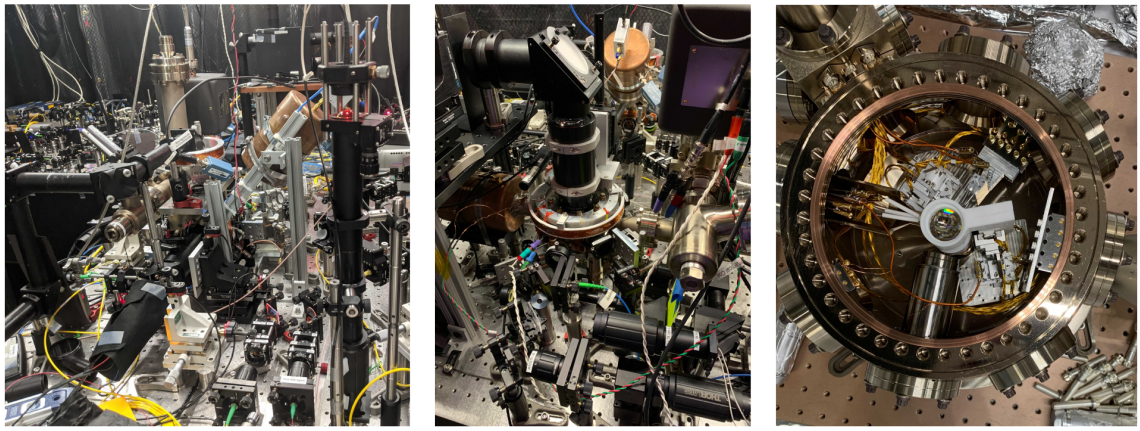

Figure 1.2: Pictures of Alice, Bob, and Cleo. (a) Photograph of Alice and its surrounding optics. (b) Photograph of Bob and its surrounding optics. The large black tube above the vacuum chamber contains the NA 0.6 lens. (c) Photograph of Cleo during construction from a top-down perspective. One of the aspheric lenses is visible in the white holder.

1.3 Thesis Outline

In this thesis, we report progress toward demonstration of a two-node quantum computer using $^{138}Ba^{+}$. We present significant improvements in the fidelity of the ion-photon entanglement and rates compared with previous work from our lab. Additionally, we have designed, built, and begun testing a redesigned ion trap system that should enable much higher rates of remote entanglement generation and can serve as a third node in an ion trap quantum network.

Chapter 2: Theory of Trapped Ion-Laser Interactions: In this chapter, we present the theoretical background behind the interactions of laser light with our ions and the necessary operations on our ions.

Chapter 3: Operations with Ytterbium and Barium Ions: We detail the atomic structure and relevant quantum operations for both $^{171}Yb^{+}$ and $^{138}Ba^{+}$ ions. The discussion of $^{138}Ba^{+}$ includes novel theoretical simulations of our state preparation protocol.

Chapter 4: RF Paul Traps: We discuss the theoretical basis of the RF Paul traps that we use to trap our ions as well as the design of our new trap. Also, we present some experimental optimization and characterization techniques.

Chapter 5: Experimental Design: This thesis as a whole focuses on improving the photonic links between traps for remote entanglement, so we first provide a detailed discussion of the optics we use for collecting these photons in our first two traps. This discussion serves as a motivation for the design of our third trap, which comprises the rest of the chapter. We present the details of the design of both the optical system and vacuum chamber and the reasoning for the choices we made in its development. We also present our tests of this system to characterize both the optics and the ion trap, since the close proximity of the lenses to the ion could have a negative impact on the trap performance.

Chapter 6: Remote Entanglement of $^{138}Ba^{+}$: In this chapter, we discuss the remote entanglement of two barium ions in separate traps. While the results presented are preliminary, we provide a thorough examination of the possible limitations to both the rate and fidelity with a focus on the fact that our implementation of the system is the first that will perform the photonic interference in fiber.

Chapter 7: Optics Considerations for Fiber Coupling Ion Light: During the course of this work, we have developed several techniques for improving the fiber coupling of ion light. We discuss background optics information to contextualize these techniques and the methods we attempted to use to increase the fraction of light successfully collected.

Chapter 8: Outlook: Finally, we conclude by examining some future directions we could take the experiment. During the course of the work discussed in this thesis, it has become apparent that the lack of deterministic state detection in $^{138}Ba^{+}$ is at the very least a significant inconvenience, so we briefly discuss the requirements for a deterministic detection protocol. We also discuss a method to improve the fidelity of the results of our remote entanglement using entanglement distillation. Next, we detail our plan for generating entanglement among three traps and examine the scaling of the protocol to higher numbers of traps. We conclude by looking at the motivation for and details of using $^{133}Ba^{+}$ as our memory qubit instead of $^{171}Yb^{+}$.

Chapter 2: Theory of Trapped Ion-Laser Interactions

In this chapter, we present a general overview of the theory behind the control of ions using lasers. We discuss here only operations that are common to both barium and ytterbium ions. The details of the operations for each specific ion will be discussed in Chapter 3.

2.1 Doppler cooling

Once ions are in trap, they must be cooled so they crystallize. We accomplish this using a process that relies on the Doppler shift of photons relative to a moving atom. Here, we discuss the theory behind this process.

A photon with wavenumber $k = 2\pi/\lambda$ carries momentum $\hbar\vec{k}$ where the directionality of the vector $\vec{k}$ is in the direction of propagation. When an atom absorbs a photon, this momentum is transferred to the atom. In particular, when an atom absorbs light from a laser beam, the resulting force on the atom is $\vec{F} = d\vec{p}/dt = \hbar\vec{k}\Gamma_{sc}$ where Γ_{sc} is the scattering rate of the atom [38]. After being excited, the atom will reemit a photon. Unlike absorption, however, emission is isotropic and thus, when averaged over many photons scattered, will not change the net momentum of the atom.

The ion scattering rate Γ_{sc} as a function of laser detuning for an approximately two-level system is [39]

$$\Gamma_{sc} = \frac{\frac{I}{I_{sat}}\frac{\gamma}{2}}{1 + \frac{I}{I_{sat}} + \frac{4\Delta_l^2}{\gamma^2}} \tag{2.1}$$

where

$$I_{sat} = \frac{\hbar\gamma\omega_0^3}{12\pi c^2}\,. \tag{2.2}$$

γ is the natural linewidth of the relevant atomic transition, ω_0 is the resonant frequency of the atomic transition, and $\Delta_l = \omega_0 - \omega_l$ is the detuning of the laser frequency ω_l from resonance. When the ion is in motion, the scattering rate is modified by the Doppler shift [38]

$$\Gamma_{sc} = \frac{\frac{I}{I_{sat}}\frac{\gamma}{2}}{1 + \frac{I}{I_{sat}} + \frac{4(\Delta_l+\omega_D)^2}{\gamma^2}}\,. \tag{2.3}$$

Here, $\omega_D = -\vec{k}\cdot\vec{v}$ is the Doppler shift seen by a moving atom. The force on the atom is thus velocity and frequency dependent.

When the velocity of the atom is in the opposite direction from the propagation of the laser beam, the force on the atom is negative and will slow the atom. In free space, it would be necessary to have beams in all three axes and both directions to ensure that there is always a cooling force on the ion. The potential of the ion trap loosens this requirement, and if the beam is not parallel to any of the principle axes and the axes are non-degenerate ($\omega_x \neq \omega_y \neq \omega_z$) [40] (see Sec. 4.3.3), a single Doppler cooling beam is sufficient [40, 41]. Additionally, it can be shown that optimal cooling for a two level atom is achieved when $\omega_l = -\gamma/2$, and the

minimum energy of the ion for a beam with equal components along all principal axes (for example, $\hat{k} = \frac{1}{\sqrt{3}}(\hat{x} + \hat{y} + \hat{z})$) is $E_{min} = \frac{\hbar\gamma}{4}$ [40]. This energy limit can be used to calculate an effective temperature limit by setting $T_{min} \approx E_{min}/k_B$, which is of order 100 μK for Yb.

2.2 Coherent Operations

Another important aspect of controlling ions is the ability to coherently rotate between the qubit states. This can be accomplished using microwave radiation for Yb and RF radiation for Ba. However, it can be advantageous to use an optical drive instead. In particular, the use of a laser beam can couple the motional state of an ion to its internal state (see Sec. 2.2.1) and thus entangle multiple ions in a chain via their Coulomb interaction. Additionally, delivering sufficient power of RF radiation to the ion can be difficult due to the shielding of the chamber. Therefore, we instead use Raman transitions driven by laser light to rotate between the qubit states. Details of these operations for each atomic species can be found in Sec. 3.1.4 for Yb and Secs. 3.2.5 and 3.2.6 for Ba.

To drive these rotations, we use a pulsed Nd:YVO_4 laser.[1] For both of these lasers, 1064 nm radiation is frequency-doubled to 532 nm light, which we use for Ba, and frequency-tripled to 355 nm, which we use for Yb. While these lasers produce a frequency comb, it has been shown that for our purposes it can be effectively treated as a continuous wave (CW) laser [42].

Let us assume that we apply a laser beam to the ion with electric field with

[1] Initially Spectra Physics Vanguard then Coherent Paladin Compact 355.

two beams labeled α and β

$$\vec{E}\left(\vec{r}\right) = \sum_{j=\alpha,\beta} \frac{E_j}{2}\left(\hat{\epsilon}_j e^{i\left(\vec{k}_j\cdot\vec{r}-\omega_j t-\phi_j\right)} + h.c.\right). \tag{2.4}$$

Here, $\hat{\epsilon}_{\alpha,\beta}$ is the polarization vector of the corresponding beam, $\vec{k}_j$ is the wave number with the direction of beam propagation, $\vec{r}$ is the ion position, ω_j is the carrier frequency of the j^{th} beam, and ϕ_j is the beam phase. The electric fields will couple to the dipole transitions from the qubit states to the excited state. These couplings create the interaction Hamiltonian

$$\begin{aligned} H_{int} &= -\vec{\mu}\cdot\vec{E} \\ &= -\vec{\mu}\cdot\sum_{j=\alpha,\beta}\frac{E_j}{2}\cdot\left(\hat{\epsilon}_j e^{i(-\omega_j t-\phi_j)} + \hat{\epsilon}_j^* e^{-i(-\omega_j t-\phi_j)}\right) \end{aligned} \tag{2.5}$$

where we have combined the positional term with the phase ϕ_j. For now, the positional dependence is unimportant, but will become relevant when we consider the coupling of two laser beams to the motion of the ions in Section 2.2.1.

Additionally, we need to account for the intrinsic atomic Hamiltonian H_{atom} for our ideal three level system (Fig. 2.1)

$$H_{atom} = \hbar\begin{pmatrix} -\frac{\omega_q}{2} & 0 & 0 \\ 0 & \frac{\omega_q}{2} & 0 \\ 0 & 0 & \omega_e \end{pmatrix}. \tag{2.6}$$

Here, I have chosen to consider the zero-energy position as halfway in between the

two qubit levels. We now consider the time-dependent Schrödinger equation

$$i\hbar\frac{\partial}{\partial t}|\Psi\rangle = H|\Psi\rangle. \tag{2.7}$$

When the interaction is turned off, the total Hamiltonian H_{total} is equal to H_{atom}. As always, we can write the wavefunction $|\Psi\rangle$ in terms of any complete basis; we choose for this purpose the eigenstates of H_{atom} $|0\rangle$, $|1\rangle$ and $|e\rangle$. The total time-dependent wavefunction of the atom is then $|\Psi\rangle = \sum_m c_m(t)|\psi_m\rangle$ where $|\psi_m\rangle$ are the eigenstates of H_{atom}. Substituting into the Schrödinger equation (Eq. 2.7) and by multiplying by $\langle\psi_n|$, we obtain

$$i\dot{c}_n = \omega_n c_n, \tag{2.8}$$

which gives us a set of differential equations. The solutions to this set of equations are $c_n(t) = Ae^{-i\omega_n t}$. We can transform into a frame rotating with the frequencies ω_n by defining $\tilde{c}_n \equiv c_n e^{i\omega_n t}$. We will use this transformation later in the calculation.

We now return to considering the effect of the interaction Hamiltonian, so the Hamiltonian is now $H_{total} = H_{atom} + H_{int}$. Like before, we express the wavefunction in terms of the eigenstates of H_{atom} and then multiply the time-dependent Schrödinger equation by $\langle\psi_n|$. This process yields the differential equations

$$\begin{aligned} i\hbar\left\langle\psi_n\left|\frac{\partial}{\partial t}\sum_m c_m\right|\psi_m\right\rangle &= \left\langle\psi_n\left|\left(-\vec{\mu}\cdot\vec{E} + H_{atom}\right)\sum_m c_m\right|\psi_m\right\rangle \\ \Rightarrow i\hbar\dot{c}_n &= \sum_m c_m\left\langle\psi_n\left|-\vec{\mu}\cdot\vec{E}\right|\psi_m\right\rangle + \hbar\omega_n c_n\,. \end{aligned} \tag{2.9}$$

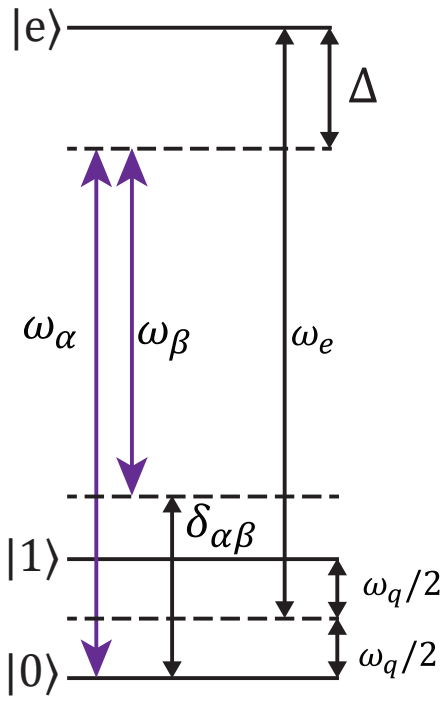

Figure 2.1: Simple level scheme for Raman transitions.

The laser beams cannot couple $|0\rangle$ and $|1\rangle$ together directly and they do not couple either state to itself, so the only relevant matrix elements for the H_{int} term are $\left\langle 0(1)\left|-\vec{\mu}_{0(1)e}\cdot\vec{E}\right|e\right\rangle$. For simplicity, we assume E_α couples only to $|0\rangle$ and E_β couples only to $|1\rangle$. Defining $V_{nm}\equiv\langle\psi_n|H_{int}|\psi_m\rangle$, we obtain the corresponding matrix elements:

$$\begin{aligned}
V_{0e} &= \frac{|E_\alpha|}{2}\left\langle 0\left|-\vec{\mu}\cdot\left(\hat{\epsilon}_\alpha e^{-i(\omega_\alpha t+\phi_\alpha)}+\hat{\epsilon}_\alpha^* e^{i(\omega_\alpha t+\phi_\alpha)}\right)\right|e\right\rangle \\
&= \hbar\left(g_{0e}e^{-i\omega_\alpha t}+g_{0e}^* e^{i\omega_\alpha t}\right) \\
V_{1e} &= \hbar\frac{|E_\beta|}{2}\left\langle 1\left|-\vec{\mu}\cdot\left(\hat{\epsilon}_\beta e^{-i\left(\omega_\beta t+\phi_\beta\right)}+\hat{\epsilon}_\beta^* e^{i\left(\omega_\beta t+\phi_\beta\right)}\right)\right|e\right\rangle \\
&= \hbar\left(g_{1e}e^{-i\omega_\beta t}+g_{1e}^* e^{i\omega_\beta t}\right)
\end{aligned} \tag{2.10}$$

where we have defined

$$g_{nm} = \frac{|E_j|}{2\hbar} \langle \psi_n | - \vec{\mu} \cdot \hat{\epsilon_j} \, |\psi_m\rangle \, e^{-i\phi_j}. \tag{2.11}$$

We can choose our coordinates such that $g^*_{nm} = \frac{|E_j|}{2\hbar} \langle \psi_n | - \vec{\mu} \cdot \hat{\epsilon_j}^* \, |\psi_m\rangle \, e^{i\phi_j}$. This choice will effectively determine our x and y axes for rotations.

With these definitions, we can now write down differential equations for the probability amplitudes of each state

$$i\dot{c}_0 = \left(g_{0e}e^{-i\omega_\alpha t} + g^*_{0e}e^{i\omega_\alpha t}\right) c_e - \frac{\omega_q}{2} c_0 \tag{2.12}$$

$$i\dot{c}_1 = \left(g_{1e}e^{-i\omega_\beta t} + g^*_{1e}e^{i\omega_\beta t}\right) c_e + \frac{\omega_q}{2} c_1 \tag{2.13}$$

$$i\dot{c}_e = \left(g^*_{0e}e^{i\omega_\alpha t} + g_{0e}e^{-i\omega_\alpha t}\right) c_0 + \left(g^*_{1e}e^{i\omega_\beta t} + g_{1e}e^{-i\omega_\beta t}\right) c_1 + \omega_e c_e. \tag{2.14}$$

In the rotating frame, these equations become

$$i\dot{\tilde{c}}_0 = \left(g_{0e}e^{-i(\omega_\alpha+\omega_e)t} + g^*_{0e}e^{-i\Delta_\alpha t}\right) e^{-i\frac{\omega_q}{2}t} \tilde{c}_e \tag{2.15}$$

$$i\dot{\tilde{c}}_1 = \left(g_{1e}e^{-i\left(\omega_\beta+\omega_e\right)t} + g^*_{1e}e^{-i\Delta_\beta t}\right) e^{i\frac{\omega_q}{2}t} \tilde{c}_e \tag{2.16}$$

$$i\dot{\tilde{c}}_e = \left(g^*_{0e}e^{i(\omega_\alpha+\omega_e)t} + g_{0e}e^{i\Delta_\alpha t}\right) e^{i\frac{\omega_q}{2}t} \tilde{c}_0 + \left(g^*_{1e}e^{i\left(\omega_\beta+\omega_e\right)t} + g_{1e}e^{i\Delta_\beta t}\right) e^{-i\frac{\omega_q}{2}t} \tilde{c}_1 \tag{2.17}$$

where the laser detuning from resonance $\Delta_{\alpha(\beta)}$ is defined as $\Delta_{\alpha(\beta)} \equiv \omega_e - \omega_{\alpha(\beta)}$.

So far, all of our calculations have been exact. To make further progress, we must make some approximations based on our experimental parameters. For our first approximation, we note that $\omega_{\alpha(\beta)} + \omega_e >> \Delta_{\alpha(\beta)}$. Thus, terms where the time

dependence scales with $\omega_{\alpha(\beta)} + \omega_e$ will oscillate much faster than those that scale with Δ and will average out. We can therefore drop those terms and perform a rotating wave approximation (RWA). This approximation yields

$$i\dot{\tilde{c}}_0 = g_{0e}^* e^{-i\left(\Delta_\alpha + \frac{\omega_q}{2}\right)t} \tilde{c}_e \tag{2.18}$$

$$i\dot{\tilde{c}}_1 = g_{1e}^* e^{-i\left(\Delta_\beta - \frac{\omega_q}{2}\right)t} \tilde{c}_e \tag{2.19}$$

$$i\dot{\tilde{c}}_e = g_{0e} e^{i\left(\Delta_\alpha + \frac{\omega_q}{2}\right)t} \tilde{c}_0 + g_{1e} e^{i\left(\Delta_\beta - \frac{\omega_q}{2}\right)t} \tilde{c}_1 \,. \tag{2.20}$$

We do not try to solve these equations exactly; instead we use a process known as adiabatic elimination [43], which effectively decouples the excited state population from c_0 and c_1. This approximation relies on the assumption that any time variation not explicitly in an exponential is much slower than the time dependence $e^{i\Delta_{\alpha(\beta)}t}$, which can be verified at the end of the calculation. In the differential equation for $\tilde{c}_e$, we therefore treat all other variables ($\tilde{c}_0$, $\tilde{c}_1$, g_{0e}, and g_{1e}) as constant and directly integrate this equation.

The result of this integration is

$$\tilde{c}_e = \frac{g_{0e}}{\Delta_\alpha + \frac{\omega_q}{2}} \left(1 - e^{-i\left(\Delta_\alpha + \frac{\omega_q}{2}\right)t}\right) \tilde{c}_0 + \frac{g_{1e}}{\Delta_\beta - \frac{\omega_q}{2}} \left(1 - e^{i\left(\Delta_\beta - \frac{\omega_q}{2}\right)t}\right) \tilde{c}_1 \tag{2.21}$$

where we have imposed the initial condition $\tilde{c}_e(0) = 0$. We now substitute this result back into Eqs. 2.18 and 2.19. Additionally, we note that $\Delta_{\alpha(\beta)} \gg \frac{\omega_q}{2}$, so we further

simplify the equations by setting $\Delta_{\alpha(\beta)} - \frac{\omega_q}{2} = \Delta_{\alpha(\beta)} + \frac{\omega_q}{2} = \Delta_{\alpha(\beta)}$. The result is

$$i\dot{\tilde{c}}_0 = \frac{|g_{0e}|^2}{\Delta_\alpha}\left(e^{-i\Delta t} - 1\right)\tilde{c}_0 + \frac{g_{0e}^* g_{1e}}{\Delta_\beta}\left(e^{-i\Delta_\alpha t} - e^{-i\delta_{\alpha\beta}t}\right)e^{-i\omega_q t}\tilde{c}_1 \tag{2.22}$$

$$i\dot{\tilde{c}}_1 = \frac{g_{1e}^* g_{0e}}{\Delta_\alpha}\left(e^{-i\Delta_\beta t} - e^{i\delta_{\alpha\beta}t}\right)e^{i\omega_q t}\tilde{c}_0 + \frac{|g_{1e}|^2}{\Delta_\beta}\left(e^{-i\Delta_\beta t} - 1\right)\tilde{c}_1 \tag{2.23}$$

where we define $\delta_{\alpha\beta} \equiv \omega_\beta - \omega_\alpha$.

The next steps of this calculation are to make one more RWA and then finally transform back into the non-rotating frame to better understand the behavior that we observe in the lab. First, we note again that $\Delta_{\alpha(\beta)} \gg \omega_q$. Similarly to the first RWA that we performed, this comparison means that when these equations are integrated, the terms with $\Delta_{\alpha(\beta)}$ dependence will oscillate much faster than those with ω_q dependence, and we thus drop all terms with $e^{\pm i\Delta_{\alpha(\beta)}t}$

$$i\dot{\tilde{c}}_0 = -\frac{|g_{0e}|^2}{\Delta_\alpha}\tilde{c}_0 - \frac{g_{0e}^* g_{1e}}{\Delta_\beta}e^{-i\left(\delta_{\alpha\beta}+\omega_q\right)t}\tilde{c}_1 \tag{2.24}$$

$$i\dot{\tilde{c}}_1 = -\frac{g_{1e}^* g_{0e}}{\Delta_\alpha}e^{i\left(\delta_{\alpha\beta}+\omega_q\right)t}\tilde{c}_0 - \frac{|g_{1e}|^2}{\Delta_\beta}\tilde{c}_1. \tag{2.25}$$

Next, we write the differential equations by undoing the transformation to the rotating frame. We also note that in our experimental regime $\Delta_\alpha \approx \Delta_\beta$, so we define $\Delta \equiv \frac{1}{2}\left(\Delta_\alpha + \Delta_\beta\right)$ and let $\Delta_\alpha = \Delta_\beta = \Delta$. After some algebra, the differential

equations become

$$i\dot{c}_0 = -\left(\frac{|g_{0e}|^2}{\Delta} + \frac{\omega_q}{2}\right) c_0 - \frac{g_{0e}^* g_{1e}}{\Delta} e^{-i\delta_{\alpha\beta}t} c_1 \tag{2.26}$$

$$i\dot{c}_1 = -\frac{g_{1e}^* g_{0e}}{\Delta} e^{i\delta_{\alpha\beta}t} c_0 - \left(\frac{|g_{1e}|^2}{\Delta} - \frac{\omega_q}{2}\right) c_1. \tag{2.27}$$

We now define a second rotating frame where

$$c_0' = c_0 e^{-i\frac{\delta_{\alpha\beta}}{2}t}$$

$$c_1' = c_1 e^{i\frac{\delta_{\alpha\beta}}{2}t}. \tag{2.28}$$

The differential equations can be written as a single matrix equation in this new rotating frame

$$i\frac{\partial}{\partial t}\begin{pmatrix} c_0' \\ c_1' \end{pmatrix} = -\begin{pmatrix} \frac{|g_{0e\alpha}|^2}{\Delta_\alpha} + \frac{\omega_q - \delta_{\alpha\beta}}{2} & \frac{g_{0e\alpha}^* g_{1e\beta}}{\Delta_\beta} \\ \frac{g_{1e\beta}^* g_{0e\alpha}}{\Delta_\alpha} & \frac{|g_{1e\beta}|^2}{\Delta_\beta} - \frac{\omega_q - \delta_{\alpha\beta}}{2} \end{pmatrix} \begin{pmatrix} c_0' \\ c_1' \end{pmatrix}. \tag{2.29}$$

We define several parameters to simplify this equation:

$$\delta_0 = \frac{|g_{0e}|^2}{\Delta} - \frac{\delta_{\alpha\beta}}{2} \tag{2.30}$$

$$\delta_1 = \frac{|g_{1e}|^2}{\Delta} + \frac{\delta_{\alpha\beta}}{2} \tag{2.31}$$

$$\delta_2 = \frac{g_{0e}^* g_{1e}}{\Delta}. \tag{2.32}$$

These equations correspond to an effective Hamiltonian

$$H_{eff} = -\hbar \begin{pmatrix} \delta_0 + \frac{\omega_q}{2} & \Omega \\ \Omega & \delta_1 - \frac{\omega_q}{2} \end{pmatrix}. \tag{2.33}$$

This result assumes that $\Omega = \Omega^*$ and specifically that $g_{0e}g_{1e}^* = g_{0e}^* g_{1e}$. This is a Hermitian matrix, and can therefore be expressed in terms of Pauli operators as [43]

$$H_{eff} = -\hbar \left[\Omega \hat{\sigma}_x + \frac{1}{2} \left(\omega_q + \delta_0 - \delta_1 \right) \hat{\sigma}_z + \left(\delta_0 + \delta_1 \right) \mathbb{1} \right]. \tag{2.34}$$

Now we can gain some insight into what the parameters defined in Eqs. 2.30-2.32 mean. The Pauli matrices are generators of rotations about the corresponding axis (see e.g. [44]), so this Hamiltonian will drive rotations about the x axis with frequency Ω. Note that, had we chosen a complex Ω, the rotation axis simply would have been a different axis in the $x-y$ plane, as there would have been a σ_y term in the Hamiltonian. Additionally, if the ion is not in one of the energy eigenstates $|0\rangle$ or $|1\rangle$, it will generally precess about the z axis with a frequency equal to the qubit splitting. The effect of the σ_z term in the Hamiltonian is to modify this precession frequency by $\delta_0 - \delta_1$. This effective energy shift corresponds to the two-photon Stark shift the ion experiences upon application of the electric field described here. δ_0 and δ_1 are the two-photon AC Stark shifts on $|0\rangle$ and $|1\rangle$, respectively; their difference is the "differential" Stark shift. The term proportional to the identity matrix does not affect the evolution of the ion state.

We can go further and solve Eq. 2.29 using standard linear algebra. While the

resulting probability amplitudes $c_0'(t)$ and $c_1'(t)$ are very complicated functions of the various parameters, the probabilities $|c_0'(t)|^2$ and $|c_1'(t)|^2$ are much simpler, and we can gain significant insight into the dynamics of the system by considering these results. In particular, solving the system for the initial conditions $|c_0'|^2(0) = 1$ and $|c_1'|^2(0) = 0$ gives the following equations for the time dependence of the qubit state populations

$$|c_0'(t)|^2 = |c_0(t)|^2 = 1 - \left(\frac{\Omega}{\Omega'}\right)^2 \sin^2(\Omega' t) \tag{2.35}$$

$$|c_1'(t)|^2 = |c_1(t)|^2 = \left(\frac{\Omega}{\Omega'}\right)^2 \sin^2(\Omega' t) \tag{2.36}$$

where we have defined the effective Rabi frequency

$$\Omega' = \sqrt{\Omega^2 + \left(\frac{\delta_0 - \delta_1 + \omega_q}{2}\right)^2}\,. \tag{2.37}$$

Thus, full population transfer from $|0\rangle$ to $|1\rangle$ will only occur if $\Omega = \Omega'$, which gives us a resonance condition. This condition will be satisfied when

$$\delta_{\alpha\beta} = \frac{|g_{0e\alpha}|^2 - |g_{1e\beta}|^2}{\Delta} + \omega_q\,, \tag{2.38}$$

or, if $|g_{0e\alpha}|^2 = |g_{1e\beta}|^2$, $\delta_{\alpha\beta} = \omega_q$, as we anticipate.

In practice, the ions have more than a single excited state, and the laser beam will couple to all allowed transitions. The results of the above discussion are easily generalized, and we find that the dynamics are the same as before, just with the

Rabi frequency and AC Stark shifts summed over all excited states.

2.2.1 Driving Ion Motion Using Coherent Operations

So far, we have disregarded the spatial dependence of the electric fields and incorporated the term $e^{i\vec{k}_{\alpha(\beta)}\cdot\vec{r}}$ into the phase $\phi_{\alpha(\beta)}$, which we, in turn, incorporated into the single photon Rabi frequencies. However, if we redefine the single photon Rabi frequencies as

$$\begin{aligned} g_{0e\alpha} &= \frac{|E_\alpha|}{2\hbar} \langle 0 | -\vec{\mu}\cdot\hat{\epsilon}_\alpha | e\rangle \\ g_{1e\beta} &= \frac{|E_\beta|}{2\hbar} \langle 1 | -\vec{\mu}\cdot\hat{\epsilon}_\beta | e\rangle \ , \end{aligned} \tag{2.39}$$

we find that the cross-terms coupling $|0\rangle$ to $|1\rangle$ depend on $e^{\pm i\Delta\vec{k}\cdot\vec{r}}$. For a single principal axis of the trap, the position operator r_i can be written in terms of raising and lowering operators for the motional modes

$$r_i = r_{i_0} + q_i\left(a + a^\dagger\right) \tag{2.40}$$

where r_{i_0} is the equilibrium position of the ion, a and $a^\dagger$ are the lowering and raising operators for the harmonic oscillator modes respectively, and

$$q_i = \sqrt{\frac{\hbar}{2m\omega_{osc_i}}}. \tag{2.41}$$

Here, m is the mass of the ion and ω_{osc_i} is the secular frequency in the i^{th} principal axis.

It can then be shown, as in [45], that transitions will be driven between the states $|0,n\rangle$ and $|1,n'\rangle$ if the detuning $\delta_{\alpha\beta}$ is set to

$$\delta_{\alpha\beta} = \omega_q + \frac{|g_{0e\alpha}|^2 - |g_{1eb}^2|}{\Delta} + (n' - n)\,\omega_{osc_i}. \tag{2.42}$$

These transitions will be driven with a modified Rabi frequency [45]

$$\Omega_{n',n} \equiv \Omega \left| \left\langle n' \left| e^{i\eta\left(a+a^\dagger\right)} \right| n \right\rangle \right| \tag{2.43}$$

$$= \Omega e^{-\frac{\eta^2}{2}} \sqrt{\frac{n_<!}{n_>!}} \eta^{|n'-n|} L_{n_<}^{|n'-n|}\left(\eta^2\right) \tag{2.44}$$

where η is the Lamb-Dicke parameter $\Delta k q_i$, $n_>$ is the larger of n, and L_n^α is the generalized Laguerre polynomial.

Here, we have discussed the coupling to the motion for a single ion, but the calculation can be easily expanded to include multiple ions. The coupling of the internal ion state of each ion to the motional state can be used to drive entangling gates between ions [46, 47]. This treatment can also be extended to ions of multiple masses, as in [48, 49]. The relevance of this discussion is limited in this work, since the results we present do not rely on local entanglement via the motion of the ions. It is important, however, to note the possibility, because it will be crucial for future work.

2.3 Calculation of Dipole Matrix Elements

In the previous section, we left the single photon Rabi frequencies written in terms of the matrix elements for a dipole transition driven by a laser beam with unit polarization vector $\hat{\epsilon}$ without delving into the calculation of those matrix elements. However, in order to compute the strength of various transitions, we need to be able to calculate these matrix elements.

The core of these calculations requires the quantum theory of angular momentum addition. In particular, the atomic energy levels are determined by their angular momenta. Depending on the atom, this can consist of their nuclear spin $\mathbf{I}$, the orbital angular momentum of the electron $\mathbf{L}$, and the spin of the electron $\mathbf{S}$. These angular momenta add to form the total angular momentum of each energy level. For a spin-0 nucleus like $^{138}Ba^{+}$, the relevant combination is the angular momenta of the spins. $\mathbf{L}$ and $\mathbf{S}$ add via spin-orbit coupling to form the fine structure, which is determined by the quantum number $\mathbf{J} = \mathbf{L} + \mathbf{S}$. For an atom where $\mathbf{I} \neq 0$, the nuclear spin must be added to $\mathbf{J}$, yielding $\mathbf{F} = \mathbf{J} + \mathbf{I}$ for the total angular momentum. We then wish to add the angular momentum carried by a photon to the intrinsic atomic angular momentum to drive transitions. First, we will calculate the matrix elements for the simpler case of $\mathbf{I} = 0$, and then expand that derivation to atoms with hyperfine structure. For all of the calculations, we follow the derivation in [50].

2.3.1 Dipole Matrix Elements for Atoms with $\mathbf{I} = 0$

To begin, we need to determine the good quantum numbers, which we will use to describe the atomic states. In the case of fine structure, we use $\mathbf{J}$. We write the matrix elements in terms of the radial quantum number α, $J = |\mathbf{J}|$ and the projection of $\mathbf{J}$ on the quantization axis m_J as $|\alpha, J, m_J\rangle$. Then, the matrix element for a transition between a ground state $|g\rangle$ and an excited state $|e\rangle$ is

$$\mu_{eg} = \langle \alpha', J', m'_J | \, \vec{\mu} \cdot \hat{\epsilon} \, | \alpha, J, m_J \rangle \tag{2.45}$$

where $\{\alpha', J', m'_J\}$ are the quantum numbers labeling $|e\rangle$ and $\{\alpha, J, m_J\}$ are the quantum numbers for $|g\rangle$. The light, however, couples to the orbital angular momentum of the electron, so we instead need to write the transitions in terms of $\mathbf{L}$. Therefore, we need to decompose J into its L and S components. To accomplish this, we write $|\alpha, J, m_J\rangle$ in the L and S bases using Clebsch-Gordan coefficients

$$|\alpha, J, m_J\rangle = \sum_i C_i \, |\alpha, L, m_L\rangle \, |S, m_S\rangle \tag{2.46}$$

where C_i are the relevant Clebsch-Gordan coefficients

$$C_i = \langle L, m_L; S, m_S \, | J, m_J \rangle = (-1)^{-L+S-m_J} \sqrt{2J+1} \begin{pmatrix} L & S & J \\ m_L & m_S & -m_J \end{pmatrix}. \tag{2.47}$$

We can now write the original matrix element in terms of the S and L bases,

accounting for the fact that the light cannot act on the spin of the electron and only on its orbital angular momentum

$$\begin{aligned}\mu_{eg} &= \sum_{ij} C_i C_j \langle \alpha, L', m'_L | \langle S', m'_S | \vec{\mu} \cdot \hat{\epsilon} | \alpha, L, m_L \rangle | S, m_S \rangle \\ &= \sum_{ij} C_i C_j \langle \alpha', L', m'_L | \vec{\mu} \cdot \hat{\epsilon} | \alpha, L, m_L \rangle \delta_{S',S} \delta m'_S, m_S \,. \end{aligned} \tag{2.48}$$

Next, we consider the matrix element $\langle \alpha', L', m'_L | \vec{\mu} \cdot \hat{\epsilon} | \alpha, L, m_L \rangle$. To proceed, we must consider the polarization vector of the light. In particular, we note that there are three relevant polarizations as seen by the atom, which can be written in terms of the spherical harmonics Y_1^q [51, 52]

$$\boldsymbol{\pi} = Y_1^0 = i\sqrt{\frac{3}{16}} \sin\theta \hat{\theta} \tag{2.49}$$

$$\boldsymbol{\sigma}^{\pm} = Y_1^{\pm 1} = ie^{\pm i\phi} \sqrt{\frac{3}{16\pi}} \left(\pm \cos\theta \hat{\theta} + i\hat{\phi} \right) \tag{2.50}$$

where θ is the polar angular coordinate and ϕ is the azimuthal coordinate with the $\hat{z}$ axis defined by the magnetic field. The dot product $\vec{\mu} \cdot \hat{\epsilon}$ can then be written in terms of an irreducible tensor operator of rank one $T_1^q = \vec{\mu} \cdot Y_1^q$. We use the Wigner-Eckart theorem to write this matrix element in terms of a Wigner-3j symbol and a reduced matrix element, which depends only on the radial quantum number α and the total orbital angular momentum L but not the projection of the orbital angular

momentum on the quantization axis m_L [53]

$$\langle \alpha', L', m'_L | \, \vec{\mu} \cdot \hat{\epsilon} \, | \alpha, L, m_L \rangle = (-1)^{L'-m'_L} \begin{pmatrix} L' & 1 & L \\ -m'_L & q & m \end{pmatrix} \langle \alpha', L' | \, |\mu| \, | \alpha, L \rangle \ . \quad (2.51)$$

When we substitute Eq. 2.51 into Eq. 2.48, we obtain [50]

$$\mu_{eg} = (-1)^{L'+S-m'_J} \begin{Bmatrix} L' & J & S \\ J & L & 1 \end{Bmatrix} \begin{pmatrix} J & 1 & J' \\ m_J & q & -m'_J \end{pmatrix} \times \sqrt{(2J+1)(2J'+1)} \, \langle \alpha', L' | \, |\mu| \, | \alpha, L \rangle \quad (2.52)$$

where the curly braces indicate the Wigner-6j symbol.

Additionally, we follow [54] to compute the reduced matrix element in terms of constants and parameters that can be experimentally determined. In particular, we use Fermi's golden rule, which gives the rate of a transition in terms of the reduced matrix element. After integrating emission over all space, the transition rate or natural linewidth γ is given by

$$\gamma = \frac{1}{4\pi\epsilon_0} \frac{4\omega_0^3}{3\hbar c^3} \frac{|\langle \alpha', L' | \, |\mu| \, | \alpha, L \rangle|^2}{2L'+1}$$
$$\Rightarrow |\langle \alpha', L' | \, |\mu| \, | \alpha, L \rangle|^2 = \frac{3\pi\epsilon_0 \hbar c^3 \gamma}{\omega_0^3} (2L'+1) \ . \quad (2.53)$$

Here, ω_0 is the resonant frequency of the relevant transition. Both ω_0 and γ can be measured, and thus we have completely determined the value of the matrix element in terms of known parameters.

An important characteristic of the Wigner-3j symbol in Eq. 2.52 is that it is only nonzero for $m_J + q - m'_J = 0$. Thus, we have the following selection rules

$$\begin{aligned} \pi: &\ \Delta m_J = 0 \\ \sigma^+: &\ \Delta m_J = 1 \\ \sigma^-: &\ \Delta m_J = -1\,. \end{aligned} \tag{2.54}$$

2.3.2 Dipole Matrix Elements of Atoms with Nonzero Nuclear Spin

The atomic eigenstates in this case now must be initially expressed in terms of the total angular momentum $\mathbf{F} = \mathbf{J} + \mathbf{I}$ where $\mathbf{I}$ is the nuclear spin. The matrix elements are therefore initially written as

$$\langle \alpha', F', m'_F |\, \vec{\mu} \cdot \hat{\epsilon}\, | \alpha, F, m_F \rangle\,. \tag{2.55}$$

First, we write $|\alpha, F, m_F\rangle$ in terms of the J and I basis using the same technique we used to write $|\alpha, J, m_J\rangle$ in terms of L and S states

$$|\alpha, F, m_F\rangle = \sum_i \langle J, m_J; I, m_I\, | F, m_F \rangle\, |\alpha, J, m_J\rangle\, |I, m_I\rangle\ . \tag{2.56}$$

We then proceed as above to write the resulting matrix elements $\langle \alpha', J', m'_J |\, \vec{\mu} \cdot \hat{\epsilon}\, | \alpha, J, m_J \rangle$ in terms of L and S. Since the remainder of this calculation is essentially

the same as above, we simply state the final result

$$\mu_{eg} = (-1)^{1+L'+S+J+J'+I-m'_F} \begin{Bmatrix} L' & J' & S \\ J & L & 1 \end{Bmatrix} \begin{Bmatrix} J' & F' & I \\ F & J & 1 \end{Bmatrix} \begin{pmatrix} F & 1 & F' \\ m_F & q & -m'_F \end{pmatrix}$$
$$\times \sqrt{(2J+1)(2J'+1)(2F+1)(2F'+1)} \langle \alpha', L' | |\mu| | \alpha, L \rangle \ . \tag{2.57}$$

Again, we also note the selection rules for this system, which are the same as stated in Eq. 2.54, but with m_F in the place of m_J. We will use these results in the following sections to calculate the Rabi frequencies and AC Stark shifts for a given intensity of light.

2.4 Optical Bloch Equations for Barium

So far, we have only treated the theory of either two-level systems or multi-level systems where significant approximations can be made. In general, however, we are working with much more complex systems. For Ba in particular, we need to consider all of the energy levels with which we interact. To simulate the dynamics of Ba, we use the optical Bloch equations. These equations can also be used to simulate Yb, and such simulations are discussed in [48, 55]. However, for this thesis we focus on Ba as it is more important for our work. We provide an overview of the theory; in Sec. 3.2, we provide more details about what dynamics we simulate and the results. Our work builds on the work in [55–57].

Because we will now not only be working with pure states since we need to account for coupling to the environment, we must use a density matrix formalism

where we define the density operator $\hat{\rho}$ in terms of eigenstates $|i\rangle$ of the atomic Hamiltonian

$$\hat{\rho} = \sum_{ij} p_{ij} |i\rangle \langle j| . \tag{2.58}$$

For unitary evolution, the time evolution is given by the Liouville equation [58]

$$\dot{\rho} = -\frac{i}{\hbar} [H, \rho] . \tag{2.59}$$

However, the atomic decays and finite laser linewidth mean that the evolution is no longer unitary. Assuming all processes are Markovian, we can describe the dynamics with the Lindblad equation [59]

$$\dot{\rho}(t) = -i [H, \rho] - \frac{1}{2} \sum_i \left(\hat{A}_i^\dagger \hat{A}_i \hat{\rho} + \hat{\rho} \hat{A}_i^\dagger \hat{A}_i - 2 \hat{A}_i \rho \hat{A}_i^\dagger \right) \tag{2.60}$$

where $\hat{A}_i$ are operators accounting for the dissipative processes involved. In our case, these processes consist of spontaneous emission and nonzero laser linewidths. For spontaneous emission, the decay operator $\hat{A}_i$ is

$$\hat{A}_i = \sqrt{\Gamma_{jk}} |j\rangle \langle k| \tag{2.61}$$

where Γ_{jk} is the decay rate from level $|k\rangle$ to level $|j\rangle$ and for nonzero laser linewidths

$$\hat{A}_i = \sqrt{2\Gamma_l} |i\rangle \langle i| \tag{2.62}$$

where Γ_l is the linewidth of the laser [56].

We can write this equation for an N level system as $N^2 \times N^2$ matrix, which can then be solved using linear algebra. To do this, we first write the density matrix as a vector $\vec{\rho} = (\rho_{11}, \rho_{12}, \ldots, \rho_{NN-1}, \rho_{NN})$. In this form, the Lindblad equation becomes

$$\dot{\vec{\rho}}_{ij} = \sum_j M_{ij,kl} \vec{\rho}_{kl} \tag{2.63}$$

where [55]

$$M_{ij,kl} = -\frac{i}{\hbar}\left[\tilde{H}_{ik}\delta_{lj} - \tilde{H}^\dagger_{lj}\delta_{ik}\right] + \sum_n \hat{A}_{n_{ik}} \hat{A}^\dagger_{n_{lj}} \tag{2.64}$$

with an effective "Hamiltonian," which is non-Hermitian, defined as

$$\tilde{H} = \hat{H} - \frac{i\hbar}{2} \sum_n \hat{A}^\dagger_n \hat{A}_n. \tag{2.65}$$

Note that although the matrix M does not technically require four indices, it is useful to use that many to clarify which matrix elements connect which atomic states.

For a time-independent M, this differential equation can be directly integrated to obtain

$$\vec{\rho}(t) = \vec{\rho}(0) e^{Mt} \tag{2.66}$$

for initial condition $\vec{\rho(0)}$. However, while M is time-independent for processes like Doppler cooling or optical pumping, we will need to account for time dependence when generating single photons (Sec. 6.1). For the problems we are interested in, we can numerically solve these equations.

2.4.1 Three-Level System

So far, we have discussed the general procedure for solving the optical Bloch equations with a generic Hamiltonian. Now we wish to consider more specifically applying this procedure to Ba. To illustrate the calculations, we'll first consider a simplified version of Ba where the only three levels are $|0\rangle \equiv \left|6S_{1/2}\right\rangle$, $|1\rangle \equiv \left|6P_{1/2}\right\rangle$ and $|2\rangle \equiv \left|5D_{3/2}\right\rangle$. The atomic Hamiltonian is then

$$\begin{aligned} H_{atom} &= \hbar \sum_i \omega_i \left|i\right\rangle \left\langle i\right| \\ &= \hbar \begin{pmatrix} \omega_S & 0 & 0 \\ 0 & 0 & 0 \\ 0 & 0 & \omega_D \end{pmatrix} \end{aligned} \tag{2.67}$$

where $\hbar\omega_S$ is the energy of $6S_{1/2}$ and $\hbar\omega_D$ is the energy of $5D_{3/2}$, and we have chosen the zero energy level to coincide with $6P_{1/2}$.

The interaction Hamiltonian, as for coherent operations, is $H_I = -\vec{\mu} \cdot \vec{E}$. For these calculations, we will assume two electric fields–one close to the resonance frequency of the $S \leftrightarrow P$ transition $\vec{E}_g$ and one close to the resonance of the $D \leftrightarrow P$ transition $\vec{E}_r$. We define these fields

$$\begin{aligned} E_g &= \frac{E_{g0}}{2}\left(\hat{\epsilon}_g e^{-i\omega_g t} + \hat{\epsilon_g}^* e^{i\omega_g t}\right) \\ E_r &= \frac{E_{r0}}{2}\left(\hat{\epsilon}_r e^{-i\omega_r t} + \hat{\epsilon_r}^* e^{i\omega_r t}\right), \end{aligned} \tag{2.68}$$

yielding an interaction Hamiltonian

$$H_{int} = \hbar \left(\Omega_g e^{-i\omega_g t} + \Omega_g^* e^{i\omega_g t}\right) \left(|0\rangle \langle 1| + |1\rangle \langle 0|\right) + \hbar \left(\Omega_r e^{-i\omega_r t} + \Omega_r^* e^{i\omega_r t}\right) \left(|2\rangle \langle 1| + |1\rangle \langle 2|\right) \tag{2.69}$$

where we have defined the Rabi frequencies

$$\Omega_g = \frac{E_{g_0}}{2\hbar} \langle 0 | \vec{\mu} \cdot \hat{\epsilon} | 1 \rangle$$
$$\Omega_r = \frac{E_{r_0}}{2\hbar} \langle 2 | \vec{\mu} \cdot \hat{\epsilon} | 1 \rangle . \tag{2.70}$$

The matrix elements $\langle i | \vec{\mu} \cdot \hat{\epsilon} | j \rangle$ can be computed as discussed in Sec. 2.3.

Next, we transform the total Hamiltonian into a rotating frame by applying the unitary [56]

$$U = e^{-i\omega_g t} |0\rangle \langle 0| + |1\rangle \langle 1| + e^{-i\omega_r t} |2\rangle \langle 2| . \tag{2.71}$$

The application of this unitary along with a RWA gives the final total Hamiltonian

$$H' = \hbar \begin{pmatrix} \Delta_g & \Omega_g & 0 \\ \Omega_g & 0 & \Omega_r \\ 0 & \Omega_r & \Delta_r \end{pmatrix} \tag{2.72}$$

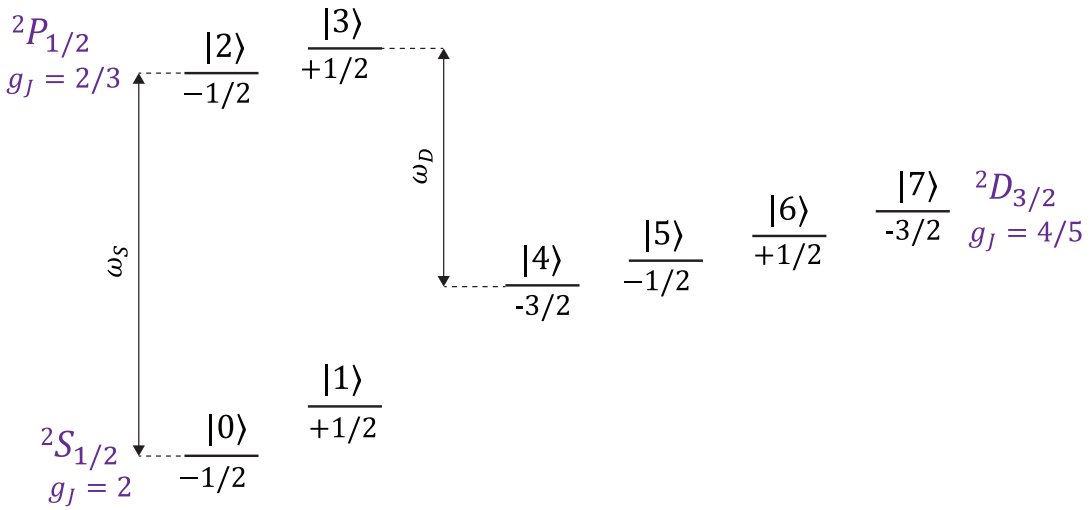

Figure 2.2: Diagram of the atomic energy levels relevant to the calculations discussed in this section. The numbers above the states indicate the label we assign, while the numbers below each level indicate the corresponding value of m_J.

where we have defined the detunings

$$\Delta_g = \omega_g - (\omega_P - \omega_S)$$
$$\Delta_r = \omega_r - (\omega_P - \omega_S)\,. \tag{2.73}$$

This final form of the Hamiltonian is the one we would use for performing simulations. In general, Ω_g and Ω_r can be time dependent, which would be the source of a time dependent M in the vector form of the Lindblad equation.

2.4.2 Eight-Level System and Multiple Polarizations

Next we consider the eight level atomic Hamiltonian. The Zeeman splitting within a fine structure level is given by [58]

$$\Delta E = \mu_B g_J m_J B \tag{2.74}$$

where μ_B is the Bohr magneton and g_J, the Landé g-factor, is

$$g_J = 1 + \frac{J(J+1) + S(S+1) - L(L+1)}{2J(J+1)} \tag{2.75}$$

The three fine structure levels we will consider are $^2S_{1/2}$, $^2P_{1/2}$, and $^2D_{3/2}$, which have values of $g_{J_S} = 2$, $g_{J_P} = \frac{2}{3}$, and $g_{J_D} = \frac{4}{5}$ respectively. We define a shorthand for the atomic states as shown in Fig. 2.2.

Then, the atomic Hamiltonian is:

$$\begin{aligned} H_{atom} = &\sum_{i=0,1} \left[(-\hbar\omega_g + \mu_B B g_{J_S} m_{J_i}) \left|i\right\rangle \left\langle i\right| \right] + \sum_{i=2,3} \left(\mu_B B g_{J_P} m_{J_i} \left|i\right\rangle \left\langle i\right| \right) \\ &+ \sum_{i=4}^{7} \left[(-\hbar\omega_r + \mu_B B g_{J_D} m_{J_i}) \left|i\right\rangle \left\langle i\right| \right] . \end{aligned} \tag{2.76}$$

For the interaction Hamiltonian, the polarization now becomes important. In previous work, it has been assumed that the light propagates perpendicular to the magnetic field and the polarization is thus constrained to have equal proportions of σ^+ and σ^- [55, 56]. In the following calculations, we generalize this treatment to

allow for arbitrary intensities of each polarization. Recall, using Eqs. 2.11, 2.52, and 2.53, the matrix element of a transition from state i to state j in the rotating frame and with a RWA when driven by an electric field with amplitude $|E_\alpha|$ is given by

$$V_{ij} = \frac{|E_\alpha|}{2\hbar}\tilde{C}_{ij}\sqrt{\frac{3\pi\epsilon_0\hbar c^3\gamma}{\omega_0^3}\,(2L'+1)} \tag{2.77}$$

where we have defined $\tilde{C}_{ij}$ as a shorthand for the coefficients dependent on angular momentum in Eq. 2.52.

We now write this matrix element in terms of the saturation intensity (Eq. 2.2) and the laser intensity

$$I_\alpha = \frac{1}{2}c\epsilon_0\,|E_\alpha|^2\,. \tag{2.78}$$

These substitutions give us

$$V_{ij} = \frac{1}{2}\tilde{C}'_{ij}\gamma\sqrt{\frac{I_\alpha}{2I_{sat_{ij}}}} \tag{2.79}$$

with $\tilde{C}'_{ij} = \tilde{C}_{ij}\sqrt{2L'+1}$. Next, we define the saturation parameter

$$s_{\alpha ij} \equiv \frac{I_\alpha}{I_{sat_{ij}}}. \tag{2.80}$$

Finally, we define a Rabi frequency in terms of these parameters for a given transition

$$\Omega_{\alpha ij} = \frac{1}{2}\gamma\sqrt{\frac{s_{\alpha ij}}{2}}, \tag{2.81}$$

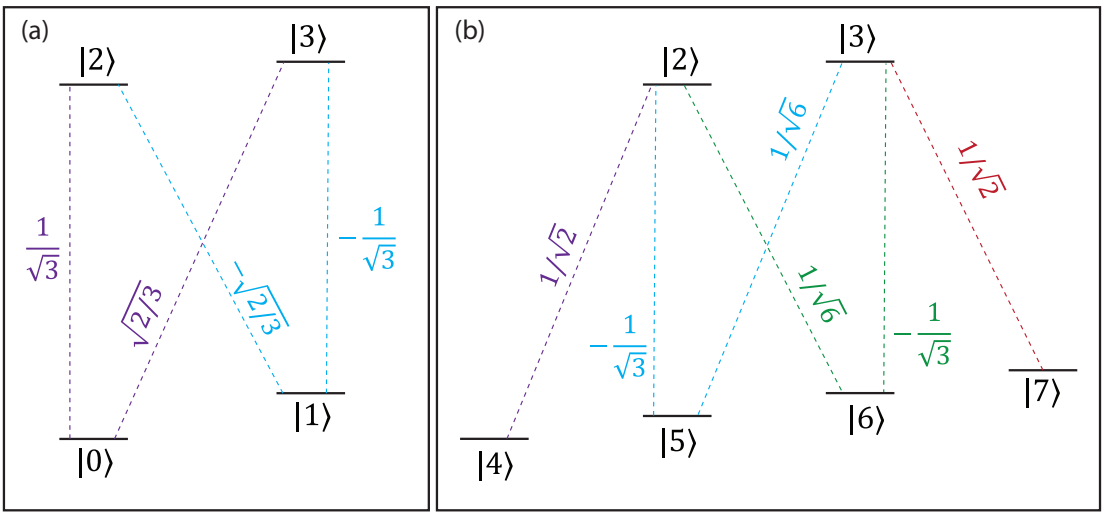

Figure 2.3: Clebsch-Gordan coefficients for transitions in Ba relevant for the optical Bloch equation calculations. States are labeled as in Fig. 2.2. (a) Clebsch-Gordan coefficients for transitions between the $6S_{1/2}$ and $6P_{1/2}$ manifolds. (b) Clebsch-Gordan coefficients for transitions between the $5D_{3/2}$ and $6P_{1/2}$ manifolds.

giving us the final form of our generic matrix element

$$V_{ij} = \tilde{C}'_{ij}\Omega_{\alpha ij}\,. \tag{2.82}$$

Note that all angular momentum dependence is encapsulated by $\tilde{C}'_{ij}$, which for the calculations performed in this section, is equal to the Clebsch-Gordan coefficient $\langle J, 1, m_J, q \,|\, J' m'_J \rangle$. However, because we will be considering polarizations with different electric field amplitudes, and which polarization is relevant for a particular transition depends on the angular momenta of the initial and final states, $\Omega_{\alpha ij}$ will not be the same for all transitions of a given wavelength.

We now consider more concretely the actual system we are studying. We effectively have six lasers–one for each polarization at both 493 nm and 650 nm.

Correspondingly, we have six Rabi frequencies

$$\begin{aligned}
\Omega_{g,\pi} &= \frac{|E_{g,\pi}|}{2}\gamma_{SP}\sqrt{\frac{I_{g,\pi}}{2I_{sat_{SP}}}} = \frac{|E_{g,\pi}|}{2}\gamma_{SP}\sqrt{\frac{s_{SP,g,\pi}}{2}} \\
\Omega_{g,\sigma^\pm} &= \frac{|E_{g,\sigma^\pm}|}{2}\gamma_{SP}\sqrt{\frac{I_{g,\sigma^\pm}}{2I_{sat_{SP}}}} = \frac{|E_{g,\sigma^\pm}|}{2}\gamma_{SP}\sqrt{\frac{s_{SP,g,\sigma^\pm}}{2}} \\
\Omega_{r,\pi} &= \frac{|E_{r,\pi}|}{2}\gamma_{DP}\sqrt{\frac{I_{r,\pi}}{I_{sat_{DP}}}} = \frac{|E_{r,\pi}|}{2}\gamma_{DP}\sqrt{\frac{s_{DP,r,\pi}}{2}} \\
\Omega_{r,\sigma^\pm} &= \frac{|E_{r,\sigma^\pm}|}{2}\gamma_{DP}\sqrt{\frac{I_{r,\sigma^\pm}}{2I_{sat_{DP}}}} = \frac{|E_{r,\sigma^\pm}|}{2}\gamma_{DP}\sqrt{\frac{s_{DP,r,\sigma^\pm}}{2}}] \,.
\end{aligned} \tag{2.83}$$

Here g indicates the green 493 nm light, and r indicates the red 650 nm light. γ_{SP} and γ_{DP} are the linewidths of the $S \leftrightarrow P$ and $D \leftrightarrow P$ transitions respectively. $I_{sat_{SP}}$ and $I_{sat_{DP}}$ are the saturation intensities for the corresponding transitions.

The coefficients $\tilde{C}'_{ij}$ are shown in Fig. 2.3. Thus, we have the full Hamiltonian, which we can then substitute back into Eq. 2.65. The decay operators for spontaneous emission, accounting for Zeeman coherences [56], are [55]

$$\begin{aligned}
A_1 &= \sqrt{\frac{2\gamma_{SP}}{3}}\,|0\rangle\langle 3| \\
A_2 &= \sqrt{\frac{2\gamma_{SP}}{3}}\,|1\rangle\langle 2| \\
A_3 &= \sqrt{\frac{\gamma_{SP}}{3}}(|0\rangle\langle 2| - |1\rangle\langle 3|) \\
A_4 &= \sqrt{\gamma_{DP}}\left(\frac{1}{\sqrt{2}}\,|4\rangle\langle 2| + \frac{1}{\sqrt{6}}\,|5\rangle\langle 4|\right) \\
A_5 &= \sqrt{\gamma_{DP}}\left(\frac{1}{\sqrt{2}}\,|7\rangle\langle 3| + \frac{1}{\sqrt{6}}\,|6\rangle\langle 2|\right) \\
A_6 &= \sqrt{\frac{\gamma_{DP}}{3}}(|5\rangle\langle 2| + |6\rangle\langle 3|)\,.
\end{aligned} \tag{2.84}$$

The decay operators to account for nonzero laser linewidth are given by [55]:

$$A_7 = \sqrt{2\Gamma_g}(|0\rangle\langle 0| + |1\rangle\langle 1|)$$
$$A_8 = \sqrt{2\Gamma_r}\sum_{i=4}^{7}|i\rangle\langle i| \tag{2.85}$$

where we assume that the linewidth is the same regardless of the polarization and Γ_g and Γ_r are the linewidths of the 493 nm and 650 nm lasers, respectively. Strictly, this may not be completely accurate, since we use different lasers for the 650 nm $\sigma^{\pm}$ and π light. However, they are both diode lasers, so the linewidth is likely the same order of magnitude, and the laser linewidth does not have a strong effect on the simulation results.

We now have all of the components that govern the dynamics of the system. Certain properties such as spectra are calculated and discussed in [48, 55]. In this thesis we focus on using these calculations to optimize state preparation in the $D_{3/2}$ manifold (Sec. 3.2.4.1) and simulate our single photon generation process (Sec. 6.1).

Chapter 3: Operations with Ytterbium and Barium Ions

In the previous chapter, we presented the general theory describing the interactions of laser light with trapped ions. Here, we delve into the specific operations for each ion in our network. We also discuss our atomic sources and the steps leading up to trapping.

3.1 $^{171}Yb^{+}$ Ions

In our network, we use $^{171}Yb^{+}$ ions for our memory qubits because of the excellent coherence times of their natural clock qubit [60]. In this section, I discuss the operations we use to trap and control these ions.

3.1.1 Atomic Sources and Photoionization

We load ∼10 mg of neutral Yb metal that has been isotopically enriched to contain primarily ^{171}Yb into a hypodermic needle 1-2 mm in diameter. We crimp the needle on one end to provide a seal and mount it in the vacuum chamber so the opening is pointed at the center of the trap. In one of our traps, we TIG welded a coiled, .016" diameter piece of tungsten to the crimped end of the hypodermic needle (Fig. 3.1). The current required for all of these ovens is ∼2 A.

Figure 3.1: Picture of an atomic source oven made of a hypodermic needle with an attached tungsten coil, which serves as a heating element.

For Yb, we use a two step photoionization process described in [61]. The first photon is resonant at ∼398.9 nm with the neutral Yb $^1S_0 \leftrightarrow ^1P_1$ transition, where $^1S_0$ is the ground state, and the second is at 369 nm, which is chosen largely out of convenience since it is the same laser used to Doppler cool Yb^+. The requirement on the second photon is simply that it have a shorter wavelength than ∼399 nm in the presence of a strong electric field like the one in the ion trap [61]. Although this process is sufficient for our purposes, different wavelengths could maximize the photoionization rate.

If the laser beam is oriented perpendicular to the direction from the oven to the trap center, the first step of the process can be used to select which isotope of Yb is trapped because the resonance is fairly narrow (∼10 MHz) compared to the isotope shifts (∼100 MHz). However, our ovens are not at 90° relative to our 399 nm laser, and thus we expect Doppler broadening of hundreds of MHz, which is larger than the isotope shifts of Yb. Thus, we have poor isotope selectivity in our loading. Since we only trap one ion at a time and we are able to hold ions for days at a time,

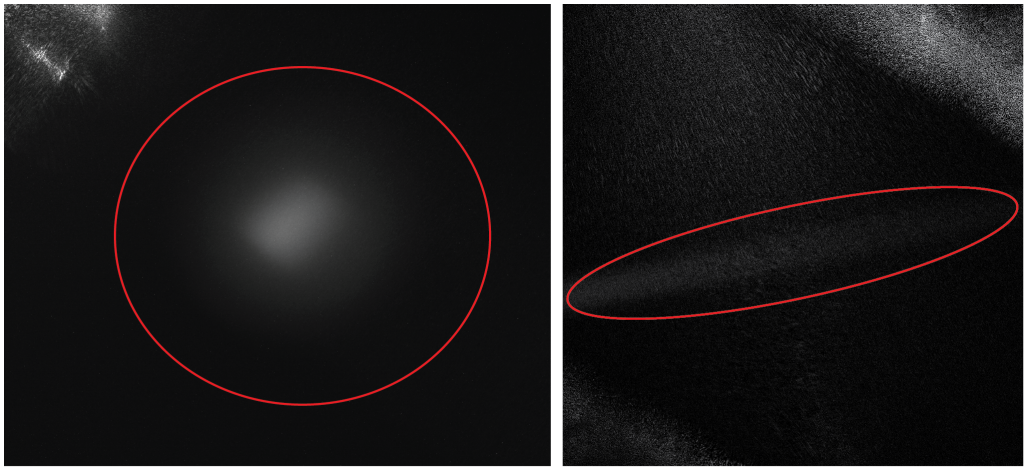

Figure 3.2: Fluorescence from neutral Yb atoms. The fluorescence in both images is circled with red to distinguish it from scattered light. (a) Yb neutral fluorescence in a test chamber with the mounting setup for the oven for our third trap. The scattered light in the upper left corner is laser light hitting the oven. The laser beam is oriented at 90° to the atomic beam. The fluorescence is observed near the oven tip, and can be used to provide a measurement of the atomic flux density. The magnification of the imaging system is approximately 1. (b) Yb neutral fluorescence in the center of an ion trap. Light outside of the red oval is laser light scattered off the trap. The laser beam is oriented at $\sim 160°$ to the atomic beam, and the fluorescence is observed much farther from the oven, so the flux is much lower. The imaging system also has a higher magnification ($\sim$x10) so the fluorescence is distributed over more pixels, reducing the signal to noise ratio.

this lack of selectivity does not cause any significant problems.

3.1.1.1 Neutral Fluorescence of Yb

For testing the atomic sources, it can be useful to first view fluorescence from neutral atoms. This step can serve several purposes, depending on the exact setup: (i) ensure the oven is getting sufficiently hot, (ii) measure the neutral atom resonance frequency, (iii) measure the atomic flux at a given oven current, and (iv) if the test is performed in the final chamber, ensure the laser alignment of the laser used for the first step of photoionization. Observing the flux can be especially important if

we are unable to trap any ions in order to ensure that the problem is not from the source itself.

For this experiment, we shine only the 399 nm laser on the atomic beam coming from the oven. We then use a simple imaging setup, preferably with a low magnification to increase the brightness on a single pixel, to collect light from the atoms (also at 399 nm) onto a camera (see Fig. 3.2). During the course of this research, we looked for neutral fluorescence for both Bob and Cleo. For Bob, we used the chamber with the ion trap (Fig. 3.2(b)), and for Cleo, we used a separate test chamber constructed specifically for this purpose (Fig. 3.2(a)).

Each has advantages and disadvantages, but overall, the test chamber is preferable. Performing the test in the chamber with the actual ion trap can be useful for checking the alignment of the laser beam and imaging system. In addition, it guarantees that the oven mounting is identical for the test and for trying to trap ions. For example, if the length of wire used in the test chamber is different from that in the actual chamber, it can affect the current required to heat the oven to the same temperature. In the test chamber, however, there are fewer surfaces for light to scatter off of, giving a much cleaner background. Also, from a practical standpoint, it is easier to design the imaging system and laser delivery system to be optimal for the neutral fluorescence in the test chamber. In particular, it is often not possible to orient the laser beam at exactly 90° in the actual chamber due to the orientation of the ovens relative to the windows and other experimental constraints. Finally, performing the test in a separate chamber protects the ion trap from atoms accumulating on the electrodes at the much higher atomic flux densities necessary for

neutral fluorescence compared with those for trapping a single ion. This accumulation can lead to increased heating of ions if it makes the surface rougher or can displace ions from the RF null, leading to increased micromotion.

3.1.2 Doppler cooling

We now turn to our discussion of control of the ionized Yb atoms. All of these operations are summarized in Fig. 3.4 and Table 3.1. As discussed above, we use the 369 nm Doppler cooling laser to provide the second photon for our photoionization procedure. This setup guarantees that as soon as the atom is ionized it will begin to cool, assuming the laser frequency is set correctly. In this section, we discuss the power and frequency requirements for this and other relevant laser beams.

Fig 3.3 shows the relevant energy levels for cooling of Yb^+, along with levels relevant to the other operations we discuss. The primary transition for cooling is the nearly-cycling transition between the $^2S_{1/2}$ and $^2P_{1/2}$ states with a resonance wavelength of 369.5 nm. We apply $\sim$10 μW of 369.5 nm light detuned from resonance by half the natural linewidth ($\sim$ 20 MHz) to the Yb ion at an angle of 45° to all trap axes. We (roughly) estimate a beam waist of 50 μm, which gives a saturation parameter I/I_{sat} of $\sim$13. We choose this power based on experimental observation of the brightness and stability of the ion. We additionally need to ensure that all levels in the $S_{1/2}$ manifold are resonantly coupled to the $P_{1/2}$ manifold. Noting that the transition $\left|S_{1/2}, F=0\right\rangle \leftrightarrow \left|P_{1/2}, F=0\right\rangle$ is forbidden, we set the frequency of the 369 nm beam to be approximately resonant with the $\left|S_{1/2}, F=1\right\rangle \leftrightarrow \left|P_{1/2}, F=0\right\rangle$.

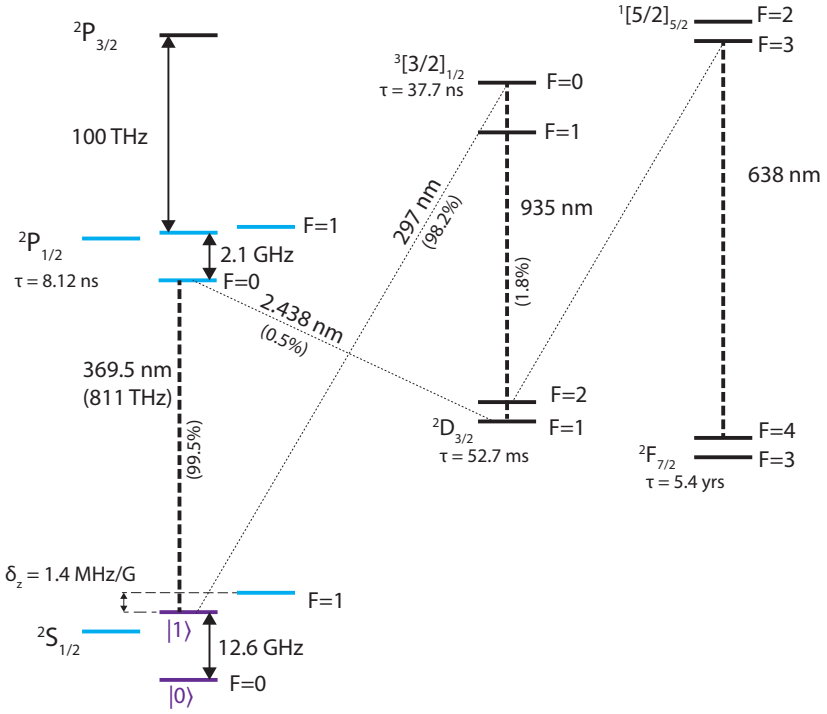

Figure 3.3: Partial energy level diagram of Yb^+. The qubit is in purple, and the other energy levels most important for our experiment are shown in blue. Additionally, Zeeman levels outside of these states are not shown, as they are not important for our work. Transitions that are driven by lasers are shown with thick dashed lines, and decays that are relevant to the experiment but not driven with a laser are shown with thin dashed lines. Laser wavelengths are approximately measured in our lab with a wavemeter. The wavelengths of the $^2S_{1/2} \leftrightarrow^3 [3/2]_{1/2}$ and $^2D_{3/2} \leftrightarrow^2 P_{1/2}$ transitions are sourced from [62] and [63] respectively. The lifetimes of the $^2P_{3/2}$, $^3[3/2]_{1/2}$, $^2D_{3/2}$, and $^2F_{7/2}$ states are from the following sources, again respectively: [64–67] . The branching ratio of the $^2P_{1/2}$ state is measured in [68], and the branching ratio of the $^3[3/2]_{1/2}$ state is from [69].

This results in the population nearly continuously cycling between these levels.

However, this cycle can be disrupted in a few ways. First, occasionally, the ion can be off-resonantly excited to the $\left|P_{1/2}, F = 1\right\rangle$ manifold, which allows the ion to decay to the $\left|S_{1/2}, F = 0\right\rangle$ state. To depopulate this level we apply a frequency sideband to our laser at 14.7 GHz, which clears out any population in $\left|S_{1/2}, F = 0\right\rangle$ via the $\left|P_{1/2}, F = 1\right\rangle$ manifold. To generate these sidebands, we currently use a resonant $LiNbO_3$ electro-optic modulator (EOM)[1] with a resonance frequency of 7.374 GHz and use the second order sideband.[2] Furthermore, once out of every 200 excitations, the ion will decay to one of the $D_{3/2}$ levels instead of the desired $S_{1/2}$ levels. We depopulate these states using a laser at 935 nm. Again, we need frequency sidebands to clear out the additional hyperfine levels, so we use another EOM[3], this time at 3.1 GHz. Finally, the ion will occasionally (approximately twice an hour) experience a collision with a background gas particle that results in population of the $F_{7/2}$ state. To avoid effectively permanent loss of ions once this happens given the extremely long lifetime of the $F_{7/2}$ state, we also use a 638 nm laser to clear out these states. In this case, we do not use an EOM to apply sidebands; rather we scan across the hyperfine structure by modifying the voltage of the laser piezo. This method is slow, but given the rarity of the events, is not limiting.

[1] New Focus Visible Phase Modulator, Model 4851

[2] This device is no longer manufactured. Additionally, there are several disadvantages to the use of this device: (i) no available anti-reflective coating for UV light, (ii) the use of second-order sidebands dramatically limits the power available at that frequency, and (iii) UV-induced photorefractive damage of $LiNbO_3$, which is an issue more generally with such devices. QuBiG now offers an alternative (PM-Yb171+_14.7M2), with first order sidebands at 14.7 GHz and a magnesium-doped $LiNbO_3$ crystal, which minimizes the photorefractive effects. This is a promising option for future setups.

[3] EOSPACE Inc., PM-0KS-10-PFU-PFU-935

Another important consideration for $^{171}Yb^+$ is the existence of coherent dark states. These states are not a single energy eigenstate but are instead a superposition of multiple states. This phenomenon is discussed in detail in [70]. For the purposes of this work, there are a couple of important considerations for destabilizing such dark states. First, for $^{171}Yb^+$, the magnetic field must be nonzero [43]. We use coils of copper wire to apply a controllable magnetic field, which defines the quantization axis for all of our experiments. This field is also extremely important for our work in barium, as will be discussed later. Additionally, the polarization of the 369.5 nm laser is important–it must not have either pure σ or π polarization [55].

It is also worth noting that the ion occasionally becomes much hotter, likely due to energy transferred in collisions with background gas particles. On these occasions, it is useful to have a 369.5 nm beam that is further detuned from resonance ($\Delta \sim 200$MHz) to address this higher velocity class. This beam typically enables recovery of even the hottest ions we have in our traps. It is also useful for initial trapping, since the ions are initially at ∼300 °C. To apply this beam, we use a motorized shutter, which can be opened or shut from the computer using a TTL signal.

3.1.3 State Initialization and Detection

We now define our qubit states: $|0\rangle \equiv \left|6S_{1/2}, F = 0, m_F = 0\right\rangle$ and $|1\rangle \equiv \left|6S_{1/2}, F = 1, m_F = 0\right\rangle$. These states are split by 12.6428121185 GHz + δ where $\delta = 310.8\,|B|^2$ in Hz [71]. Both state initialization and detection rely on the large

detuning from $|0\rangle$ when the 369.5 nm light is resonant with the transition from $|1\rangle$ to one of the $6P_{1/2}$ states. For both of these processes, the 935 nm repumping light is left on. First, we will detail the operation of state initialization then detection.

For state initialization, we always initially prepare in $|0\rangle$. If an application ever requires preparation in $|1\rangle$, the qubit state could be coherently rotated to $|1\rangle$ (see Sec. 3.1.4). As discussed in Sec. 3.1.2, the transition $|0\rangle \leftrightarrow \left|P_{1/2}, F = 0\right\rangle$ is forbidden, so exciting to that state would not rapidly transfer population from $|1\rangle$ to $|0\rangle$. Instead, we apply 2.1 GHz frequency sidebands to the 369.5 nm laser beam with another EOM.[4] This laser frequency is then resonant with the $|1\rangle \leftrightarrow |6P_{1/2}, F = 1\rangle$ transition. From that excited state, the ion can decay to any state in the $6S_{1/2}$ manifold, including $|0\rangle$. However, since $|1\rangle$ and the other Zeeman levels in the $F = 1$ manifold are coupled to an excited state, any population left there will eventually be transferred to the dark $|0\rangle$ state. This process takes a few μs and can be performed with high fidelity ($\gg 99\%$ [72]).

The goal for state detection is to detect as many photons as possible if the ion is in $|1\rangle$ while collecting none if the ion is in $|0\rangle$. This is achieved by applying light that is resonant only with the $|1\rangle \leftrightarrow \left|6P_{1/2}, F = 0\right\rangle$ transition. While this light will eventually off-resonantly couple to $\left|6P_{1/2}, F = 1\right\rangle$, allowing decay to $|0\rangle$, it is still possible to achieve fidelities of above 99% [48]. To determine the state, we set a threshold value based on the observed counts for the dark $|0\rangle$ and bright $|1\rangle$ states. Typically, if we detect either 0 or 1 photons, we say the ion was in $|0\rangle$, while more than 1 photon indicates the state was $|1\rangle$.

[4] QuBiG EO-T2100M3

The success of our detection scheme is in large part determined by the imaging setup we use for collecting ion fluorescence since the fidelity is determined by how many photons we can collect before the ion is off-resonantly pumped to $|0\rangle$. For Alice, we use a custom, multi-element, 0.39 NA objective from Special Optics. For Bob, we use a custom aspheric lens from Thorlabs (see Sec. 5.1.2) that is designed to have an NA of 0.55. However, the number of photons we see from Ba indicates an effective NA of slightly over 0.4 due to loss along the imaging optics path. Yb detection has not yet been performed on Bob; however, we expect similar or slightly improved results given the slightly higher numerical aperture of the objective at 370 nm than at 493 nm. The quantum efficiency of the detectors also matters; we use PMTs with a quantum efficiency at 369 nm of about 25%.[5] The fidelity can be increased to over 99.9% by using an NA 0.6 lens and higher efficiency superconducting nanowire detectors [72].

	Cooling	Pumping	State Detection
Resonant 369.5 nm $\left(\left\|S_{1/2}, F=1\right\rangle\right)$	✓	✓	✓
14.7 GHz Sidebands	✓	×	×
2.1 GHz Sidebands	×	✓	×

Table 3.1: Summary of which 369 nm frequencies are applied for each stage of an experiment (Doppler cooling, optical pumping, and state detection).

[5] Hamamatsu H10682-210

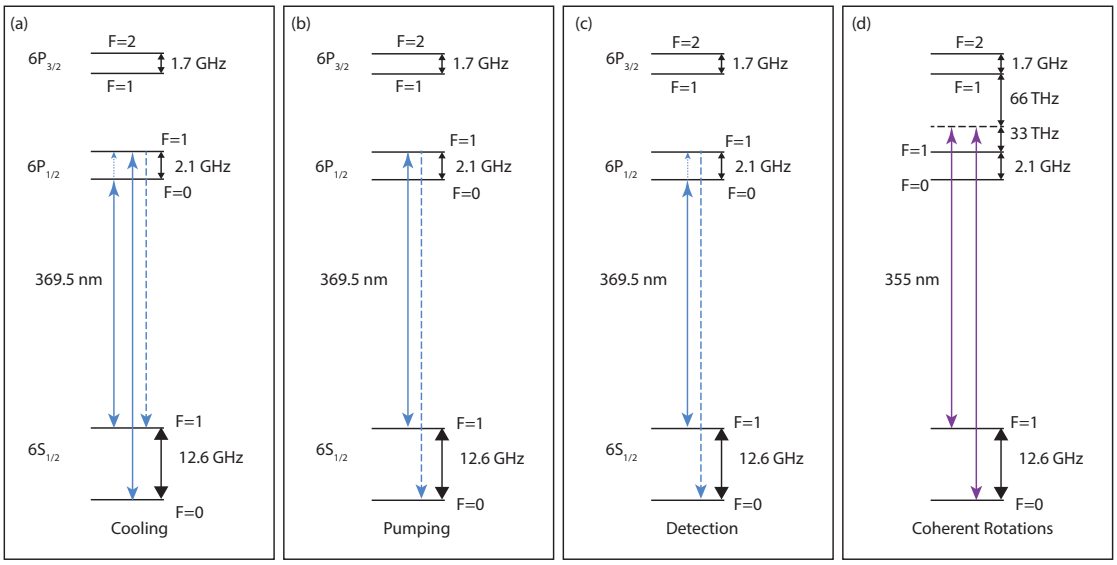

Figure 3.4: Diagrams showing each operation in $^{171}Yb^{+}$. (a) Doppler cooling. 369.5 nm light 10 MHz detuned from the $\left|S_{1/2}, F=1\right\rangle \leftrightarrow \left|P_{1/2}, F=0\right\rangle$ transition is applied, along with sidebands at 14.7 GHz. (b) Preparation to $\left|S_{1/2}, F=0\right\rangle$. The nearly resonant light is still applied, now with 2.1 GHz sidebands and no 14.7 GHz sidebands. This configuration leaves the state $\left|S_{1/2}, F=0\right\rangle$ dark, and thus transfers all of the population to that state. (c) State detection. No sidebands are used. This configuration takes advantage of the nearly cycling transition to scatter many photons if the ion is in $\left|S_{1/2}, F=1\right\rangle$, and none if the ion is in $\left|S_{1/2}, F=0\right\rangle$. (d) Coherent operations. 355 nm light drives off-resonant two-photon transitions via a virtual level detuned from the $\left|P_{1/2}\right\rangle$ and $\left|P_{3/2}\right\rangle$ states by 33 and 66 THz respectively. Two beams are applied with a splitting of 12.6 GHz (equal to the splitting between $\left|S_{1/2}, F=0\right\rangle$ and $\left|S_{1/2}, F=1\right\rangle$).

3.1.4 Coherent Operations

We utilize two methods to drive coherent rotations between the qubit states. We can either drive them directly with microwave radiation at 12.6 GHz or use a Raman transition as shown in Fig. 3.4(d). The theoretical details of driving rotations using microwaves are discussed in [68]. Here, I briefly summarize the experimental implementation.

To generate the 12.64 GHz signal, we mix the output of a clock at 12.45 GHz

with a ∼200 MHz DDS signal and filter out only the sum frequency. This microwave signal is then sent to a microwave horn placed directly outside one of the windows of the vacuum chamber. The time to fully rotate between the qubit states (the π time of a rotation) is typically tens of μs.

Microwaves can be useful for diagnostics and testing and can be more stable than laser rotations. However, the low momentum of microwave photons means that they cannot couple to the ion's motional modes and thus cannot be used to drive entangling operations. Additionally, the microwave horn blocks optical access from one port, which may make it desirable to operate without microwaves once the experiment is setup and running stably.

We can also perform coherent rotations using laser beams, as discussed in Sec. 2.2, which provide enough momentum to couple to the ion's motion and drive entangling gates, as discussed specifically in Sec. 2.2.1. Additionally, we have achieved higher Rabi frequencies (shorter π times) with lasers than with microwaves.

To drive rotations in Yb, as discussed above, we use a frequency comb centered at about 355 nm with two beams, either in a co-propagating configuration or with $\Delta\vec{k}$ parallel to the axial direction of the trap if we wish to couple to the motion of the ions. We use multiple comb teeth from the frequency comb to span the hyperfine splitting in $^{171}Yb^{+}$. The lasers we use have a fixed repetition rate of either approximately 80 MHz for the Spectra Physics Vanguard and 120 MHz for the Coherent Paladin. The resonance requirement consists of a comb tooth in each beam matching the 12.64 GHz hyperfine splitting (plus any AC Stark shifts, which we in general attempt to null). In general, the resonance condition will not be

satisfied without frequency modulation, so we introduce AOMs into the beam paths to satisfy the condition:

$$\omega_{HF} = n\omega_{rep} + \Delta\omega_{AOM} \tag{3.1}$$

where $\Delta\omega_{AOM}$ is the difference between the AOM frequencies on the two beam paths.

Additionally, while the Paladin can be modified to lock the repetition rate of the laser [73], we have not performed this procedure for our lasers and the repetition rate therefore drifts. We must therefore feed-forward on the AOM frequency to ensure the resonance condition remains satisfied. This feed-forward is performed by using a beatnote lock as described in [74, 75].

3.2 $^{138}Ba^{+}$ Ions

We now discuss the specifics of control of Ba ions. While much of this discussion is very similar to that for Yb ions, the presence of a low-lying D state in Ba introduces additional complexity and opportunities to all of our operations.

3.2.1 Atomic Sources and Photoionization

For sources of Ba, we build our own ovens containing pure Ba metal. Barium requires a significantly higher temperature than Yb for comparable atomic flux densities. In Alice, to load barium, we run the oven at 8 Amps (the ytterbium oven is run at ∼2.5 Amps). For Bob and Cleo, we attach a tungsten coil as described in Sec. 3.1.1. On Bob, for which we have tungsten on the Ba oven but not on the

Yb oven, both ovens require currents of about 2.5 Amps. The Ba oven in Cleo is also run at a current of about 2 Amps. The procedure for loading barium into the chamber is more complicated than that for Yb due to the rapid oxidation of Ba. To load barium into the oven, we first pump the chamber down to high vacuum and run the oven for a few minutes while it glows at least red hot to remove any residual water, which can increase the rate of oxidation. We then fill the chamber with argon without exposing it to air. This can be accomplished by using a CF flange fitted with a Swagelok adapter on the air/pump side of the valve. The chamber is then opened with the argon continuing to flow through with greater than 1 atm of pressure. When the only window opened is on top of the chamber, the heavier weight of argon compared to air along with the positive pressure should minimize the amount of air that gets in to the oven. All tools that come in contact with the barium are also baked under vacuum for at least several hours beforehand. The barium is packaged in glass ampules filled with argon, which we break into a glass dish. Over the course of a couple of minutes, we load as many of the barium beads as we can into the oven using tweezers. This procedure minimizes the exposure of the barium to air to a couple of minutes, during which time the barium will have oxidized to the point that the surface will be noticeably whiter than when it started but not so much that we will not be able to get barium out from under the oxide layer.

To create Ba ions, we use a two-photon protocol. Both photons are 413 nm. The first photon resonantly drives the transition from $6s^2\ {}^1S_0 \rightarrow 5d6p\ {}^3D_1$, and the

Higher Energy Level	Lifetime	Lower Energy Level	Wavelength	Branching Ratio
$6s6p\ ^1P_1$	8.4 ns	$6s^2\ ^1S_0$	553.70 nm	0.9966
		$6s5d\ ^1D_2$	1500.40 nm	0.0025
		$6s5d\ ^3D_1$	1107.87 nm	8×10^{-5}
		$6s5d\ ^3D_2$	1130.61 nm	9×10^{-4}
$5d6p\ ^3D_1$	17 ns	$6s^2\ ^1S_0$	413.35 nm	0.026
		$6s5d\ ^3D_1$	659.71 nm	0.64
		$6s5d\ ^3D_2$	667.71 nm	0.32
		$6s5d\ ^1D_2$	781.45 nm	<0.001
		Others	-	0.013

Table 3.2: Partial list of transitions in neutral Ba. These transitions comprise all of the relevant ones for our work. Energies of the levels (and thus wavelengths) are from [76] and lifetimes and branching ratios are from [77].

second provides enough energy to ionize the atom (see Fig. 3.5). We use 1.5-5 mW of loosely focused 413 nm light, which is sufficient for trapping in about 4-5 minutes in Alice, 1-2 minutes in Bob, and 1-2 minutes in Cleo. The exact frequency of the light is dependent on the angle of the laser beam relative to the atoms. In Alice, the laser beam is 167.5° to the atomic beam, and in Bob, the angle is 22.5°. For temperatures of the atoms of approximately 590 K, there is a resonance frequency difference for the 413 nm beams for Alice and Bob of about 1.5 GHz. Additionally, at these angles, there is a large amount of Doppler broadening so our isotope selectivity is poor and we routinely trap $^{136}Ba^+$ or $^{137}Ba^+$ instead of $^{138}Ba^+$.

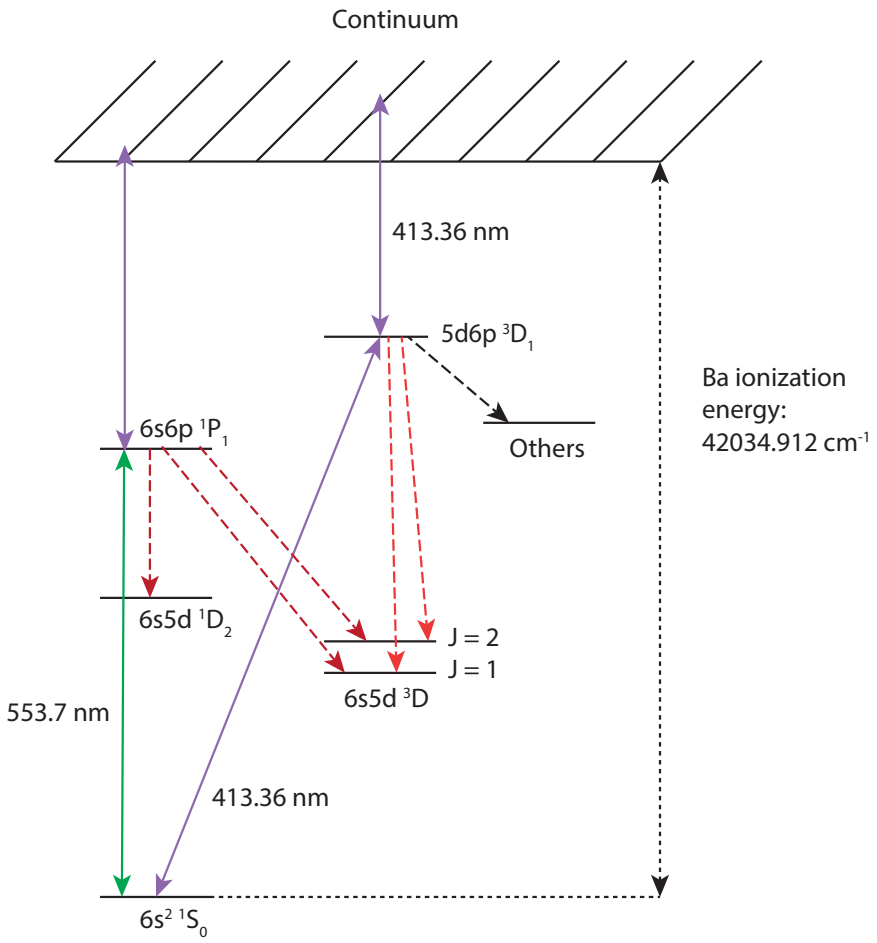

Figure 3.5: Partial energy level diagram of neutral Ba (not showing hyperfine structure), adapted from [78]. The ionization energy is found in [79], and the relevant wavelengths in [76]. This figure shows two possible ionization schemes–the one we currently use, which utilizes two 413 nm photons, first to drive the transition $6s^2 {}^1S_0 \rightarrow 5d6p {}^3D_1$, and then to excite the electron to the continuum, and another possible scheme using 553 nm for the first photon and then a photon with wavelength $\leq$ 417 nm to ionize. The branching ratios and decay wavelengths are presented in Table 3.2.

As mentioned above, the resonant transition we use as the first step in our photoionization process is from $^1S_0 \rightarrow {}^3D_1$. This transition is an electric dipole-forbidden transition, so we would expect it to be weak. Indeed, it is about 100 times weaker than the transition $^1S_0 \rightarrow {}^1P_1$ transition, and, correspondingly, the linewidth of the transition is only 240 kHz instead of almost 20 MHz. However,

since we use a relatively high power of laser light and there is significant Doppler broadening, our ionization rates are comparable to those in Yb. There are, however, more efficient ionization schemes. One such scheme is shown in Fig. 3.5, where the first photon at 553.7 nm drives the neutral atom $^1S_0 \rightarrow {}^1P_1$ transition. The second photon can then have any wavelength shorter than 417 nm. The disadvantage of this scheme compared with ours is the difficulty of obtaining a 553 nm laser; however, if this technical obstacle can be overcome, this protocol could provide more efficient ionization. Other ionization schemes are discussed in [57].

3.2.1.1 Neutral Fluorescence in Barium

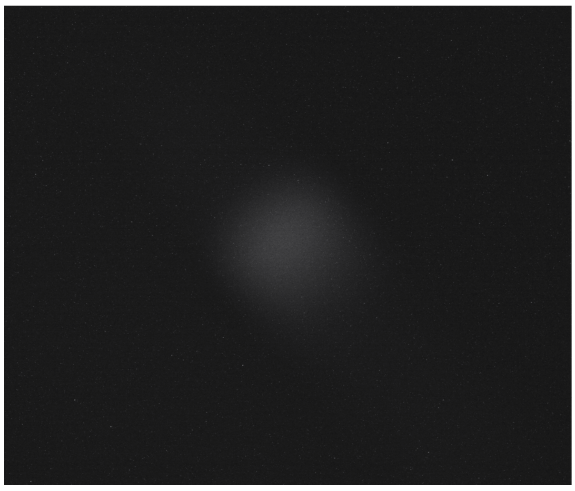

Figure 3.6: Neutral fluorescence of Ba atoms. This image was taken in the test chamber with the laser beam at approximately 90° to the atomic beam and the current of the oven at 3 A.

As in Yb (Sec 3.1.1.1), we can observe fluorescence from neutral Ba atoms. The amount of fluorescence we will see, however, is much lower for a given atomic flux, since the transition in the neutral atom we drive is not cycling. From the excited state $5d6p\ {}^3D_1$, there are several possible decay paths–see Fig. 3.5 and Ta-

ble 3.2–and the atom will only decay back to $^1S_0$ after about 2% of excitations. The majority of the time (64%), the atom will decay to $6s5d\ ^3D_1$ and emit a photon at 659.7 nm. The other most common decay is to $6s5d\ ^3D_2$, for which the wavelength is 667.71 nm. For Bob, we observed neutral fluorescence in the vacuum chamber in the center of the trap, and, for Cleo, in the test chamber. One difficulty with neutral fluorescence observation for Ba is the sizeable amount of red light emitted via blackbody radiation from the oven. This light can cause background on the camera that makes observation of the atomic fluorescence considerably harder to find. In Bob, this was our primary motivation for observing the fluorescence in the center of the trap rather than close to the tip of the oven. A sample image of the neutral fluorescence for the Cleo oven design is shown in Fig. 3.6. This image was taken with the current of the oven at 3 A.

3.2.2 Doppler Cooling

Higher Energy Level	**Lifetime**	**Lower Energy Level**	**Wavelength**	**Branching Ratio**	**Linewidth** $\left(\frac{\gamma}{2\pi}\right)$
$6P_{1/2}$	7.9 ns	$6S_{1/2}$	493.4 nm	0.732	14.7 MHz
		$5D_{3/2}$	649.7 nm	0.268	5.5 MHz
$6P_{3/2}$	6.3 ns	$6S_{1/2}$	455.4 nm	0.742	18.7 MHz
		$5D_{3/2}$	585.4 nm	0.028	0.71 MHz
		$5D_{5/2}$	614.2 nm	0.230	5.8 MHz
$5D_{3/2}$	80 s	$6S_{1/2}$	2051.8 nm	-	2.0 mHz
$5D_{5/2}$	31.2 s	$6S_{1/2}$	1762.2 nm	-	6.1 mHz

Table 3.3: Relevant transitions in $^{138}Ba^+$ with wavelengths and branching ratios. The sources are as follows: wavelengths [76], lifetime of the $P_{1/2}$ state [80], lifetimes of the $P_{3/2}$ states [81, 82], lifetime of the $D_{3/2}$ state [83], lifetime of the $D_{5/2}$ state [84], branching ratios from the $P_{1/2}$ state [80], and branching ratios from the $P_{3/2}$ state [85].

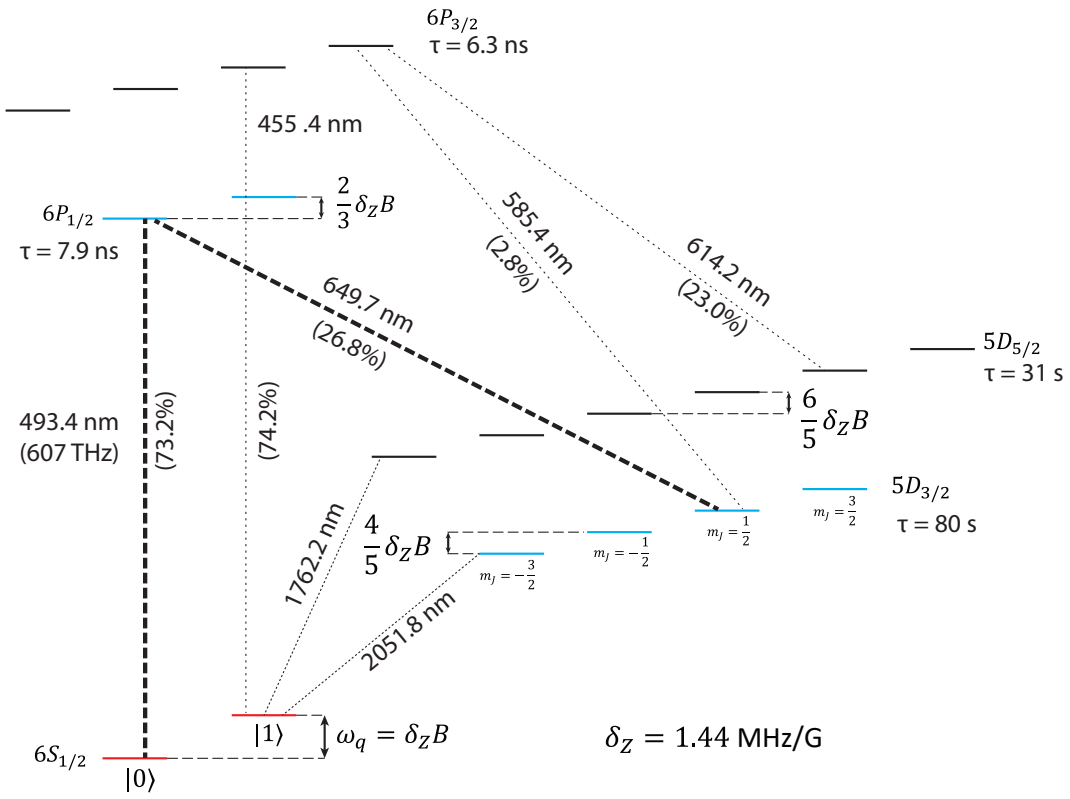

Figure 3.7: Partial energy level diagram of $^{138}Ba^{+}$. Qubit levels are shown in red, and other energy levels that are commonly populated are shown in cyan. Transitions that we currently drive with lasers are shown in the thick dashed lines, while transitions that can occur but do not routinely do so are shown with the thin dotted lines. Note that the lifetimes shown are not for individual transitions but rather the total lifetime for the energy level. More details are available in Table 3.3, and the sources are listed in the caption for the table.

In Ba^{+}, there is a low-lying D state with a fairly high branching ratio from the $6P_{1/2}$ state (Fig. 3.7, Table 3.3). Thus, Doppler cooling is not quite as simple as in Yb. In particular, we can no longer focus only on the beam driving the $S \leftrightarrow P$ transition without considering the repumping beam in more detail. In the case of Ba, the repumper is a beam at about 650 nm that drives the $5D_{3/2} \leftrightarrow 6P_{1/2}$ transition. Because of the high branching ratio, the atomic structure effectively forms a Λ system. More details of the implications of this structure are presented

in [48, 55, 57], including the resulting spectra. As an example of the impact of the structure, the spectrum of the 493 nm laser now depends on the intensity and frequency of the repumper, as detailed in the sources cited above.

In [86], there is some discussion of the dependence of the cooling rate on the 493 and 650 frequencies for a particular configuration. These calculations show that the dependence on the 650 nm frequency is minimal for laser detunings of the 493 nm laser of $\lesssim 10$ MHz. One other interesting conclusion from this paper is that the cooling rate is symmetric about the 650 nm resonance, instead of the typical heating on one side of resonance.

We can expand upon the calculations of this paper with some experimental observations as well, especially since the calculations in this paper are performed only for limited laser settings (i.e. fixed intensity, only $\sigma^{\pm}$ polarization). In particular, we have observed that there is a regime with higher intensities on the 650 nm beam where we can in fact cool on that transition instead of the 493 nm transition. While the parameters for this regime have not been well characterized, there is a clear signature in the behavior of the ion that leads us to this conclusion. In general, there is a sharp drop in ion fluorescence as the cooling laser is scanned across resonance from red detunings to blue detunings. Often, the ion crystal melts as observed concurrently on a camera image. When we are in the regime where cooling is occurring on the 650 nm transition, we observe this behavior only when scanning the frequency of the 650 nm laser, but not that of the 493 nm laser. Indeed, in this regime, the 493 nm frequency can be scanned over a wide range without the ion crystal melting. We typically do not operate in this regime; however, it is a

strong indicator that the laser intensities have significantly changed.

It is also important to note that the Λ system leads to coherent dark states for certain relative detunings of the two lasers [87]. While the linewidth of these states are likely narrower than the linewidth of the laser, they will reduce the brightness and thus the cooling rate since the cooling rate is proportional to the scattering rate. To avoid this, we ensure that one beam, typically the 493 nm beam, is always red-detuned from resonance while the other is blue detuned.

3.2.3 State Preparation and Detection in the $6S_{1/2}$ Manifold

In $^{138}Ba^{+}$, there is no hyperfine qubit available. Instead, the only possible choice for a ground state qubit consists of the Zeeman levels in the $6S_{1/2}$ manifold. We define the qubit levels $|0\rangle \equiv \left|6S_{1/2}, m_J = -\frac{1}{2}\right\rangle$ and $|1\rangle \equiv \left|6S_{1/2}, \frac{1}{2}\right\rangle$, which are split by 2.88 $\frac{\text{MHz}}{\text{G}} * |B|$. Typically, we work with a splitting of order 10 MHz. It is important to note that this splitting is sensitive to magnetic field fluctuations to first order, and our coherence time in Ba is much lower than that in Yb. This splitting is not large enough to resolve using frequency selectivity, since we only lock our lasers to $\sim$10 MHz (using a wavemeter), and the natural linewidth of the $6S_{1/2} \leftrightarrow 6P_{1/2}$ transition is over 10 MHz. Therefore we rely on polarization to resolve the qubit states instead.

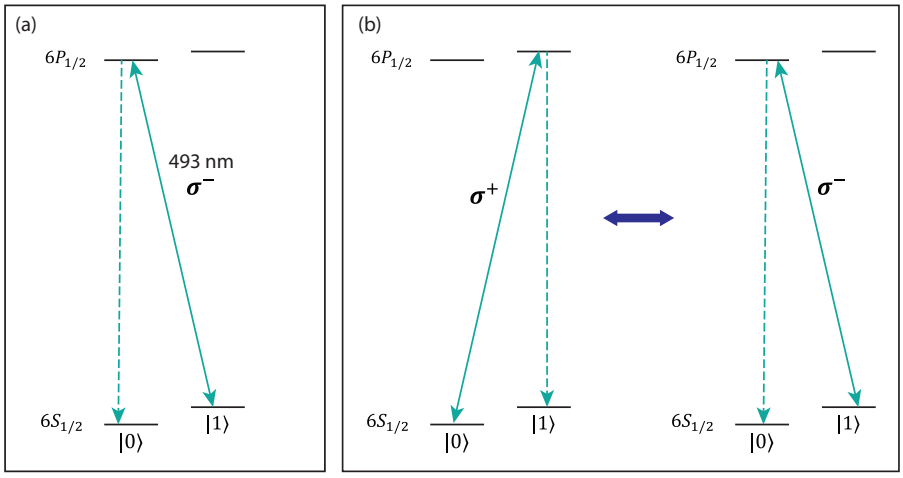

Figure 3.8: State preparation and measurement in the $^{138}Ba^+$ $6S_{1/2}$ manifold. The qubit is defined as the Zeeman sublevels, and transitions to the excited $6P_{1/2}$ state are driven with a 493 nm laser. For simplicity, the $5D_{3/2}$ state is not shown in the figures; however, for all operations in this section, all polarizations of the 650 nm repumper beam are on to clear out all of the sublevels in that manifold. In each diagram within an energy level, the states on the left have $m_J = -\frac{1}{2}$ and those on the right have $m_J = \frac{1}{2}$ (a) State preparation. To prepare $|0\rangle$, we turn on only σ^- light. Since there is no available transition with 493 nm σ^- light from $|0\rangle$, all population is transferred to this state. If we wish to prepare $|1\rangle$, we simply pump with σ^+ light instead. (b) Measurement of the qubit state. On each shot, we turn on either σ^+ or σ^- light. $|0\rangle$ is dark to σ^- light, while $|1\rangle$ is dark to σ^+ light. Thus, we can distinguish which state the ion is in based on the average number of photons collected with each polarization.

3.2.3.1 State Preparation

To prepare a particular state, we first note which transitions are allowed for each polarization as determined by the selection rules in Eq. 2.54. The $P_{1/2}$ manifold only contains states with magnetic quantum numbers $\pm\frac{1}{2}$. Therefore, from $|0\rangle$, we can drive transitions with $\Delta m_J = 0, +1$, corresponding to π and σ^+ polarizations respectively. From $|1\rangle$, the available transitions have $\Delta m_J = 0, -1$, which can be driven with π and σ^- light, respectively. Note that π light can drive transitions from both qubit states, and thus cannot be used for optical pumping. Therefore, if

we wish to pump to $|0\rangle$ ($|1\rangle$), we use only σ^- (σ^+) polarized light [48]. This process is depicted in Fig. 3.8(a). During optical pumping, all polarizations of 650 nm light are also applied to the ion to prevent any population from being pumped to the $5D_{3/2}$ state. The entire process typically takes $\lesssim$1 μs.

3.2.3.2 State Detection

Detection relies on similar principles. As discussed above, one of the qubit states is dark to one σ polarization while the other is bright. Because there is no available cycling transition and the ion will be quickly pumped to the dark state, most shots we will not observe any photons during state detection. Specifically, on average, 2.8 photons will be scattered per shot before the ion is pumped dark if it is in a single qubit state and the applied light is the correct polarization [75]. However, the ion emits isotropically while our imaging system subtends only part of the 4π solid angle of all of space, and we collect only a small portion of these photons. We therefore must rely on a probabilistic detection scheme.[6] For each shot, we either apply σ^+ or σ^- light to the ion. Over many trials, the average number of photons collected determines the populations. We can express this result in terms of a matrix equation

$$\begin{pmatrix} n_+ \\ n_- \end{pmatrix} = E \begin{pmatrix} 2.8 & 0 \\ 0 & 2.8 \end{pmatrix} \begin{pmatrix} P_0 \\ P_1 \end{pmatrix} \tag{3.2}$$

where $n_\pm$ is the average number of photons collected for each $\sigma^\pm$ trial respectively, E is the overall light collection efficiency, and P_0 and P_1 are the populations in $|0\rangle$ and $|1\rangle$. Using this equation along with the constraint $P_0 + P_1 = 1$, we can solve for

the state populations and the efficiency of light collection

$$P_0 = \frac{n_+}{n_+ + n_-}$$
$$P_1 = \frac{n_-}{n_+ + n_-}$$
$$E = \frac{1}{2.8}\left(n_+ + n_-\right). \tag{3.3}$$

We rarely consider the efficiency and just focus on P_0 and P_1, but we have the ability to measure it if desired. While frequency and intensity fluctuations can occur and result in changes in n_+ and n_-, this detection scheme will not be sensitive to fluctuations common to both polarizations. It is thus fairly robust to slow drifts in frequency and intensity [48]. The matrix formulation here is unnecessary and the equations can be written down directly; however, it provides a useful starting point for understanding the detection scheme discussed in Sec. 3.2.4.2.

3.2.3.3 Experimental Considerations for Ba S State SPAM

For light propagating parallel to the quantization axis ($\theta = 0$), there will be no π component to the light, and perpendicular to the magnetic field $\left(\theta = \frac{\pi}{2}\right)$, σ^+ and σ^- are indistinguishable except for a phase.[7] Therefore, we are not able to control whether a beam propagating perpendicular to the magnetic field has σ^+ or σ^- polarization, so for state preparation, we must deliver the light along the

[6] An alternative detection scheme consists of shelving to the $5D_{5/2}$ state as detailed in [88]. For our current setup, we chose not to implement this scheme because of practical considerations and because ultimately all state readout will be performed after swapping the state onto Yb and reading out the Yb qubit state. However, we discuss the possibility of using this scheme in an all Ba network in Sec. 8.4.

quantization axis.

We assume the beam is perfectly aligned to the field. If we deliver any two orthogonal polarizations through the same fiber, we can rotate those polarizations to left-handed and right-handed circular polarizations, which correspond to σ^+ and σ^-. We do not use polarization maintaining fibers in the current experiment because of previous difficulty in achieving adequate stability in the coupling. As a result, we routinely have to perform minimal adjustments to the polarization to ensure it remains correct. For future experiments, polarization maintaining fibers can be used only if the relative phase of the two polarizations does not matter.

It is important that the σ^+ and σ^- beams have the same intensity and result in the same background level when there is no ion in the trap. To optimize the polarization, we look at fluorescence from the ion with only one of the σ beams on. If everything is perfectly configured, the ion should be completely dark. If the polarization does not correspond perfectly to either σ^+ or σ^-, however, the ion will have some residual fluorescence. We adjust a series of zero-order waveplates–a quarter waveplate, followed by a half waveplate, then another quarter waveplate–either before or after the fiber to minimize the ion fluorescence. This procedure must be performed for both of the polarizations, since there can be local minima in the polarization landscape where one of the polarizations gives very little ion fluorescence but the other does not.

Furthermore, if the beam is not well aligned to the magnetic field it may not

[7]This statement is only strictly true for an infinitely small beam. However, the laser beams are small enough that the deviation from being directly along the axis or perpendicular to it within the beam, assuming it is aligned well, is not significant.

be possible to minimize the fluorescence with both polarizations simultaneously. Certain polarization-dependent loss in the fiber or optics after the fiber can also lead to imperfections in the polarization the ion sees, since it can make the two polarizations nonorthogonal. This issue will not arise if the polarization-dependent loss is in the basis of the orthogonal polarizations, as that can be compensated by increasing the power in one beam relative to the other. However, as an example, if the two circular polarizations pass through an optic that has greater loss for horizontally polarized light, the two polarizations will no longer be orthogonal. In this case, the fidelity of the pumping will be lower as a result.

We currently obtain fidelities of over 98% for qubit state preparation and measurement. The limitations are different between traps and have not been quantified. However, the contributions, qualitatively, consist of background photons from scattered light and polarization impurity, either from misalignment to the magnetic field, polarization-dependent loss, drifting polarization, or imperfect polarizers.

3.2.4 State Preparation and Detection in the $5D_{3/2}$ Manifold

For generating single photons from a barium ion (see Sec. 6.1), we must prepare the ion in one of the edge states $\left(m_J = \pm\frac{3}{2}\right)$ of the $5D_{3/2}$ manifold. While we do not detect the state in the course of an experiment, it is useful to be able to perform state detection to verify that the optical pumping is working.

In this section, we first discuss how we optically pump in the D manifold and then how we perform state detection. Finally, we discuss how we optimize these

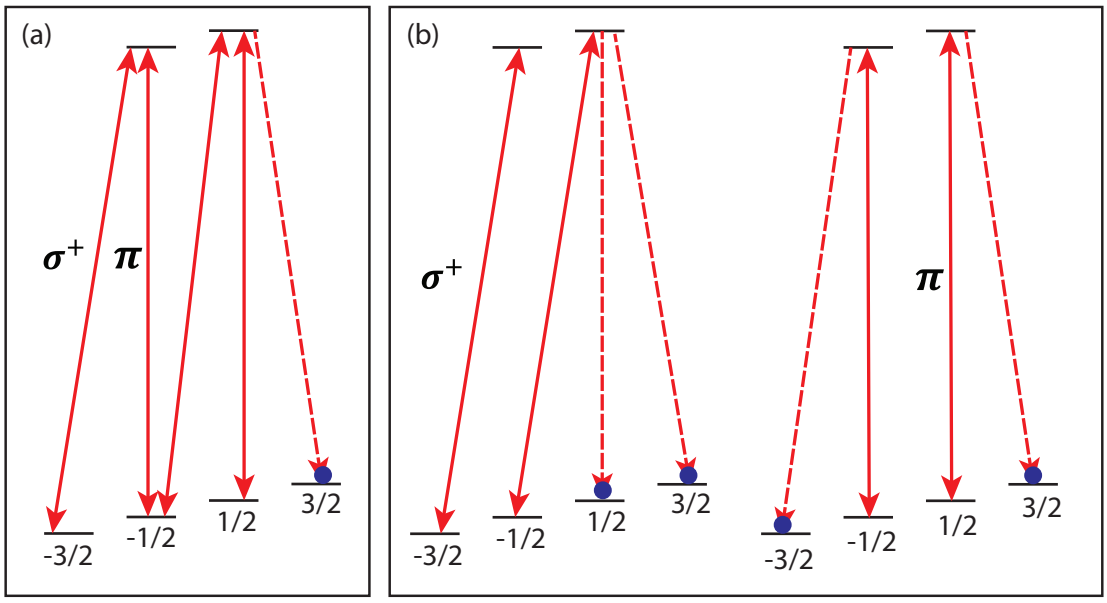

Figure 3.9: 650 nm laser beam configurations for state preparation and measurement in the $^{138}Ba^{+}$ $5D_{3/2}$ manifold. For simplicity, only the D sublevels and 650 nm beams are depicted and not the S states or 493 nm beams. In all of the diagrams, dashed lines represent decays that occur where a transition is not driven, while solid lines indicate transitions driven by a laser. Not all possible decays are shown. The purple circles indicate population in dark states for a given beam configuration. (a) Optical pumping to $\left|5D_{3/2}, m_J = +3/2\right\rangle$. 650 nm light with σ^+ and π polarizations is applied to the ion, leaving only the $m_J = +3/2$ state dark. (b) Detection of population in the $D_{3/2}$ sublevels. We cycle through 5 polarization combinations: σ^+ and π individually as shown in (b), plus σ^+ with π (shown in (a)), σ^-, and σ^- with π. The last two configurations are not shown, but are mirror images of the first diagram in (b) and the diagram in (a) respectively. Population is extracted based on the relative number of photons collected for each configuration over many shots.

procedures.

3.2.4.1 State Preparation

As shown in Fig. 3.9(a), we apply both σ^+ and π polarizations of 650 nm light to prepare the edge state. These two beams can be switched on and off independently. Both polarizations are necessary due to the selection rules laid out in Eq. 2.54. Specifically, if only σ^+ light were applied, for example, there would be

population left in the sublevels with $m_J = +1/2$ and $m_J = +3/2$ (Fig. 3.9(b), first diagram), or if only π light were applied, there would be population in the sublevels with $m_J = \pm 3/2$. Meanwhile, we also leave both σ^+ and σ^- polarizations of 493 nm light on the ion to clear out the S manifold. 493 nm light that is π polarized can be used in addition to or instead of the σ polarization. However, as discussed in Secs. 3.2.3, we require the σ polarizations already, and the addition of π light does not significantly decrease our pumping time, so we only use the σ beams.

The rate of pumping depends on many factors including the magnetic field amplitude, the powers of all of the 650 nm polarization beams, the power of the 493 nm light, and the frequencies of all of the beams. If we operate with the same optical powers throughout the experiment, we are constrained by the single photon generation process (Sec. 6.1) to a saturation parameter for 650 nm σ^- light of about 510. Using the optical Bloch equations discussed in Sec. 2.4.2, we can calculate how much time will be required before at least 98% of the population is in the state $\left|D_{3/2}, m_J = +3/2\right\rangle$. For a magnetic field of about 2 G, where we have typically operated in the past, we find that for any detunings and saturation intensities, the minimum pumping time is at least 2.8 μs.

However, for larger magnetic fields, we can decrease the pumping time considerably (see Fig. 3.10 for example). While pumping, we also must not heat the ion. Thus, the 493 nm beams must still be detuned to the red of resonance while the 650 nm beams must be blue-detuned. Furthermore, we note that given the saturation intensities of the 493 nm and 650 nm transitions, we need considerably higher 493 nm powers to achieve the same saturation parameter. Also, in practice,

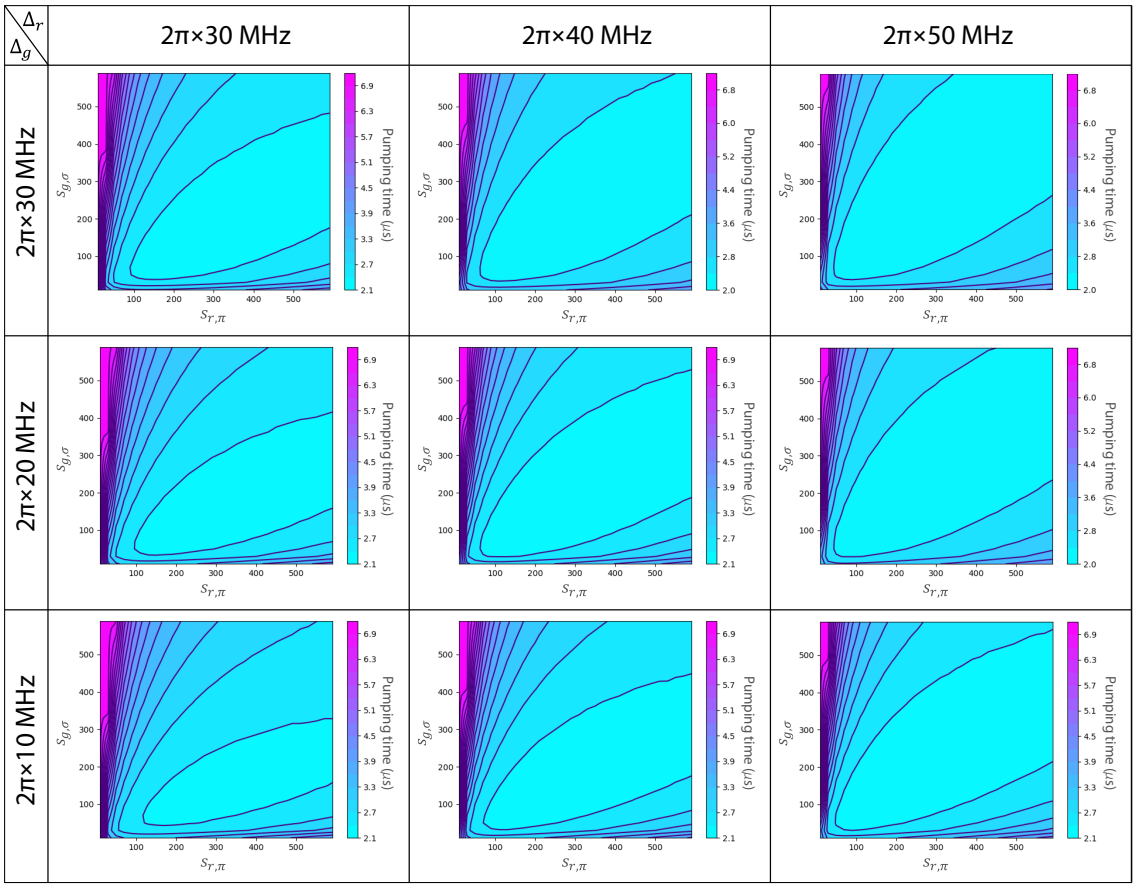

Figure 3.10: Pumping times to the $\left|D_{3/2}, m_J = +3/2\right\rangle$ state for various detunings of the 650 nm laser beam and the 493 nm laser beam at a magnetic field of 4.2 G. The horizontal axis in each plot is the saturation parameter for the 650 nm π beam while the vertical axis is the saturation parameter for each 493 nm σ ($s_{g,\sigma} = s_{g,\sigma^+} = s_{g,\sigma^-}$). For larger detunings of the 493 nm beam, the 650 nm beam can be closer to resonance to achieve the same pumping time; however, larger 493 nm saturation parameters are required. On the other hand, when the 493 nm beam is tuned closer to resonance, lower 493 nm powers can be used but higher 650 nm powers are required. To explore optimization of D state pumping, a far wider parameter space was explored, but the plots shown here depict a feasible regime while achieving 2 μs pumping times.

we have much less 493 nm power available in the lab than 650 nm. This limitation can in theory be overcome by tighter focusing of laser beams, but that would require a major overhaul of our experimental setup. For a magnetic field of twice what we have used in the past ($B = 4.2G,\ \omega_q/(2\pi) = 12.1\text{MHz}$), we see that we can achieve pumping times of about 2 μs with a saturation parameter for 493 nm of well under

100 if we detune the 493 nm beam close to resonance ($\Delta_g/(2\pi) = -10$ MHz), and the 650 nm beam farther from resonance ($\Delta_r/(2\pi) = 40$ MHz). We then require a saturation parameter for 650 nm of about 100, which is readily achievable in the lab.

Additionally, we actually use two separate lasers for 650 nm π polarized light and 650 nm σ polarized light. Because of this configuration, we can have different detunings for the two 650 nm lasers. This will likely affect our pumping times; however, we have not yet been able to incorporate multiple laser detunings into our simulations. We can experimentally explore this regime and see if we can further improve beyond the theoretical calculation. We do not observe significant improvements in the optimal pumping time, although the observed ideal detunings differ from the predictions from the simulations.

One other option for improving pumping times is varying the laser power depending on the phase of the experiment. For example, we can use a lower RF power on the AOM that controls the 650 σ beam during pumping compared with single photon generation. With a lower 650 σ power, we would be able to use correspondingly lower 493 power and 650 π power, as well as using a lower magnetic field. After thoroughly exploring the above regime and struggling to decrease the pumping times below about 3 μs for achievable magnetic fields, we decided that this direction is more promising despite the increased complexity in the control software. More details of this implementation are discussed in Sec. 6.4.

3.2.4.2 State Detection

While the principles behind state readout in the D manifold are an extension of those describing the qubit state detection discussed in Sec. 3.2.3.2, the larger number of levels dramatically increases the complexity. We now must be able to determine the populations in four levels instead of two, and any given polarization has at least two bright states associated with it. However, by increasing the number of polarization configurations we use from two to five, we can in fact achieve state measurement in this manifold.

The five polarization combinations must all be linearly independent. There are only three individual polarizations, of course, but certain polarizations can be combined to give us the desired result. We use all three of the individual polarizations–σ^+, σ^-, and π–as well as the two combinations σ^+ with π and σ^- with π. As with the qubit readout scheme, this protocol is probabilistic, and we cannot obtain results from a single trial. Over thousands of trials, however, each only approximately 1 μs in duration, we can build up enough statistics for each polarization setting to deduce the populations.

For the following discussion, we will refer to each sublevel as $|m_J\rangle$. Mathematically, we write the relationship between the number of photons collected and

the population in each sublevel as follows [55]:

$$\begin{pmatrix} n_+ \\ n_- \\ n_\pi \\ n_{+\pi} \\ n_{-\pi} \end{pmatrix} = E \begin{pmatrix} 6.6 & 5.4 & 0 & 0 \\ 0 & 0 & 5.4 & 6.6 \\ 0 & 6 & 6 & 0 \\ 13.3 & 12.6 & 11.4 & 0 \\ 0 & 11.4 & 12.6 & 13.3 \end{pmatrix} \begin{pmatrix} P(|-3/2\rangle) \\ P(|-1/2\rangle) \\ P(|+1/2\rangle) \\ P(|+3/2\rangle) \end{pmatrix} \tag{3.4}$$

where n_ϵ corresponds to the polarization ϵ with $+$ and $-$ short for σ^+ and σ^- respectively. This matrix is calculated using a Monte Carlo simulation with the assumptions that the intensities of all polarizations of 493 nm light are the same as each other and all polarizations of 650 nm light have the same intensity as well [75]. We do not always operate exactly in this regime and are still able to obtain reasonable results, and since we use this protocol only as a diagnostic tool, it is not extremely important that the fidelity is maximized.

In addition to these equations, the populations must also sum to 1, and the population in any given level must be between 0 and 1. The problem is thus over-constrained given the number of equations. However, we can find a best fit using a constrained linear least-squares solver as discussed in [55] and obtain equations for the populations and efficiency in terms of the number of photons collected for each polarization combination. These equations are complicated so we do not include them explicitly here, but they can be found in [55].

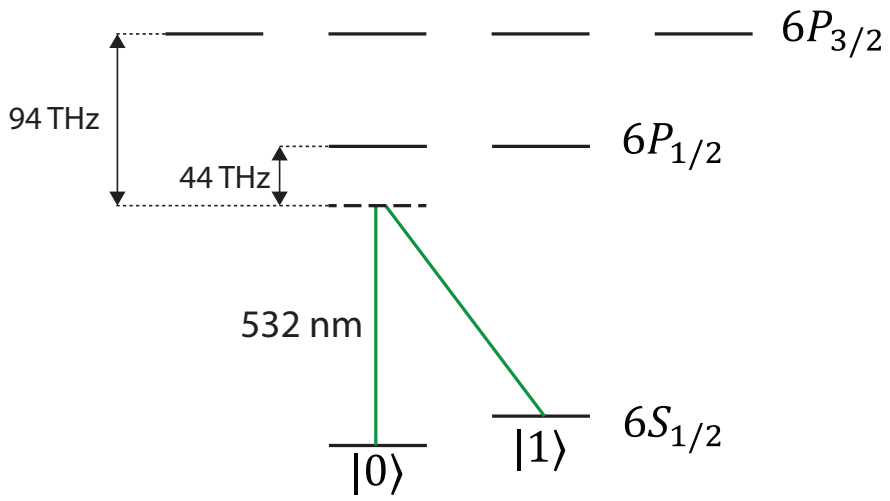

Figure 3.11: Diagram of Raman transitions in the Ba S manifold. 532 nm light couples to a virtual level 44 THz detuned for the $P_{1/2}$ manifold and 94 THz from the $P_{3/2}$ manifold.

3.2.5 Coherent Operations in the $6S_{1/2}$ Manifold

As with Yb, we need to be able to rotate between the qubit states coherently. For Ba, this can be accomplished either with RF radiation with frequency equal to the Zeeman splitting or with laser light. In addition to the considerations for microwaves with Yb, the long wavelength of the frequencies required means the vacuum chamber will very effectively screen radiation delivered from outside the chamber, so high powers of RF are required. While radiation could be applied directly to the electrodes of the trap, the frequencies of the Zeeman splitting is typically close to the secular frequency of the trap, and it is preferable to have strong filtering on the trap electrodes at this frequency to avoid coupling to the ion's motion and resultant heating of the ion. Instead, we choose to rely on laser-driven rotations only.

We drive these rotations with the same laser used for driving coherent rota-

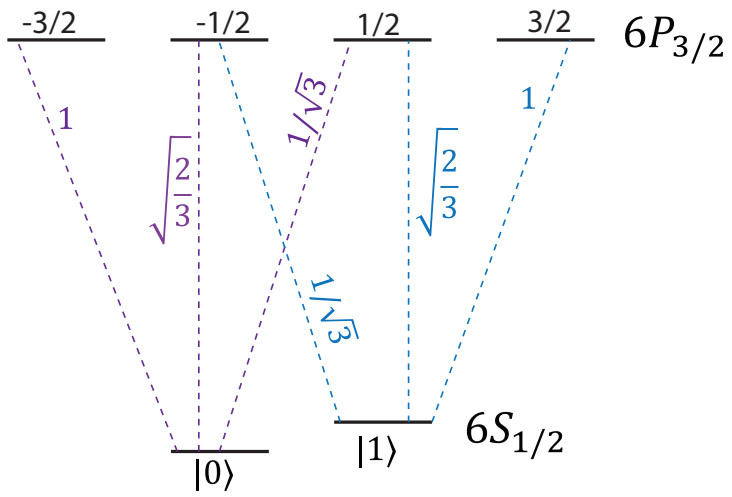

Figure 3.12: Clebsch-Gordan coefficients for transitions between the $6S_{1/2}$ and $6P_{3/2}$ manifolds.

tions in Yb. These lasers are primarily designed to produce the 355 nm light that we use for Yb; however, the frequency tripling process does not have 100% efficiency, and there is inevitably a significant amount of residual light at the second harmonic at 532 nm. We take advantage of this light to drive coherent rotations in Ba, since the 355 nm light is too far detuned from the Ba resonance to drive transitions with a reasonable Rabi frequency. Because of the small qubit splitting in Ba, it is unnecessary to rely on multiple comb teeth of the laser to span the qubit splitting, which is typically approximately 5 MHz, and we can achieve this simply with AOMs in each beam path. Using the results of Sec. 2.2, we can calculate the Rabi frequencies and AC Stark shifts. The same selection rules relevant for resonant dipole transitions (Eq. 2.54) apply here also, so we can see that, at a minimum, we must have both π and either σ^+ or σ^- polarization. For most of the results in this thesis, our only Raman beam is perpendicular to the magnetic field, so the intensity of the σ^+ light is the same as that of the σ^- light.

We can write the interaction Hamiltonian matrix elements, as in Eq. 2.79, in terms of the saturation intensity for a given transition. The two relevant saturation intensities for Raman are $I_{sat_{SP_{1/2}}} = 16.5\ \frac{\text{mW}}{\text{cm}^2}$ for the $S_{1/2} \leftrightarrow P_{1/2}$ transition and $I_{sat_{SP_{3/2}}} = 26.3\ \frac{\text{mW}}{\text{cm}^2}$ for the $S_{1/2} \leftrightarrow P_{3/2}$ transition. The Clebsch-Gordan coefficients for $S_{1/2} \leftrightarrow P_{1/2}$ transitions are given in Fig. 2.3 and those for $S_{1/2} \leftrightarrow P_{3/2}$ transitions are shown in Fig. 3.12. With this information, we can calculate the single photon Rabi frequencies for all possible transitions and thus the two photon Rabi frequencies and AC Stark shifts.

We assume that the detuning of the two Raman beams are equal to the qubit splitting including the AC Stark shifts. Then the two photon Rabi frequencies are given by:

$$\Omega = \sum_e \frac{g_{0e}^* g_{1e}}{\Delta_e} \tag{3.5}$$

where the detuning is the same for all polarizations but is different depending on if the excited state is in the $P_{1/2}$ or $P_{3/2}$ manifold. Explicitly, the two photon Rabi frequency is:

$$\Omega_{tot} = 0.061\sqrt{I_\pi}\left(\sqrt{I_{\sigma^+}} + \sqrt{I_{\sigma^-}}\right) \tag{3.6}$$

This equation confirms our previous statement that driving Raman transitions requires at least π polarized light and one of the σ polarizations.

Next, we calculate the two photon AC Stark shifts. The Stark shift must be summed over the contribution from all excited states to which the laser light couples the ground state of interest, even those that do not contribute to the Rabi frequency because they do not couple to the other ground state. The two photon Stark shifts,

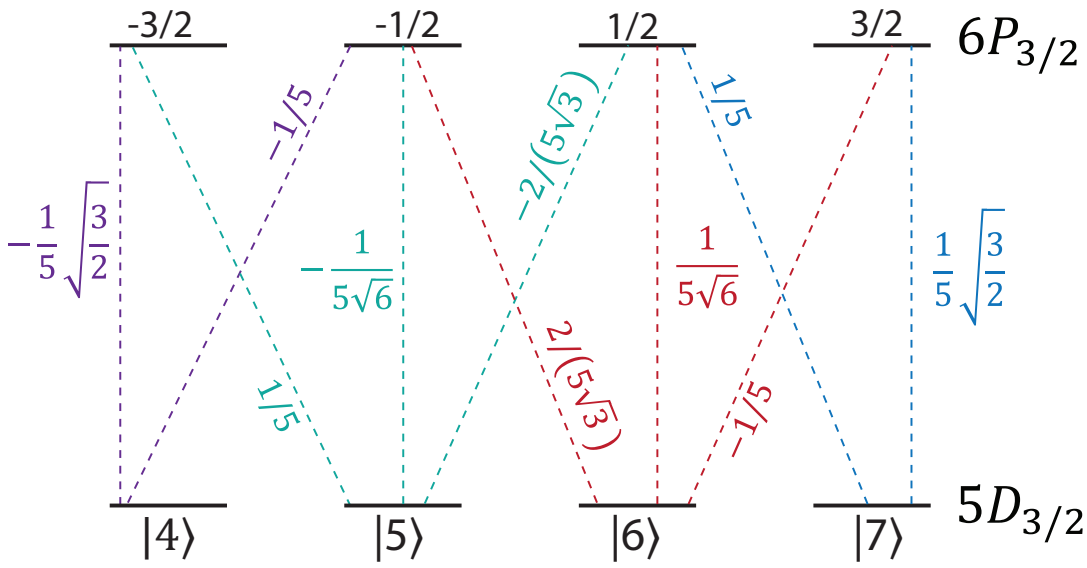

Figure 3.13: Coefficients for transition strengths between the $5D_{3/2}$ and $6P_{3/2}$ manifolds. These are not equivalent to the Clebsch-Gordan coefficients and must be calculated using Wigner-3j and Wigner-6j symbols.

calculated using Eqs. 2.31 and 2.32, are:

$$\delta_0 = -\left(0.16I_\pi + 0.11I_{\sigma^-} + 0.20I_{\sigma^+}\right)$$
$$\delta_1 = -\left(0.16I_\pi + 0.11I_{\sigma^+} + 0.20I_{\sigma^-}\right) \tag{3.7}$$

The absolute shift of the energy levels is not very important; we care more about the differential shift. We can see from this equation that the differential shift will be zero if $I_{\sigma^+} = I_{\sigma^-}$. This condition will always be satisfied for any beam propagating perpendicular to the quantization axis. It can also be satisfied for a beam propagating along the quantization axis if the polarization is linear.

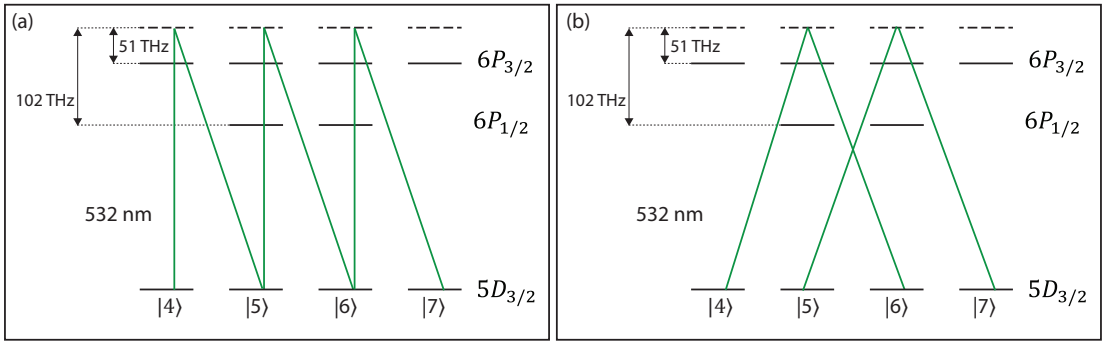

Figure 3.14: Raman transitions in the $5D_{3/2}$ state in Ba. The 532 nm laser is detuned by 51 THz from the $6P_{3/2}$ manifold and 102 THz from the $6P_{1/2}$ manifold. (a) $\Delta m_J = 1$ transitions. Not all possible couplings are shown for simplicity. (b) $\Delta m_J = 2$ transitions.

3.2.6 Coherent Operations in the $5D_{3/2}$ Manifold

While most of our operations rely on the qubit in the $6S_{1/2}$ manifold, it can be useful to be able to perform coherent rotations among the Zeeman sublevels in the $5D_{3/2}$ manifold as well [55].

For these transitions, the Raman lasers couple to both the $6P_{1/2}$ states and the $6P_{3/2}$ states with detunings of 102 THz and 51 THz respectively (Fig. 3.14). However, due to the transition strengths, the coupling to the $6P_{3/2}$ state is considerably weaker than that to the $6P_{1/2}$ state, although the detuning is smaller.

Because Raman transitions are two photon processes, we can change the angular momentum projection on the z axis m_J in the D manifold by either 1 or 2 quanta, as shown in Fig. 3.14 (a) and (b) respectively. Which transition we drive is selected based on the detuning of the Raman beams. In particular, to drive $\Delta m_J = 1$ transitions, the detuning is set to $\frac{4}{5} * 1.44 \frac{\text{MHz}}{\text{G}} * |B|$, while for $\Delta m_J = 2$ transitions the detuning is set to $\frac{8}{5} * 1.44 \frac{\text{MHz}}{\text{G}} * |B|$. The Rabi frequencies for both

Transition	Rabi Frequency, $P_{1/2}$ Coupling	Rabi Frequency, $P_{3/2}$ Coupling	Total Rabi Frequency
$\|4\rangle \leftrightarrow \|5\rangle$	$-0.033\sqrt{I_\pi I_{\sigma^+}}$	$-10^{-4}\sqrt{I_\pi}\left(8.0\sqrt{I_{\sigma^-}} - 2.7\sqrt{I_{\sigma^+}}\right)$	$-\sqrt{I_\pi}\left(0.033\sqrt{I_{\sigma^+}} + 8.0\times10^{-4}\sqrt{I_{\sigma^-}}\right)$
$\|5\rangle \leftrightarrow \|6\rangle$	$-0.019\sqrt{I_\pi}\left(\sqrt{I_{\sigma^+}} + \sqrt{I_{\sigma^-}}\right)$	$-3.1\times10^{-4}\sqrt{I_\pi}\left(\sqrt{I_{\sigma^+}} + \sqrt{I_{\sigma^-}}\right)$	$-0.019\sqrt{I_\pi}\left(\sqrt{I_{\sigma^-}} + \sqrt{I_{\sigma^+}}\right)$
$\|6\rangle \leftrightarrow \|7\rangle$	$-0.033\sqrt{I_\pi I_{\sigma^+}}$	$-10^{-4}\sqrt{I_\pi}\left(8.0\sqrt{I_{\sigma^-}} - 2.7\sqrt{I_{\sigma^+}}\right)$	$-\sqrt{I_\pi}\left(0.033\sqrt{I_{\sigma^+}} + 8.0\times10^{-4}\sqrt{I_{\sigma^-}}\right)$
$\|4\rangle \leftrightarrow \|6\rangle$ $\|5\rangle \leftrightarrow \|7\rangle$	$0.023\sqrt{I_{\sigma^+}I_{\sigma^-}}$	$-7.5\times10^{-4}\sqrt{I_{\sigma^+}I_{\sigma^-}}$	$0.022\sqrt{I_{\sigma^+}I_{\sigma^-}}$

Table 3.4: Two-photon Rabi frequencies for $5D_{3/2}$ manifold Raman transitions. The first section of the table contains the frequencies for $\Delta m_J = 1$ transitions and the second for $\Delta m_J = 2$ transitions. The second column shows the two-photon Rabi frequencies considering only coupling to the $P_{1/2}$ manifold, while the third column contains the two-photon Rabi frequencies due only to coupling to the $P_{3/2}$ manifold. The last column contains the overall two-photon Rabi frequency, which for all transitions, is nearly the same as that due only to coupling to the $P_{1/2}$ manifold. I_π, I_{σ^+} and I_{σ^-} are the intensities of π, σ^+, and σ^- 532 nm light respectively. States are labeled as in Fig. 3.14.

types of transition are discussed below, and the motivations for each are discussed in [55].

To determine the Rabi frequencies and Stark shifts, we calculate the strength of each transition from all Zeeman sublevels in the $5D_{3/2}$ manifold to those in both P manifolds. We calculate these coefficients using Eqs. 2.52 and 2.53 and define the transition strength coefficient $\tilde{C}'$ as in Eq. 2.79. For the transitions to the $P_{1/2}$ manifold, these coefficients are shown in Fig. 2.3, and for transitions to the $P_{3/2}$ manifold, they are shown in Fig. 3.13.

Once we have the coefficients, it is straightforward to find the two photon Rabi frequencies and AC Stark shifts as we did in Sec. 3.2.5, although there are now more transitions to consider. We divide the results into the contributions from coupling to the $P_{1/2}$ versus $P_{3/2}$ manifold to illustrate the much weaker coupling to the $P_{3/2}$ manifold.

State	AC Stark shift
$\|4\rangle$	$0.04I_{\sigma^+} + 9.7 \times 10^{-4} I_\pi$
$\|5\rangle$	$0.08I_\pi + 6.5 \times 10^{-4} I_{\sigma^-} + 0.014 I_{\sigma^+}$
$\|6\rangle$	$0.08I_\pi + 6.5 \times 10^{-4} I_{\sigma^+} + 0.014 I_{\sigma^-}$
$\|7\rangle$	$0.04I_{\sigma^-} + 9.7 \times 10^{-4} I_\pi$

Table 3.5: Two-photon AC Stark shifts in the $5D_{3/2}$ manifold from 532 nm light of arbitrary polarization.

For $\Delta m_J = 1$ transitions the Rabi frequncies between the $m_J = \pm\frac{3}{2}$ and $m_J = \pm\frac{1}{2}$ states will in general be different from that for the transition between $m_J = -\frac{1}{2}$ and $m_J = +\frac{1}{2}$. These frequencies, along with those for $\Delta m_J = 2$ transitions are shown in Table 3.4. The two photon AC Stark shifts of each state are shown in Table 3.5.

There are two considerations for optimizing the polarization of the light driving Raman transitions. First, for $\Delta m_J = 1$ transitions, the Rabi frequencies may be unequal depending on the relative intensities of the different polarizations. Second, for either type of transition, differential AC Stark shifts for different transitions can lead to different detunings and thus different times to drive a π rotation. For the first consideration, it is clear from the equations in Table 3.4 that it is preferable for the intensities I_{σ^+} and I_{σ^-} to be equal. Given this constraint, it is not possible for all of the Rabi frequencies to be exactly equal. However, the differential Stark shift between $|5\rangle$ and $|6\rangle$ will always be 0 given this condition, while in general, the differential Stark shift between $|4\rangle$ and $|5\rangle$ or $|6\rangle$ and $|7\rangle$ will be nonzero. By changing the detuning of the laser, it would then, in principle, be possible to make the π times more similar; however, this would sacrifice full population transfer.

On the other hand, the differential Stark shifts can all be made zero by setting $I_\pi = 0.67 I_{\sigma^+} = 0.67 I_{\sigma^-}$. This configuration will ensure that the resonance condition for all transitions will be the same and thus ensure maximum population transfer.

Chapter 4: RF Paul Traps

The most basic experimental requirement for the work presented in this thesis is a confined, cold, charged atom. In this chapter, we will focus on the confinement of an ion and discuss the theory behind it. We will also discuss practical optimization of a trap in a lab setting where the reality deviates from the theory.

4.1 RF Paul Trap Theory

An advantage of using ions is the strong interaction between the charge of the atom and external electromagnetic fields. While intuitively it may seem that we could use an electric field to confine a charged particle, Gauss's law tells us that an electric field cannot point toward the same point in all three dimensions and thus cannot confine a charged particle to a single spot [89]. This result constitutes Earnshaw's theorem [90].

Thus, to trap a charged particle, we must consider alternative solutions. One such option is to use electric and magnetic fields, as in [91]. However, in our work we instead use an RF Paul trap, as proposed in [92]. This style of trap relies on the time-averaged force experienced by an ion in an oscillating field, which yields a ponderomotive potential with an effective minimum near the center of the trap.

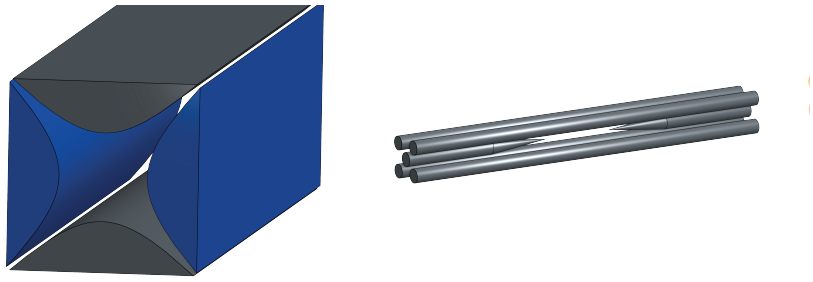

Figure 4.1: RF Paul ion trap geometries. (a) Ideal trap with hyperbolic electrodes. (b) The type of trap used in this work–a four rod trap with four cylinders in place of the hyperbolas and needles to provide axial confinement.

To begin our discussion of the physics of the trap, we assume that the ion, with charge e and mass m, is surrounded by hyperbolic electrodes in two dimensions as shown in Figure 4.1(a). We define the direction along which the electrodes are extended as the "axial" direction z, the direction between the two blue electrodes in the hyperbolic geometry as x and the direction between the grey electrodes as y. If we were to apply a static voltage V_0 to the hyperbolic electrodes, as in [92], the potential would be

$$V = \frac{V_0}{2r_0^2}\left(x^2 - y^2\right) \tag{4.1}$$

where r_0 is the minimum distance from the ion to the electrode. If we momentarily ignore the axial direction, this potential will provide a confining force in one direction and anti-confining in the other.

Consider if we instead apply an oscillating voltage $V_0 \cos\left(\Omega_T t\right)$ to one pair of

opposite electrodes while grounding the others [45]. The potential experienced by the ion is then

$$V = \frac{1}{2} V_0 \cos\left(\Omega_T t\right) \left(1 + \frac{x^2 - y^2}{r_0^2}\right). \tag{4.2}$$

If we take the time average of the resulting force on the ion, we see that this potential provides a confining force in both directions.

So far, we have not addressed how the ion is confined in the axial direction. To accomplish this final dimension of trapping, we can add endcaps, such as the needles shown on the four-rod trap in Fig. 4.1, and apply a static voltage U_0. This gives rise to an axial potential

$$U \simeq \frac{\kappa U_0}{z_0^2} \left(z^2 - \frac{x^2 + y^2}{2}\right). \tag{4.3}$$

We have stated the potential only for a trap with hyperbolic electrodes. In practice, this trap geometry is inconvenient since it allows very little optical access, and, as discussed in Chapter 3, we require laser beams to control the ions and the ability to collect photons emitted from the ions. Instead, many more feasible trap geometries have been proposed and implemented [45, 93–98]. These trap designs are only a sample of the possibilities. However, for many different geometries, the physics can be described nearly identically to that for the hyperbolic trap with the simple modification of an added geometric factor η to the radial potential [45]

$$V = \frac{\eta}{2} V_0 \cos\left(\Omega_T t\right) \left(1 + \frac{x^2 - y^2}{r_0^2}\right) \tag{4.4}$$

when considering the motion of the ion near the trap axis. This relatively straightforward result is based on the assumption that any confining potential can be expressed as nearly quadratic for small oscillations around the minimum. In this work, we use the four rod geometry shown in Fig. 4.1(b). All discussions in this chapter, while derived from the hyperbolic trap potential, will apply to this trap equally well as long as the ion motion remains small, which we require anyway for our work.

Proceeding with the calculation, we now wish to derive the equations of motion. The total potential is

$$V_{tot} = V + U = \frac{\eta}{2} V_0 \cos(\Omega_T t) \left(1 + \frac{x^2 - y^2}{r_0^2}\right) + \frac{\kappa U_0}{z_0^2} \left(z^2 - \frac{x^2 + y^2}{2}\right). \tag{4.5}$$

Following [99], we now calculate the electric field

$$\mathbf{E}(x, y, z, t) = -\eta V_0 \left(\frac{x\hat{x} - y\hat{y}}{r_0^2}\right) \cos(\Omega_T t) - \frac{\kappa U_0}{z_0^2} \left(-x\hat{x} - y\hat{y} + 2z\hat{z}\right). \tag{4.6}$$

Now, since $F = e\mathbf{E} = m\ddot{\mathbf{r}}$ where $\mathbf{r} = x\hat{x} + y\hat{y} + z\hat{z}$ we have

$$\begin{aligned}
\ddot{x} &= -\frac{e\eta V_0}{m r_0^2} x \cos(\Omega_T t) + \frac{e\kappa U_0}{z_0^2} x \\
\ddot{y} &= \frac{e\eta V_0}{m r_0^2} y \cos(\Omega_T t) + \frac{e\kappa U_0}{z_0^2} y \\
\ddot{z} &= -\frac{2e\kappa U_0}{m z_0^2} z \,.
\end{aligned} \tag{4.7}$$

Noting the similarities in these equations, we can write them in a more consolidated

form as the Mathieu equation [99]

$$\ddot{r}_i + [a_i + 2q_i \cos(\Omega_T t)] \frac{\Omega_T^2}{4} r_i = 0 \tag{4.8}$$

where

$$a_x = a_y = -\frac{1}{2} a_z = -\frac{4e\kappa U_0}{m z_0^2 \Omega_T^2} \tag{4.9}$$

$$q_x = -q_y = \frac{2e\eta V_0}{m r_0^2 \Omega_T^2}, \qquad q_z = 0. \tag{4.10}$$

The solution for motion in the axial direction is a simple harmonic oscillator with frequency

$$\omega_{osc_z} = \sqrt{\frac{2e\kappa U_0}{m z_0^2}} \tag{4.11}$$

The solutions in the transverse directions, however, are nontrivial. Floquet theory can be used to find a series solution, as shown in [68, 100], but here we simply state the result to first order in q_i and a_i [99]:

$$r_i(t) \approx A_i \cos(\omega_{osc_i} t + \phi_i) \left[1 + \frac{q_i}{2} \cos(\Omega_T t)\right] \tag{4.12}$$

where

$$\omega_{osc_i} \simeq \frac{1}{2} \Omega_t \sqrt{a_i + \frac{1}{2} q_i^2}, \tag{4.13}$$

and ϕ_i is a phase on the ion motion determined by initial conditions. A_i is a constant describing the amplitude of the ion's motion, and is set by the initial conditions.

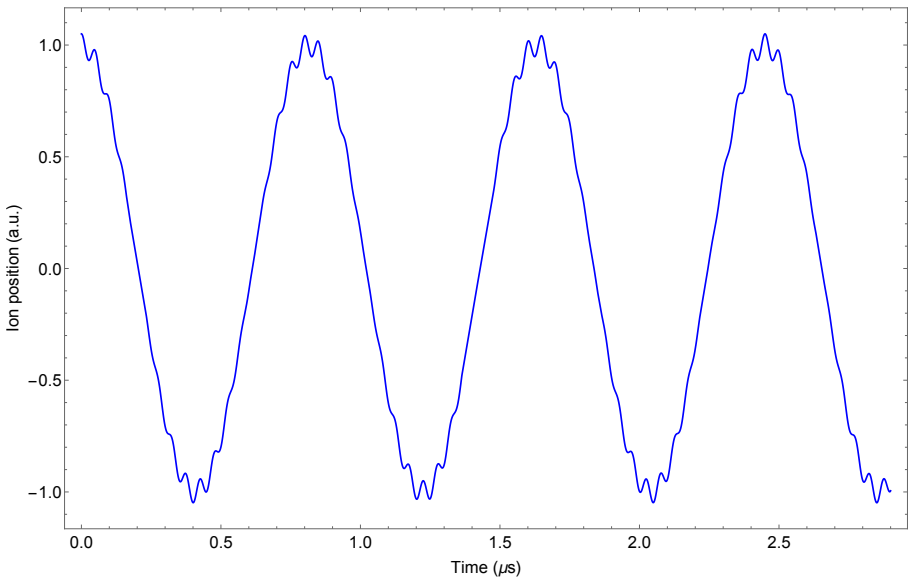

Figure 4.2: Motion of an ion in an RF Paul trap with $a_i = 0.01$, $q_i = .1$, and $\Omega_T = 20$ MHz $* 2\pi$. The small amplitude oscillations with frequency Ω_T are the micromotion, and the larger amplitude oscillations with frequency $\omega = \frac{1}{2}\Omega_T\sqrt{a_i + \frac{1}{2}q_i^2}$ are the secular motion.

The motion described in Eq. 4.12 consists of two oscillations–one at frequency ω_i and one at frequency Ω_T, as shown in Fig. 4.2. The small-amplitude, high-frequency oscillations are known as the ion's micromotion whereas the slower, larger oscillations are the secular motion. The trap is stable when $a_i << 1$ and $q_i < 1$ [101].

4.2 Trap Design and Simulations

As mentioned previously, a perfect quadrupole trap would consist of hyperbolic electrodes, but in practice this configuration is impractical. Instead, we use a four-rod style trap, which allows for more optical access and still approximates the hyperbolic electrode configuration. Before building or while working with a trap, it is useful to have a thorough understanding of the trap properties. We wish to know

the overlap between our actual trap geometry and the ideal quadrupole trap, the secular frequency in every dimension, and the principal axes of the trap. Because the electrodes are no longer hyperbolic, the problem cannot be solved analytically.

There are several software options we can use to perform these calculations. For calculating the frequencies and principal axes, we use COMSOL Multiphysics®. To begin, we define the trap geometry. While COMSOL allows importation of CAD files, since our trap has a very simple structure, we can define it in COMSOL itself.

First, we define the relevant parameters in "Global Definitions" → "Parameters." Needed values include all dimensions for the trap geometry, the voltages with which we operate, and physics properties such as the mass and charge of the ions. Then, we build the model of the trap using the "Geometry" capabilities of the software. Finally, we input the calculations that we want to perform. In the "Study" tab, we "Add Study," and select "Stationary." After pressing "Compute," the solution for the trap "sol1" is found. We can further define "Derived Values," which is where we define the specific numbers we want to find. In particular, we calculate the secular frequencies in x, y, and z, the directions of the principal axes, and the secular frequency in each of the principal axes.

When the radial frequencies in the simulation approximately match the measured trap frequencies, the calculated axial frequency is too low. This may be a result of the setup of the simulation or discrepancies between the actual trap construction and the design. As such, we only use these simulations for predictions in the transverse or radial directions, and for relative comparisons in the axial direction.

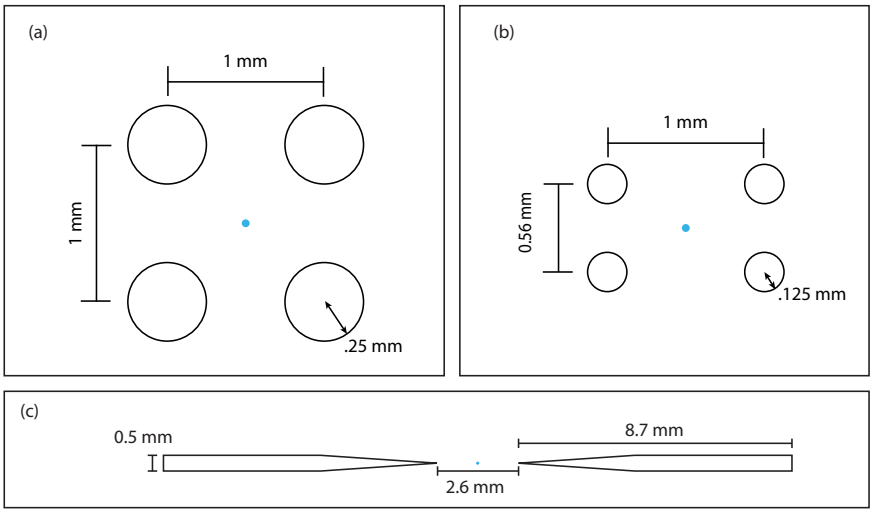

Figure 4.3: Dimensions of trap designs for which simulations are performed. All figures are individually to scale, and (a) and (b) are to scale relative to each other. (a) XY-plane cross section of trap design for our first two traps. (b) XY-plane cross section for high numerical aperture trap design. (c) XZ-plane cross section of both trap designs.

4.2.1 Simulation Results

First, we present the results of the simulation of the design for our first two traps (Fig 4.3(a)). For these simulations, we use 200 V for the voltage on the needles (approximately the value used in lab) and 470 V for the RF voltage. The RF voltage is chosen such that the radial secular frequency from the simulation gives the same result as we measure in the lab. No DC potential is applied to the rods. The resulting potentials are shown in Fig. 4.4.

From these simulations or measured frequencies (see Sec. 4.3.1) and Eqs. 4.9 and 4.10, we can also estimate the approximate geometric scaling factors for our trap. We do not have an independent measurement of the RF voltage, so we use the simulation to determine the voltage that corresponds to a particular radial secular

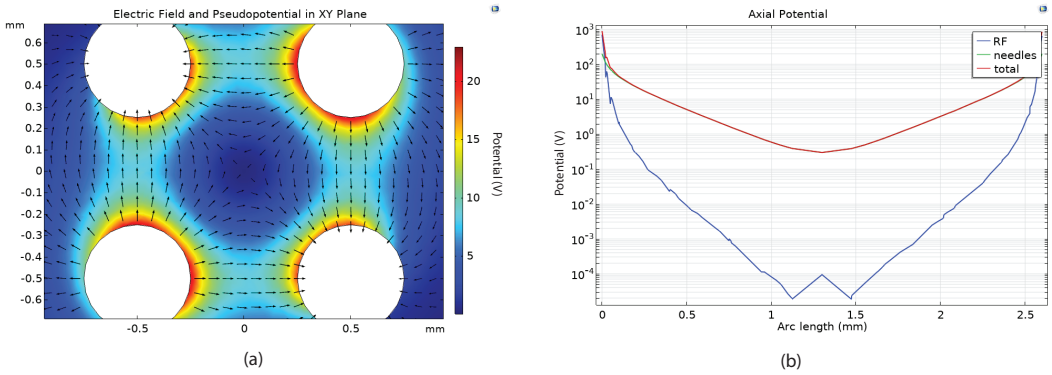

Figure 4.4: Simulated potentials for four rod trap with a square geometry. The geometry is shown in Fig. 4.3 (a) and (c). The RF voltage is set to 470 V to match the experimentally determined secular frequency, and the needle voltage is set to 200 V. (a) Pseudopotential and electric field in the XY plane. The pseudopotential is shown in the colored surface plot, and the arrows represent the electric field. (b) Axial potential (logarithmic scale). The blue curve shows the contribution from the RF voltage, which should be negligible. The green curve shows the contribution from the needles, which almost exactly matches the total potential, shown in red.

frequency. The measured axial frequency is 0.97 MHz (the simulated frequency is 0.32 MHz), and the measured radial frequency is 1.39 MHz with the simulation set to give approximately the same result. First, from Eq. 4.11 and the measured axial frequency, we obtain $\kappa \sim 0.2$. We can then substitute this value into the equation for the radial secular frequencies (Eq. 4.13) and we obtain a value for η of ~ 0.8, which as we expect is of order 1.

For the design of our third trap (Sec. 5.2), we needed to change the trap dimensions in order to increase the amount of light we could collect from between the rods in one direction. However, we also wanted to ensure that we would not be sacrificing too much in terms of the efficacy of the trap, and in particular, that our secular frequencies would still be comparable to our previous traps, since higher secular frequencies assist in achieving higher gate fidelities [102]. Thus, we also simulated the trap with the larger aspect ratio shown in Fig 4.3(b). The design for

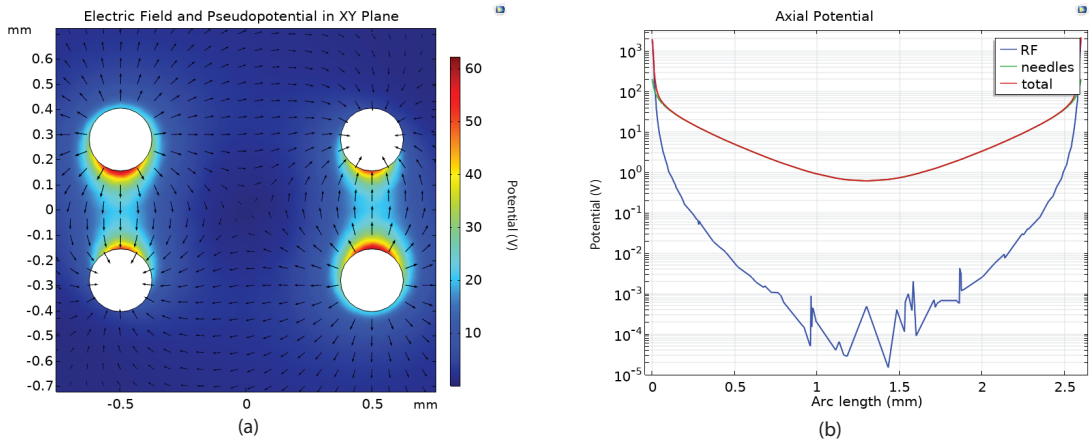

Figure 4.5: Simulated potentials for a four rod trap with rectangular geometry. The trap geometry is shown in Fig 4.3 (b) and (c). The voltages are the same as for the previous simulations, for the sake of comparison (470 V for the RF, 200 V for the DC needle voltages). (a) Pseudopotential and electric field in the XY plane. The pseudopotential is plotted as the colored surface plot, and the arrows represent the electric field. Note that the color scale differs from the scale for the previous trap. (b) Axial potential. The blue curve is the contribution from the RF voltage, the green curve is the contribution from the needles, and the red is the total potential. The green and red curves are essentially the same near the trap center.

confinement in the needle axis is the same. The results are shown in Fig 4.5.

These simulations predict radial frequencies of 1.24 MHz and 1.14 MHz in the two radial principal axes and .33 MHz in the axial direction. Given the experimental results observed in our first trap, we expect the axial frequency to be about a factor of 3 higher. Again, we can predict the geometric scaling factors for this trap. For the axial direction, since the geometry is the same and our simulations are unreliable, we assume $\kappa \sim 0.2$ as with Alice and Bob. We then obtain a radial geometric factor η of 0.6, so this trap potential does deviate more from that of the ideal hyperbolic trap. However, given the similar secular frequencies, we expect that for our purposes this design will be adequate.

While we can estimate η from this method, a full calculation would require

a more detailed analysis. To perform this analysis, we would need to calculate the overlap integral of the pseudopotential with the ideal quadrupolar potential. For this thesis, we did not perform this calculation; however, it should be possible by exporting the potential from COMSOL and then numerically integrating or using an alternate software.

4.3 Trap Parameter Optimization and Measurement

4.3.1 Measurement of Trap Secular Frequencies

Knowing the secular frequencies of a trap is important for determining the Mathieu q parameters and deciding if changes need to be made to increase or decrease the secular frequencies. Another particular concern is the distance between the needles since it is difficult to measure well and the needles can slide, so even if we did get a solid measurement, it is possible for that to change after the vacuum chamber is closed. The secular frequencies will also later be important for optimizing local entangling gates.

4.3.1.1 Measurement of Trap Secular Frequencies using Raman Transitions

As discussed in Sec. 2.2.1, coherent operations can couple to the motional modes of an ion. This coupling will be strongest for the resonance condition

$$\delta_{\alpha\beta} = \omega_0 \pm \omega_{osc_i} \tag{4.14}$$

where $\delta_{\alpha\beta}$ is the detuning between the two Raman beams and ω_0 is the qubit splitting. Thus, by scanning $\delta_{\alpha\beta}$, we can obtain a spectrum of the ion's motion.

For this measurement, the Raman beams must be configured such that $\Delta\vec{k}$ has a component along all of the principle axes whose frequencies we wish to measure. We performed this measurement on Alice and configured the Raman beams so they coupled to the axial motion and one of the radial modes. We assume the secular frequency of the other radial mode will differ from the observed mode by tens of kHz at most. The resulting measured frequencies were 1.39 MHz and 0.97 MHz for the radial and axial modes respectively.

4.3.1.2 Measurement of Trap Secular Frequencies with "Tickle" Spectroscopy

For a new trap, setting up all the lasers and optimizing all the operations necessary for performing motional spectroscopy using the Raman beams is time intensive and may not be an immediate priority. A straightforward alternative technique for measuring the secular frequencies consists of applying a "tickle" voltage to the trap, as discussed, for example, in [103]. This applied voltage has a frequency that is scanned through the expected range for secular frequencies (typically several hundred kHz to a few MHz). When the frequency matches one of the secular frequencies, the ion will rapidly heat. The primary difficulty with this technique is the likelihood of heating the ion out of the trap entirely. Additionally, if the trap has in-vacuum RF filters, it may not be possible to apply the needed tickle voltage.

We performed this procedure on Cleo by applying a signal with amplitude 0.1 V to one of the DC rods. We scanned the frequency in 10 kHz increments while observing an ion on the camera. We observed melting of the ion crystal at 1.34 MHz, 1.27 MHz, and 740 kHz. Based on the orientation of the chain when multiple ions are trapped, the confinement is weaker along the axial direction, so the lowest frequency must correspond to the axial secular frequency. From these numbers, we can compute the Mathieu q parameter for each principle axis as well as the distance between the needles. The RF frequency for these measurements was about 26 MHz. We obtain an average q for the transverse modes of 0.17. If we assume the simulated value of η (0.6, Sec. 4.2.1) is correct, this gives an RF voltage of 878 V. We also obtain a needle-ion distance of 3.6 mm$*\sqrt{\kappa}$, or 1.6 mm if $\kappa = 0.2$, which is slightly larger than the design distance.

4.3.2 Micromotion Compensation

While the micromotion mentioned above is intrinsic to any RF Paul trap, ions can also exhibit additional micromotion. Either a mismatch of the phase of the RF on the two RF rods or a displacement of the ion from the RF null due to an imperfect trap geometry or stray electric fields can result in this excess micromotion. In turn, the excess micromotion can lead to heating of the ions [104] and cause infidelity in our remote entanglement [105].

For example, the ion can experience a stray, static, homogeneous electric field

$\vec{E}_{dc}$. Then the equation of motion becomes [99]

$$\ddot{r}_i + [d_i + 2q_i \cos(\Omega_T t)] \frac{\Omega_T^2}{4} r_i = \frac{e\vec{E}_{dc} \cdot \hat{r}_i}{m} . \tag{4.15}$$

The solution is then

$$r_i(t) \simeq [d_i + A_i \cos(\omega_i t + \phi_i)] \left[1 + \frac{q_i}{2} \cos(\Omega_T t)\right] \tag{4.16}$$

where

$$d_i \simeq \frac{e\vec{E}_{dc} \cdot \hat{r}_i}{m\omega_i^2} . \tag{4.17}$$

Thus, the ion is pushed away from the RF null by $\vec{d}$, and the micromotion in the i^{th} direction is increased by $\frac{1}{2} q_i d_i$. As discussed in [99], micromotion can also be caused by a phase difference between the two RF rods; however, we mitigate this experimentally by placing a large capacitor between the wires for the inputs for the two rods just before the vacuum feedthrough. This effectively shorts the RF on the two rods, keeping the phase in sync. Our observed ability to compensate the micromotion by applying DC potentials to our electrodes also indicates that the micromotion is caused predominately by either trap misalignment or excess electric fields. Micromotion usually occurs due to displacement from the RF null in a radial direction but can also occur in the axial direction if the ion is located closer to one needle than the other. Axial micromotion is typically much smaller than radial micromotion.

We can find the correct micromotion compensation voltages using several tech-

niques. A simple, but imprecise, method is to look at a camera image of the ion and change the RF voltage. This change should not cause the ion to move, since the RF null should remain in the same location. However, we sometimes see that the ion does move, and we can attempt to minimize this distance. As currently implemented, this approach is entirely qualitative. Thus, it is challenging to make the small adjustments we typically require.

Instead, since the micromotion is at the frequency of the trap RF, we can correlate a signal from the ion that depends on the phase of the micromotion with the RF cycle and minimize the amplitude of the variation in the correlation to compensate the micromotion. If we have a Doppler cooling laser beam interacting with the ion, the fluorescence will depend on the direction and speed of the ion's motion, since the ion's resonance frequency will be shifted relative to the frequency of the laser beam due to the Doppler effect.

The ion scattering rate as a function of laser detuning for an approximately two-level system is given above in Eq. 2.1. For a laser beam with wavevector $\vec{k}$, and an ion with velocity $\vec{v}$, the ion will see the laser frequency shifted by $\omega_l' = \omega_l - \vec{k} \cdot \vec{v}$. To find the velocity of the ion, we can simply take the derivative of the position of the ion. The velocity of the ion due to the excess micromotion is [99]

$$\vec{v}_\mu(t) = -\frac{1}{2} \sum_{i=x,y} d_i q_i \Omega_T \sin\left(\Omega_T t + \phi\right) \hat{r}_i \tag{4.18}$$

where we have assumed that the difference in phase between the RF on the two rods is 0. The Doppler shift is then $-\vec{k} \cdot \vec{v}_\mu$. Assuming the laser is detuned for optimal

Doppler cooling, such that $\Delta_l = \omega_0 - \omega_l = -\gamma/2$ where ω_0 is the resonance of the atom, the scattering rate is then

$$R = \frac{I}{I_{sat}}\frac{\gamma}{2}\frac{1}{1 + \frac{I}{I_{sat}} + \frac{1}{(\gamma c)^2}\left(\omega_0 - \frac{\gamma}{2}\right)^2\left[\sum_{i=x,y} d_i q_i \Omega_T \sin\left(\Omega_T t + \phi\right)\cos\theta_i\right]^2}. \quad (4.19)$$

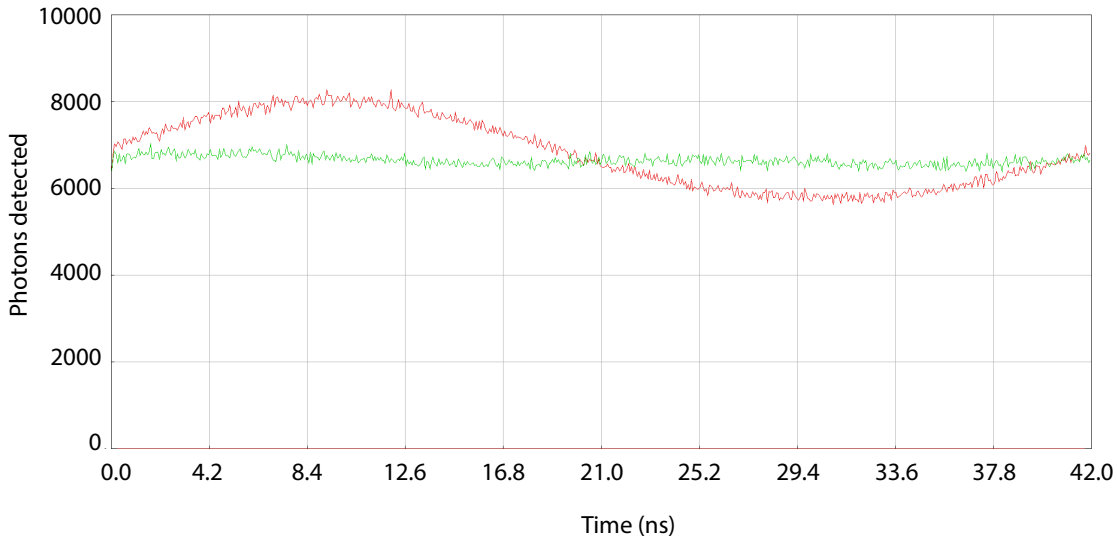

Figure 4.6: Photons collected as a function of time relative to the RF cycle. The green curve shows the approximately time-independent signal from an ion when the micromotion is well compensated. The red curve shows the time dependence of the scattering rate when one of the rod voltages is changed by 0.09 V.

The ion's fluorescence then depends on the phase of the RF cycle. We are able to observe this correlation using the PicoHarp 300,[1] which is capable of a resolution of 4 ps. We trigger on the start of the RF cycle, and then observe the ion fluorescence as a function of time. By adjusting the DC voltages on the trap electrodes, we are able to reduce the amplitude of the correlation between the ion's fluorescence and the RF signal, thus indicating an improvement in the stray field

[1] PicoQuant

compensation. The results of this test are shown in Fig. 4.6 for the case of well-compensated micromotion and when one of the DC voltages has been changed by 0.09 V.

In general, for Doppler cooling, only one laser beam resonant with the ion's primary transition is necessary. However, the use of a single beam restricts the directions in which we are able to observe micromotion, since we will only see fluorescence modulations from the direction along which the beam propagates. However, our experimental setup for barium already requires multiple Doppler cooling laser beams (see Section 3.2), so we are already able to observe micromotion in two directions as long as both beams contribute comparably to the ion fluorescence. Currently, however, we are unable to observe micromotion in the remaining direction, which is the direction along which we collect photons for our single photon experiments. Micromotion in this direction can be especially problematic, since the frequency of the emitted photons will be modulated at the trap RF frequency, and will therefore make the photons from different traps not identical. Nonidentical photons will result in reduced interference in a Hong-Ou-Mandel (HOM) setup (see Sec. 6.3.1), which, in turn, causes reduced fidelity in our overall remote entanglement protocol [105].

Measuring micromotion using this current technique along the direction of light collection is experimentally challenging, since it requires shining a beam either into the photon detection setup or backwards along the same path. Either of these setups can result in too much light hitting the sensitive single photon detectors and damaging them. Furthermore, the second configuration is technically difficult to implement. In the results in the similar experiment discussed in [32], no significant

decrease in fidelity due to residual micromotion was observed; however, our systems are not identical and their result does not necessarily indicate that micromotion will not hurt our fidelity. In the case that we do decide to attempt to compensate micromotion in this remaining direction, there is one proposed method in [105]; this protocol, however, relies on collecting ion light through a fiber. When the necessary changes to the trap electrode voltages are made to compensate micromotion, the fiber coupling will inherently decrease, likely to the point where it would be impossible to proceed with the micromotion compensation without realigning the fiber. The process would then be prohibitively slow, as each adjustment step would likely take tens of minutes rather than about ten seconds.

Here, we present an alternative approach utilizing the unique level structure of the barium ion. As discussed in Sec. 3.2, barium has an unusually high branching ratio between the primary $6P_{1/2} \rightarrow 6S_{1/2}$ decay, which generates the photons we collect, and the $6P_{1/2} \rightarrow 5D_{3/2}$ decay. This structure allows us to cool on the $D \leftrightarrow P$ transition rather than the $S \leftrightarrow P$ transition by adjusting the relative optical powers

We configure the powers and polarizations of the laser beams such that we are cooling as stated above on the 650 nm $5D_{3/2} \leftrightarrow 6P_{1/2}$ transition while still collecting 493 nm photons emitted from the ion. The 650 nm cooling beam is sent backward through the objective lens that we use to collect the single photons as shown in Fig. 4.7. The directionality of the light already will mostly solve the problem of the possibility of intense laser beam light damaging the detector. However, we can further suppress the chances of damage, and improve our signal to noise, by using

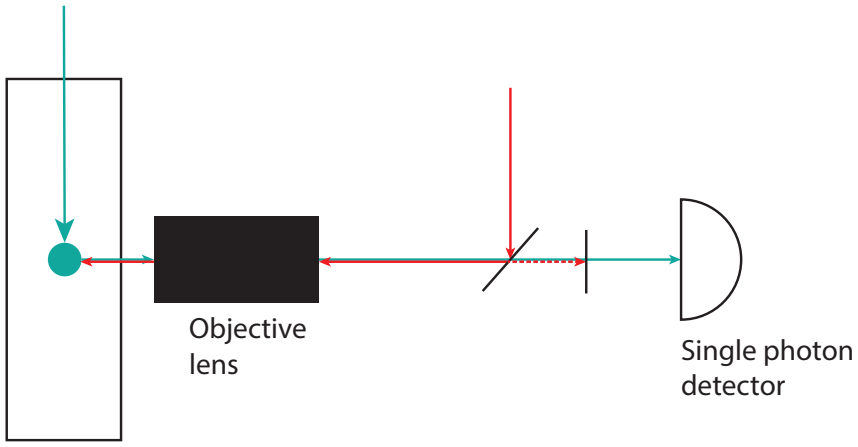

Figure 4.7: Scheme for detection of micromotion in direction of light collection. 493 nm light is still sent in perpendicular to the light collection direction. A 650 nm beam is sent in such that it is counterpropagating with the 493 nm photons collected from the ion. The use of a dichroic mirror to send the 650 nm light into the trap and an additional color filter to remove any back-scattered 650 nm photons ensures that light from the 650 nm beam cannot damage the highly sensitive single photon detector, and should also suppress any background to near zero levels.

spectral filtering. First, we send in the 650 nm light by reflecting it off a short-pass dichroic mirror, allowing the 493 nm light to pass through to the detector. It is possible, however, that light sent in could then scatter back to the detector, either reflecting off of optics along the path or the trap itself. For additional filtering, we can add a bandpass filter just before the single photon detector to block any residual 650 nm photons. This setup should result in a very clean detection signal without the sensitivity to ion position that sending in a counterpropagating 493 nm beam and collecting light through a fiber would introduce.

Another option, which we have previously implemented, is to use a Raman beam sent in this direction to directly observe the micromotion sidebands. The Raman spectrum includes peaks at the carrier frequency ω_0 and $\omega_0 \pm \omega_{osc_i}$ (see Sec. 4.3.1), but there are also sidebands on those peaks at $\omega_0 \pm \Omega_T$ and $\omega_0 \pm \omega_{osc_i} \pm \Omega_T$

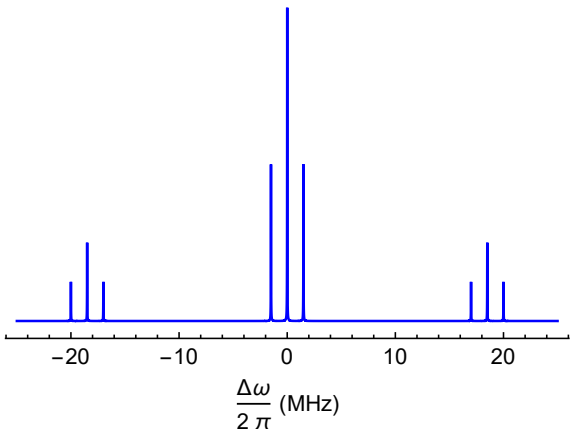

Figure 4.8: Motional mode spectrum of an ion with micromotion with $\omega_{osc}/2\pi = 1.5$ MHz and $\Omega_T/2\pi = 18.5$ MHz. Amplitudes and widths of the peaks are not to scale. The carrier transition is shown at $\Delta\omega = 0$. while the secular motion sidebands are at ± 1.5 MHz. The other peaks are the micromotion sidebands both off the carrier peak and the secular peaks. Only one motional mode is shown for simplicity.

(see Fig. 4.8). The orientation of the Raman beams must differ from our normal setup in order to observe the micromotion along the direction of light collection. In this Raman configuration, we couple to one of the radial modes along with the axial mode.

The goal is then to minimize the amplitude of the micromotion sidebands by adjusting the trap voltages. One difficulty of this method is that as the voltages are changed, the alignment of the beam to the ion will also change. This problem is exacerbated because we send one Raman beam through the Photon Gear objective (Sec. 5.1.3), so one of the beams is very tightly focused. We can mitigate this issue somewhat by purposely defocusing the beam going into the lens. However, the amplitude of the peak decreasing could still be an indication of an actual micromotion improvement or simply the beam being misaligned. Thus, the π time must routinely be checked to ensure a full π pulse is being driven with each scan. The method using

650 nm light to detect micromotion in this direction would not have this issue.

Using the Raman procedure, along with the standard micromotion compensation technique, we were able to significantly improve the micromotion in Alice. However, setting this up is fairly invasive and prevents us from fiber coupling the ion light well. The resulting lower photon number on the detector also makes state readout much noisier. This technique, therefore, cannot be used routinely, and we only chose to implement it because we were having difficulty compensating micromotion using the standard technique alone. So far, we have not had similar issues with the other traps.

4.3.3 Application of a DC Radial Quadrupole

In a standard four rod trap, the two transverse modes are degenerate. When the radial modes are degenerate, it is not possible for the ion to distinguish the principle axes so the cooling will not affect motion in the direction perpendicular to the beam [41, 106]. While it is still possible to trap in this case, and there is typically some slight difference in the secular frequencies in the two principle axes due to trap imperfections or the presence of the needles, we observe difficulties in keeping the ions crystallized, especially at higher RF amplitudes.

This problem can be addressed by adding a DC quadrupolar potential to the trap rods. As discussed previously, each rod can have a DC offset applied to it, which we have used in the past primarily for compensating micromotion. To break the degeneracy of our transverse modes, we apply a voltage of +4 V to the RF rods

and -4 V to the DC rods. This significantly improves the cooling of our ion. After applying these voltages, we are able to operate at higher RF amplitudes without the ion crystal melting, we need <5 μs of cooling during an experimental cycle instead of 30 μs, and we were able to decrease the residual micromotion. Additionally, we were able to observe the motional spectrum of an ion in Alice only with the quadrupole potential applied.

Due to the rectangular geometry of our third trap, as opposed to the square geometry of the first two, we expect that the splitting between the mode frequencies is larger. We observe a splitting between the modes of 70 kHz without any DC quadrupole, as discussed in Sec. 4.3.1.2. However, we still see an improvement in the stability of the ion crystal when we apply a similar potential.

Chapter 5: Experimental Design and Testing

The experiment discussed in this thesis has stringent and complicated design requirements, especially with regards to optical systems. In this chapter, we discuss the imaging setups for the first two traps. We also describe the design and testing of our third trap, which contains high numerical aperture aspheric lenses in vacuo for single photon collection.

5.1 Imaging Systems for the First Two Traps

For every trap in our experiment, we have several light collection needs: (i) collection of 370 nm photons for Yb state readout (free space), (ii) collection of 493 nm photons for Ba state readout (free space or in fiber), and (iii) collection of 493 nm photons into a fiber for remote entanglement. The last two can be combined, but depending on the lenses used and the fiber coupling efficiency, it may be preferable to have a free space imaging system for state readout. The free-space imaging can also be useful for alignment and the ability to observe the ions on a camera. In this section, we discuss the imaging systems we use for our first two traps.

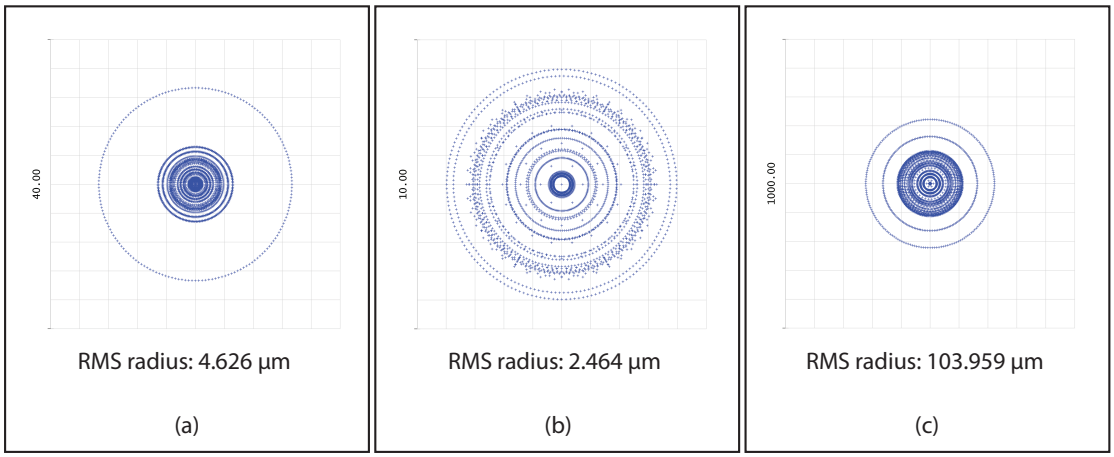

Figure 5.1: Ray tracing spot diagrams at the image plane for the free space objective used for Alice. These diagrams show the distribution of 30 rays in the image plane traced from the object plane through the objective. The outermost ray at the object plane has an angle to the optical axis corresponding to an NA of 0.39. The scale bars are in μm. (a) Spot diagram for 493 nm light with the lens optimized accordingly. The RMS radius of the image is 4.626 μm. (b) Spot diagram for 370 nm light in the optimal configuration. The RMS radius of the image is 2.464 μm. (c) Spot diagram for 370 nm light when the ion-lens distance is set for 493 nm light. This diagram is at the focus of the 370 nm light; however, due to the different object-lens distance from the configuration for (b), the spot size is much larger with an RMS radius of 103.959 mm.

5.1.1 Alice Free Space Imaging Setup

For imaging Ba and Yb in free space in Alice, we use a custom objective with numerical aperture (NA) of 0.39 consisting of five spherical lenses.[1] The properties of these lenses are shown in Table 5.1. This objective is not corrected for chromatic aberrations, so it cannot be optimized simultaneously for 493 nm and 370 nm photons. For 493 nm, the best object-lens distance is 21.888 mm in air and vacuum and 4 mm through the fused silica vacuum window and the back focal length (lens-image distance) is 182.326 mm. For 370 nm, the equivalent optimal object-lens distance is 20.481 mm with the same window while the back focal length is 227.031 mm. If pho-

[1] Special Optics

Surface description	Radius of curvature (mm)	Thickness (mm)
Object	Infinity	8.976
Vacuum Window	Infinity	4.000
-	Infinity	12.912 (11.505)
CVI PLCX-25.4-25.8-UV	Infinity	5.3
-	-25.800	2.980
CVI PLCX-25.4-38.6-UV	Infinity	3.600
-	-38.600	0.500
CVI PLCX-25.4-38.6-UV	Infinity	3.600
-	-38.600	0.500
CVI BICX-25.4-76.6-UV	76.600	4.100
-	-76.600	9.088
Newport SPC034	-22.950	2.500
-	Infinity	182.326 (227.031)

Table 5.1: Design for the imaging objective used for free space light collection for both Ba and Yb in Alice. The part numbers for the lenses are listed for the first surface of the lens, and then the subsequent surface is the other side of the lens. The thickness column indicates the distance between the center of the surface in that row and that of the next surface. Where the ideal thickness differs for barium and ytterbium, the thickness optimized for barium is listed without parentheses and that for ytterbium is in parentheses. All glass surfaces (the vacuum window and all lenses) are made of fused silica.

tons of both wavelengths are collected simultaneously and the object-lens distance is optimized for 493 nm, there is still an image plane for 370 nm with a back focal distance of 138.319 mm. However, the spot size is much larger in this configuration (see Fig. 5.1).

The laser beams used to control the ions that are at the same wavelengths as the collected photons will scatter off the trap and contribute a large background signal if we cannot spatially filter this light. Therefore, we do not detect the photons at the first image plane but rather put an adjustable aperture at this plane and then reimage the light using either another single finite conjugate lens or a telescope. The single lens is simpler to align, but standard plano-convex lenses will typically give

a much larger spot in this configuration. To decide which setup is preferable, we must consider the detector we are using to observe the fluorescence. For Yb, we use photomultiplier tubes (PMTs), which have active areas with a diameter of ∼5 mm. Thus, a spot size of several hundred microns is sufficient for observation of the full signal, and we can use a single reimaging lens. For Ba, on the other hand, we use avalanche photodiodes (APDs) with active area diameters of only 100 μm. It is therefore crucial for Ba that the spot size remain significantly smaller than 100 μm in order not to lose photons unnecessarily. We thus utilize a telescope for Ba rather than a single lens and use an aspheric lens as the final lens to focus onto the APD.

For detecting multiple wavelengths simultaneously, the aperture cannot be closed all the way since the size of one of the colors at that plane will always be much larger. Therefore, if an experiment is being performed that requires light collection from both ion species, the wavelengths must be divided using a dichroic beam splitter, and each path must then have its own aperture and reimaging stage.

5.1.2 Bob Free Space Imaging Setup

While the ultimate goal for this setup is similar to that for Alice, we had several additional constraints in its design. First, while the vacuum window used for free space imaging on Alice is reentrant, the one on Bob is not, and we therefore cannot use the objective we used for Alice. Second, Bob is mounted with the window we use for this imaging on the bottom of the chamber and there is only about 11.5 cm between the table and the window. This short distance imposes significant

constraints on the imaging system setup.

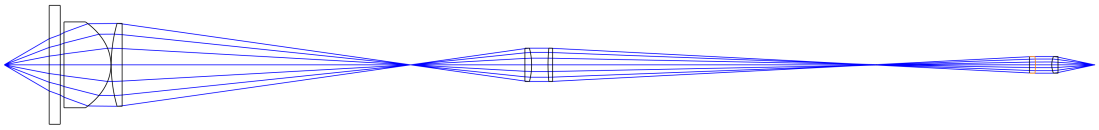

Figure 5.2: Cross section of the ray trace for the Bob 493 nm free space imaging system. The distances where the light is collimated are shown as being very small for convenience, but can be made much larger in the lab.

With both of these constraints in mind, we decided to use a single aspheric lens with NA 0.5.[2] This lens is 50 mm in diameter and has an object to lens distance of 29.665 mm in vacuum or air plus 6.782 mm through a fused silica window and is infinite-conjugate for 493 nm but finite-conjugate for 370 nm at the same working distance. The lens is made of fused silica. In general, an even asphere such as the one used here is described by the equation [107]

$$z(r) = \frac{r^2/R}{1 + \sqrt{1 - (1+\kappa)\left(\frac{r}{R}\right)^2}} + \sum_n A_n r^n \tag{5.1}$$

where z is the distance along the optical axis, r is the distance from the optical axis, R is the radius of curvature of the surface, and κ indicates the conic constant of the lens. The sum is over even n. For the aspheric lens in this system, one surface is planar and the other is described by this equation with the aspheric parameters and the lens thickness shown in Table 5.2.

The entire imaging system for 493 nm light is detailed in Table 5.3, and a cross sectional view of the ray trace is shown in Fig. 5.2. While we have not yet

[2]Thorlabs, custom design.

Parameter	Value
Thickness	28.637 mm
R	25.273 mm
κ	-0.601
A_4	-5.169×10^{-7}
A_6	-3.081×10^{-10}
A_8	-2.211×10^{-16}
A_{10}	-1.242×10^{-19}
A_{12}	3.471×10^{-22}

Table 5.2: Design parameters for the free space imaging aspheric lens on Bob. All other coefficients for the sum of polynomials are zero. The thickness is the distance from the vertex of the curved surface to the planar surface.

constructed the Yb imaging path, the 370 nm light would propagate through the custom asphere and the next two lenses before it is separated from the 493 nm light. The 493 nm light is collimated at this point, so the Ba imaging is not affected by the dichroic beam splitter.

5.1.3 High Numerical Aperture Imaging System for Fiber Coupling

The third requirement for our light collection is the most difficult and also the most crucial for our experiment. Here, we present the setup that we use for coupling light from a barium ion into a single mode fiber and summarize its performance.

The objective we use for this purpose on both Alice and Bob is designed and manufactured by Photon Gear, consists of multiple elements, and has a NA of 0.6. We are not informed of the constituent elements; however, we are still able to calculate the performance of the lens using a "black box" design file that the company provided. From this information, we can determine the optimal working distance and back focal length for multiple wavelengths and determine the decrease

Surface description	Radius of curvature (mm)	Thickness (mm)
Object	Infinity	27.400
Vacuum Window	Infinity	6.782
-	Infinity	2.265
Custom asphere	Infinity	28.637
-	-25.273*	0.200
Thorlabs LA1399-A	90.130	6.650
-	Infinity	245.776
Thorlabs LA1608-A	Infinity	4.100
-	-38.600	-
Thorlabs LA1708-A	103.000	2.800
-	Infinity	291.000
Thorlabs LA1509-A	Infinity	3.600
-	-51.500	-
Thorlabs AL1225G-A	12.987*	3.800
-	Infinity	22.569

Table 5.3: Bob free space imaging system design. The vacuum window and the custom asphere are fused silica, while all other glass surfaces are made of N-BK7. Asterisks on the radius of curvature indicate an aspheric lens, which cannot be completely described by the information in this table. The parameters describing the first asphere are listed in Table 5.2, while the aspheric parameters for the standard Thorlabs asphere are not listed here for simplicity. Dashes in the thickness column indicate the light is collimated at this point and therefore the distance is not important for the construction of the system.

in performance from misalignment. For 493 nm, the total object-vertex distance is 23.027 mm, while the back focal distance is 132.023 mm. The lens is designed to match the measured numerical aperture of the fiber we use of 0.0925.

The performance of this lens is diffraction limited with a calculated RMS radius (ignoring diffraction) of 0.435 μm as shown in Fig. 5.4. In reality, diffraction causes the beam size to closely match the mode field diameter of our fiber, and we calculate a theoretical maximum fiber coupling of 0.76 (see Chapter 7).

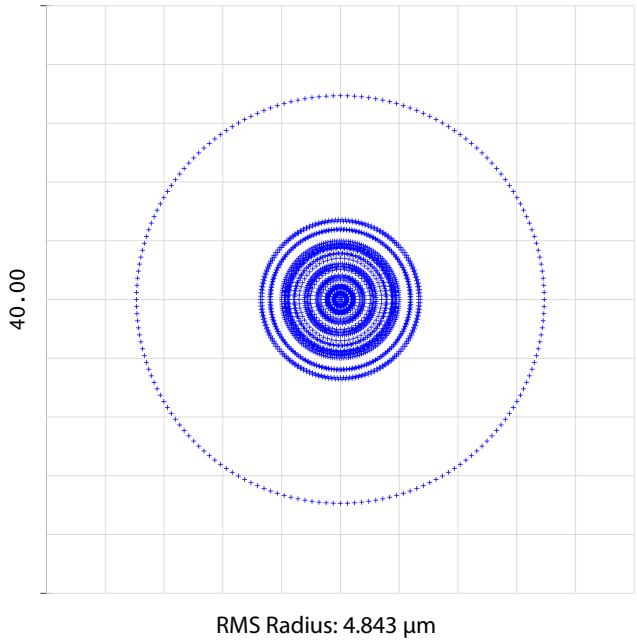

Figure 5.3: Spot diagram for the Bob free space imaging system for 493 nm. The scale is given in μm.

5.2 Design of an Ion Trap with In-Vacuum High Numerical Aperture Imaging

As will be discussed in more detail in Chapter 6, one of the main limitations of our remote entanglement generation success rate is the fact that a lens with an NA of 0.6 collects only 10% of the light emitted from the ion. Additionally, in our first two chambers, we only have enough optical access for a high NA lens on one side of the trap. Having high NA objectives in multiple directions facilitates connections with multiple other chambers. Finally, another significant reduction in our entanglement generation rates comes from our fiber coupling efficiencies, which, when we first started designing this system, were limited to about 25%. Since then, we have switched to a different lens and seen improvements up to 40%; however,

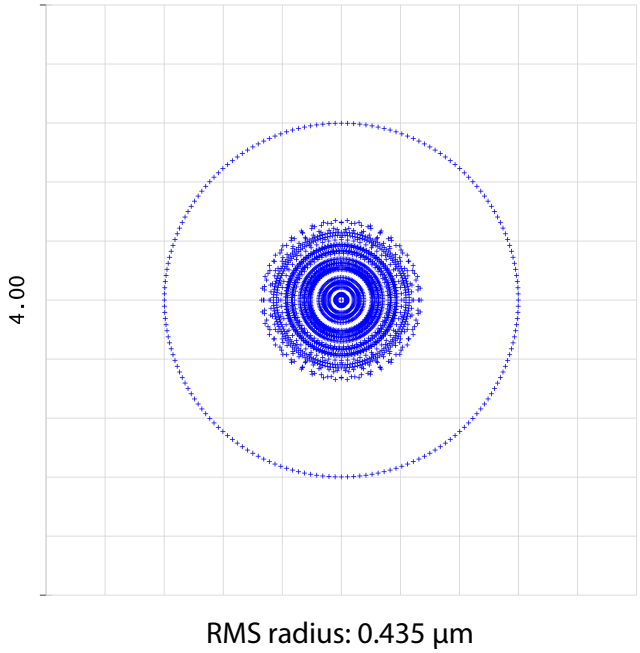

Figure 5.4: Spot diagram for 493 nm light through Alice and Bob fiber coupling objective. This diagram does not account for diffractive effects. The scale bar is in μm.

this is still significantly lower than the theoretical maximum of 76%. Some of this discrepancy may be due to deformations in the vacuum chamber window. Together, these limitations motivated us to design a new system that would hopefully improve on all of these factors.

5.2.1 Imaging Systems Design

5.2.1.1 High Numerical Aperture Aspheres for Ba Light Collection

For this system, we put a custom aspheric lens[3] on each side of the trap inside the vacuum chamber. These lenses have a NA of 0.8, are placed 6 mm from the ion, and are 1 inch in diameter. The glass for this lens is S-TIH53, which is a high-index

[3] Asphericon

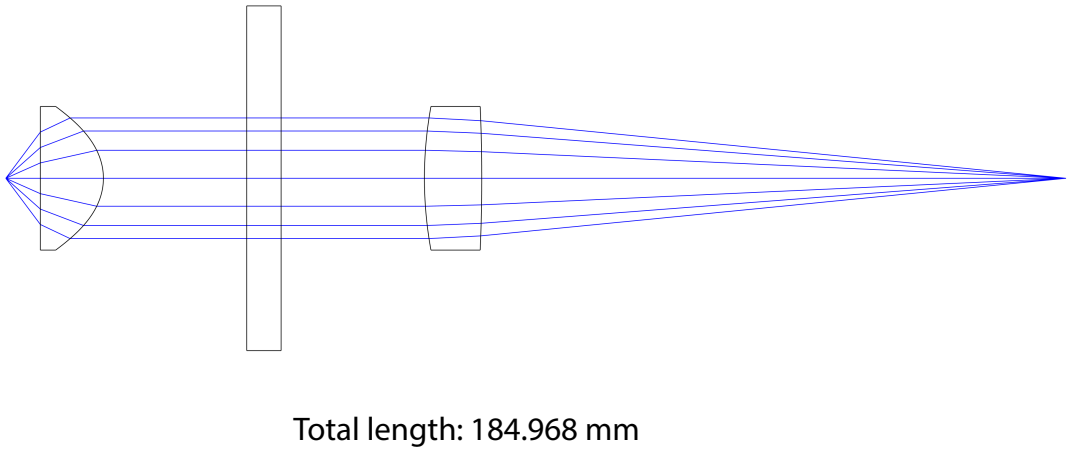

Figure 5.5: Cross section of high NA asphere system for Ba fluorescence collection. The middle object is the vacuum window, through which the light is collimated.

glass with refractive index at 486 nm of 1.87 [108]. They collimate the light from the ion through the window, which should reduce sensitivity to deformations in the window since the angle of light going through the window will deviate less from perpendicular to the surface than the light in a diverging beam. According to the manufacturer, the RMS wavefront error is expected to be less than 0.1 waves, and is limited by manufacturing tolerances.

Outside of the vacuum chamber, we use a second custom aspheric lens[4] that focuses the collimated light from the first asphere into a fiber with a numerical aperture of 0.0925 to match the in-fiber beam splitter we use for remote entanglement. This lens is also robust to a tilt angle of the incoming light of up to 0.5°. A cross section of this system is shown in Fig. 5.5. The performance of this system is diffraction limited and has a theoretical maximum fiber coupling efficiency of 56% for a uniform input apodization (the distribution of input rays) in Zemax.

[4] Asphericon

Parameter	**Value**
Thickness	11.000 mm
R	10.367 mm
κ	-1.059
A_4	5.598×10^{-5}
A_6	-3.664×10^{-9}
A_8	-5.966×10^{-10}
A_{10}	-3.201×10^{-13}
A_{12}	-3.700×10^{-14}
A_{14}	3.644×10^{-16}
A_{16}	-8.843×10^{-19}

Table 5.4: Parameters describing the in-vacuum Ba light collection high NA asphere.

Surface	Radius of Curvature (mm)	Thickness (mm)	κ
1	68.592	10.0	-1
2	-291.000	-	0.000

Table 5.5: Parameters describing the out-of-vacuum asphere for focusing Ba light into a fiber. Both sides of the lens are convex. All polynomial coefficients are zero.

A difficulty with the high NA aspheres is their small field of view and depth of focus. As observed with the ion, moving the lens by 1 μm in the transverse directions introduces significant comatic aberrations while a similar translation in the focal direction causes significant defocus (see Sec. 5.3.1). These aberrations will decrease our fiber coupling efficiency as will be discussed in more depth in Chapter 7. Thus, we require the ability to make submicron adjustments of the in-vacuum aspheres.

Finding optomechanics capable of the necessary control is difficult due to the strict ultra-high vacuum (UHV) requirements for trapped ions. We aim for our chamber to have a pressure of order 10^{-11} Torr, and most translation stages with the necessary precision will contribute far too much outgassing to a vacuum chamber

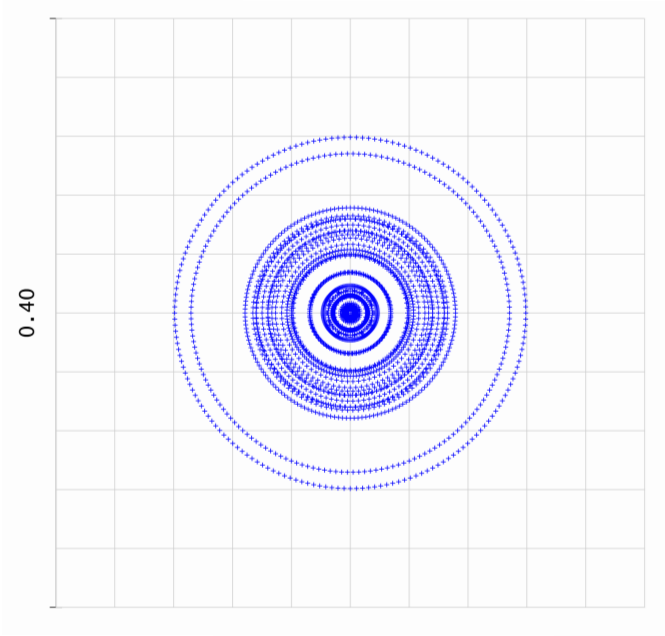

Figure 5.6: Spot diagram showing distribution of light in the image plane for the high NA asphere system. The spot size is much smaller than the diffraction limit. Units are in μm.

to achieve these pressures. However, Smaract manufactures a stage[5] that is specified to pressures of $< 1 \times 10^{-11}$ Torr. In addition, the stage has (closed loop) resolution of 1 nm and repeatability of ± 30 nm. This stage therefore allows sufficient control of the asphere location.

Another important consideration is how the aspheres are mounted. Stress on the glass could cause deviations from the ideal design, which, in turn, could lead to worse fiber coupling. In day-to-day operation, if the asphere is fixed in place only at a few points, those points will have greater stress. Thus, we want cylindrically symmetric mounting. Furthermore, during the bake of the chamber (see Appendix A), the changes in temperature can cause materials in the mount to

[5]SLC-1730-O20-W-S-UHV-NM

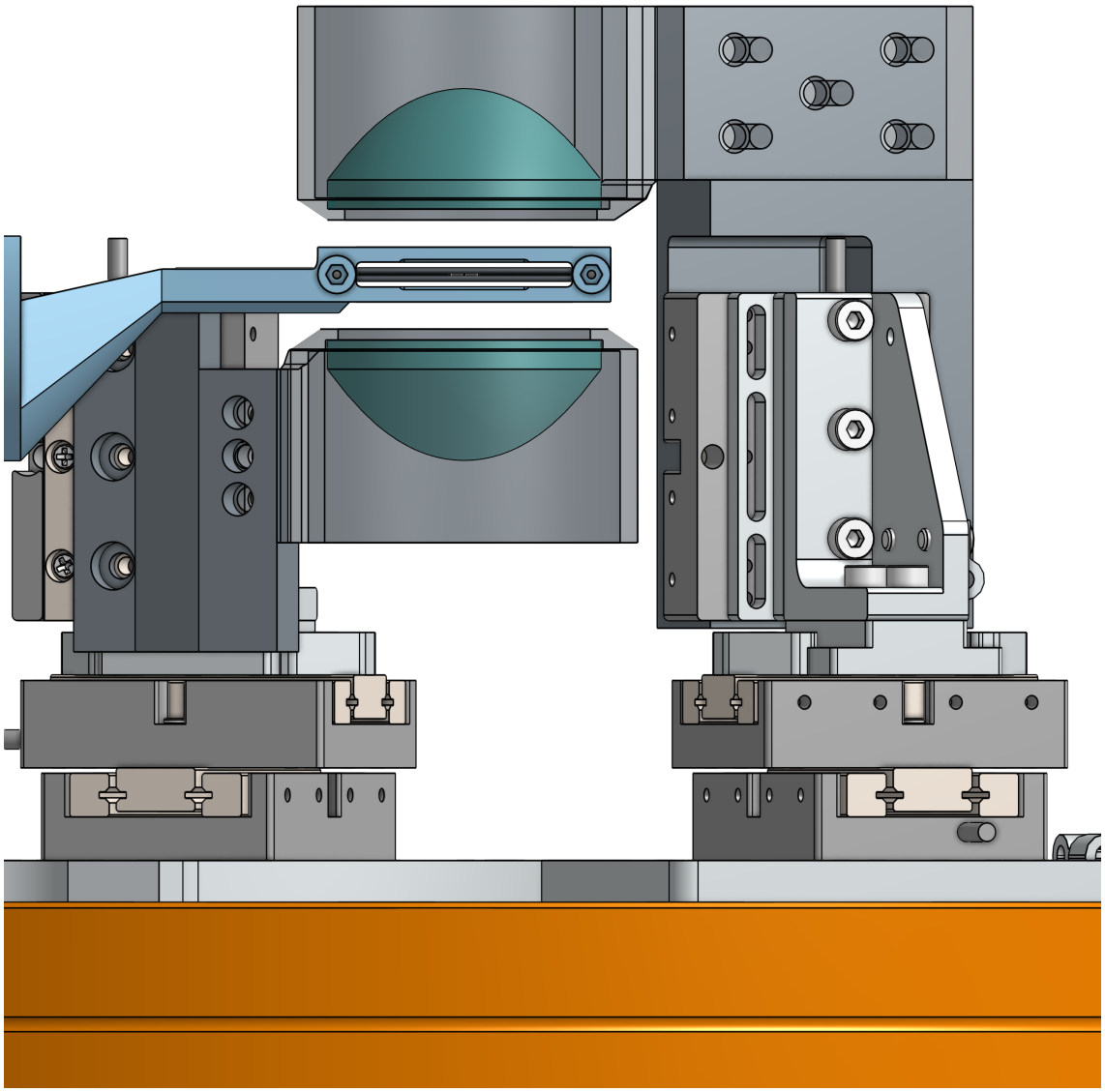

Figure 5.7: CAD model of the in-vacuum asphere mounting setup.. The blue object in the vertical center of the image is the ion trap holder, and the ion is located at the approximate center of the opening between the screws. The green objects above and below the trap are the aspheres, with a distance from the front surface of the asphere to the ion of 6 mm. The retaining rings for the aspheres are not shown. The piezo stages are located at the sides of the figure.

expand more or less than the lens itself. Lens holders are often manufactured from a metal, typically aluminum or stainless steel, which have linear thermal expansion coefficients of more than twice the coefficient for the glass [109]. Although the metal would expand more when hot than the lens, and therefore it might seem that there

would not be stress on the lens as a result, the subsequent cooling down and possible shifts in position could still lead to deformation.

For the second consideration, we choose to minimize the stress induced from temperature changes in a few ways. First, we had the main holder manufactured from Macor, a material with a fairly similar thermal expansion coefficient to the glass of the lens. S-TIH53 has a linear thermal expansion coefficient of $88 \times 10^{-7}/°\text{C}$ in the range -30-70 °C and $104 \times 10^{-7}/°\text{C}$ in the range 100-300 °C [108]. Macor, which is a machineable ceramic, has a linear thermal expansion coefficient of $90 \times 10^{-7}/°\text{C}$ in the range 25-300 °C [110]. This material is therefore preferable to the standard metals discussed above. The lens holder consists of an internally threaded tube with an inner diameter of 25.4 mm and a retaining ring that screws into the tube to hold the lens in place, both of which are made from Macor. An image of the CAD model for this mounting setup is shown in Figure 5.7. Additionally, we place a piece of indium wire between the retaining ring and the lens so that any thermal expansion will primarily affect this wire rather than the lens.

Another issue that could arise due to the presence of these lenses is excessive heating of the nearby trapped ions. Charge buildup on insulators can cause trapped ions to heat and the time-varying nature of such potentials leads to difficulty compensating micromotion [111]. While the ions are relatively far from the asphere surface compared to the length scales for some of the effects discussed in [111], the large exposed surface area may still contribute to such effects. To reduce the likelihood of this being an issue, we coated the front surface of the asphere with indium tin oxide (ITO), a conductive coating that is transparent at 493 nm. A gold

wire was then placed between the lens and the Macor holder and connected to the chamber to ground the surface and remove any charges that may build up. For one asphere, the resulting measured sheet resistance is 5 kOhm/square, while the other is 3.9 kOhm/square.[6]The thickness of the deposited layer is about 10 nm.

ITO is not completely transparent at 493 nm. While the internal transmission of the lens is expected to be about 96% and the surface away from the ion is coated to have $< 0.4\%$ reflection, the measured transmission of both lenses after coating is $\sim$91%. Part of the loss may be due to reflection at the first surface, but depending on the thickness of the layer, the transmissivity of a layer of ITO at 500 nm is about 80-90%. This transmissivity depends on thickness, but can actually increase or decrease with thicker layers due to interference effects [112], so it is difficult to predict exactly what we expect for our lenses.

5.2.1.2 Imaging for Yb State Detection

While the design of this chamber is primarily focused on the imaging for Ba, we do still need to be able to perform state readout on our memory qubit. However, limitations due to beam delivery and the Ba imaging constrain us to detect light from Yb from farther away than the working distance of any of our previously existing lenses. We are also fairly limited in the NA that we can use for this lens due to this relatively large distance, the trap geometry (Section 4.2), and the design of the vacuum chamber (Section 5.2). The high-NA aspheres have poor transmission at 370 nm and will introduce large chromatic aberrations. For Yb detection, therefore,

[6]The unit Ohm/square indicates that that is the sheet resistivity for a square of any size.

we observe from one of the sides of the trap with the more closely spaced rods as shown in Fig. 4.3(b) because the sides with the larger rod distance are used only for Ba imaging. The rod spacing limits the NA to roughly 0.3.

Parameter	**Value**
Thickness	5.8 mm
R	13.163 mm
κ	-0.693
A_4	-3.519×10^{-6}
A_6	-4.473×10^{-9}
A_8	-3.282×10^{-12}
A_{10}	5.578×10^{-15}

Table 5.6: Parameters for the asphere used for Yb fluorescence detection.

The distance from the lens to the ion is 27.701 mm including a 3.175 mm thick fused silica window. For the back focal length, we wish to have a fairly long path for convenience with optics mounting, so we semi-arbitrarily set the back focal distance to 300 mm. While we attempted to design an objective using multiple standard spherical lenses with these constraints, we were unable to achieve satisfactory performance. Instead, we turned to another custom aspheric lens.[7] The lens is made of fused silica, and the parameters for this lens are listed in Table 5.6. The performance of this lens as designed is diffraction limited.

[7] Thorlabs

5.2.2 Vacuum Chamber Design

The design decisions for this chamber were made according to the following priorities, although not necessarily in this order:

1. Accommodate and stably mount the asphere-piezo systems.
2. Make the system modular and replicable.
3. Allow imaging of Yb with an NA of 0.3.
4. Deliver all necessary laser beams with sufficient intensity.
5. Achieve a vacuum pressure of $< 10^{-10}$ Torr.

The first priority mainly determined the size and orientation of the chamber. In order to mount both piezos on the bottom of the chamber for maximum stability, we needed a large flat surface as the bottom of the chamber. Furthermore, due to the height of the mounts, a standard 4.5" spherical octagon would have been much too short. Therefore, we used an 8" spherical octagon[8] and oriented it so the large openings were facing vertically. We were also able to increase the modularity of the system by mounting the trap and making all electrical connections to a single feedthrough (see Fig. 5.8). The flange is an off-the shelf part[9] but with custom holes for mounting screws.

For Yb imaging, we use a custom reentrant window[10] that protrudes 84.4 mm into the vacuum chamber. The inner diameter of the reentrant tube is 31.24 mm.

[8] Kimball Physics MCF800-SphOct-G2C8
[9] Kurt J. Lesker EFT0265063
[10] MPF Products

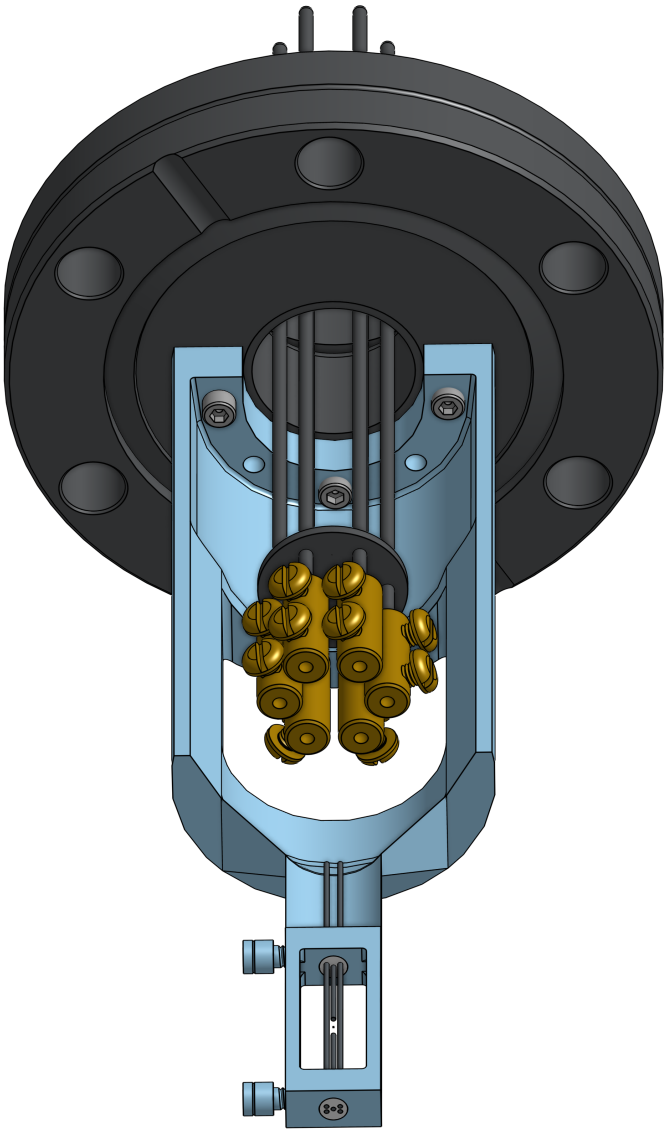

Figure 5.8: CAD model of the trap and its holder mounted to a single flange. The blue piece is the trap mount, which attaches to the flange. The actual trap is located near the bottom of the figure, with the rectangular pattern of the rods visible in the white circle at the edge of the holder. This gray circle is a Macor piece used to hold the rods and one needle in place. The other side of the trap has an identical piece that keeps the rods straight and holds the other needle. The side screws then hold that Macor pieces in the trap holder. Not shown are the connections from the rods to the feedthrough pins. In the actual setup, the barrel connectors shown in the figure in gold simply screw directly onto the trap rods and needles.

The tube also narrows to a diameter of 24.6 mm for the 7 mm outside of the window.

This is too small to fit standard 1" optics and optomechanics, so the asphere has

a diameter of 18 mm and we will use a custom lens tube. It is worth noting that at the time of writing, we have not yet set up this imaging system, so unforeseen issues may still arise and the design of the optics discussed above may need to be modified as a result.

Laser beams are delivered to the trap as shown in Fig. 5.9. The needed beams are discussed in Chapter 3. Beams that don't need to be well focused are delivered through the lower right window in the diagram because that window is farther from the ion than the others or through the reentrant window for Yb detection since the asphere used for fluorescence collection will not focus other wavelengths well. Raman beams have $\Delta\vec{k}$ along the trap axis as required for driving axial motional gates. The bottom left window is used for the beams that require pure σ polarizations so they can be aligned with the magnetic field. Unlike the other windows, the bottom window in the figure does not have an antireflection coating so future experiments can use a 1762 nm laser (see Sec. 8.1) for shelving Ba if necessary. The remaining sides on the octagon are for the electrical feedthrough for the trap (right) and vacuum equipment (left).

Finally, we needed to consider how to achieve the best vacuum pressure possible. More details on what goes into such a design are discussed in Appendix A. For now, there are several important points. First, the rate of gas flow in a vacuum system and thus the pumping speed of that system is determined in part by the property of conductance. For a circular tube (all of the elements of our chamber except the spherical octagon), the conductance is proportional to the diameter of the tube cubed [113]. Therefore, somewhat counterintuitively, tubes with larger di-

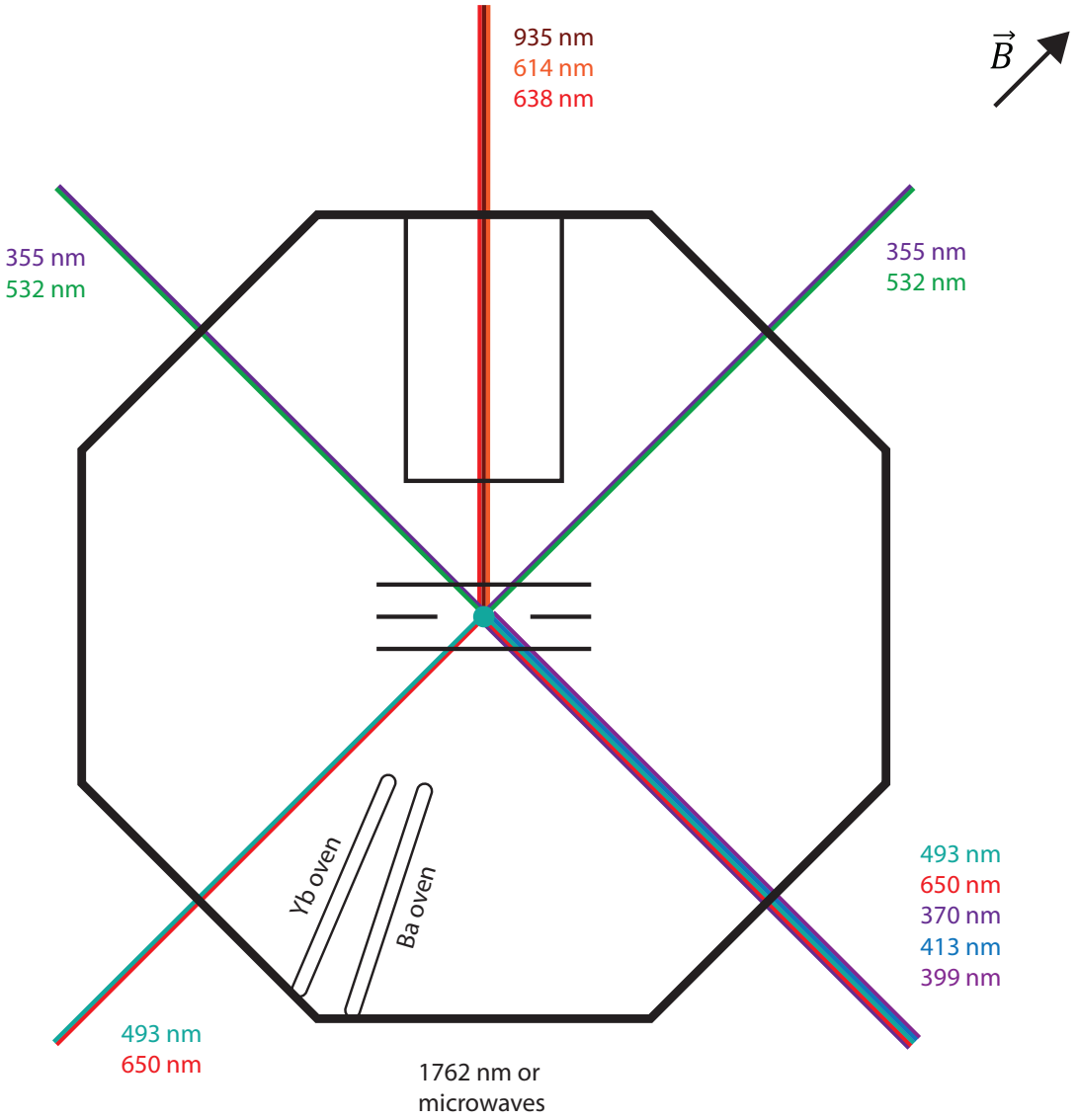

Figure 5.9: Diagram of laser beams for the third trap. The magnetic field points up and to the right, so beams propagating parallel or anti-parallel to that direction have only σ polarizations. The trap axis is horizontal, and the reentrant window for Yb imaging is at the top. Raman beams (355 nm and 532 nm) are delivered through the upper left and upper right windows. The left and right sides do not have optical access. The lower left shows the location of the atomic ovens.

ameters will lead to lower vacuum pressures. Additionally, our vacuum is primarily limited by hydrogen from the steel chamber surfaces, so our primary concern for selecting vacuum pumps is their pumping speed for hydrogen. For the first con-

sideration, since our chamber is large, we use only vacuum nipples in our chamber that are at least CF2.75 size, and much of the chamber is made from CF4.5 parts. Second, we use both a StarCell ion pump[11] with 20 L/s pumping speed for N_2 and a titanium sublimation pump[12] (TSP) to achieve very high pumping speeds. The StarCell pump is preferable to a more traditional diode ion pump since it can pump higher volumes of hydrogen (as well as noble gases). The TSP adds even more pumping capability. With just the ion pump, we achieved a pressure of $\sim 2 \times 10^{-10}$ Torr on the ion gauge, and after firing the TSP for ∼10 minutes and waiting for several days, we achieved a final pressure of 2×10^{-11} Torr.

5.3 Testing of the Trap with In-Vacuum High Numerical Aperture Imaging

5.3.1 Optics Testing

5.3.1.1 Out-of-Vacuum Testing of Lenses

Once the lenses are placed in the vacuum chamber, it becomes much more difficult and time-consuming to replace them if there is a problem. To minimize the chances that we would discover poor performance once the system was already built, it was important that we test the lenses ahead of time.

This test is challenging because of the high NA (0.8) of the aspheres and because our test source needed to fill the whole aperture to give reliable results.

[11] Agilent 9191145
[12] Agilent 9160050

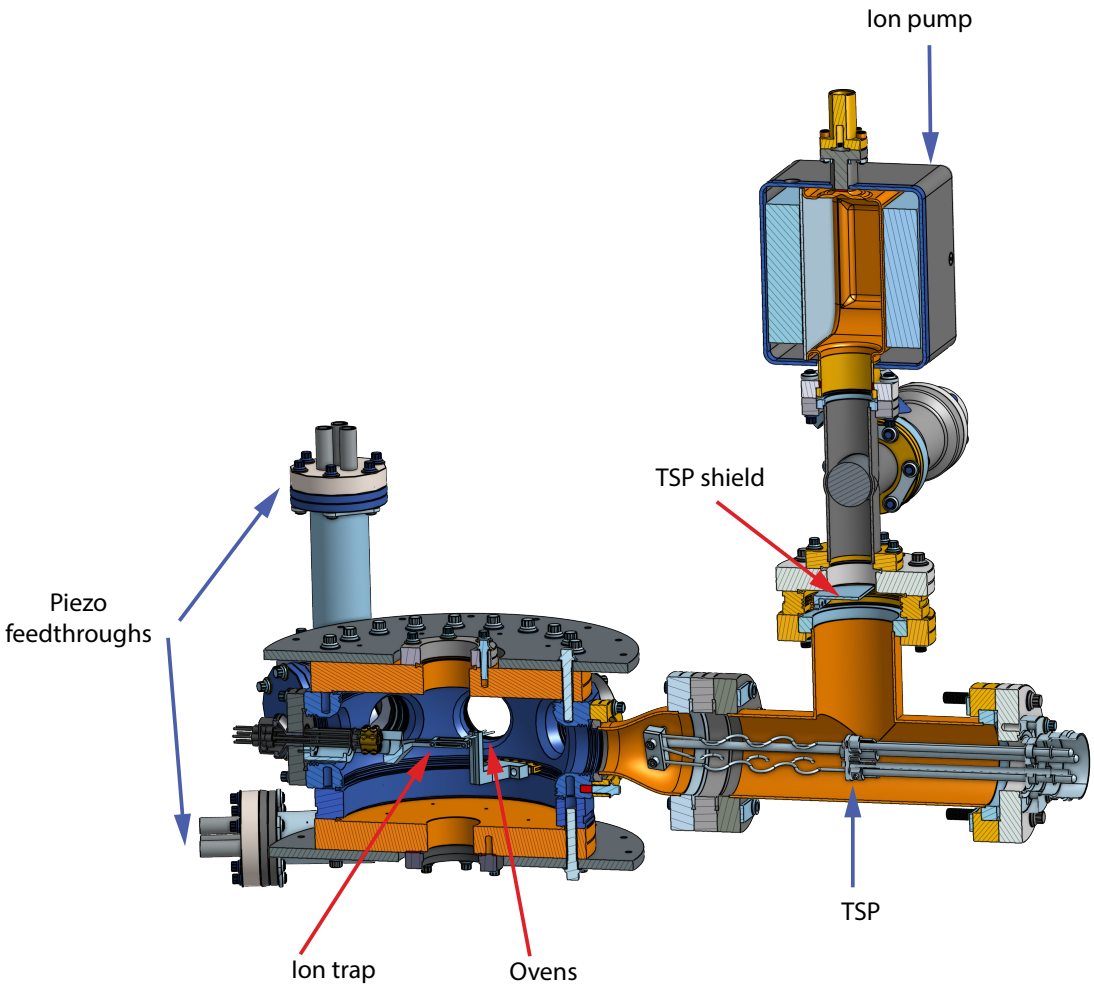

Figure 5.10: Partial CAD model of the chamber for the third ion trap in our experiment. The aspheres and piezos are not shown for simplicity. The piezo feedthroughs connect the piezo stages to their controllers. Also highlighted are the trap and the ovens, as well as the vacuum pumps. The TSP shield prevents a direct line-of-sight from the TSP to the ion pump as a precautionary measure against shorts in the ion pump from titanium deposited from the TSP. There is another shield (not shown here) between the TSP and the main body of the chamber as well to avoid depositing titanium on the piezos and aspheres.

Often, the sources for such testing will be small pinholes. When light is sent through such an opening, it diffracts and diverges with an angle inversely proportional to the diameter of the aperture. For example, for a 1 μm aperture, the angle of divergence corresponds to an NA of $\sim$0.6. It is not feasible to obtain a pinhole with a diameter smaller than 1 μm, so we must come up with an alternative.

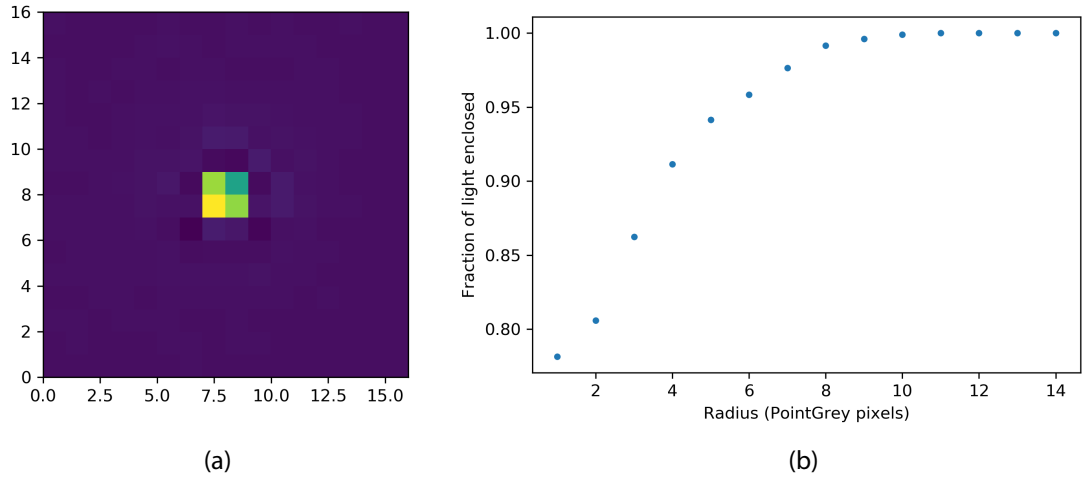

Figure 5.11: Image analysis of high-NA aspheres using an artificial point source. (a) Camera image of the light after propagating through both the high-NA in-vacuum asphere and the lower-NA fiber coupling lens. Both the horizontal and vertical axes are pixel numbers. (b) Measurement of the spot size of the image. Fraction of the enclosed light is plotted versus pixel distance from the ion (pixel size is 2.2×2.2 μm^2). The fraction of the total light in the image enclosed in a circle around the image centroid is plotted versus the radius of that circle in pixels. Sec. 7.2 contains more details about this technique.

Instead, we use an aluminum-coated tapered optical fiber tip as in [114]. These fiber tips are commercially available, and we use tips with both 100 and 200 nm diameters. Since these are smaller than the wavelength of light, they will emit like a point source. We then carefully align the high NA asphere to the fiber tip and use techniques discussed in Sec. 7.2 to assess the performance of the lens.

We are able to align the apparatus well enough that the aberrations are minimal, and we can just look at the spot size of the image. These results are shown in Fig. 5.11 with both the image and analysis plot. The results are much better than those obtained with the Photon Gear objective when looking at an actual ion. We thus had reasonable confidence that the asphere was performing approximately as expected before we placed it in the vacuum chamber.

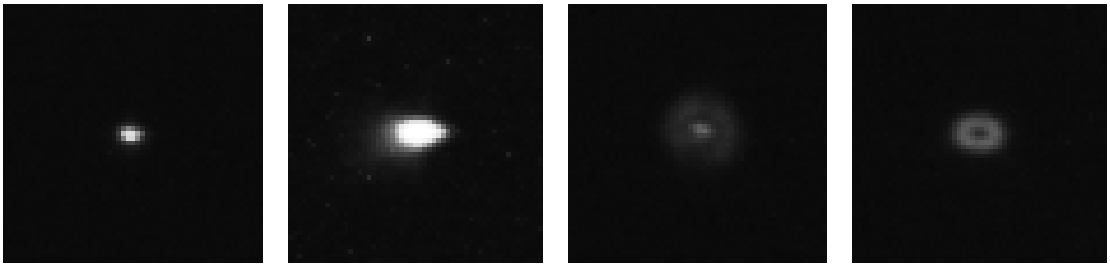

Figure 5.12: Ion images with high-NA aspheres. (a) Approximately optimized image of ion, with a small amount of residual astigmatism. (b) Image with asphere translated by 8 μm to induce coma. (c) Ion image when the asphere is 2 μm too close to the ion. (d) Ion image when the asphere is 2 μm too far from the ion.

5.3.1.2 Testing Lenses with a Trapped Ion

The ultimate test for the lenses is of course their performance when integrated into the system. The performance in the system may not be exactly the same due to the presence of the vacuum window, for example. In these tests, we look at both how sensitive the lenses are to misalignment and how well they perform when the alignment is optimized.

Images of a trapped Ba ion with the asphere at different positions are shown in Fig. 5.12. The first image shows a nearly optimized image. Note that in comparison to the image in Fig. 5.11(a), this image is saturated making the spot size look artificially large. Translating the lens by just a few μm so the ion is not centered on the lens introduces significant coma, as shown in Fig. 5.12. Even with a displacement of 1 μm there is a noticeable difference in coma, so we require submicron adjustability. We can easily accomplish this with the in-vacuum piezo stages (Sec. 5.2.1). The focusing of the asphere is also extremely sensitive as can be seen in Fig. 5.12(c) and (d). A two micron change in the distance from the ion to the lens is enough to in-

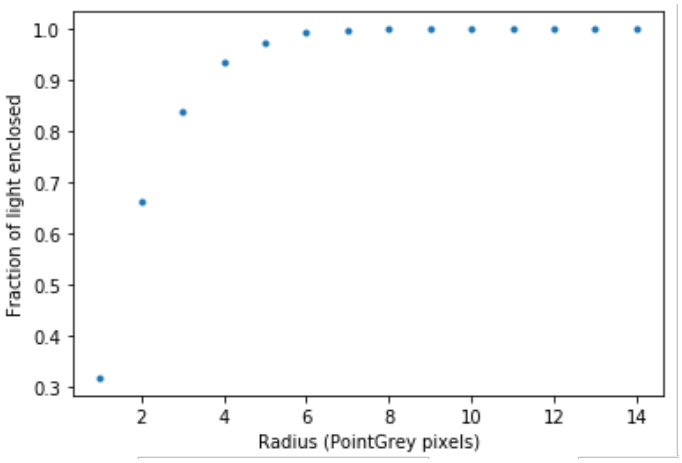

Figure 5.13: Spot size analysis of the image of an ion through a high-NA asphere.

duce large amounts of defocus although that can be compensated to some extent by changing the distance from the out-of-vacuum asphere to the camera. In the third image, it is also apparent that there is some clipping on the trap rods as evidenced by the dark spots in the upper right and bottom left of the outer ring. We noticed some asymmetry in these dark spots which could not be corrected without moving the middle spot away from the center of the outer ring. We believe this is likely due to the asphere being mounted at a slight tilt relative to the trap, which causes one of the rods to clip more than the other.

Once the aberrations are minimized, we analyze the spot size and observe the light transmitted through progressively smaller pinholes as steps toward fiber coupling the ion light. The results of the spot size analysis using the same method discussed in Sec. 7.2 are shown in Fig. 5.13. Note that the results here are significantly worse than those from before we put the asphere in the vacuum chamber (see Fig. 5.11). We think this discrepancy is likely due to curvature in the vacuum window which effectively introduces defocus to the image that cannot be compensated.

This result is still comparable with the results in Alice and Bob, however.

Pinhole Diameter (μm)	**Light lost compared with 100 μm pinhole**		
	Cleo	**Alice**	**Bob**
50 μm	3%	4%	7%
25 μm	11.7%	11.7%	11.2%

Table 5.7: Comparison of loss of ion light through various pinholes on each trap. The results in Cleo are comparable to those in Alice and Bob. The numbers in Cleo are preliminary and it is possible they could be further optimized.

The fraction of light that is transmitted through the pinholes of various sizes is listed in Table 5.7. The numbers listed here are the percentage of photons lost when the light is sent through the pinholes listed on the left compared with the photons through a pinhole with a diameter of 100 μm. This result confirms that the focusing performance of the aspheres in Cleo, even with the observed degradation from the measurement before placing the lenses in the vacuum chamber, is similar to that of the objectives for Alice and Bob. The ultimate test, of course, will be the fiber coupling efficiency but at the time of writing we have not yet performed that measurement.

5.3.1.3 Vacuum Window Birefringence Testing

One possible cause for infidelity in our remote entanglement is inhomogeneous birefringence in the window of the vacuum chamber. In previous works, we have attributed an error of order 1% to this issue [33, 52]. This birefringence is due to stress on the glass [115], largely from the glass to metal seal [116]. There may also be some stress on the glass due to the pressure differential and the bolts holding the

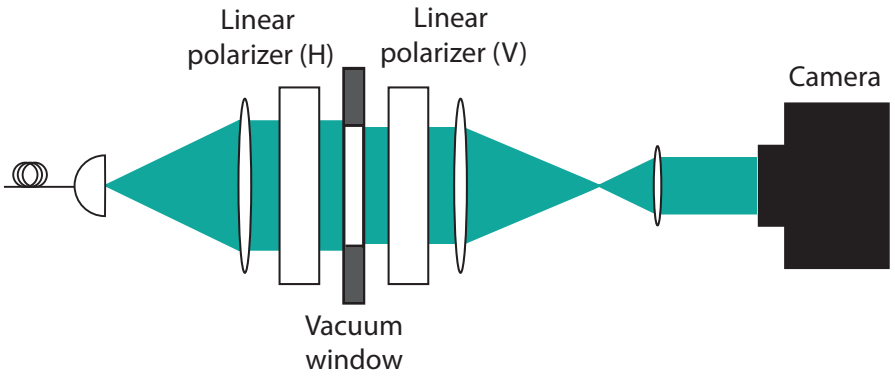

Figure 5.14: Setup for testing vacuum window birefringence. Light from a fiber passes through a polarizer, then is magnified to fill the vacuum window. It is then demagnified to fit through a crossed polarizer and onto a camera.

window in place once it is mounted. However, since measuring the birefringence of a single window becomes much more difficult once it is mounted to the chamber, and because the uncertainty about the performance of the windows in our first two chambers limits our ability to determine error sources accurately, we decided to measure the windows used for light collection for the third trap before mounting them on the chamber.

The most basic version of our setup consists of light propagating through crossed polarizers with the window in between. Additional lenses are added to change the beam size to fill the window, and the result is imaged with a camera. Before inserting the window, we take a baseline image and then take images with the window rotated at various angles about its center. Based on the differences between these images and the original, we can obtain a measurement of the birefringence.

The birefriengence of the window can be written as the Jones matrix [117]

$$e^{-\frac{i\eta}{2}}\begin{pmatrix}\cos^2\theta + e^{i\eta}\sin^2\theta & (1-e^{i\eta})\,e^{-i\phi}\cos\theta\sin\theta \\ (1-e^{i\eta})\,e^{i\phi}\cos\theta\sin\theta & \sin^2\theta + e^{i\eta}cos^2\theta\end{pmatrix} \tag{5.2}$$

where η is the phase retardation, θ is the fast axis, and ϕ is the circularity of the material. The values can be the same for the whole window, in which case it will not affect the fidelity of our ion-photon entangled state, or they can vary across the window. If, for example, the input light is horizontally polarized, the electric field after the window will be

$$E = E_0\begin{pmatrix}e^{-\frac{I\eta}{2}}\left(\cos^2\theta + e^{i\eta}\sin^2\theta\right) \\ e^{-\frac{i\eta}{2}+i\phi}\,(1-e^{i\eta})\cos\theta\sin\theta\end{pmatrix}. \tag{5.3}$$

Passing this field through a vertical polarizer and taking a camera image gives the spatial distribution of the intensity

$$I = I_0\sin^2\left(\frac{\eta}{2}\right)\sin^2(2\theta) \tag{5.4}$$

where η and θ can depend on the spatial coordinates.

The results of this measurement are shown in Fig. 5.15. Again, note that overall birefringence is not a problem, but spatial variation is. Near the centers of the windows the retardance is more uniform while the largest variations are near the edges of the window. We find overall that window 1 has a standard deviation in retardance of 0.60 degrees and window 2 has a standard deviation of 0.52 degrees.

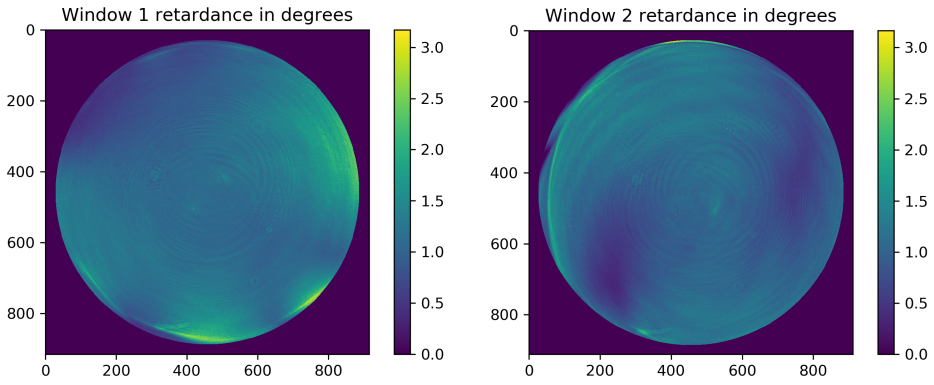

Figure 5.15: Measurement of the retardance on the two windows for single photon collection in Cleo. The vertical and horizontal axes are pixels.

This number, however, is including the edges of the windows so is an upper limit on the actual birefringence variation seen by the photons, which mostly pass through the window near the center.

5.3.2 Testing of Trap Properties

The presence of insulating surfaces near the ions can lead to heating and excess micromotion due to charging of the surface varying in time [118]. We attempted to mitigate any such effects by coating the surface of the aspheres with ITO, but if the coating was not performed correctly or the connection to ground is poor, there could still be residual issues.

When we measured the micromotion of the ion using the correlation technique presented in Sec. 4.3.2 with one of the aspheres 6 mm from the ion, we found that there was minimal micromotion to start and what was there was easily compensated. Preliminary data seems to indicate, however, that there is some charging that varies in time after the RF is temporarily turned off and then turned back on. We observe

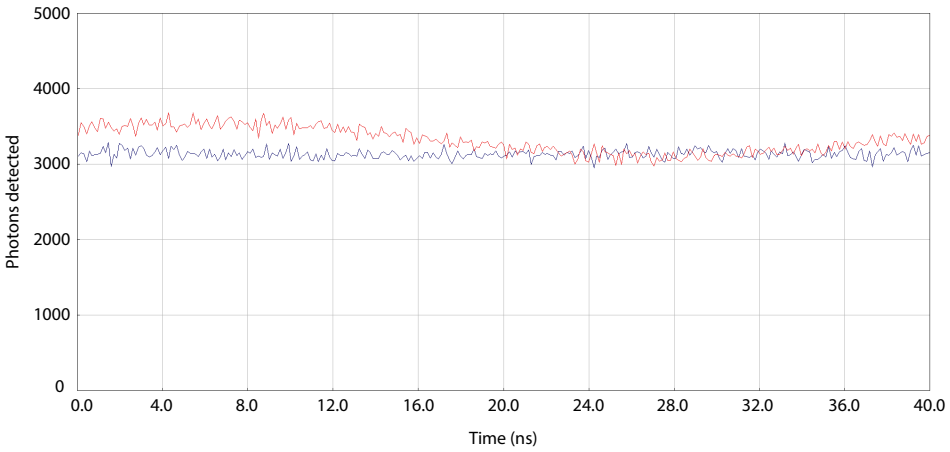

Figure 5.16: Dependence of micromotion in Cleo on bottom asphere position. Micromotion is measured using the technique of correlating photon arrivals with the trap RF cycle (see Sec. 4.3.2 and Fig. 4.6) for two asphere positions. The black curve shows the micromotion when the bottom asphere is at approximately the correct focus. The red curve was taken with the asphere moved away from the ion by 1 mm.

a shift in the position of the ion relative to the asphere, which induces significant coma and will likely hurt our fiber coupling if the charging is not compensated with the trap electrodes. It may therefore be necessary to implement some form of feedback with the trap voltages to maintain our optimal fiber coupling.

Since there are two aspheres, a further test of the charging that we can perform is to adjust the distance between the ion and the asphere we are not using to image the ion (the bottom asphere) and observe if the micromotion changes with distance. If the micromotion remains unchanged, this test provides convincing evidence that the asphere surface is not affecting the behavior of the ion. However, when we performed this test, we observed a significant increase in the micromotion when the bottom asphere was moved away from the ion by 1 mm (see Fig. 5.16). This result does not confirm that there is time-dependent charging on the asphere but does indicate that the aspheres contribute to the electric field at the ion.

We can further explore the time dependence of this charging by turning the RF voltage on and off and observing the subsequent time-dependence of the micromotion for different asphere locations. Eventually, it will also be important to measure the heating rate of the trap and ensure that it is as low as desired ($\lesssim$100 quanta/s), since this can also be affected by the charging. This test requires Raman operations, however, which we have not yet implemented on Cleo.

Chapter 6: Remote Entanglement of $^{138}Ba^{+}$ Ions

A primary building block of a quantum network in the architecture we are using is the photonic link between two ion traps. This link serves to generate the entanglement between multiple nodes, which is necessary for utilizing all of the ions in a quantum computation. As discussed previously, we use $^{138}Ba^{+}$ as our communication qubit because of the visible wavelength of its primary transition and its (relatively) similar mass to $^{171}Yb^{+}$.

Entanglement using photons can take advantage of their many different quantum properties, such as number of photons [51], polarization of the photons [119], frequency [120, 121], time-bin of a photon arrival [122, 123], and others [124, 125]. Unlike the previous results in [120] in Yb^{+}, however, Ba^{+} does not lend itself naturally to a frequency qubit. In addition, the use of polarization allows for more straightforward manipulation and control, as will be discussed in Secs. 6.2 and 6.3.2. The disadvantage of polarization as a qubit relates to how easily it can be controlled– while this can be advantageous for rotations of the qubit, for example, it also means error can easily be introduced. Additional steps to stabilize the polarization may be required [126, 127] for longer distance transmission as would be desired in a quantum repeater [128] or a quantum network with nodes that are further separated

than in our system. For the short distances in our lab, however, any errors due to polarization are fairly stable and can be characterized. Much of this chapter is devoted to discussing these sources of error.

Using photons as an intermediary also requires that the degree of freedom we choose as our photon qubit must be entangled with the qubit states of the ion. As mentioned above, the polarization degree of freedom is a natural choice for Ba given its atomic structure. The details of generating this entanglement will be discussed in the first two sections of this chapter. From there, we will proceed with presenting how we establish the photonic connection and verify entanglement, as well as discussing some experimental details.

6.1 Generating Single Photons from $^{138}Ba^{+}$

Preparation in a pure state in the $6P_{1/2}$ manifold is the primary requirement for generating a single photon entangled with the ion. For example, the excitation of the ion only to the $\left|6P_{1/2}, m_J = +1/2\right\rangle$ state will result in a photon with a polarization entangled with the state of the ion. One scheme that has previously been used is weak excitation with a 493 nm laser [49]. This scheme, however, has an inherent trade-off between rate and fidelity–the larger the probability of excitation, and thus successful entanglement generation, the lower the fidelity. Another option is excitation on the $S \leftrightarrow P$ transition with a pulsed laser with pulse length of order 10-100 ps. Previous attempts at this scheme have been unsuccessful because of the difficulty of obtaining high power pulses at 493 nm [48]. In the future, however, this

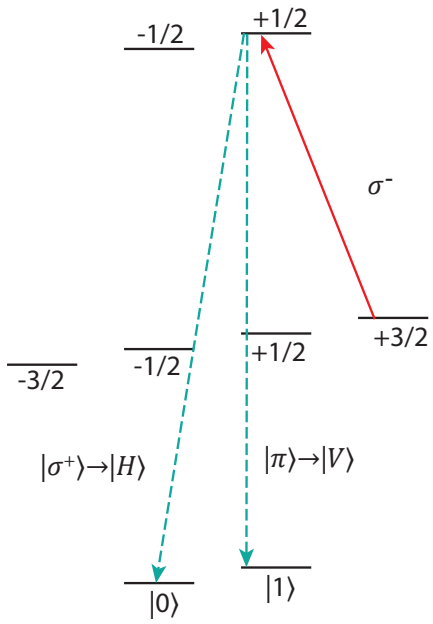

Figure 6.1: Single photon generation scheme for $^{138}Ba^{+}$. 650 nm σ^{-} polarized light excites population in the $D_{3/2}, m_J = +3/2$ state to the $6P_{1/2}, m_J = +1/2$ state. The decay to the S manifold results in a photon which has a polarization entangled with the state of the ion.

may be a promising direction.

For this work, we instead excite using 650 nm light to drive the $D_{3/2} \rightarrow P_{1/2}$ transition, as discussed in [52]. Exciting on this line is advantageous because of the easy filtering of scattered excitation light, reduced rate of double excitations, and increased availability of optical technology at this wavelength. Similar schemes had previously been used in [129, 130]; however, these either left the light on continuously or did not prepare a pure state in the D manifold, and thus did not obtain an entangled state between the ion and photon. In our scheme, we optically pump to the $\left|D_{3/2}, m_J = +3/2\right\rangle$ state using the method described in Sec. 3.2.4. Once the state is successfully prepared, we excite with a 10 ns pulse of σ^{-} polarized 650 nm light (Fig. 6.1). Because of the relatively long pulse length, we do not need a pulsed

laser for this excitation and can switch the light instead using a standard acousto-optic modulator (AOM),[1] which has a rise time of 5.1 ns. If we wish to drive a shorter pulse, we also have a 1 ns in-fiber electro-optic modulator (EOM)-based optical switch[2] that we could insert in place of the fast AOM.

We need to be able to operate this AOM in both a "pulse mode" for generating the excitation pulses and a "CW mode" for the other parts of the experiment (see Sec. 6.4.1 and Table 6.4.1.2). A schematic of the necessary electronics for both modes is shown in Fig. 6.2. We cannot generate sufficiently short RF pulses directly with our RF source, so we instead use an external pulse generator[3] that is triggered by TTL A. The pulse generator puts out a 10 ns pulse upon arrival of a signal of arbitrary length from TTL A. TTL B is used for the CW mode, and the two are combined on an RF combiner, so there will be a signal if either is on. The combined signal is then fed into an RF switch, which outputs a signal to the AOM via an amplifier if the TTL is on. Thus, we are able to either generate a fast pulse or turn on a longer signal on demand.

When the ion decays from the $\left|P_{1/2}, m_J = +1/2\right\rangle$ state, if it decays to $|0\rangle$, the polarization of the photon will be σ^+, whereas if it decays to $|1\rangle$, the polarization of the photon will be π. Although the decay from the ion results in the state

$$|\psi\rangle = \sqrt{\frac{2}{3}}\,|0\rangle\left|\sigma^+\right\rangle + \sqrt{\frac{1}{3}}\,|1\rangle\,|\pi\rangle\,, \tag{6.1}$$

[1] Brimrose GPM-400-100-650
[2] Jenoptik AM660, with two modulators used in an interferometric setup
[3] SRS DG535

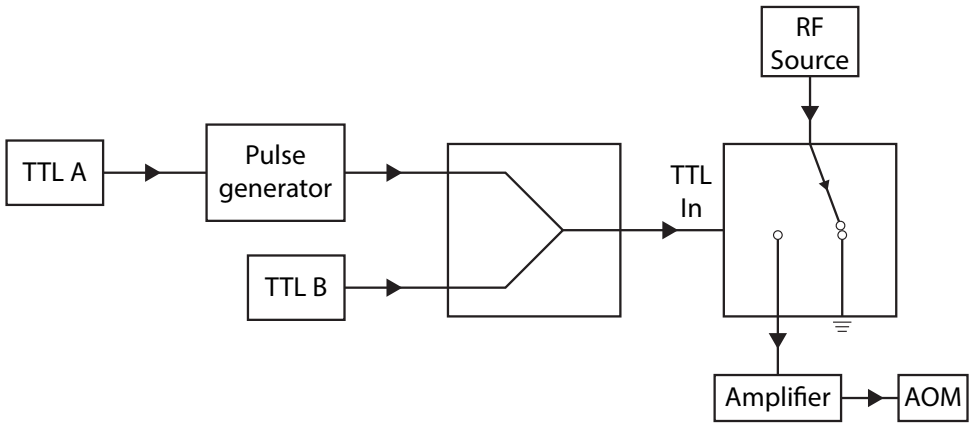

Figure 6.2: Setup for the electronics for generating 10 ns 650 nm pulses. TTL A triggers a pulse, while TTL B is left on continuously for the CW mode. If the TTL input to the RF switch is on, the RF switch outputs the RF signal for the AOM.

when collected, the angular dependence of the polarizations ensures that there are an approximately equal number of σ and π photons collected. We then obtain the state

$$|\psi\rangle = \frac{1}{\sqrt{2}}\left(|0\rangle\left|\sigma^{+}\right\rangle + |1\rangle|\pi\rangle\right). \tag{6.2}$$

When we collect light perpendicular to the magnetic field with an infinitely small angle of light collection, σ^{+} and π polarizations project onto H and V polarizations respectively. This projection then leads us to the final ion-photon state

$$|\psi\rangle = \frac{1}{\sqrt{2}}\left(|0\rangle|H\rangle + |1\rangle|V\rangle\right). \tag{6.3}$$

For a finite angle, the resulting state will vary slightly from the ideal. This effect is thoroughly examined in [75], and we discuss how this discrepancy will effect the fidelity of our ion-photon entangled state in Sec. 6.2.1.

6.1.1 Double Excitations

This pulse length can be much longer than what would be required for a 493 nm pulse because of several factors that conspire in our favor. The first is simply that if a 493 nm photon has already been emitted, a second 650 nm excitation can never happen. The first factor is aided by the branching ratio and the fact that the majority of the time the ion will indeed decay on the $S \leftrightarrow P$ line and emit a 493 nm photon. Additionally, the Clebsch-Gordan coefficients of the various $D \leftrightarrow P$ transitions and the suppression of excitations that are not driven with σ^- polarized light assist in reducing the error rate further. In particular, assuming the polarization of our light is pure, we have only one possible excitation that can hurt our fidelity–if the ion decays to the $\left|D_{3/2}, m_J = +1/2\right\rangle$ state and then is reexcited to the $\left|P_{1/2}, m_J = -1/2\right\rangle$ state and then decays to the S manifold. If this sequence of events happens, the resulting state, in contrast to Eq. 6.3, will be

$$\begin{aligned} |\psi'\rangle &= \frac{1}{\sqrt{2}}\left(|0\rangle|\pi\rangle + |1\rangle\left|\sigma^-\right\rangle\right) \\ &\Rightarrow \frac{1}{\sqrt{2}}\left(|0\rangle|V\rangle + |1\rangle|H\rangle\right). \end{aligned} \tag{6.4}$$

We can quantify the impact of all of these factors using the optical Bloch equations discussed in Sec. 2.4.2. For this configuration, the Rabi frequencies of all 493 nm transitions and the 650 nm π and σ^+ transitions are set to 0, and we use a time dependent calculation to account for the finite duration of the pulse. This time dependence can also accommodate different pulse shapes (square, Gaussian,

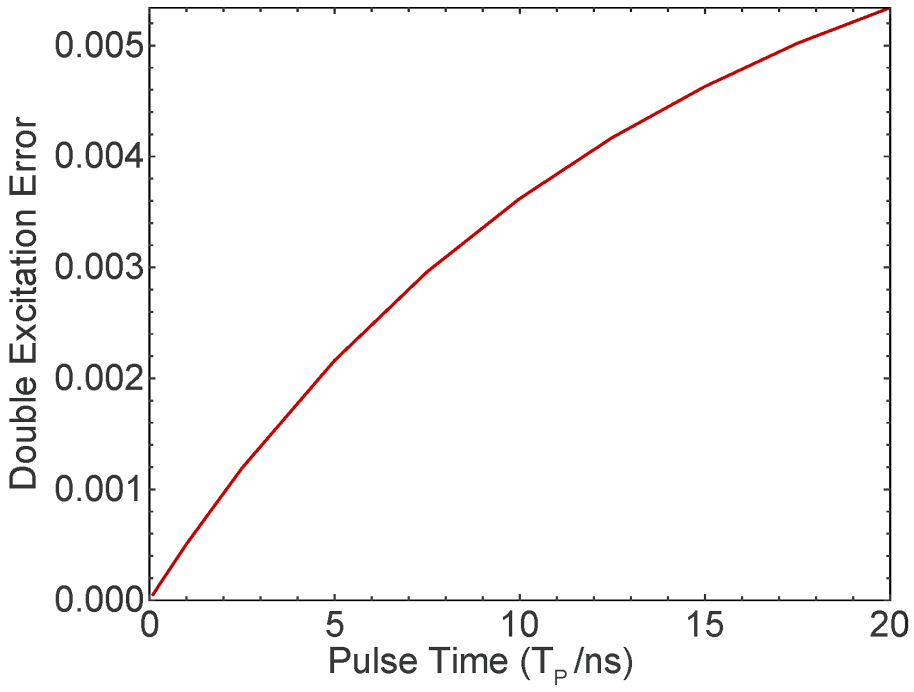

Figure 6.3: Plot of error from double excitations versus pulse length.

hyperbolic secant, for example), but the differences in the results are small, so for simplicity, I present only the results for the square pulse.

To track decays from the $|P_{1/2}, m_J = -1/2\rangle$ state, we add a ninth artificial level to our simulation and modify the effective Hamiltonian so decays from the incorrect P level only go to this state or the D manifold and not to the actual S states. We assume that we always drive a full π pulse, so as much population is transferred as possible. Then by scanning the pulse time and counting the number of decays to the artificial state as opposed to the correct decays, we can determine the fidelity loss due to double excitations. The results are plotted in Fig. 6.3. For a 10 ns pulse, the error is about 0.36%, while for a 1 ns pulse, the error is $< 0.1\%$. For other pulse shapes, the error is slightly lower [55], so this is an upper limit.

We can also verify the purity of the single photon (although not check for

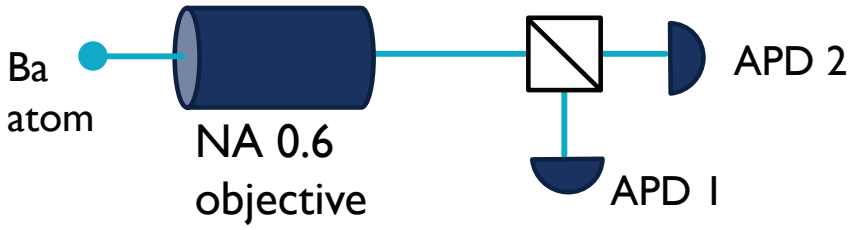

Figure 6.4: Hanbury Brown Twiss setup for measuring $g^{(2)}(\tau)$ for photons from the ion.

multiple excitations from the D manifold) by measuring the autocorrelation function $g^{(2)}(\tau)$. The expression for $g^{(2)}(\tau)$ can be written as [55]

$$g^{(2)}(\tau) = \frac{\langle n(t)n(t+\tau)\rangle}{\langle n(t)\rangle^2} \tag{6.5}$$

where $n(t)$ is the number of photons detected at time t. If a photon is detected at $t = 0$ and the source is a true single photon source, $n(t+\tau)$ for $\tau = 0$ should be 0. Thus, by measuring the $g^{(2)}$ value, we can measure how pure the single photon is.

We use a Hanbury Brown Twiss type setup [131] as shown in Fig. 6.4. When a photon is detected on APD 1, that event serves as a trigger, and the delay until a photon arrival event on APD 2 is measured. Details of both the experiments and results have been discussed in [52, 55], so here we will simply summarize the results. We obtain a $g^{(2)}(0)$ value of $(8.1 \pm 2.3) \times 10^{-5}$ [52], which is consistent with the previously reported lowest value from any system [132] and improves upon the previously best trapped ion result by over an order of magnitude [129]. The data for this experiment are shown in Fig. 6.5. In Fig. 6.5(a) the normalized autocorrelation function is plotted as a function of delay from the arrival time of a photon on APD

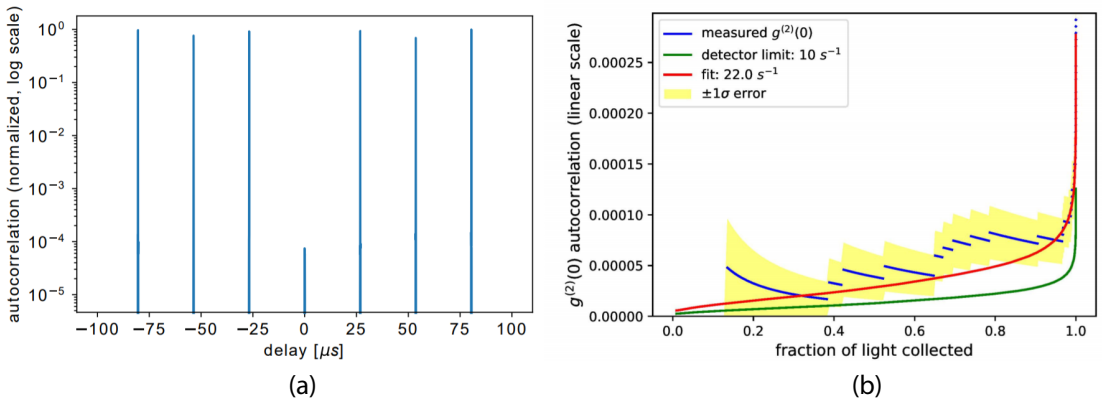

Figure 6.5: Results from the measurement of the $g^{(2)}$ autocorrelation function of our single photon source. (a) Photon arrival incidents on APD 2 vs. time since a photon arrival incident on APD 1. While the peaks look infinitely narrow, they do in fact have finite widths. The presence of peaks as opposed to a continuous signal is due to the pulsed excitation, and the spacing is equal to the repetition rate of our experiment. The peak at $\tau = 0$ is strongly suppressed compared to the other peaks, resulting in the low value of our $g^{(2)}(0)$. (b) Plot of $g^{(2)}$ value vs. integration window in terms of the fraction of light included in the analysis. The blue points are the measured value. The jumps in the blue curve arise because of the inclusion of another photon in the $t = 0$ peak within the integration window. For instance, before the blue curve starts, the integration window around $t = 0$ is small enough that no photons have been counted. As the integration window is expanded, we begin to see more photons in the $t = 0$ peak. The green curve shows what our $g^{(2)}$ would be if we were entirely limited by dark counts on our APDs, and the red curve is a fit to our data assuming a constant background rate. The yellow represents a 1σ error bar on the blue points.

1. The peak centered at $\tau = 0$ is strongly suppressed compared with the others. Each of those peaks has a finite width, so the choice of integration window effects the number we obtain as our result. In Fig. 6.5(b), we plot this dependence. As we increase the limits of integration, we include a larger fraction of the photons detected, but the value of our $g^{(2)}$ also increases. For our final reported value, we choose to use an integration window of 30 ns. This window encapsulates more than 97% of the photons collected, and for longer integration times, we reach a point of diminishing returns. In this plot, we also explore why our $g^{(2)}$ is not exactly 0.

The APDs we use[4] have a very low but nonzero intrinsic dark count rate of 10 s^{-1}. For a 30 ns integration window, this alone would give a $g^{(2)}$ value of $\sim 3 \times 10^{-5}$. However, the value we obtain is not limited by this alone, as shown in the red curve. This curve is a fit to our data assuming a constant background count rate, and which yields a rate of 22 s^{-1}. As discussed in [55], we determined that this residual background is due to leakage through the 493 nm AOMs.

6.2 Ion-Photon Entanglement

A crucial first step in demonstrating remote ion-ion entanglement via photonic interconnects is verifying the entanglement of the ion's electronic state and the photon's polarization. This step is useful for finding any sources of fidelity loss on the individual traps and ensuring everything is working as expected before we perform the final experiment.

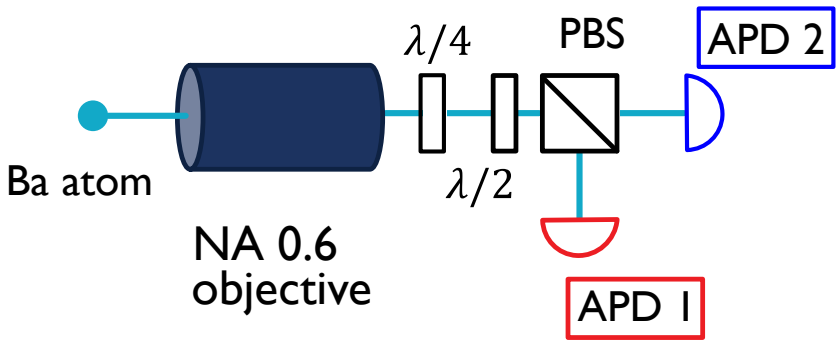

Figure 6.6: Experimental setup for ion-photon entanglement verification experiments. The APDS are colored in accordance with the data shown in Fig. 6.7.

Previously, our lab has demonstrated ion-photon entanglement with Ba ions in free space using our current photon generation scheme, as presented in [52]. The

[4]Laser Components CountBlue

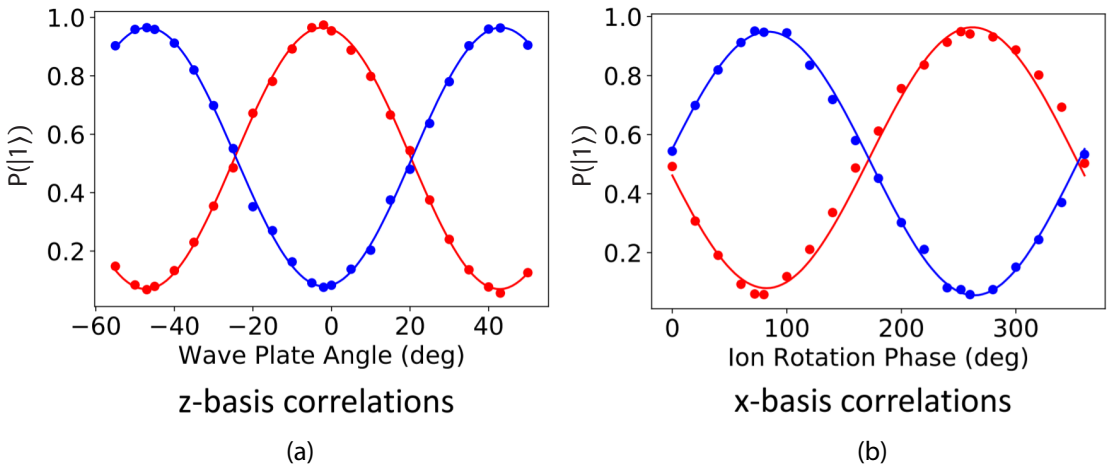

Figure 6.7: Ion-photon entanglement data when the light is not fiber coupled. In both plots, the red curve indicates the probability of the ion being in $|1\rangle$ when a photon is detected on APD 1, while the blue curve shows the probability of the ion being in $|1\rangle$ when a photon is detected on APD 2. (a) Ion-photon correlations in the z basis. The probability of being in $|1\rangle$ for a photon detected on each APD is plotted versus the angle of the half wave plate. (b) Ion-photon correlations in the x basis. The wave plate is set to perform a $\pi/2$ rotation on the photon polarization. The ion state is then coherently rotated to recover the contrast when the phase of the rotation is scanned.

setup for these experiments is shown in Fig. 6.6. It is similar to that used for the $g^{(2)}$ experiments except the 50:50 beam splitter is replaced with a polarizing beam splitter and a half wave plate is placed before that to control the polarizations.

To verify entanglement, we first will measure the correlation between photon polarization and the ion state in the z basis. An experimental cycle consists of the following steps:

1. Optically pump to $\left|D_{3/2}, m_J = +3/2\right\rangle$ (Sec. 3.2.4).

2. Excite with 10 ns 650 nm pulse (Sec. 6.1).

3. If a photon is detected on one of the APDs, measure the state of the ion (Sec. 3.2.3.2).

These steps are performed repeatedly while scanning the angle of the half wave plate to rotate the photon polarization. The results are plotted in Fig. 6.7(a). The red curve shows the probability that the ion is in $|1\rangle$ if a photon is detected on APD 1, while the blue curve shows the same, but if the photon is detected on APD 2. Ideally, when the wave plate is at an angle of zero, a detection on APD 1 should correspond perfectly to the ion being state $|1\rangle$.

To ensure that the ion and photon are indeed entangled and are not simply classically correlated, we must also make a similar measurement in an alternative basis [133]. For this measurement, we set the wave plate to perform a $\pi/2$ rotation on the photon polarization, and then perform the following steps:

1. Prepare the ion in $|D_{3,2}, m_J = +3/2\rangle$.
2. Perform the 650 nm excitation.
3. When a photon is detected, perform a Raman $\pi/2$ rotation on the qubit with variable phase (Sec. 3.2.5).
4. Detect the state of the ion.

More details on this process are available in [55, 119]. The results of these experiments are shown in Fig. 6.7(b). In this case, the plot still shows the probability of the ion being in a certain state given detection of a photon on a particular APD, but the horizontal axis now is the phase of the Raman rotation. As expected, for certain phases, we recover contrast, thus verifying that we do indeed see quantum entanglement [133].

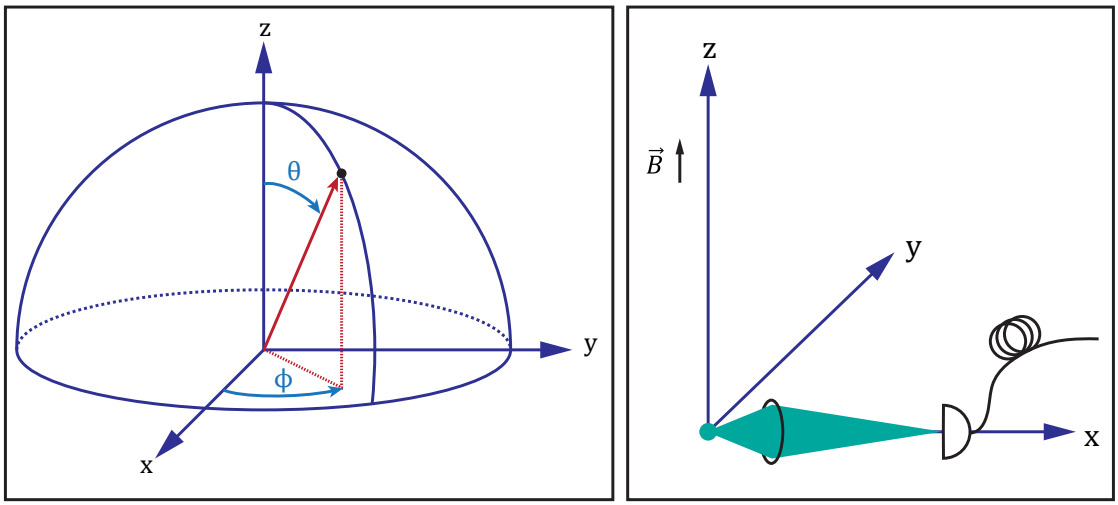

Figure 6.8: Coordinates for fiber coupling and polarization analysis. (a) Spherical coordinates used for the discussion of polarization mixing and lens alignment. (b) Diagram showing fiber and magnetic field relative to the coordinates used for the discussion of polarization mixing and lens alignment.

6.2.1 Ion-Photon Entanglement Fidelity and Sources of Error

The fidelity is obtained by fitting the points in all four curves to a squared sinusoidal function and averaging the amplitudes of all four fits. For the free space experimental data shown in Fig. 6.7, we obtain a fidelity of 0.884(4) [52]. In large part, this is limited by the imperfect projections of the atomic polarizations σ and π onto the lab polarizations H and V. In [52], we explored the spatial dependence of this infidelity. In free space, the fidelity can be improved by trading off collection efficiency for fidelity by reducing the collection angle in θ but not in ϕ where θ is the polar angular coordinate and ϕ is the azimuthal coordinate as shown in Fig. 6.8.

It turns out, however, that fiber coupling the light solves this problem altogether [134, 135]. Specifically, the $\hat{\theta}$ component of the σ polarized light does not couple at all into the fiber. Intuitively, this can be visualized by noting that the

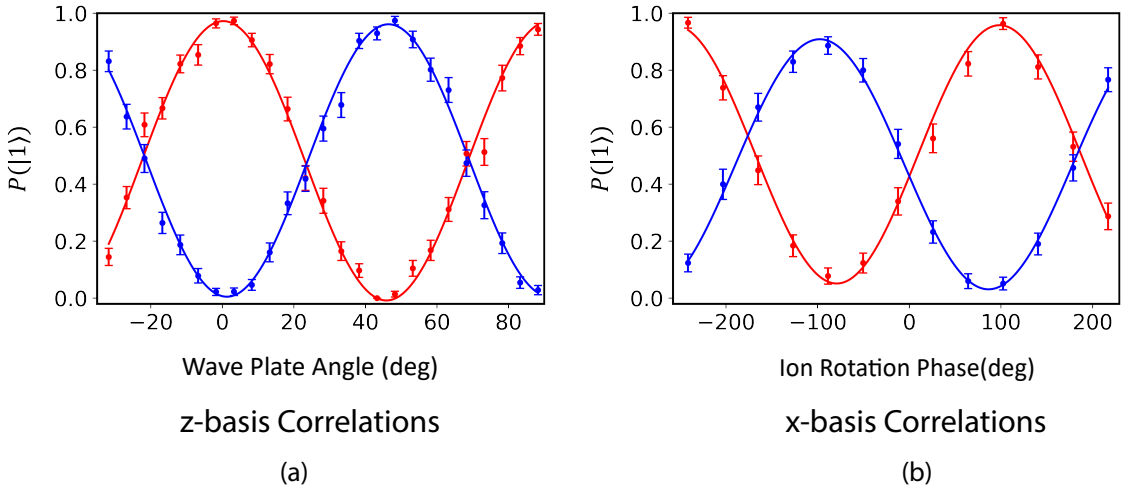

Figure 6.9: Ion-photon entanglement data when the light is fiber coupled. As in Fig. 6.7, the red curve shows the probability of the ion state being $|1\rangle$ when there is a photon detected on APD 1, while blue is the same but for APD 2. (a) Measurement in the z basis. (b) Measurement in the x basis.

$\cos\theta$ spatial dependence is odd about $\theta = \pi/2$, and therefore, when integrated over a symmetric interval, will yield zero. Thus, all of the σ polarized light that couples into the fiber will be H polarized as desired.

Indeed, in preliminary data taken with the light fiber coupled (Fig. 6.9), we see significant improvements in the fidelity. Using the same measure of fidelity as was previously used, we now obtain an average fidelity of 0.968 for z-basis correlations. For x-basis correlations, we measure a lower fidelity of 0.892. The primary reason for this decrease is timing jitter in the delay between the photon arrival and the beginning of the Raman rotations. The evidence that this effect contributes the vast majority of the decrease in fidelity consists of the facts that our Raman operations otherwise introduce no observable decrease in fidelity, and that narrowing the window during which we look for photon events from 50 ns to 2 ns increased the fidelity from 0.78 to 0.88. To eliminate this infidelity completely, we would either

need to time-tag the arrival of the photons and adjust the data in post-processing or trigger the Raman directly on the photon arrival [75]. We currently cannot do either of these because of software limitations, but this timing issue will not be relevant for ion-ion entanglement.

As discussed in Sec. 6.1.1, another 0.5% error is due to double excitations on the fast 650 nm pulse. However, there still remains some further infidelity. At least part of this is likely due to spatially inhomogeneous birefringence on the vacuum window; however, before attributing the error to that source we should consider other possibilities as well.

6.2.1.1 State Preparation and Measurement Errors

Some of the residual error ($\sim 2\%$) is due to state preparation and measurement (SPAM) errors. This error is a bit difficult to characterize because the preparation and measurement parts of the error cannot easily be separated. This is especially true since we prepare and perform state detection using different processes–state preparation is in the D manifold (Sec. 3.2.4) while detection is in the S manifold (Sec. 3.2.3). Additionally, determining the fidelity from the D manifold state readout is difficult because our method gives nonphysical results (populations less than 0 or greater than 1) when the experimental conditions do not match the ideal conditions. To obtain the estimate of 2%, we assume equal contributions to the overall errors from state preparation and measurement when state preparation is performed until the percentange in $\left|D_{3/2}, m_J = +3/2\right\rangle$ stabilizes. For example, if the measured

fidelity on S state SPAM is 0.98, we assume the fidelity of state preparation is $0.99 = \sqrt{0.98}$. We would not make this assumption if there was a high background or if the purities of the various polarizations clearly differed significantly. If we ultimately wish to spend less on time pumping (see Sec. 6.4.1.1), we may choose to do so at the cost of an increase in infidelity because of incomplete population transfer. These excess errors would clearly then be due to state preparation and not measurement.

Furthermore, while readout of the resulting qubit state will directly contribute to the error in the result, an error in state preparation (population in the incorrect Zeeman sublevel in the D manifold) does not have a one-to-one correspondence to error in the final entangled state. If the ion is prepared in the $\left|5D_{3/2}, m_J = -3/2\right\rangle$ or $\left|5D_{3/2}, m_J = -1/2\right\rangle$ states, for instance, and the light polarization is in fact purely σ^- polarized, those populations will not contribute losses in fidelity, but rather rate, as there is no available transition. On the other hand, if there is population in the $\left|5D_{3/2}, m_J = +1/2\right\rangle$ state, then there is an available transition, and the resulting decay will lead to swapped polarization-ion state correlations. This excitation will only occur at $\frac{1}{3}$ the rate of the desired excitation, however, so the probability of an error will be approximately

$$P(\text{error}) \approx \frac{1}{3} P\left(\left|+\frac{1}{2}\right\rangle\right) \tag{6.6}$$

where $P\left(\left|+\frac{1}{2}\right\rangle\right)$ is the population in $\left|D_{3/2}, m_J = +3/2\right\rangle$.

6.2.1.2 Unequal Numbers of Photons with Each Polarization

While we already mentioned that collecting light over a finite angle will lead to polarization mixing errors in free space, it also means that there will be slightly unequal numbers of σ^+ and π photons collected from the ion. This difference will result in the decay not resulting in a perfect Bell state as desired. We can calculate the size of this effect by integrating over the spherical harmonic for each polarization with an aperture corresponding to the lens we use.

The most difficult part of this calculation is determining the limits of integration, so we will briefly discuss how we determined these. First, we note that we want to take the section of the unit sphere subtended by a cone with half-angle $\alpha = \arcsin(\mathrm{NA})$. In θ, the limits can be set to $\pi/2 \pm \alpha$. The limits in ϕ, however, are more complicated, as they must depend on θ. We can think of the bounds as the set of points with unit position vectors at angle α relative to the x axis (chosen arbitrarily–y would work equally well). The dot product of any of these position vectors with the unit vector defining the x axis then must equal $\cos\alpha$. Using these expressions along with basic coordinate transformations, we can determine that the limits for ϕ are

$$\phi_\pm = \pm \arctan\left[\frac{\sqrt{1-(\cos^2\alpha+\cos^2\theta)}}{\cos\alpha}\right]. \tag{6.7}$$

In the basis $\{|0H\rangle, |0V\rangle, |1H\rangle, |1V\rangle\}$, the ideal state is

$$|\psi_0\rangle = \frac{1}{\sqrt{2}}(1,0,0,1), \tag{6.8}$$

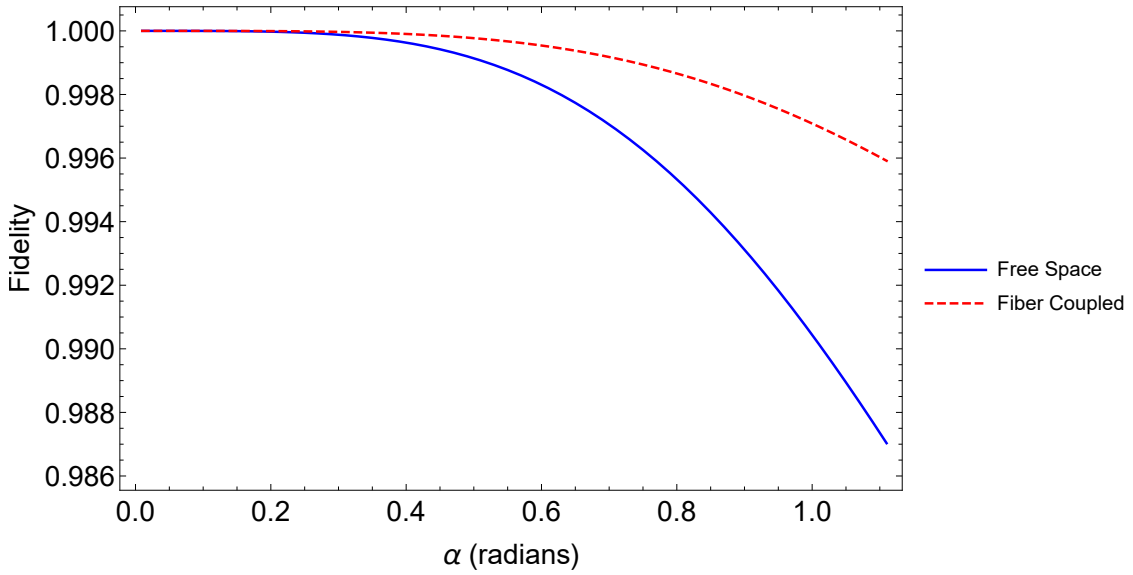

Figure 6.10: Plot of fidelity vs. light collection angle ($\alpha = \arcsin(\mathrm{NA})$) accounting for unequal numbers of H and V photons. The blue curve shows the calculation results in free space, while the red dashed curve shows the result when the light is fiber coupled (only including the ϕ component of the σ polarized light).

while the actual state is

$$|\psi\rangle = (\sqrt{P(H)}, 0, 0, \sqrt{P(V)}) \tag{6.9}$$

where $P(H)$ and $P(V)$ are the relative probabilities of detecting a H or V polarized photon respectively and $P(H) + P(V) = 1$. Note that we are not accounting here for any polarization mixing effects and just assuming that there is a one-to-one correspondence of $\sigma \leftrightarrow H$. We plot the resulting fidelity $F = |\langle \psi_0 | \psi \rangle|^2$ in Fig. 6.10. Of particular note are the values corresponding to the numerical apertures of our lenses. When only the ϕ component of the σ light is considered, the fidelity losses for NA=0.6 and NA=0.8 are 0.06% and 0.23% respectively.

These errors are already small, but the fact that we herald entanglement means that this loss cannot actually decrease the ion-photon entanglement fidelity. We

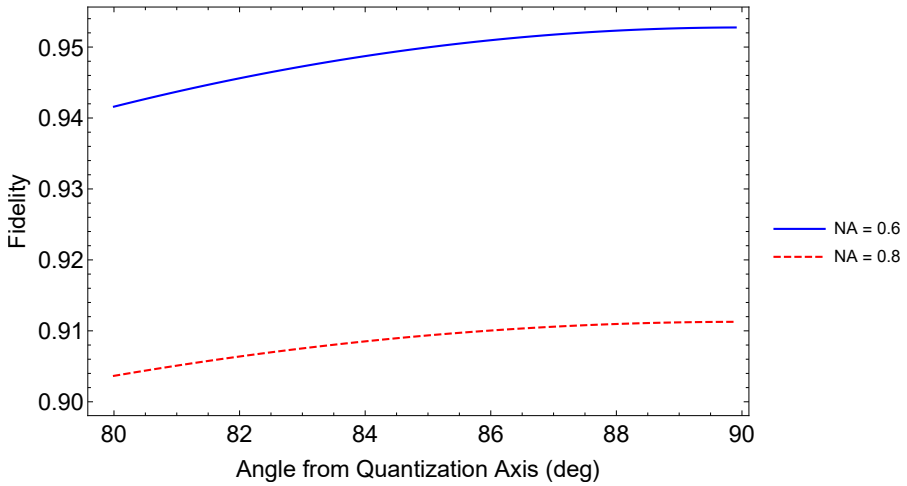

Figure 6.11: Plot of ion-photon entanglement fidelity versus angle from the quantization axis (θ_0). This plot includes the effects from both unequal numbers of σ and π polarized photons and polarization mixing. The blue, solid curve is the fidelity for NA 0.6, and the red, dashed curve is that for NA 0.8.

include it here, however, because we will discuss later how and if it impacts remote ion-ion entanglement fidelity. This effect can be understood similarly to polarization-dependent loss in the fiber, which for ion-photon entanglement is also not an issue.

6.2.1.3 Off-Axis Light Collection

If the light collection lens is not aligned perfectly perpendicular to the quantization axis, the polarizations of the light collected may deviate further from the ideal. In particular, the $\hat{\theta}$ component of the σ polarization will make up a larger portion of the light, and because the distribution is now asymmetric, will not cancel when fiber coupled.

We now write the axis for light collection as a unit vector with angle θ_0 relative to the z axis ($\theta_0 = \pi/2$ corresponds to the x axis):

$$\vec{r_0} = (\sin\theta_0, 0, \cos\theta_0)\,, \tag{6.10}$$

and the limits of our integration are the set of points with vectors at angle α relative to $\vec{r}_0$. We then obtain the integration limits $\phi_\pm = \pm \arctan\left(\frac{y}{x}\right)$ where:

$$y = \sqrt{1 - \left[\left(\frac{\cos\alpha - \cos\theta\cos\theta_0}{\sin\theta_0}\right)^2 + \cos^2\theta\right]}$$
$$x = \frac{\cos\alpha - \cos\theta\cos\theta_0}{\sin\theta_0}. \tag{6.11}$$

We perform these calculations for both NA=0.6 and NA=0.8, and the results are plotted in Fig. 6.11. The maximum fidelities for both are lower because of the polarization mixing discussed in detail in [52]. The dependence on angle from the quantization axis is gradual, especially for the higher numerical aperture. We should be able to align the lens much closer to perpendicular the field than the 10 degrees deviation shown as the maximum in the figure.

When the lens is not exactly perpendicular to the magnetic field, there will be some residual polarization mixing through the fiber. However, because the angle subtended by the lens is so much smaller than the likely deviation from the correct angle, we expect the fraction of the light that exhibits this asymmetry to be very small. As an aside, asymmetric aberrations in the ion image (see Chapter 7) may have similar effects [135]. However, since we optimize the lens alignment carefully to minimize the aberrations, we expect any resulting asymmetry from misalignment to be small as well.

6.2.1.4 Other Polarization Errors

Any other polarization errors would not be intrinsic to the ion or atomic physics, but rather a function of the optics through which the ion light propagates. For example, in general, glass itself is not birefringent, but when stress is applied, it can become birefringent. If the birefringence is uniform across the surface, we can easily undo its effect with wave plates, but if it varies in space, it becomes more complicated to correct. We have long suspected this as a significant, although not fundamental, source of error in our ion-photon entanglement experiments [105]. We discuss the birefringence of our vacuum windows for our third trap in more detail in Sec. 5.3.1.3, but there is no simple way to characterize the birefringence of the windows on our already existing traps without significantly disrupting our setup. Other optics in the system could also contribute in a similar manner, although the stresses are likely highest on the windows because of the glass to metal seal.

The results of the free space experiments combined with the experiments with the light fiber coupled suggest that the residual few percent of error is present without the fiber. However, since the fiber is a new element it merits a brief discussion. In general, strain on a non-polarization maintaining fiber will impart birefringence, and thus affect the polarization of the light propagating through the fiber. However, this effect is unitary and can be undone either with wave plates or purposeful application of strain to the fiber [105]. The major concern with this effect is thermal drifts that result in changes in the birefringence. We do in fact observe these drifts; however, they are on the time scale of hours to a day and can be compensated with

occasional adjustment of the wave plates in the optical path.

The final possible source of polarization errors is the polarizers we use to filter H and V light. Depending on the type of polarizing beam splitter, significant errors may be introduced because of the impurity of polarization filtering in one or more directions. To minimize this effect, we use a Wollaston prism[5] instead of a standard polarizing beam splitter cube. These have extinction ratios of $> 100,000 : 1$, so should have a completely negligible impact on our fidelity.

6.2.1.5 Time Decay of Ion Coherence

Our experimental control software (see Sec. 6.4.2) imposes significant limitations on how quickly we can progress from generating entanglement of the photon and ion to measuring that entanglement. We can perform a Ramsey-type experiment to measure the coherence time of our qubit. On Alice, we obtain a value for τ of 200 μs, and on Bob, we find $\tau \approx 400$ μs. The fidelity of a state that started as a pure state but is observed a time t later is given by [135]

$$F = \frac{2}{3} + \frac{1}{3} e^{-\frac{1}{2}\frac{t^2}{\tau^2}}. \tag{6.12}$$

Typical times between entanglement generation and state readout for us are $\sim$ 50 μs,which would result in a decrease of fidelity of 0.99 for a 200 μs coherence time.

[5] Thorlabs WP10-A

6.3 Ion-Ion Entanglement

Once we have a photon entangled with the ions in each trap, we need to establish a connection between the two ions. Remote entanglement can be generated with a photon from only one of the traps [136]; however, without further efforts, the fidelities of this type of protocol are typically lower [42]. Instead, we choose to use a protocol that relies on collecting a photon from each ion and interfering the photons on a beam splitter.

The entanglement process is probabilistic since the majority of the photons are lost before they arrive at the detectors. However, this does not hurt our fidelity since we herald entanglement only when we detect the arrival of two photons simultaneously, which guarantees no loss occurred.

6.3.1 Hong-Ou-Mandel Effect

The entanglement generated from the two photon scheme we use relies on the Hong-Ou-Mandel effect. This result demonstrated that when two identical photons are incident on a 50:50 beam splitter, they will always exit from the same port [137]. Mathematically, we can understand this result by examining the effect of a 50:50 beam splitter on a photon. We can think of the effect of a beam splitter as a unitary matrix constrained so that both outputs will have an equal probability of a photon exiting. Additionally, accounting for the bosonic nature of photons [138], we obtain the following relationship between the output and input ports (which can

be modified by an overall phase) [55]

$$\begin{pmatrix} a_3^\dagger \\ a_4^\dagger \end{pmatrix} = \frac{1}{\sqrt{2}} \begin{pmatrix} 1 & 1 \\ 1 & -1 \end{pmatrix} \begin{pmatrix} a_1^\dagger \\ a_2^\dagger \end{pmatrix} \tag{6.13}$$

where $a_i^\dagger$ is the photon raising operator for the i^{th} port of the beam splitter, and $i = \{1, 2\}$ are the input ports while $i = \{3, 4\}$ correspond to the output ports. This matrix equation can be inverted to find $a_1^\dagger$ and $a_2^\dagger$ in terms of $a_3^\dagger$ and $a_4^\dagger$.

To illustrate the effect of the beam splitter, we first consider the case of the arrival of a single photon at port 1, which can be written as $a_1^\dagger |0_1 0_2\rangle$. Then, the output result will be given by

$$a_1^\dagger |0_1 0_2\rangle = \frac{1}{\sqrt{2}} \left(a_3^\dagger + a_4^\dagger\right) |0_3 0_4\rangle = \frac{1}{\sqrt{2}} \left(|1_3 0_4\rangle + |0_3 1_4\rangle\right). \tag{6.14}$$

Next, we consider the arrival of a photon on both ports simultaneously $a_1^\dagger a_2^\dagger |0_1 0_2\rangle$

$$\begin{aligned} a_1^\dagger a_2^\dagger |0_1 0_2\rangle &= \frac{1}{2} \left(a_3^\dagger + a_4^\dagger\right) \left(a_3^\dagger - a_4^\dagger\right) |0_3 0_4\rangle \\ &= \frac{1}{2} \left(|2_3 0_4\rangle + |0_3 2_4\rangle\right) \end{aligned} \tag{6.15}$$

where we have made use of the fact that $a_1^\dagger$ and $a_2^\dagger$ commute since they do not operate on the same state. This result is known as the Hong-Ou-Mandel (HOM) effect.

Now, we expand this theory to the case of non-identical photons. We consider only two photon states, and in the context of this thesis it makes sense to consider H

and V polarizations as the two possibilities. We define $a_i^\dagger$ as the creation operator for an H polarized photon at the i^{th} port and $b_i^\dagger$ as the creation operator for a V polarized photon at the corresponding port. Note that $a_i^\dagger$ and $b_i^\dagger$ commute and do not act on photons without the correct polarization. Also, both sets of raising operators are related as described by Eq. 6.13. If an H photon arrives at port 1 and a V photon at port 2 ($a_1^\dagger b_2^\dagger |0_1 0_2\rangle$), we obtain the following

$$\begin{aligned} a_1^\dagger b_2^\dagger |0_1 0_2\rangle &= \frac{1}{2}\left(a_3^\dagger + a_4^\dagger\right)\left(b_3^\dagger - b_4^\dagger\right)|0_3 0_4\rangle \\ &= \frac{1}{2}\left(|(HV)_3 0_4\rangle - |H_3 V_4\rangle + |V_3 H_4\rangle - |0_3 (HV)_4\rangle\right). \end{aligned} \tag{6.16}$$

We have modified our notation slightly here to indicate the polarizations of the output photons, so $|(HV)_3 0_4\rangle$ would correspond to 2 photons at port 3, but one with each polarization. This equation shows the lack of interference between distinguishable photons, and the resulting possibility of one photon at each output port or two photons at one port.

6.3.2 Bell State Measurements and Ion Entanglement

Assume photons from each ion arrive at the beam splitter simultaneously. We then have the following possibilities:

$$
\begin{aligned}
|H_1H_2\rangle \rightarrow |\psi_1\rangle &\equiv \frac{1}{\sqrt{2}}\left(|(HH)_3 0_4\rangle - |0_3(HH)_4\rangle\right) \\
|V_1V_2\rangle \rightarrow |\psi_2\rangle &\equiv \frac{1}{\sqrt{2}}\left(|(VV)_3 0_4\rangle - |0_3(VV)_4\rangle\right) \\
|H_1V_2\rangle \rightarrow |\psi_3\rangle &\equiv \frac{1}{2}\left(|(HV)_3 0_4\rangle - |H_3V_4\rangle + |V_3H_4\rangle - |0_3(HV)_4\rangle\right) \\
|V_1H_2\rangle \rightarrow |\psi_4\rangle &\equiv \frac{1}{2}\left(|(HV)_3 0_4\rangle - |V_3H_4\rangle + |H_3V_4\rangle - |0_3(HV)_4\rangle\right). \qquad (6.17)
\end{aligned}
$$

If we have one detector at each output of the beam splitter, we would only herald entanglement if the two input photons have different polarizations and the output photons leave from different ports. In this setup, therefore, we only successfully generate entanglement 1/4 of the time that two photons successfully propagate through the fiber system. We can double the rate by using the setup shown in Fig. 6.12. Here, we place a polarizing beam splitter at the output of each exit port of the in-fiber beam splitter. This configuration allows us to detect when the two incident photons have different polarizations but exit through the same output of the 50:50 beam splitter, which will increase this factor in our efficiency to 1/2.

Ultimately, we wish to end up with the ions in a maximally entangled state, which, for two qubits, entails a Bell state. Thus, we perform our measurement in

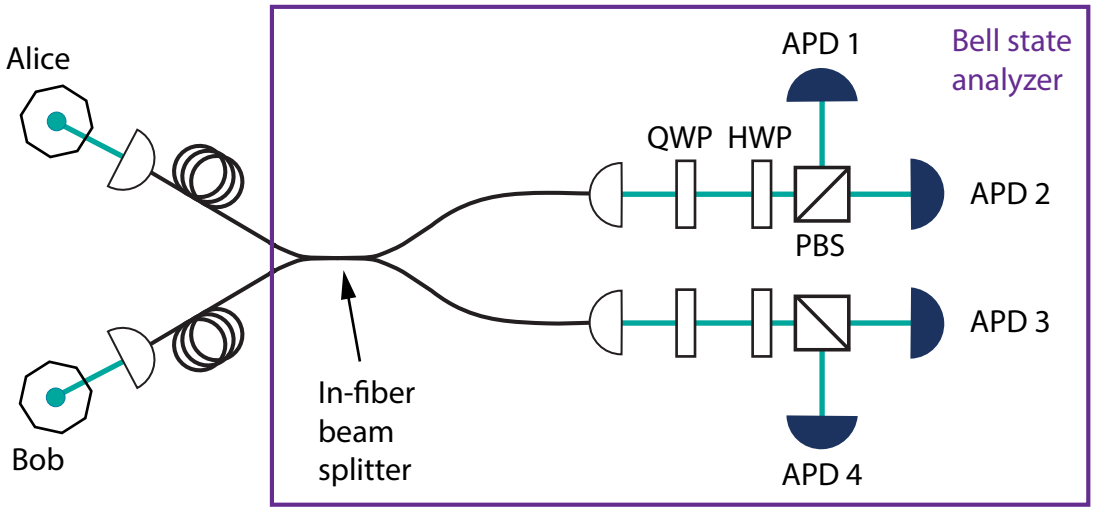

Figure 6.12: Experimental setup for remote entanglement experiments. Light from an ion in each chamber is fiber coupled and sent through an in-fiber beam splitter. The output light of each port of the beam splitter is then sent through a polarizing beam splitter. Each of the four possible final outputs has its own single photon detector. The optical elements in the bottom path are the same as those in the top path.

the basis defined by the Bell states

$$\begin{aligned} \left|\Phi^{\pm}\right\rangle &= \frac{1}{\sqrt{2}}\left(|00\rangle \pm |11\rangle\right) \\ \left|\Psi^{\pm}\right\rangle &= \frac{1}{\sqrt{2}}\left(|01\rangle \pm |10\rangle\right) . \end{aligned} \tag{6.18}$$

At this point, we must also remember that the ions are in fact entangled with the states of the photons with an overall state at the inputs of the beam splitter

$$|\psi_0\rangle = \frac{1}{2}\left(|0_A H_1\rangle + |1_A V_1\rangle\right) \otimes \left(|0_B H_2\rangle + |1_B V_2\rangle\right) \tag{6.19}$$

where an A (B) subscript on the ion state indicates the ion in Alice (Bob). This

joint state can be written in terms of the Bell states

$$|\psi_0\rangle = \frac{1}{2}\left(\left|\Psi_i^+\right\rangle\left|\Psi_p^+\right\rangle + \left|\Psi_i^-\right\rangle\left|\Psi_p^-\right\rangle + \left|\Phi_i^+\right\rangle\left|\Phi_p^+\right\rangle + \left|\Phi_i^-\right\rangle\left|\Phi_p^-\right\rangle\right) \tag{6.20}$$

where the subscripts i and p indicate the ion and photon states respectively. For the photonic Bell states, we will let $H \leftrightarrow 0$ and $V \leftrightarrow 1$ for the sake of the definitions in Eq. 6.18. For both ion and photon states, the first qubit state in each term will be the one corresponding to Alice (or port 1 on the beam splitter for the photon) and the second will be the state of the qubits from Bob (or port 2 on the beam splitter).

Next, following [55], we find the effect of the beam splitter on each of the photonic Bell states using Eq. 6.13. We find that for the input states $|\Phi^{\pm}\rangle$ and $|\Psi^{\pm}\rangle$ we obtain the following outputs

$$\begin{aligned}
\left|\Phi^{\pm}\right\rangle &\rightarrow \frac{1}{2}\left(|(HH)_3 0_4\rangle - |0_3(HH)_4\rangle \pm |(VV)_3 0_4\rangle \mp |0_3(VV)_4\rangle\right) \\
\left|\Psi^{+}\right\rangle &\rightarrow \frac{1}{\sqrt{2}}\left(|(HV)_3 0_4\rangle - |0_3(HV)_4\rangle\right) \\
\left|\Psi^{-}\right\rangle &\rightarrow \frac{1}{\sqrt{2}}\left(|H_3 V_4\rangle - |V_3 H_4\rangle\right).
\end{aligned} \tag{6.21}$$

We note that since there is a direct correspondence between a given photonic Bell state and an ion Bell state as shown in Eq. 6.20, if the photon is determined to be in a particular Bell state, the ions must be in that same state. Furthermore, from Eq. 6.21, we can see that if the ions (or photons) are in either of the $|\Phi\rangle$ Bell states, the photons will always end up on the same APD, and thus we will never observe these states. On the other hand, for $|\Psi^-\rangle$, we would have been able to

detect this state even without the polarizing beam splitters. $|\Psi^+\rangle$ is also observable with the setup with the polarizing beam splitters. This result is consistent with the conclusion that it is not possible to measure all four Bell states using only linear optics [139, 140].

The result of this measurement, then, is clearly an ion-ion entangled state of either $|\Psi^+\rangle$ or $|\Psi^-\rangle$. Which state the ion is in can be distinguished based on which APDs receive photons. In particular, the possible results for simultaneous detection events are

$$\text{APD 1 and APD 2} \rightarrow \left|\Psi^+\right\rangle$$

$$\text{APD 3 and APD 4} \rightarrow \left|\Psi^+\right\rangle$$

$$\text{APD 1 and APD 3} \rightarrow \left|\Psi^-\right\rangle$$

$$\text{APD 2 and APD 4} \rightarrow \left|\Psi^-\right\rangle$$

$$\text{APD 1 and APD 4} \rightarrow \text{Error}$$

$$\text{APD 2 and APD 3} \rightarrow \text{Error.}$$

We include the last two to emphasize that coincident photon arrivals on these two detectors do not herald entanglement. Such coincidences do not affect the fidelity of our results as we do not treat those cases as a successful entanglement generation event.

It is always possible to rotate from one Bell state to another using only local (non-entangling) operations, so we can easily change the resulting ion state from

$|\Psi^+\rangle$ to $|\Psi^-\rangle$ or vice versa if so desired using separate Raman operations in Alice and Bob. This ability to rotate between the states and knowing we generate the same entangled state after every successful entanglement attempt may be important for subsequent quantum operations.

6.4 Experimental Procedure

In the previous sections, we have discussed the theory underlying the entanglement of two ions that are each entangled with a photon. We now proceed to discuss the details of our experimental implementation.

6.4.1 Experimental Sequence

The overarching structure of our experiment consists of two primary phases–(i) the fast loop and (ii) the slow loop. The fast loop consists of all remote entanglement generation attempts and the subsequent decision about how to proceed based on any photons that arrive on the APDs. The slow loop, on the other hand, encompasses many cycles of the fast loop as well as periodic cooling of the ion and entanglement verification. Understanding the role of these two phases is primarily important for determining the rates with which we successfully generate entanglement, but also provides a useful framework for discussing the steps of the experiment.

6.4.1.1 The Fast Loop

The steps in the fast loop are very similar to those for the ion-photon entanglement experiment discussed in Sec. 6.2 but performed on both traps simultaneously. Specifically, the steps are:

1. Prepare ions in both Alice and Bob in either $\left|D_{3/2}, m_J = +3/2\right\rangle$ or $\left|D_{3/2}, m_J = -3/2\right\rangle$. For simplicity, we assume we prepare in $\left|D_{3/2}, m_J = +3/2\right\rangle$. The other steps would be the same but with σ^+ and σ^- 650 polarizations switched.

2. Excite both ions with a 10 ns 650 nm pulse.

3. Look for coincident photon arrivals.

4. If there is a coincidence, decide to end the fast loop. If there is not a coincidence, either repeat the fast loop or break out of the fast loop to cool the ion.

We have already discussed in detail the processes for both of the first two steps in Secs. 3.2.4.1 and 6.1 respectively. For the third step we set a detection window of ∼30 ns starting with the 650 nm pulse. This timing is optimized by looking for the maximum rate of photon arrivals to compensate for any delays in the APDs or in the control software or hardware. If, during this window, we observe no photons or a single photon arrival, we do not herald entanglement. In addition, as we explained in Sec. 6.3.2, certain apparent coincidences do not correspond to physically possible entangled states. Therefore, we do not consider those events as

successful entanglements since they would inherently increase the error in our results. If, however, there is a coincidence event on a correct combination of photons we must immediately stop the entanglement attempts and break out of the fast loop.

In Fig. 6.13, we show the timings for each laser beam being turned on. Each beam is controlled by at least one AOM. For the 650 nm σ beams, there are two AOMs–one fast one (rise time $\sim$5 ns) with the primary purpose of generating the excitation pulse, and one for each polarization to be able to switch them independently. In the figure, the line for "Fast 650 σ" shows the control sequence for the fast AOM, where the optical signal is that between the fast AOM and the slow AOMs. The lines for the slow AOMs show the optical signals at their outputs. However, even if the RF is on for the slow AOMs, if the RF for the fast AOM is off, there will not be any light transmitted. As a result, for example, the optical pulse for "Slow 650 σ^-" is much shorter than the RF pulse and than the rise time of the slow AOM.

The time that the fast loop takes is dominated by optical pumping. While we generally want to be limited by the atomic physics as we currently are, pumping times to achieve full population transfer were initially much longer than desired. The details of this timing are discussed in Sec. 3.2.4.1. We were, however, able to improve the speed somewhat by lowering the 650 σ powers while pumping compared with the power used for excitation. We also examined the trade-off between complete pumping and fidelity of ion-photon entanglement and found that we could reduce the pumping time from almost 3 μs to $\sim$ 1 μs without a significant decrease in the fidelity of the resulting entangled state (see Sec. 6.2.1.1).

To change the power of a given beam, we change the RF power used to drive

the AOM. We cannot make this change with a single RF source during the entangler core, the part of the experimental control software that runs the "fast loop" phase of the experiment (see Sec. 6.4.2 for details on the entangler core). We work around this limitation by using multiple RF sources and switching them separately. We use a similar approach for our other laser beams as well. After discussing the details of the slow loop, we will summarize all of the laser control requirements (Table 6.4.1.2).

In addition to the pumping time, the other primary contributor to the length of the fast loop is the delay between when the RF signal is sent from the FPGA to the AOM and when the AOM actually puts out the optical signal. While there is a short delay intrinsic to the FPGA and some additional time from the propagation of the signal in cables ($\lesssim$ 10 ns), this latency is primarily due to the distance the sound wave in the AOM must travel from the transducer to the beam. The speed of sound in our modulators is typically about 5000 m/s, so sound propagation over a distance of 1 mm takes about 200 ns. We adjust the alignment of the AOMs to place the beams as close to the transducers as possible without clipping on the transducer or the AOM cover, but the minimum time until the pulse reaches the beam is still of order hundreds of nanoseconds. Some of this time is also comprised of the acoustic wave travelling across the laser beam, which typically has a waist about 1 mm, so we could improve this time somewhat by focusing the beams through the AOM more tightly. However, tight focusing through an AOM results in a significant decrease in the diffraction efficiency of the beam [141], so there is somewhat of a trade-off if we are power limited.

Finally, after the detection window, there is a small amount of time ($\sim$60 ns)

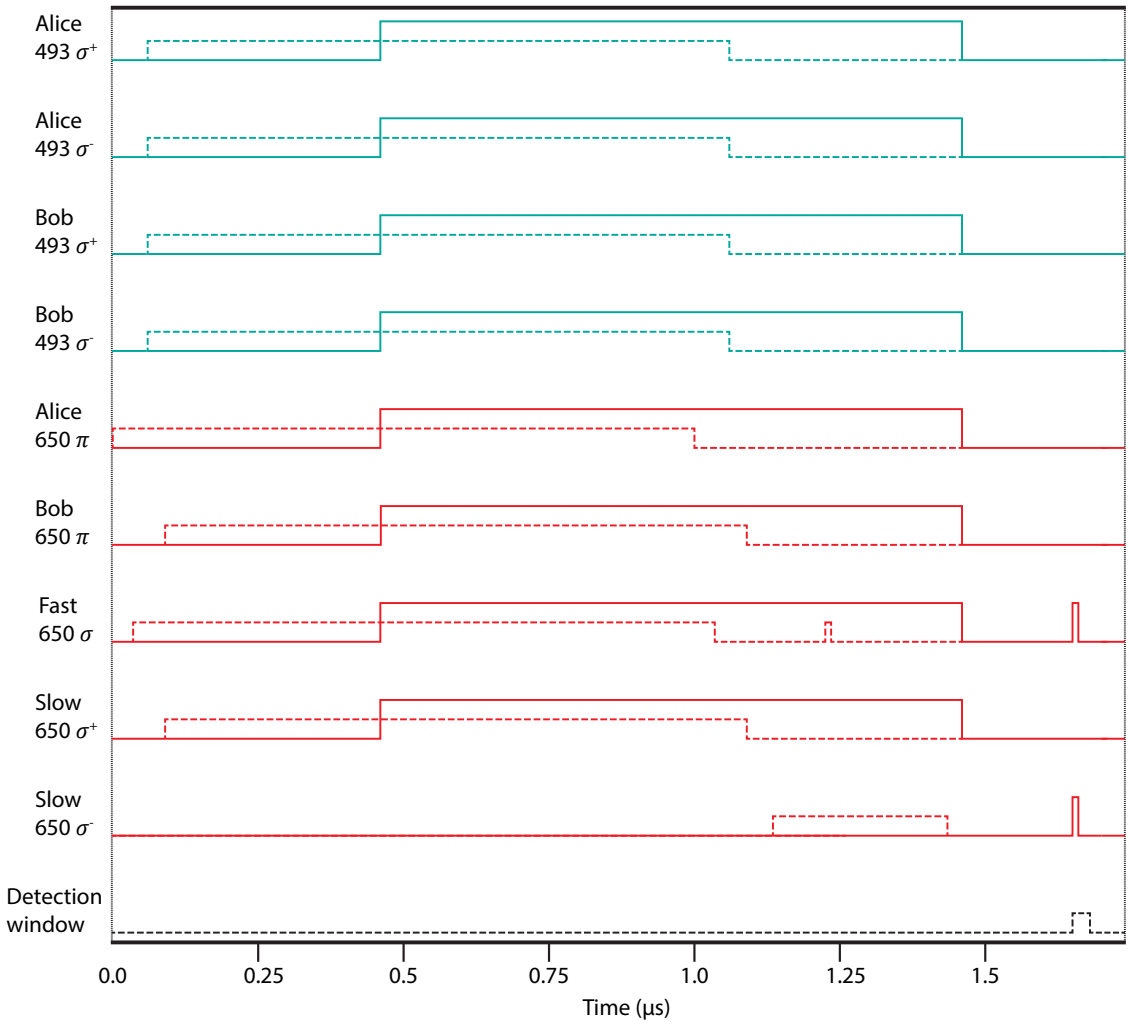

Figure 6.13: Timing of optical control events in the remote entanglement fast loop. We show when each relevant laser beam is turned on (solid lines) and when the RF signal to turn on the AOM that controls the laser beam is sent (dashed lines). The event where the majority of the laser beams are turned on for a few microseconds corresponds to optical pumping. The subsequent small peaks show the excitation pulse. Finally, the black line at the bottom shows the window when the APDs are allowed to look for photons, the beginning of which coincides with the excitation pulse. Note also the direct correspondence in general of the length of the RF signal to the length of the optical pulse does not apply to the light for the excitation pulse (slow 650 σ^-) because the pulse length is limited not by the RF on the slow AOM but on the fast AOM. Timings are shown to scale.

for the decision about how to proceed. The brevity of this step was the main challenge in implementing the control software of this experiment. Our approach for achieving this time will be discussed further in Sec. 6.4.2.

6.4.1.2 The Slow Loop

The slow loop encompasses cooling of the ion, repetitions of the fast loop, and entanglement verification. This part of the experiment is not controlled by the entangler core (Sec. 6.4.2), so there is much more software overhead time for each step. However, because most of the time in the experiment is spent running the fast loop repeatedly, the length of these operations has a minimal impact on the rate of our experiment.

The basic steps of the slow loop consist of the following:

1. Cool the ion for $\sim$100 μs.
2. Run the fast loop until a successful entanglement herald event or until $\sim$500 μs have lapsed (approximately 170 attempts).
3. If we stopped the fast loop because too much time had passed, return to step 1.
4. Otherwise, perform any necessary local coherent operations (Raman rotations).
5. Perform state detection to verify entanglement.

At the time of writing, we were still in the early phases of conducting these experiments so these timings are not necessarily optimized. For the first step, we perform Doppler cooling as described in Sec. 3.2.2. The exact length of both of the first two steps will be optimized to minimize the cooling time and maximize the fast

RF source	Cooling	State Preparation	Excitation	Qubit State Readout	Optical Power
493 σ^+ High Power	×	✓	×	×	40 μW
493 σ^+ Low Power	✓	×	×	✓	8 μW
493 σ^- High Power	×	✓	×	×	40 μW
493 σ^+ Low Power	✓	×	×	✓	8 μW
650 π High Power	×	✓	×	×	195 μW
650 π Low Power	✓	×	×	✓	118 μW
650 σ^+ High Power	✓	×	×	✓	36.5 μW
650 σ^- Low Power	×	✓	×	×	13 μW
650 σ^+ High Power	×	×	✓	×	47 μW
650 σ^+ Low Power	✓	×	×	✓	33 μW
650 fast AOM pulsed mode	×	×	✓	×	-
650 fast AOM CW mode	✓	✓	×	✓	-

Table 6.1: Phases of the experiment when each high or low power RF control is turned on. Alice and Bob have the same beams on for the same sections, but may have different powers because the focusing is different. For the 650 σ beams, the high power σ^+ beam and the low power σ^- beam actually have similar optical powers, because of their different purposes. Measured optical powers for Alice are included to show of the relative powers in each beam. Powers for the 650 fast AOM are the same in both modes and also do not correspond to the optical power at the ion for any beam so are not included.

loop repetitions without excessive ion heating.

Raman rotations may be necessary if we want to rotate from one Bell state to the other, if we account for differing phases on the two ions (for more on this issue see Sec. 6.4.4.2, for example), or for rotating the ion state to perform measurements in different bases. For both this experiment and the ion-photon experiments discussed above, Raman rotations must be performed using an arbitrary waveform generator

(AWG) to maintain a consistent phase from shot to shot. For the more recent experiments we use an AWG from Keysight[6]. Using an AWG as opposed to a free-running DDS or other RF source guarantees control over the starting phase of the Raman rotation.

There are multiple options for entanglement verification (Sec. 6.4.1.3), but all have in common the need to be able to read out the states of both ions. As discussed in Sec. 3.2.3.2, our current detection scheme is probabilistic, but by repeating trials enough we should eventually be able to build up the necessary statistics to perform the required measurements.

We read out the state of the ion using the technique described in Sec. 3.2.3.2. We use the same APDs for state readout on Alice as for entanglement heralding because of the high background in the free space detection setup. Bob, on the other hand, has a much lower background count rate on its free space imaging setup, so we are able to perform readout using another APD located after this setup. Because of the need to perform state detection on Alice on the fiber coupled APDs, we must perform the detections sequentially. However, the length of detection is only a few hundred ns so this does not impose significant delays on the experiment.

The optimal optical powers for each beam for Doppler cooling and state readout differ from those for state preparation and excitation. To address this issue, we choose to increase our experimental complexity in order to optimize each segment of our experiment. Each AOM, aside from the fast 650 AOM, therefore actually has two RF sources that can provide the necessary power. One of these sources is

[6] M3202A

set to output a lower power than the other. The powers of each of the beams and the parts of the experiment for which they are used are shown in Table 6.4.1.2. For cooling and state readout, the 493, 650 π, and 650 σ^- beams operate in their lower power configurations, while the power is the higher setting for 650 σ^+ beam, since it needs to be very low for optimal pumping. Conversely, for state preparation, we use the high power settings of all of the beams that are on except for the 650 σ^+ beam.

6.4.1.3 Entanglement Verification

The simplest option to verify entanglement is one analogous to our method for verifying ion-photon entanglement. For this method, we would perform rotations of varying angles on the ion in one of the traps, measure the qubit state populations on that ion, and correlate those results with the populations in each qubit state on the other ion. This measurement would comprise our z basis measurement. We could then perform an x basis measurement by performing a $\pi/2$ rotation on one of the ions, and then performing $\pi/2$ rotations with varying phase on the other. This method was used in the first demonstration of remote entanglement in our group [142].

Another option is to perform full state tomography using maximum likelihood estimation as in [32]. For this process, we would need to make 16 different measurements with various combinations of rotations of the ion states. The requirements for these measurements are detailed in [143]. From there, these data are numeri-

cally compared with the possible physical density matrices, until the one that best matches the experimental data is found. Once the density matrix $\hat{\rho}$ is obtained, we would compare it to the ideal state $|\Psi^+\rangle$ as defined in Eq. 6.18. Note that, while some trials will result in the state $|\Psi^-\rangle$, we can easily rotate between the states with local operations, so we can always compare to a single state. The fidelity is then given by $F = \langle\Psi^+|\,\hat{\rho}\,|\Psi^+\rangle$. Alternatively, we can treat the two Bell states $|\Psi^+\rangle$ and $|\Psi^-\rangle$ separately and adjust our tomography steps depending on which state is heralded. The advantage of full tomography compared with the first is that it more completely determines the entire density matrix at the cost of significantly more elaborate data analysis needs.

6.4.2 Experimental Control System

The control requirements for this experiment are fairly complex and the timing needs are extremely demanding. For instance, as will be discussed in Sec. 6.4.3, we must have software overhead in the fast loop of $\ll 1$ μs. We use the ARTIQ control system, which provides an interface between Python-based software control and an FPGA and associated hardware.

In its standard form, ARTIQ provides deterministic control with very precise timing, and allows for relatively straightforward integration of the required hardware. However, it does not have the inherent capability of performing fast (< 1 μs) non-deterministic operations. The ion trapping group at the University of Oxford, however, has demonstrated a workaround to this issue that we adapted for this

experiment (discussed in [135]).

The basic features of our system are the same as the one described in [135], and the part of the control system that handles the most challenging aspects is referred to as the "entangler core." This part of the control program takes inputs that determine the timing of various events and then runs a sequence of events from the FPGA without communicating with the CPU. It also encompasses the branching decision discussed in Sec. 6.4.1.1 about how to proceed based on photon arrivals (or lack thereof) on the APD. Using this program, we have been able to improve our software overhead from of order 100 μs to about 60 ns. The main difference between our control system and that of the Oxford group is that we use a single FPGA to control both traps, whereas they use a primary FPGA that controls one of their traps as well as another, secondary FPGA, which controls the other trap.

In the slow loop, we do not worry as much about the rate, because the overall entanglement rate is not as heavily dependent on this part of the experiment. However, if we naively output signals in the default ARTIQ mode, we have hundreds of microseconds of overhead, which is unacceptable even for the slow loop. Another mode in ARTIQ is "Direct Memory Access" (DMA), which allows pre-programming of a sequence of certain real time input/output (RTIO) events. This sequence can then be recalled and carried out with much less overhead. For DMA, the overhead is primarily a one time occurrence to record the sequence and takes about 10-100 μs, but because it is a single event, is much faster than having that lag every cycle. Therefore, we take advantage of this mode as much as possible in the slow loop to further minimize the software overhead. Since it can only perform deterministic

events, this mode cannot be used for the fast loop, however.

6.4.3 Entanglement Generation Rate

For the remote entanglement generation link to be a useful part of a modular quantum computing architecture, the time it takes to generate remote entanglement should be as short as possible. Additionally, with higher rates, the current fidelity limitations on photonic entanglement will not be so severe because entanglement distillation can be used to purify the remotely entangled states [144]. While the atomic physics in principle allows for very fast generation of single photons, current rates are limited by technical challenges in efficient light collection, primarily the finite light collection angle and fiber coupling efficiencies.

One option for increasing photon collection efficiency consists of placing the ion in an optical cavity, preferably in the strong coupling regime for maximum effect. There has been a lot of work in this direction [145–152], and especially in [151], shows promising results for the rate of photon collection. However, cavities inherently require dielectric surfaces located in close proximity to the ion, which can dramatically increase heating rates [153]. If local entangling operations are not needed, then the rapid heating may not have much of an impact. However, we must connect our communication qubit to the memory qubit, which will ultimately make this consideration important for us. The rates of photon generation with cavities in the weak-coupling regime have not been significantly higher than those in free space.

Because of these difficulties with optical cavities, we are limited by the lenses that we use. The probability for generating, collecting, and detecting photons from a single trap is given by:

$$p_1 = r_{br} p_c p_f \eta_d \tag{6.22}$$

where r_{br} is the branching ratio of the atom, p_c is the probability of collecting the photon through the lens, p_f is the probability of coupling the light into the fiber, and η_d is the detector efficiency. p_c can further be broken down into the fraction of light collected by the lens without the trap $\frac{\Omega}{4\pi}$ and the probability of the light making it through the trap rods p_{trap} (see Secs. 4.2 and 7.2). The rate for a coincidence detection is then:

$$R_{tot} = \frac{1}{2} R_{rep} p_{1_A} p_{1_B} \tag{6.23}$$

Here, p_{1_A} and p_{1_B} are the probabilities for Alice and Bob, respectively, which can differ because of the fiber coupling efficiencies. R_{rep} is the rate at which we attempt remote entanglement generation, which is approximately equal to $1/\tau_{fast}$ where τ_{fast} is the length of the fast loop. In practice, the rate will be slightly lower due to the operations in the slow loop. The factor of 1/2 results from the fact that we only can detect half of the Bell states.

In Table 6.4.3, we present the values for the factors that determine our current rate as outlined in Eqs. 6.22 and 6.23. We implement some of the improvements listed in this table in Cleo (Sec. 5.2). We have already pushed the state preparation time for full population transfer close to the simulated minimum of ~ 2 μs (see Sec. 3.2.4.1), so we likely cannot improve it much further as long as we continue

preparing in the D manifold. We have shortened the time we spend pumping to about 1 μs, however. At this pumping time, the fidelity loss due to incomplete population transfer is much smaller than our other errors. Furthermore, even with the decreased rate of excitation as a result of incomplete pumping, the overall entanglement rate is higher because we can cycle through the fast loop more rapidly.

Variable	**Current Value**	**Limitations**	**Possible Improvements**
R_{rep}	0.7 MHz	State preparation time	Increase magnetic field and powers Different excitation scheme
$\frac{\Omega}{4\pi}$	0.1	Objective NA	Larger NA lenses (Cleo)
p_{trap}	0.85	Trap geometry	Modified trap structure (Cleo)
p_{fiber_A} (p_{fiber_B})	0.4 (0.25-0.40)	Possibly vacuum window	Collimating light through window may help (Cleo)
r_{br}	0.75	Atomic structure	Use cavities Different atomic species
η_d	.71	Quantum efficiency of APDs	Use SNSPDs

Table 6.2: Factors determining the rate of remote entanglement generation success, along with their current values, limitations, and possible improvements. If (Cleo) is listed in the possible improvements, we attempted to implement these improvements in the third trap.

The branching ratio is an intrinsic property of the barium ion and can not easily be modified. Placing the ion in a cavity could accomplish this effect [154], but as discussed previously, imposes significant technical difficulties. Therefore, we choose to accept the branching ratio as is, and the resulting rate loss. The detector efficiency could be improved using superconducting nanowire single photon detectors (SNSPDs), but because of the much higher cost and relatively marginal gains, we have decided that they are not a worthwhile upgrade.

With all of these factors combined, we end up with a predicted entanglement generation rate of 70-110 s^{-1} depending on the fiber coupling we ultimately achieve in Bob, which still needs to be determined. This is more than an order of magnitude

higher than the previous results from our group [33], but is significantly slower than the results reported in [32], largely due to the long pumping times. However, this result will be the first result where the entire path from the ion to the Bell state analyzer, including the 50:50 beam splitter, is in fiber.

6.4.4 Sources of Fidelity Loss in Remote Entanglement

6.4.4.1 Photon Arrival Timing

Many of the possible sources of error contribute to the fidelity of the ion-photon entanglement, and therefore, were already examined in Sec. 6.2.1. However, there are a few additional possible factors that could further decrease the fidelity of the remote entanglement.

Perhaps the most obvious possible issue is that of the timing between the photons generated from the two traps. In the extreme case that the wave packet of the first photon to arrive passes through the beam splitter completely before that of the second, it is clear, for instance, that no interference will occur. In this case, two photons that have the same polarization could arrive at different detectors and appear to herald entanglement. This effect can be mitigated by narrowing the window over which photon arrival events are counted toward possible entanglement. What is important, however, is not the specific time that the photon hits the detector but that the distribution of photons from the two traps match [135]. We use the same pulse to excite both ions, and their decay profiles are equivalent, so the timing depends only on the path lengths. The path lengths after the ion are very close to

identical because they propagate through the same lens and in-fiber beam splitter. On the other hand, the beam delivery paths must be adjusted to approximately the same length. To have $< 1\%$ error, the difference should be on the order of 1 mm [42].

We can directly observe the timing of the photon arrival distributions from each trap using the PicoHarp that we use for micromotion compensation. Since this instrument has timing down to 4 ps, we can observe the path length difference down to $\sim$1 mm as desired and adjust the path lengths accordingly.

6.4.4.2 Qubit Phase Evolution

The terms in the phase evolution of the qubit after detection of the photons that could affect our fidelity are primarily $\frac{1}{2}\Delta\omega\Delta t$, Δkz, and $\frac{1}{2}\left(k_A + k_B\right)\Delta z$ where $\Delta\omega$ is the difference in Zeeman frequencies between Alice and Bob, $k_{A(B)}$ is the wavenumber of the photon emitted from Alice (Bob), z is the average path length of both traps, and $\Delta z = z_A - z_B$ [135]. If the qubit splitting is identical, the first and second terms will not contribute. However, if the splittings differ, we can still observe the interference of the photons [155]. Nonetheless, in practice, it is simplest to get $\Delta\omega$ as close to 0 as possible. Futhermore, this splitting will in general fluctuate due to changes in the magnetic field, as discussed in Sec. 6.2.1.5, and these fluctuations will impact our fidelity as discussed in that section

For the other two terms, we must consider the contributions from both noise on the qubit splitting and path length fluctuations. We estimate that we can measure

the average qubit splitting to better than 10 kHz using Raman spectroscopy, so we use a splitting of 10 kHz to calculate an upper bound on our infidelity. Also, we note we are less interested in the static offset than the fluctuations. With this in mind, we see that fluctuations of at least several meters would be needed to introduce an error of 10^{-3} in the Δkz term. For the other term, the relevant length scale is about 15 m rather than tens of km, so much shorter path length fluctuations could affect the fidelity. However, these fluctuations would still need to be several mm and not in the part of the path where both beams propagate, so any observable effect is unlikely.

6.4.5 Beam Splitter and Fiber Errors

In [135], they provide a thorough examination of the effects of a beam splitter that does not have perfect 50:50 splitting. The splitter we use in practice has splitting closer to 47:53. From [135], the fidelity for arbitrary transmissivity and reflectivity is:

$$\frac{1}{2} + \frac{r^2 t^2}{r^4 + t^4} \tag{6.24}$$

where r is the reflection coefficient and t is the transmission coefficient. For our beam splitter, this gives a fidelity of 0.996.

Because we encode our photonic qubit in polarization, we must also consider the possibility of polarization-dependent splitting in the beam splitter and polarization-dependent loss in the fiber and beam splitter and how this would affect our fidelity. This consideration is especially important because of the fact the beam

splitter is in fiber, so its behavior is not quite as predictable as free space beam splitters.

We first consider the case of polarization-dependent beam splitting. For both H and V polarized light, we must modify the beam splitter operator to account for this effect. In general, we have:

$$\begin{pmatrix} a_3^\dagger \\ \\ a_4^\dagger \end{pmatrix} = \begin{pmatrix} t & r \\ \\ r & -t \end{pmatrix} \begin{pmatrix} a_1^\dagger \\ \\ a_2^\dagger \end{pmatrix} \tag{6.25}$$

where $t^2 + r^2 = 1$. For a 50:50 beam splitter $t = r = \frac{1}{\sqrt{2}}$. For a polarization-dependent beam splitter, we modify both the matrix for $a^\dagger$ (horizontal polarization raising operators) and $b^\dagger$ (vertical polarization raising oprators) to have coefficients of transmission and reflection (t_a, r_a) and (t_b, r_b) respectively. The calculation is conceptually simple, but somewhat heavy on algebra, so we simply state the results. The fidelities for the case of $|\Psi^+\rangle$ and $|\Psi^-\rangle$ differ, and are, respectively

$$F_+ = \frac{1}{2} + \frac{r_a r_b \sqrt{\left(1 - r_a^2\right)\left(1 - r_b^2\right)}}{r_a^2\left(1 - r_b^2\right) + r_b^2\left(1 - r_a^2\right)} \tag{6.26}$$

$$F_- = \frac{1}{2} + \frac{r_a r_b \sqrt{\left(1 - r_a^2\right)\left(1 - r_b^2\right)}}{\left(r_a r_b\right)^2 + \left(1 - r_a^2\right)\left(1 - r_b^2\right)}. \tag{6.27}$$

To find the overall fidelity, we average F_+ and F_-, and we plot the results in Fig. 6.14. In this figure, we plot the fidelity versus r_b for various values of r_a. Note that these two are interchangeable, but the ratio alone does not determine the fidelity. For a polarization dependence of $\lesssim 5\%$, the error is $< 1\%$, but could still

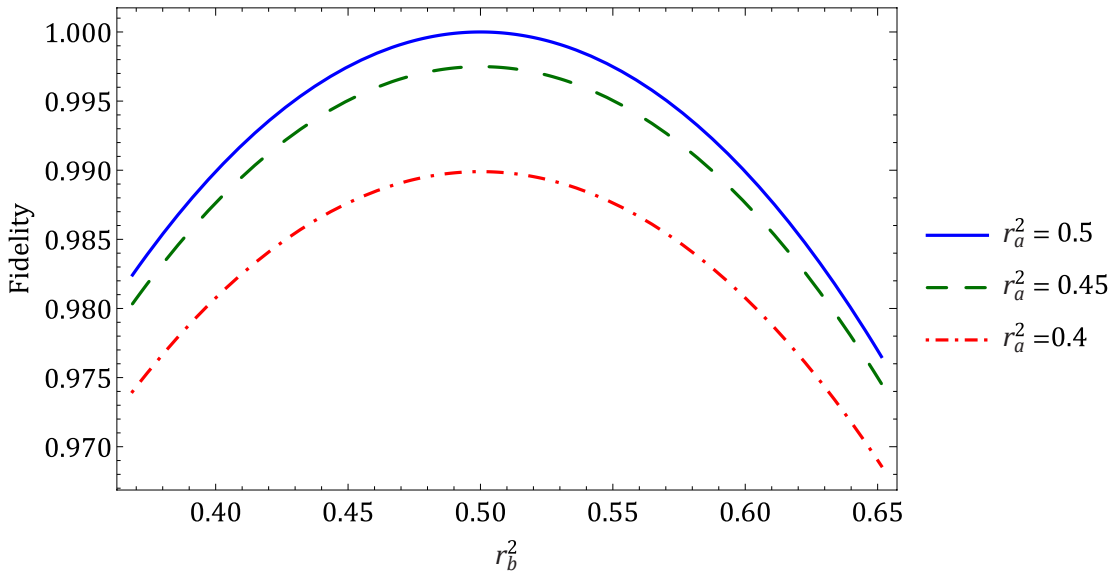

Figure 6.14: Plot of the fidelity of the final entangled state as a function of polarization dependence in the beam splitter. The horizontal axis is the fraction of vertically polarized light reflected. Curves for various values of the reflection coefficient for horizontally polarized light are plotted.

contribute somewhat to our final error budget.

If loss in the photon path is polarization-dependent it can actually impact the final state we obtain because of the relative prevalence of H and V polarized photons. There are six possible cases for polarization-dependent loss: (i) symmetric before the beam splitter, (ii) asymmetric before the beam splitter, (iii) symmetric after the beam splitter, (iv) asymmetric after the beam splitter, (v) symmetric in the beam splitter, and (vi) asymmetric in the beam splitter. By symmetric and asymmetric, we mean that either the loss is the same in all possible paths, or the loss is different in the different paths.

For fiber losses, we define a transmission coefficient $\frac{1}{\alpha_i}$ for one of the polarizations on the i^{th} path. Of course, both polarizations will have some loss, but any common loss can be factored out. For cases (i), (iii), and (iv), we find that there is

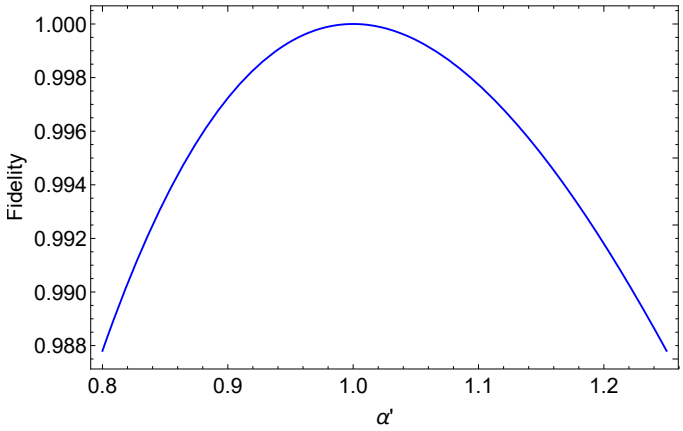

Figure 6.15: Fidelity loss due to polarization-dependent loss before the beam splitter. Fidelity is plotted versus the ratio of loss in the two input paths.

no effect on our resulting fidelity. We will consider the other cases in more detail. For case (ii), the state at the beam splitter is:

$$|\psi\rangle = \left(|0H\rangle_1 + \frac{1}{\alpha_1}|1V\rangle_1\right) \otimes \left(|0H\rangle_2 + \frac{1}{\alpha_2}|1V\rangle_2\right) \tag{6.28}$$

where the states $|0\rangle$ and $|1\rangle$ correspond to the ion states and the index 1 (2) indicates the ion from Alice or Bob respectively and correspondingly, the photon at port 1 or 2 of the beam splitter. Also, for now, we ignore normalization and renormalize at the end, which is acceptable because of the heralding. After applying the beam splitter operators defined in Sec. 6.3.1 and ignoring the terms that will only result in photons impinging on the same detector, we obtain the state:

$$\begin{aligned}|\psi'\rangle = \Bigg[&\frac{1}{\alpha_2}|01\rangle\left(|(HV)_3 0_4\rangle - |H_3V_4\rangle + |V_3H_4\rangle - |0_3(HV)_4\rangle\right) \\ &+\frac{1}{\alpha_1}|10\rangle\left(|(HV)_3 0_4\rangle - |V_3H_4\rangle + |H_3V_4\rangle - |0_3(HV)_4\rangle\right)\Bigg].\end{aligned} \tag{6.29}$$

We can break this state down into the four possible heralding coincidences:

(1) APD 1 and APD 2, (2) APD 3 and APD 4, (3) APD 1 and APD 3, and (4) APD 2 and APD 4, where APD 1 and APD 2 are after port 3 of the beam splitter and APD 3 and APD 4 are after port 4 of the beam splitter. We then end up with the following ion states for each detection case (indices on ψ indicate the corresponding coincidence case):

$$\begin{aligned} \left|\psi_{(1,2)}\right\rangle &= \frac{\alpha_1\alpha_2}{\sqrt{\alpha_1^2+\alpha_2^2}}\left(\frac{1}{\alpha_2}\left|01\right\rangle + \frac{1}{\alpha_1}\left|10\right\rangle\right) \\ \left|\psi_{(3,4)}\right\rangle &= \frac{\alpha_1\alpha_2}{\sqrt{\alpha_1^2+\alpha_2^2}}\left(\frac{1}{\alpha_2}\left|01\right\rangle - \frac{1}{\alpha_1}\left|10\right\rangle\right) \end{aligned} \tag{6.30}$$

The fidelity of both of these states to the corresponding Bell states $|\Psi^+\rangle$ and $|\Psi^-\rangle$ in terms of the ratio $\alpha' \equiv \frac{\alpha_1}{\alpha_2}$ is:

$$F = \left|\left\langle \Psi^{\pm}\right| \psi_{(1,2,3,4)}\right\rangle\Big|^2 = \frac{1}{2\left(1+\alpha'^2\right)}\left(1+\alpha'\right)^2 \tag{6.31}$$

We plot the fidelity as a function of α' in Fig. 6.15. From this plot we see that the dependence is very gradual, and the asymmetry must be quite large in order to impact the fidelity at even the 10^{-2} level. It is difficult to characterize the polarization-dependent loss, because it may change due to varying birefringence on the fiber, and the resulting different polarizations at different fiber locations. However, preliminary measurements indicate that this effect is minimal. Note that these results will also apply to diiffering numbers of H and V photons from each ion. If the discrepancy is the same from each trap, it will not affect the fidelity. On the other hand, if the ratio of H photons to V photons differs in Alice and Bob, perhaps

due to misalignment of the lens to the magnetic field for example, the fidelity will decrease.

Now, we turn to cases (v) and (vi). For these situations, rather than modifying the transmission, we adjust the beam splitter operator. First, we consider the symmetric case. The operation on $|H\rangle$ is still the same, but for $|V\rangle$, the operator now is

$$\begin{pmatrix} b_3^\dagger \\ \\ b_4^\dagger \end{pmatrix} = \frac{\alpha}{\sqrt{2}} \begin{pmatrix} 1 & 1 \\ \\ 1 & -1 \end{pmatrix} \begin{pmatrix} b_1^\dagger \\ \\ b_2^\dagger \end{pmatrix} \tag{6.32}$$

with $\alpha > 1$. When we write out the resulting algebra, we find that the final state will be unaffected up to a normalization constant, which is then removed due to the heralding anyway.

For the asymmetric beam splitter case, we allow the coefficients for each of the four possible paths for vertically polarized light to differ

$$\begin{pmatrix} b_3^\dagger \\ \\ b_4^\dagger \end{pmatrix} = \frac{1}{\sqrt{2}} \begin{pmatrix} \alpha_{13} & \alpha_{23} \\ \\ \alpha_{14} & -\alpha_{24} \end{pmatrix} \begin{pmatrix} b_1^\dagger \\ \\ b_2^\dagger \end{pmatrix}. \tag{6.33}$$

Note that this operator is explicitly not unitary. For the sake of simplicity, we assume the beam splitter is a perfect 50:50 lossless beam splitter for horizontally polarized light, but calculations similar to the previous ones could account for this effect as well. We then use this operator as well as the standard beam splitter operator to find the final state. We list the ion states for the four possible heralding

coincidences

$$\begin{aligned}
\left|\psi_{(1)}\right\rangle &= \frac{1}{\sqrt{\alpha_{14}^2+\alpha_{24}^2}}\left(\alpha_{14}\left|01\right\rangle+\alpha_{24}\left|10\right\rangle\right)\\
\left|\psi_{(2)}\right\rangle &= \frac{1}{\sqrt{\alpha_{13}^2+\alpha_{23}^2}}\left(\alpha_{13}\left|01\right\rangle+\alpha_{23}\left|10\right\rangle\right)\\
\left|\psi_{(3)}\right\rangle &= \frac{1}{\sqrt{\alpha_{13}^2+\alpha_{23}^2}}\left(\alpha_{13}\left|01\right\rangle-\alpha_{23}\left|10\right\rangle\right)\\
\left|\psi_{(4)}\right\rangle &= \frac{1}{\sqrt{\alpha_{14}^2+\alpha_{24}^2}}\left(\alpha_{14}\left|01\right\rangle-\alpha_{24}\left|10\right\rangle\right).
\end{aligned} \tag{6.34}$$

For all of these, the fidelity compared to the appropriate Bell state is

$$F = \frac{1}{2\left(1+\alpha'^2\right)}\left(1+\alpha'\right)^2 \tag{6.35}$$

where α' depends on which coincidence is detected:

$$\begin{aligned}
\alpha'_{(1)} &= \frac{\alpha_{14}}{\alpha_{24}}\\
\alpha'_{(2)} &= \frac{\alpha_{13}}{\alpha_{23}}\\
\alpha'_{(3)} &= \frac{\alpha_{23}}{\alpha_{13}}\\
\alpha'_{(4)} &= \frac{\alpha_{24}}{\alpha_{14}}.
\end{aligned} \tag{6.36}$$

This is the same functional form as the result for asymmetric polarization-dependent loss in the input fibers, so we can see from the same plot (Fig. 6.15) how the fidelity will decrease as a function of the ratio α', although the resulting number will be different depending on the path of the photon.

The polarization-dependent loss can be characterized to some extent using polarized classical light. It is difficult, however, to determine the contributions of losses in different parts of the fiber. However, assuming as a worst-case scenario that all polarization-dependent loss is in the inputs or in the beam splitter itself, we can still bound the fidelity loss to $\lesssim 1\%$.

Chapter 7: Optics Considerations for Fiber Coupling Ion Light

One of the main limitations for the rate with which we can generate remote entanglement is how much light is lost trying to couple photons emitted from an ion into a fiber. This efficiency is determined by how well the spatial mode of the collected ion light is matched to the spatial mode of the single mode fiber. Here, we explore in depth what affects this mode matching and how we can experimentally improve it.

7.1 Theoretical Calculations of Fiber Coupling Efficiencies

We can approximate the spatial mode of a single mode fiber as a Gaussian beam with an ideal, normalized electric field [156]

$$E_0(r) = \sqrt{\frac{2}{\pi w_0^2}} e^{-r^2/w_0^2} \tag{7.1}$$

where w_0, the beam waist, is equivalent to half the mode field diameter of the fiber. The mode field diameter can be easily measured in the lab and is also often provided by the manufacturer.

The condition of coupling light into a single mode fiber can then be expressed

as an overlap integral between the ideal fiber mode (Eq. 7.1) and the mode of the input light

$$\epsilon = \frac{\left|\int E_i^*(r,\theta)E_0(r)dA\right|^2}{\int |E_i(r,\theta)|^2 dA \int |E_0(r)|^2 dA} \tag{7.2}$$

where $E_i(r,\theta)$ is the field of the input light. We have assumed here that the fiber is in fact at the focus of the input light so there is no dependence on z, the direction of propagation. The denominator is simply a normalization factor and does not include an integral over E_0 since, by definition, E_0 is already normalized.

This integral will allow us to account for multiple effects that can decrease our coupling efficiency: the effect of differences in beam waist between the input beam and the ideal fiber mode and misalignment of the imaging system that can introduce aberrations.

7.1.1 Waist Measurement and Mismatch

Even if an imaging system is perfectly aligned, if the beam waist at the fiber and the mode field diameter of the fiber do not correspond, light will not be able to be coupled as efficiently. We therefore must use a lens designed to match this parameter.

To measure the mode field diameter of the fiber, we note that for a Gaussian beam, the angle of divergence far from the waist will uniquely determine the waist at the focus. The full equation for the intensity of a Gaussian beam at any location is given by [157]

$$I(r,z) = I_0 \left(\frac{w_0}{w(z)}\right)^2 e^{-\frac{2r^2}{w(z)^2}} \tag{7.3}$$

where I_0 is the peak intensity at $z = 0$ and

$$w(z) = w_0\sqrt{1 + \left(\frac{z}{z_R}\right)^2}. \tag{7.4}$$

In these equations we have introduced the parameter z_R, which is called the Rayleigh range, and is defined as

$$z_R = \frac{\pi w_0^2}{\lambda}. \tag{7.5}$$

For $z \gg z_R$, the beam waist will diverge approximately linearly as can be seen from Eq. 7.4. For the output beam of a fiber, the angle of this divergence determines the effective NA of the fiber. By taking images of a beam coming out of the fiber and fitting them to a Gaussian intensity profile, we can extract the waist at the location of the camera. When we take several of these images at multiple locations and measure the distance between the locations, we can obtain a divergence angle as long as the location is far from the fiber on the scale of its Rayleigh range. For a typical fiber with a mode field diameter of about 2 μm, the Rayleigh range is only of order 10 μm, so any measurement will satisfy this criterion. For the first in-fiber beam splitter that we used, we measured an average NA of 0.0925 (the input ports differ slightly). We have not yet measured our newer in-fiber beam splitters; however, we performed this measurement on several different fibers and obtained similar results.

We can calculate how much a deviation in the NA of the input beam from the NA of the fiber will degrade the coupling both in the case of an ideal beam and for

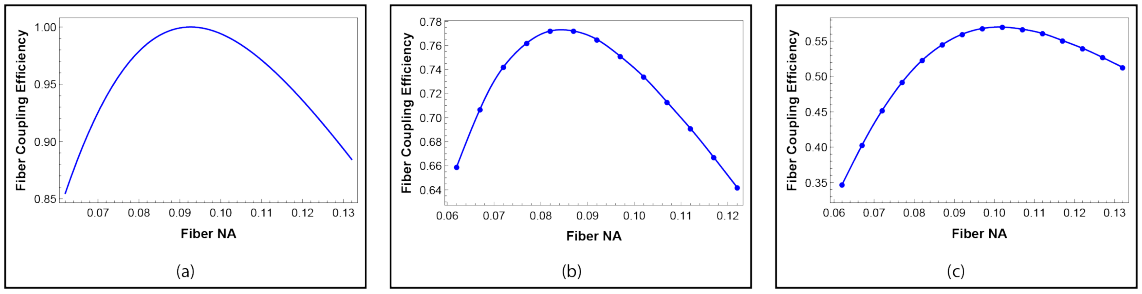

Figure 7.1: Plots showing the dependence of fiber coupling efficiency on the NA of the fiber. For (b) and (c) the curves are interpolated between points. (a) Fiber coupling efficiency vs. fiber NA for an ideal Gaussian beam. When the NA of the Gaussian beam equals the NA of the fiber, the coupling efficiency is 1. The NA of the input beam is set to 0.0925 to match the measured NA of the first in-fiber beam splitter we used, and the NA of the fiber is scanned to account for possible discrepancies in newer fibers. (b) Fiber coupling efficiency vs. fiber NA for the Photon Gear lens used for fiber coupling light from our first two traps (see Sec. 5.1.3). The lens is nominally designed to match the NA of our fiber, but the computations show the peak coupling is actually at a slightly lower NA. The maximum efficiency is lower because the lens does not produce an ideal beam even when optimally aligned. (c) Coupling efficiency vs. fiber NA for the system of aspheric lenses used in our third trap (Sec. 5.2.1.1). The NA for peak coupling corresponds very closely to the measured NA of our fiber and sharply falls off for lower NAs while more gradually decreasing for higher NAs. The maximum efficiency is again lower because of the deviation from the ideal fiber mode.

our specific lens. For an ideal beam, we use the overlap integral defined in Eq. 7.2. There is a direct correspondence between the waist at $z = 0$ of a Gaussian beam and the NA of the beam in the far-field, so we calculate what the waist would be at $z = 0$ as a function of NA. Specifically, the angle will be equal to the large z limit of the derivative of $w(z)$

$$\theta \equiv \arcsin(\mathrm{NA}) = \frac{dw}{dz} \approx \frac{\lambda}{\pi w_0}\,. \tag{7.6}$$

We can then solve for w_0 in terms of the NA, and substitute that into the equation for a Gaussian beam electric field (Eq. 7.1) for both the fiber and the

input beam to compute the efficiency integral (Eq. 7.2). In this case, the electric field of the input beam also has the form of an ideal Gaussian, but the waist may differ. Evaluating the efficiency integral for an angle of divergence of the input beam θ_i and for the fiber θ_f gives the analytical expression for the efficiency:

$$\epsilon = \frac{4\theta_i^2\theta_f^2}{\left(\theta_i^2 + \theta_f^2\right)^2}, \tag{7.7}$$

which, as expected, equals 1 when $\theta_i = \theta_f$. This function is plotted in Fig. 7.1(a). The function is asymmetric about the peak because the ideal divergence angle is nonzero. Over even fairly large variations in NA, the loss in efficiency is $< 15\%$.

This calculation, however, does not account for the deviations from an ideal Gaussian beam that our imaging systems inherently introduce. The computations accounting for the effects of the lenses are significantly more complicated, so we rely on Zemax OpticStudio to perform these calculations. After the lens data is entered and the system is optimized, we can compute the predicted single mode fiber coupling. This information is found in the "Analyze" tab under "Fiber Coupling" $\rightarrow$ "Single Mode Coupling." In "Settings," we then set "Sampling" to 128×128 and select "Ignore Source Fiber" and "Use Huygens Integral." "Ignore Source Fiber" ensures that the input is defined externally to the fiber coupling computation, since we will have already set up the input separately. "Use Huygens Integral" sets the computation to be performed using the Huygens wavelets method (see [158] for example), which accounts for diffraction. If this is not checked, diffraction will not be accounted for and the fiber coupling efficiency may be inaccurate. The sampling

is a tradeoff between speed and accuracy; typically the result does not change much with samplings higher than 128×128. The computation, however, does become frustratingly slow. Finally, the NA of the receiving fiber must be set to that of the fiber in the lab.

Once all of the settings are correct, it is straightforward to read off the coupling efficiency. In the "Single-Mode Fiber Coupling" window, three efficiencies are listed–"System Efficiency," "Receiver Efficiency," and "Coupling Efficiency." "System Efficiency" accounts for loss in the imaging system before the fiber and will typically be equal to 1. "Receiver Efficiency" is the efficiency solely of the fiber coupling, and then "Coupling Efficiency" computes the total loss. If "System Efficiency" equals 1, "Coupling Efficiency" and "Receiver Efficiency" will give the same result, which is the number we use as our theoretical fiber coupling efficiency.

The results for both the lens used on our first two traps and the aspheres used on our third trap are shown in Fig. 7.1(b) and (c). These lenses have significantly different dependences on NA. For the Photon Gear lens performance shown in Fig. 7.1(b), the coupling falls off more quickly for higher numerical apertures. This is not ideal because the specified range of the fibers we use has a measured NA on the lower end of the range, so for future fibers, this may be more of an issue. However, as discussed in Sec. 5.2.1.1, the maximum fiber coupling efficiency for the aspheric lens system is lower to begin with. As long as the NA of the fiber is not significantly lower than the design NA we do not expect much of a decrease in the fiber coupling efficiency in this system.

If there is a significant mismatch between the NA of the fiber and the design

NA of the lens, we can compensate using additional lenses. By collimating the light from the ion after the first image plane and reimaging with a lens of a different focal length, we can adjust the NA to better match the fiber and recover at least some of the loss in efficiency. However, the introduction of additional lenses also always poses the risk of additional aberrations, so the improvement in performance may be limited. We have tried this compensation previously with objectives not discussed in this thesis and where the deviation from the fiber NA was unknown and have seen improvements of only $\sim 2\%$ in coupling efficiencies.

7.2 Experimental Characterization of Beam Aberrations

When an ion is first observed with an imaging system, the alignment of the lens to the ion will typically be incorrect. While this misalignment will in general not completely prevent observation of the ion, it will certainly decrease the fiber coupling efficiency. In this section, we discuss various facets of our approach to optimizing this alignment.

7.2.1 Defocus

When the ion-lens distance in a setup differs from the design distance, the resulting waist at the image plane will be too large, and the fiber coupling efficiency will decrease as a result. We measure the beam waist by placing a camera in the image plane, ensuring that it is indeed at the focus by minimizing the spot size on the camera. Then, we take several images and add them together in post-processing.

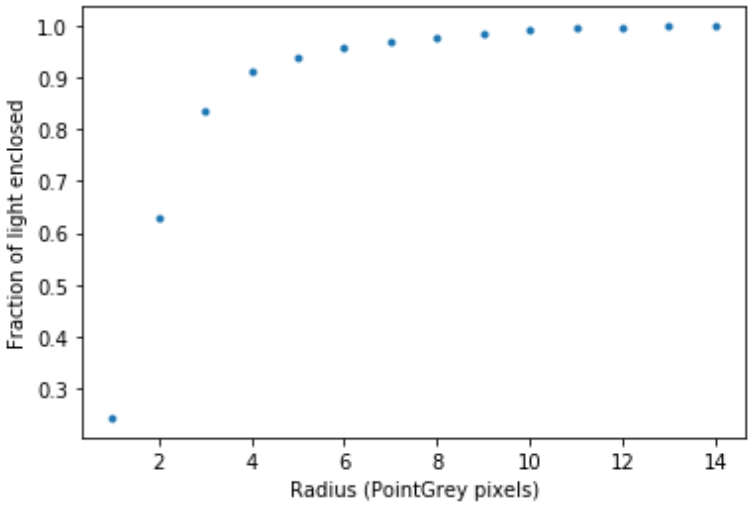

Figure 7.2: Plot of the fraction of light enclosed vs. radius in pixels (2.2 μm$\times$2.2 μm size) for a well aligned lens.

We subtract the background by taking an image while blocking the 650 nm light and subtracting this image from the images we are analyzing. We crop the image close to the ion, while ensuring all ion light is still included and find the total light in the image by summing over all pixels. Finally, we compute the fraction of light in a circle of various pixel sizes around the image centroid and plot the results (see Fig. 7.2). The camera[1] we use for this measurement has a pixel size of 2.2 μm $\times$ 2.2 μm, and we expect $> 90\%$ of the light to be within 5 pixels when the lens is well aligned for the Photon Gear lens used for Alice and Bob (Sec. 5.1.3).

7.2.1.1 Defocus in Alice and Bob

The rods in Alice and Bob are too closely spaced to allow the full NA of the imaging objective in one direction. While this is unfortunate in terms of our remote entanglement generation rate, it does provide useful information for the alignment

[1]FLIR BFLY-PGE-50A2M-C

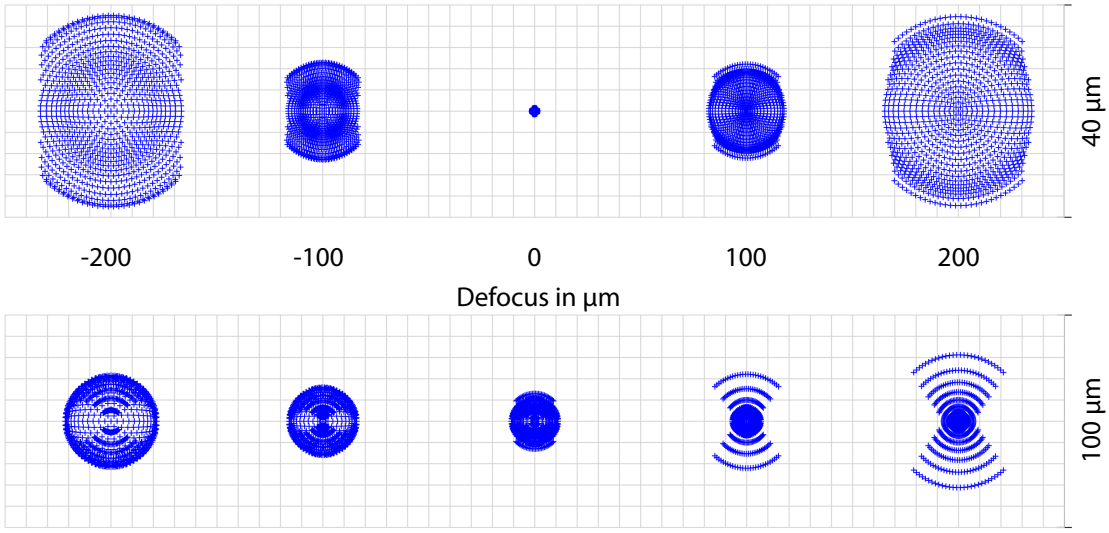

Figure 7.3: Spot diagrams showing the effect of the rod clipping on the light from the ion. In each row, the spot diagram is shown at a different distance from the image plane (-200 μm to +200 μm in 100 μm increments). The top row shows the spot diagrams when the ion-lens distance is correct; the bottom is when the lens is 50 μm too far from the ion.

of our lens in the focus direction. In particular, the rectangular aperture creates a characteristic shape that varies depending on if the lens is at its ideal location or whether it is too close or too far. In Fig 7.3, we show the spot diagram when a ray trace is performed including the rectangular aperture representing the rods. When the lens is too far from the ion, as the camera is moved from the image plane, we expect to see more dramatically differing shapes on each side of the focus. In particular, when the camera is also too far from the lens, the middle of the ion image will be very narrow, while the lower and upper portions will be much wider, somewhat like a bow tie shape. When the camera is too close to the lens on the other hand, we expect to see a ring with two dark spots with a bright spot in the middle. Fig. 7.4 shows actual ion images with these patterns.

When the lens is too close to the ion, the sides of the image plane on which

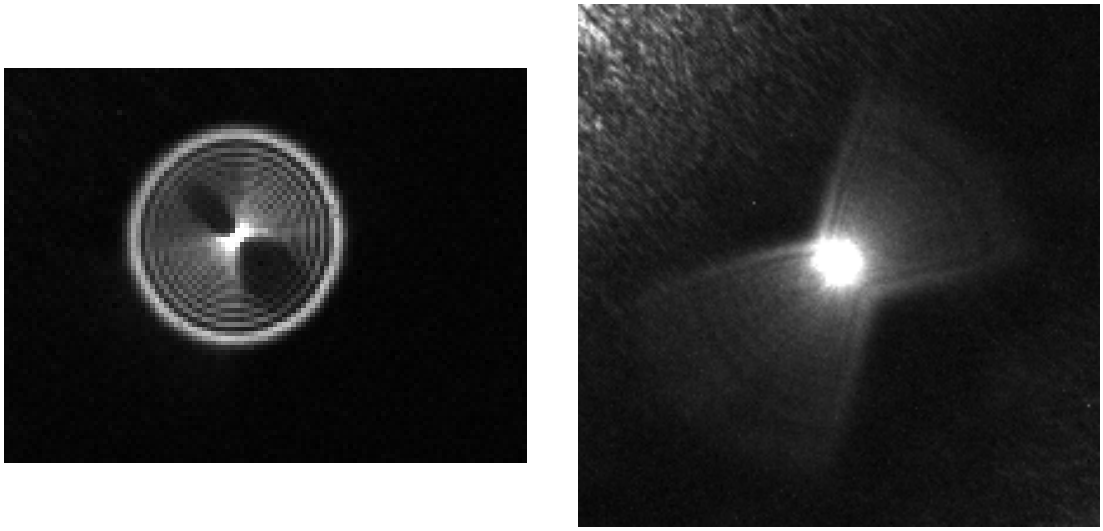

Figure 7.4: Ion images showing effect of rectangular aperture. The image on the left shows the pattern with an exterior bright ring, central bright spot, and dark spots on the sides. The image on the right shows the bow tie shape on the other side of the focus.

these patterns appear is reversed. In this case, the bow tie shape appears when the camera is too close to the lens while the opposite pattern appears when the camera is too far. This reversal allows us not only to determine when the lens is the wrong distance from the ion, but also in which direction we need to move it. We can therefore typically find the correct focus much more quickly than we would be able to otherwise.

7.2.2 Zernike Polynomials for Describing Aberrations

Other aberrations are not quite as simple to characterize, and, especially when multiple aberrations are present, it can be difficult to determine what the contributing issues are. The two other primary aberrations we deal with are coma and astigmatism, since they arise directly from misalignment of the lens. We can in

general qualitatively distinguish astigmatism and coma to some extent by looking at how many axes of symmetry there are in the image. First order astigmatism will generally have reflective symmetry about two axes while coma will only have one such axis. However, it can be useful at times to obtain a more quantitative description.

It is convenient to be able to mathematically represent the aberrations using a set of orthonormal polynomials. A common choice is the Zernike polynomials, which are orthonormal when the domain is limited to a unit circle [159]. There are limitations to their use, however, and in particular, they cannot reproduce the result of manufacturing errors from diamond polishing with linear combinations to a reasonable order [159]. This process is relevant to our work because it is often used for fabricating aspheric lenses. Nevertheless, the Zernike polynomials can be useful for describing the aberrations resulting from misalignment of a lens.

The Zernike polynomials are defined in terms of a radial and angular part as [160]

$$Z_n^m(\rho,\theta) = \begin{cases} N_n^m R_n^{|m|}(\rho)\cos(m\theta), & m \geq 0 \\ N_n^m R_n^{|m|}(\rho)\sin(m\theta), & m < 0 \end{cases} \tag{7.8}$$

where

$$\begin{aligned} N_n^m &= \sqrt{\frac{2(n+1)}{1+\delta_{m0}}} \\ R_n^{|m|} &= \sum_{j=0}^{(n-|m|)/2} \frac{(-1)^j (n-j)!}{j!\left(\frac{n+|m|}{2}-j\right)!\left(\frac{n-|m|}{2}-j\right)!}\rho^{n-2j} \end{aligned} \tag{7.9}$$

for integer n and with $m = -n, -n+2, \ldots, n-2, n$ and $0 \leq \rho \leq 1$. Here, we have scaled ρ to be in the unit circle by dividing by the exit pupil diameter.

7.2.2.1 Analysis of Images of Ion Light Intensity

We can then fit images of the atoms to determine in part their aberrations. We use a similar method to [161] and note that the intensity image can be described by a point spread function (PSF)

$$\mathrm{PSF}(\rho, \theta) = \left| \mathscr{F} \left[A \exp\left(-\frac{r^2}{w_0^2} \right) \exp\left(-ik \sum_{m,n} c_n^m Z_n^m(\rho, \theta) \right) \right] \right|^2 . \tag{7.10}$$

This equation differs slightly from that in [161] because of the inclusion of a Gaussian envelope, which we found slightly improves the fit results. The actual fitting is performed using the SciPy function `optimize.curve_fit` and returns an amplitude, exit pupil diameter, Gaussian waist, and the set of c_n^m for however many polynomials we choose to fit.

This procedure is not well suited, however, to fitting the images of ions that have passed through a rectangular aperture. If we know the lens data, we can calculate an approximate result using ray tracing. Ignoring the effects of diffraction, we trace the rays through the whole system then numerically perform an inverse fast Fourier transform. It is important to note that, given the high NA of our system, the paraxial (small angle) approximation is not valid and the tracing must be performed exactly. The result of this calculation then becomes a multiplicative factor in the PSF. We do lose phase information in this calculation; however, we

have verified that this computation results in much better fits than without the ray tracing. The major difficulty with this protocol is that it requires knowing all of the lens surfaces in the imaging system. At the time we initially implemented it, we did have all of this information. However, for the new Photon Gear lens, we were only provided with a black box file and therefore can no longer use this technique as is. Additionally, the technique of analytically performing a ray trace through a high numerical aperture asphere is infeasible because it requires inverting polynomials of degree > 10. However, all that would be required to obtain fits for images with the newer lenses would be figuring out a way to export the calculated PSF from Zemax. In practice, recently, we have been able to rely on the qualitative visual assessment, which also is much faster when the aberrations are sufficiently simple.

Based on the aberrations we see, we can use this information to adjust the alignment of the lens. In general, astigmatism arises from the ion being off-center on the lens (translation) or mounting of the lens that breaks its cylindrical symmetry. Coma is a bit more complicated, as it can be a result of either a translation misalignment or tilt misalignment.

When coma is visible without astigmatism, we typically start by adjusting the tilt of the lens. The mount often will introduce translation when the tilt is adjusted, which needs to be compensated afterwards. If the tilt does not improve the aberrations, we turn to adjusting translation instead. This process of course requires significant iteration, but typically eventually converges on an image that is nearly aberration-free. We also check the aberrations with the image defocused, as aberrations are often not visible at the image plane, but will show up at other

locations.

7.2.2.2 Use of a Shack-Hartmann Wavefront Sensor

The intensity image analysis discussed in the previous section is easy to use but necessarily gives incomplete information because the PSF takes the magnitude squared of the function. A method for obtaining complementary information is using a Shack-Hartmann wavefront sensor, which provides a measurement of the phase of the wavefront [162].

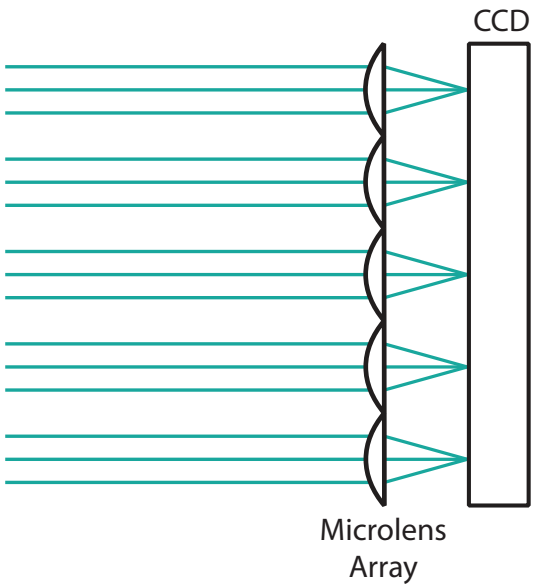

Figure 7.5: Cross section of a Shack-Hartmann wavefront sensor. Collimated light hits an array of small lenses (microlens or lenslet array) and is focused in multiple spots onto a detector. We use a CCD camera for this purpose in our setup.

This wavefront sensor consists of a microlens array followed by a detector with spatial resolution. In our setup, we use a CCD. If the light is collimated going into the lenslet array, a spot of light will be observed at the locations on the CCD corresponding to the center of each lens. If, however, the light entering one of the

lenses is tilted, there will be a resulting displacement on the camera. While this tilt may result from the entire beam entering at an angle, if the beam is aberrated, different parts of the beam will have different tilts. We can use this information to determine the aberrations.

We define the location of the spot corresponding to the i^{th} lenslet for an ideal beam as (x_{0_i}, y_{0_i}). The electric field of the incoming beam can be written as

$$E(x, y, z) = |E(x, y, z)| \, e^{i\phi(x,y,z)}. \tag{7.11}$$

Then, a displacement on the camera in x (or y) indicates the following [162]

$$\frac{\delta x_i}{f} = \frac{x_i - x_{0_i}}{f} = \frac{\partial \phi}{\partial x} \tag{7.12}$$

where f is the focal length of the lenses in the microlens array. We can also write an equivalent expression for y.

We can also write ϕ in terms of the Zernike polynomials

$$\phi(x, y)|_{z=z_0} = \sum_{n,m}^{M} c_n^m Z_n^m(x, y) = \sum_j c_j Z_j(x, y) \tag{7.13}$$

where z_0 is the plane of the microlens array and we have written the Zernike polynomials in terms of Cartesian coordinates and with a single index that accounts for both n and m. Then, the displacements of the spots on the camera can be written

in terms of the Zernike polynomials:

$$\frac{\delta x_{i,j}\left(x_i, y_j\right)}{f} = \frac{\partial}{\partial x} \sum_{n,m} c_n^m Z_n^m(x,y) \Bigg|_{x=x_i, y=y_j} \tag{7.14}$$

where (x_i, y_j) are the coordinates of the center of the pixel in the i^{th} column and j^{th} row.

The displacements in x and y for each spot can be written as a vector, and the derivatives of the Zernike polynomials at each location can be written as a matrix. We can then obtain a matrix equation relating the aberrations to the measured displacements

$$\frac{1}{f}\begin{pmatrix} \delta x_{0,0} \\ \delta x_{0,1} \\ \vdots \\ \delta x_{N,N} \\ \delta y_{0,0} \\ \delta y_{0,1} \\ \vdots \\ \delta y_{N,N} \end{pmatrix} = \begin{pmatrix} \partial_x Z_0\left(x_0, y_0\right) & \partial_x Z_1\left(x_0, y_0\right) & \dots & Z_M\left(x_0, y_0\right) \\ \partial_x Z_0\left(x_0, y_1\right) & \partial_x Z_1\left(x_0, y_1\right) & \dots & \partial_x Z_M\left(x_0, y_1\right) \\ \vdots & \ddots & & \\ \partial_x Z_0\left(x_N, y_N\right) & \partial_x Z_1\left(x_N, y_N\right) & \dots & \partial_x Z_M\left(x_N, y_N\right) \\ \partial_y Z_0\left(x_0, y_0\right) & \partial_y Z_1\left(x_0, y_0\right) & \dots & \partial_y Z_M\left(x_0, y_0\right) \\ \partial_y Z_0\left(x_0, y_1\right) & \partial_y Z_1\left(x_0, y_1\right) & \dots & \partial_y Z_M\left(x_0, y_1\right) \\ \vdots & \ddots & & \\ \partial_y Z_0\left(x_N, y_N\right) & \partial_y Z_1\left(x_N, y_N\right) & \dots & \partial_y Z_M\left(x_N, y_N\right) \end{pmatrix} \begin{pmatrix} c_0 \\ c_1 \\ \vdots \\ c_M \end{pmatrix}. \tag{7.15}$$

This system of equations can then be solved for the coefficients c_i using a least-squares fit. From this fit, we can determine the aberrations in our phase.

There are, however, several practical disadvantages to this method of determining aberrations. The first challenge is obtaining a reference image to which we

can compare to find the displacements. We can achieve this to some extent, however, in software if we know the lens spacing by making a grid of evenly spaced points and then aligning that with the actual image. This method would make it so we cannot determine tilt, but since tilt in general will not affect our fiber coupling this is a nonissue. The bigger challenge is the fact that in order to use a wavefront sensor, the light must be spread out over a large area–our microlens array, for example, is 10 mm×10 mm. Even if we only use a portion of this area, spreading the light collected from an ion over even 5 mm will result in a very dim signal on the camera. However, this method can be used for characterizing aberrations in test setups where the source light is much brighter than that from an ion.

7.3 Adding Optics for Improving Fiber Coupling

Previously, we discussed improving the alignment of the lens to minimize the aberrations. However, sometimes it is not possible to completely eliminate aberrations purely from alignment. We have considered several options for improving the image further.

As mentioned in Sec. 7.1.1, for example, we can reimage the light to improve the matching of the NA of the input light to the NA of the fiber. There are several other options for correcting other aberrations. One option, which was used in [161], is to add a cylindrical lens to correct astigmatism. A cylindrical lens will not correct astigmatism due to misalignment, but will correct astigmatism which results from asymmetry in the mounting system. For example, if the lens is mounted in such a

way that it is compressed in one direction, a cylindrical lens could fix the resulting astigmatism. We have tried compensating the small amount of residual astigmatism in our image with a cylindrical lens without success. The reason behind this may be that the astigmatism is in fact due to a small amount of residual misalignment or because the cylindrical lenses we tried had focal lengths that were too short and thus introduced more astigmatism than they compensated.

A more general option is the use of a deformable mirror. We use a piezoelectric based deformable mirror with 40 piezo actuators, plus tip and tilt controls.[2] The software that accompanies this mirror conveniently translates Zernike polynomial amplitude to an actuator displacement pattern, so we can directly compensate the aberrations that one of our analysis methods determine are present.

In order to integrate the mirror into our setup, we collimate the ion light before the mirror. The mirror works best at small angles of incidence, so we angle it only slightly from the normal to accommodate our optics. We then fiber coupled the light and attempted to adjust the mirror to improve the coupling efficiency. We attempted this both manually and with a gradient descent optimization algorithm. Neither method resulted in significant improvements in efficiency. For the optimization algorithm, part of the problem may be the hysteresis intrinsic in piezoelectric materials. We attempted to mitigate this effect by "relaxing" the mirror, which rapidly moved the actuators in all directions to minimize the directional dependence. We did this at each optimization step. However, each step then took several seconds, so the optimizer ran very slowly. Additionally, the fiber coupling naturally

[2]Thorlabs DMP40-P01

decays over time and the signal was noisy, so the feedback on the optimizer was not of a high quality. Another issue may be that the aberrations that are limiting our fiber coupling efficiencies are too high order to have been corrected with this mirror, which is only capable of applying up to fifth order Zernike polynomials.

Chapter 8: Outlook

In the previous chapters, we have discussed work leading up to the preliminary demonstration of a two-node Ba^+ network and the construction of a third, upgraded node. In addition to the obvious immediate steps of finishing the demonstration of the two node network and the testing of the third node, there are several other directions we can go with this and related systems in the medium to long term. We now turn to discussion of some future possible experiments and improvements. This chapter is by no means an attempt to explore all possible directions but contains some ideas we have considered over the course of this work.

8.1 Deterministic State Readout of Barium Ions

Our current detection scheme on Ba (Sec. 3.2.3.2) is probabilistic. So far, this scheme has not prevented us from obtaining results, and ultimately we hope to perform most readout on Yb^+ rather than Ba^+ anyway, so we have not put much effort into an improved detection protocol for Ba. However, it has become apparent that for certain experiments it would be useful to have the option of reliable and efficient state readout on barium. For example, in the three trap entanglement protocol (see Sec. 8.3), we can reduce the number of local entangling gates required

if we are able to measure the communication qubit rather than the memory qubit. Additionally, as we will discuss in Sec. 8.4, we may ultimately turn to a network with all barium ions using different isotopes. For this configuration, we would also need to be able to perform deterministic state readout on Ba.

We use the current detection scheme for $^{138}Ba^{+}$ because there is no frequency-resolved, electric dipole, cycling transition involving only one of the qubit states like there is for $^{171}Yb^{+}$ (Sec. 3.1.3). The fact that our qubit states are not frequency-resolved also forces us to rely on polarization purity. An alternative scheme that resolves both of these issues is shelving to the $5D_{5/2}$ state (see Fig. 3.7) using a narrow linewidth 1762 nm laser [163]. After transferring the population in one of the qubit levels, $|1\rangle$ for example, the Doppler cooling beams can be turned on and any resulting photons will indicate population in $|0\rangle$. Since the Doppler cooling beams together create a closed cycle, the lack of a detected photon definitively indicates the qubit was in $|1\rangle$.

The linewidth of the $S_{1/2} \leftrightarrow D_{5/2}$ transition is only 6.1 mHz, so driving it directly is possible but requires significant effort to reduce the linewidth of a laser. Additionally, the frequency and optical power must be well-stabilized to avoid fluctuations in the time it takes to fully transfer population from the $S_{1/2}$ manifold to the $D_{5/2}$ manifold. An alternative is adiabatic rapid passage [88, 163, 164], where the frequency of the laser is scanned from some detuning far from resonance on one side of the transition to a detuning far from resonance on the other side of the transition. The fidelity of this technique is determined by the ratio of the laser linewidth to the Rabi frequency with which the transition is driven and the sweep

rate across resonance [88]. Fidelities have been demonstrated of at least 98% using this technique, but results using the same technique in other ions have achieved fidelities of over 99% [165, 166]. For comparison, our current detection fidelities are 98-99% as well.

Implementing this shelving scheme in our lab, with either direct excitation or adiabatic rapid passage, will require the purchase of two new lasers and a high-finesse ultra-stable optical cavity. We of course require the 1762 nm laser, but we will also need a 614 nm laser to depopulate the $5D_{5/2}$ manifold when we have finished reading out the state. Currently, we occasionally have population decay to this manifold from off-resonant excitations during Raman operations but use an LED to repump to the levels involved in the cooling cycle. This setup is feasible because of the infrequency of populating the $D_{5/2}$ manifold, but a laser would be required if we needed to utilize this state every experimental cycle. The cavity is necessary for locking and narrowing the frequency of the laser. Delivering sufficient power to the ions in Alice and Bob may also be challenging because none of the vacuum windows are coated for a wavelength so far into the infrared, and we expect there will be large losses at the window ($\sim 30\%$). Cleo, however, was designed with the possibility of adding a 1762 nm laser, and therefore has one uncoated window that should cause losses of only a few percent.

8.2 Two-Trap Entanglement Experiments

The first step after demonstrating remote entanglement between two traps will be the reintroduction of the memory ($^{171}Yb^{+}$) qubits. While the work presented in this thesis has relied solely on $^{138}Ba^{+}$, the limitations imposed by the short coherence times of Zeeman qubits will pose more of an issue for performing quantum computations. While the coherence time of these qubits can be increased to seconds [167], this involves a considerable amount of work and experimental complexity. Hyperfine qubits, on the other hand, can have coherence times of order 1 s without much effort and can be improved up to thousands of seconds [14].

After we establish the remote entanglement discussed in Chapter 6, we can swap the entanglement to neighboring memory qubits using local XX gates, as discussed in [48, 49]. The previous demonstrations of these interspecies gates had very low fidelities due to extremely high heating rates in the trap in which they were performed. Since then, we have replaced that trap with two new traps (Alice and Bob), which hopefully will have much less heating.

8.2.1 Entanglement Distillation

The state we generate via remote entanglement will likely have a fidelity of not more than $\sim 95\%$. If we wish to achieve higher fidelities, we can utilize the memory qubits to purify the fidelity using an entanglement distillation procedure along the lines of the one described in [168]. This procedure allows for the creation of a single, purified Bell state from multiple lower-fidelity pure states using only LOCC. There-

fore, we could generate remote entanglement once on the communication qubits, swap it to the memory qubits, and then regenerate remote entanglement on the communication qubits. We would then have two lower fidelity Bell states that we could use as a resource for entanglement distillation resulting in a single, higher-fidelity Bell state on the memory qubits. Entanglement distillation has previously been demonstrated on locally entangled trapped ions [169] and in a network with NV centers in diamonds [170]. The interspecies nature of our setup and the long coherence times of the memory qubits will ensure that there is minimal decoherence during the attempts at generating the second remotely entangled pair.

8.3 Protocols for Networks with More Than Two Traps

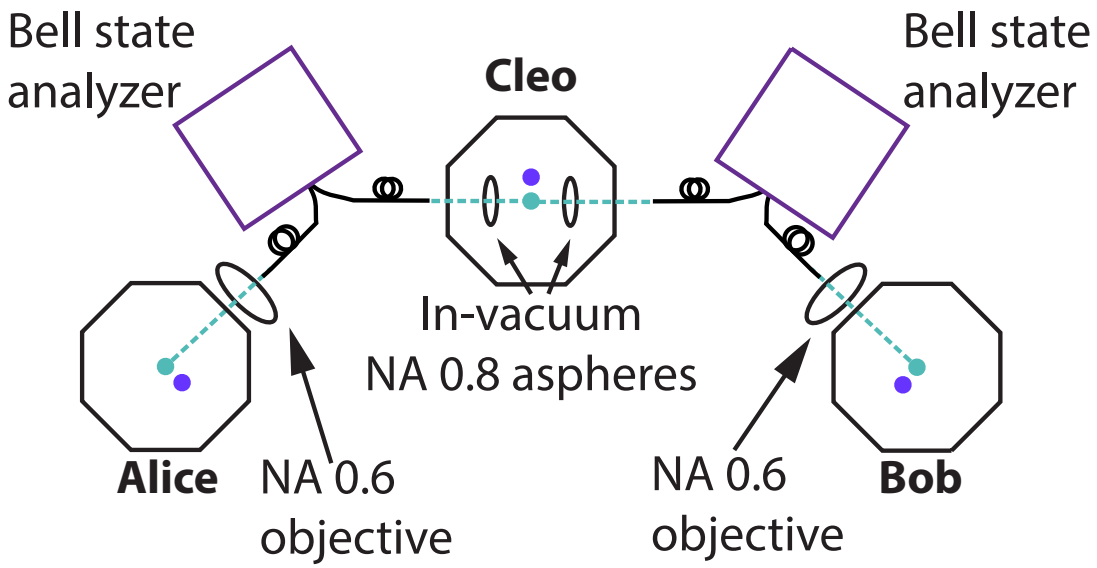

Figure 8.1: Schematic for a three trap network. One central trap with two high NA objectives (Cleo) is connected via photonic links with Alice and Bob separately. Yb ions are shown in purple and Ba in teal.

In this thesis, we have described nearly all of the necessary building blocks

for a three trap network with the exception of interspecies gates, which have been previously demonstrated. We have not yet discussed, however, our plans for linking them all together. The setup is shown in Fig. 8.1. Cleo serves as a central node with links to both Alice and Bob. A direct connection between Alice and Bob is not necessary for the protocol we will use. Between each trap, there is a Bell state analyzer with the same setup shown in Fig. 6.12. Each trap contains a single Ba ion and a single Yb ion. Not shown in the figure but present on each trap is a lens for collecting photons emitted from the Yb ion for state readout.

The specific application on which we focus here is the generation of a GHZ state. There are certainly other possible directions to explore with this system, but the generation of a GHZ state demonstrates that we can maximally entangle Yb ions in the three traps. These states can serve as a starting point for various quantum information applications and are a necessary fundamental building block for a quantum network with memory [171]. We first provide an overview of the steps required for generating such a state and then delve into the specifics of some of the steps. We also consider the rate with which we can generate a GHZ state and the required fidelities for each component of the protocol.

For convenience, we label the ions in each trap with the first letter of the trap name–for example Ba_A is the barium ion in Alice. After each step in the below protocol, we note the state of the ions, including only those that are entangled with another ion at that point in the procedure. The steps in the entanglement generation procedure are:

1. Generate remote entanglement of either $\mathrm{Ba_A}$ and $\mathrm{Ba_C}$ or $\mathrm{Ba_B}$ and $\mathrm{Ba_C}$ using the same procedure described in Sec. 6.3. To simplify the discussion, we assume $\mathrm{Ba_A}$ is the ion entangled with $\mathrm{Ba_C}$. If it is instead $\mathrm{Ba_B}$, the subsequent steps remain the same but with Alice and Bob switched. The resulting state is either $|\Psi^+\rangle$ or $|\Psi^-\rangle$. For the sake of simple discuss, we include a rotation to $|\Psi^+\rangle$ in this step if necessary. With the ordering of the ions $|\mathrm{Ba_A}\rangle\,|\mathrm{Ba_C}\rangle$, the state is then

$$|\psi_1\rangle = \frac{1}{\sqrt{2}}\left(|01\rangle + |10\rangle\right) \tag{8.1}$$

2. Upon successful entanglement generation between Alice and Cleo, perform a local SWAP operation in both Alice and Cleo. This step results in an entangled state between $\mathrm{Yb_A}$ and $\mathrm{Yb_C}$. The state is the same as that after the first step, but with the respective Yb ions instead of Ba.

3. Generate remote entanglement between $\mathrm{Ba_C}$ and $\mathrm{Ba_B}$. Again, we assume we end in $|\Psi^+\rangle$ and obtain the overall state (order $|\mathrm{Yb_A}\rangle\,|\mathrm{Yb_C}\rangle\,|\mathrm{Ba_B}\rangle\,|\mathrm{Ba_C}\rangle$)

$$|\psi_3\rangle = \frac{1}{2}\left(|01\rangle + |10\rangle\right) \otimes \left(|01\rangle + |10\rangle\right) \tag{8.2}$$

4. Perform a SWAP operation in Bob, which leaves $\mathrm{Ba_C}$ entangled with $\mathrm{Yb_B}$. The state is the same as after step 3 but with $\mathrm{Ba_B} \rightarrow \mathrm{Yb_B}$.

5. Perform a CNOT gate in Cleo with $\mathrm{Ba_C}$ as the control and $\mathrm{Yb_C}$ as the target.

With the ordering $|\mathrm{Yb_A}\rangle\,|\mathrm{Yb_B}\rangle\,|\mathrm{Yb_C}\rangle\,|\mathrm{Ba_C}\rangle$, the state becomes

$$|\psi_5\rangle = \frac{1}{2}(|0001\rangle + |0110\rangle + |1011\rangle + |1100\rangle) \tag{8.3}$$

6. Read out the state of $\mathrm{Yb_C}$. If $\mathrm{Yb_C}$ is in $|0\rangle$, perform a π rotation on $\mathrm{Ba_C}$. If $\mathrm{Yb_C}$ is in $|1\rangle$ perform a π rotation on $\mathrm{Yb_B}$. Either way, the resulting state will be the GHZ state (with the ion state ordering $|\mathrm{Yb_A}\rangle\,|\mathrm{Yb_B}\rangle\,|\mathrm{Ba_C}\rangle$):

$$|\psi_6\rangle = \frac{1}{\sqrt{2}}(|000\rangle + |111\rangle) \tag{8.4}$$

   The π rotations serve only to end up with the same GHZ state for the sake of convenience. Even without those, the state at the end of this step will be a maximally entangled tripartite state.

7. Finally, perform another SWAP operation in Cleo so $\mathrm{Ba_C}$ is no longer part of the entangled state and $\mathrm{Yb_C}$ is instead.

A SWAP gate can be performed by preparing one of the qubits, in our case Yb, in $|0\rangle$ and then performing two Mølmer-Sørensen (MS) gates with a phase difference of π between the two gates [105]. A CNOT gate can be broken down into a single MS gate and local operations [172]. Thus, overall, this procedure requires nine MS gates. This number can be reduced to seven if we are willing to perform the detection in step 6 on $\mathrm{Ba_C}$ instead of $\mathrm{Yb_C}$, perhaps using the shelving described in Sec. 8.1. In this case, the CNOT must be performed with Yb as the control, and there are a different set of π rotations depending on the result. The last SWAP

operation (step 7) is then unnecessary as we will be left with an entangled state of just the three Yb ions after step 6.

The fidelity requirements for this protocol are quite strict because of the overall number of operations. To generate the final state, we require two remote entanglement generations, up to three single-qubit Raman rotations, 2-3 state preparations of Yb, one state readout, and 7-9 MS gates. If we assume perfect state preparation and readout and local single-qubit operations and estimate a remote entanglement fidelity of 93% for both pairs of traps, a fidelity of 95% on the MS gates still gives us only a resulting fidelity of 0.55 for the nine MS gate version of the protocol, which is barely sufficient to verify the quantum nature of the state. With slightly imperfect SPAM and single qubit operations, this fidelity will be a few percent lower. This is also not accounting for any decoherence of the Ba qubit due to magnetic field fluctuations. We should be able to achieve coherence times of about 4 ms, so the sequences during which Ba is entangled with other qubits must be kept to less than $\sim$1 ms. All of these numbers are certainly achievable, and individual operations of each type with sufficiently high fidelities have been demonstrated, but it will require a fair amount of work to get to this point.

It is important to note, however, that the scaling of the rate of this protocol compared with our two trap protocol is quite favorable. In particular, for step 1, the rate will be twice as high as for the two trap network because entanglement can be heralded between either pair of traps. Step 3 will be the same rate as remote entanglement in the two trap network because it has to be between Cleo and whichever trap was not successfully entangled in step 1. If we just consider the

time for these two steps, the time for success will be:

$$T = \frac{1}{2R} + \frac{1}{R} = \frac{3}{2R}, \tag{8.5}$$

so the scaling in time taken is better than linear with the number of traps.

8.3.1 Four Trap Protocol

Although experimentally we have a fair amount of work before we can demonstrate a three node network, let alone four, we are interested in how our entanglement generation protocol would scale to more traps. The extension of the previous scheme to four traps is fairly straightforward and could be determined for five or more as well. For four traps, we still consider the case where the traps are arranged in a line. We let traps 1 and 4 be the end traps and 2 and 3 be the intermediate traps (1 is connected to 2, 2 is connected to 3, and 3 is connected to 4). For this protocol, we do not write out the state at every step but just provide an overview of the procedure and results and consider the final number of operations needed. We choose to present the variation of the protocol where we measure Ba since it has fewer operations and we will likely have implemented shelving by the time we have a four trap network.

The steps are as follows:

1. Generate remote entanglement between traps 1 and 2 and between traps 3 and 4 on Ba.

2. Perform SWAP operations on all traps, so the Yb ions in traps 1 and 2 are entangled, and those in traps 3 and 4 are entangled.

3. Generate remote entanglement between traps 2 and 3.

4. Perform CNOTs on traps 2 and 3 with the Yb as the control and Ba as the target in each trap.

5. Measure Ba_2 and Ba_3. There are four possible outcomes (the states of Ba_2 and Ba_3 respectively being $|00\rangle$, $|01\rangle$, $|10\rangle$, and $|11\rangle$. After these measurements, the possible states of the Yb ions ($|Yb_1Yb_2Yb_3Yb_4\rangle$) are:

$$|\psi_{00}\rangle = |\psi_{11}\rangle = \frac{1}{\sqrt{2}}(|0101\rangle + |1010\rangle)$$
$$|\psi_{01}\rangle = |\psi_{10}\rangle = \frac{1}{\sqrt{2}}(|0110\rangle + |1001\rangle) \tag{8.6}$$

   These states can obviously both be rotated to the GHZ state $\frac{1}{\sqrt{2}}(|0000\rangle + |1111\rangle)$ using only local, single-qubit operations if desired.

A similar sequence will also work if remote entanglement is heralded on traps 2 and 3 first.

The required resources for this procedure are three remote entanglement generations, up to 5 single-qubit rotations, 4 state preparations of Yb, 2 state readouts (barium), and 10 MS gates. For remote entanglement time, the overall rate is still proportional to p^2 as desired. Because the remote entanglement between traps 1 and 2 can be established in parallel with that in traps 3 and 4, on average, the time spent generating remote entanglement will in fact be the same as for the three trap

protocol. This statement has a slight caveat, since if remote entanglement is first generated between the middle traps, SWAP operations that are in parallel in the above steps must be split into two separate steps, so there will be a slight increase in the time spent in the slow loop. It is clear, however, that the scaling in fidelity will be more prohibitive than the scaling in time.

8.4 Other Ion Combinations for an Interspecies Quantum Network

8.4.1 Motivation for a Different Ion Combination

Currently, we utilize $^{171}Yb^{+}$ as our memory qubit and $^{138}Ba^{+}$ as our communication qubit. For swapping information from the communication qubit to the memory qubit, it is important to be able to perform high-fidelity local entangling operations via the motional modes of the ion trap. MS gates can be performed using either the transverse (radial) modes of the trap or the axial (longitudinal) modes, but the transverse modes are generally preferable. The advantage of the transverse modes is their lower heating due to the fact that RF Paul traps are typically operated with stronger confinement in the radial direction than in the axial direction.

Nonetheless, for ions of significantly different masses, including Yb and Ba, entangling gates have only been performed on the axial modes [49, 173, 174]. The reason for choosing this apparently disadvantageous method is the importance of the participation of each ion in the motional modes for the success of the gate [175, 176] and the fact that ions with different masses have dramatically different mode

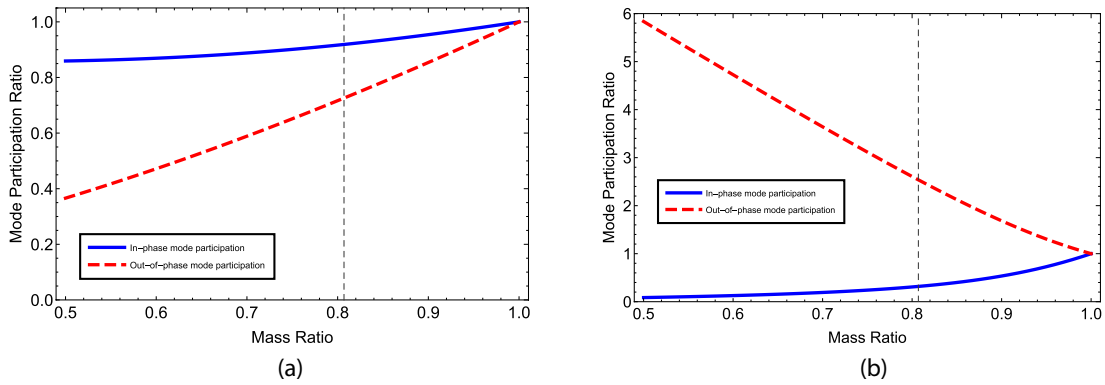

Figure 8.2: Plot of mode participation for different mass ratios $\alpha = m_2/m_1$ where m_2 is the lighter ion (Ba in our case). The ratio of the participation of the heavier ion to the lighter ion is plotted on the vertical axis, while the horizontal axis is the ratio of the lighter ion mass to the heavier ion mass. Both plots show the "in-phase" and "out-of-phase" modes where the ions move in the same and opposite directions respectively. The dashed vertical lines show the Ba-Yb mass ratio. (a) Axial mode participation ratios. (b) Transverse mode participation ratios. We assume a transverse mode frequency that is about 2.5 times higher than the axial frequency for a single ion as in [48].

participation especially in the radial modes [48]. The larger the mass discrepancy, the larger the discrepancy in participation, as shown in Fig. 8.2.

In [177], we examined this dependence for more than two ions and considered how gate fidelity would be affected. Longer chains will ultimately be an integral part of our modular quantum architecture, so it is important that our building blocks can be expanded. We found that the effect of the mass discrepancy on the radial modes becomes even more extreme for longer chains, eventually reaching the point where the motion of the Ba ion is nearly completely decoupled from the motion of the Yb ions, as shown in Fig. 8.3. In addition to the decoupling in the radial modes, as the chain increases in length the heating rate scales dramatically with the number of ions in the chain because the confinement must be loosened [21], further disincentivizing axial gates.

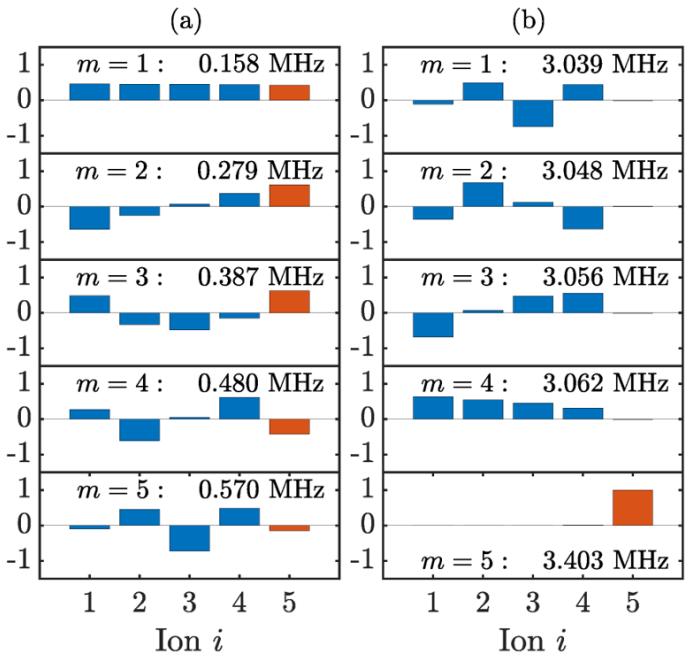

Figure 8.3: Mode participation in a five ion chain with 4 $^{171}Yb^{+}$ ions and 1 $^{138}Ba^{+}$ ion at the end of the chain. The eigenvector components for the Yb ions are shown in blue, and those for Ba are shown in red. The rows correspond to the five motional modes for one of the trap principle axes. (a) Axial mode participation. The participation of the Ba ion is fairly similar to that of the Yb ions. (b) Radial mode participation. The motion of the Ba ion is nearly completely decoupled from the motion of the Yb ions.

8.4.2 Use of $^{133}Ba^{+}$ as a Memory Qubit

We thus decided to consider other combinations of ions for our architecture. We wish to continue using $^{138}Ba^{+}$ as our communication qubit because of its relatively red wavelength and the resulting increased fiber compatibility. Our preference for a memory qubit is an atom with nuclear spin 1/2 like $^{171}Yb^{+}$ because of the simple hyperfine structure of such an atom. Among ions that have commonly been trapped, there are none that satisfy this criterion and have a closer mass to $^{138}Ba^{+}$. However, recent work has demonstrated trapping of and basic operations with a synthetic radioactive isotope of barium, $^{133}Ba^{+}$, that does have a nuclear spin of

1/2 [18, 178].

This choice of qubit would have several advantages. The first and most obvious is that it addresses the issues of motional mode participation mismatch to a large extent. The second is that much of the experimental complexity due to our current ion combination could be significantly reduced because the same lasers, with the addition of frequency sidebands, could be used to control both the communication and memory qubits. This factor would be especially advantageous for Raman operations as it would completely eliminate the need for high-power UV light, which is difficult to fiber couple and can cause charging of the trap or nearby insulating surfaces. A third factor is the extremely high SPAM fidelity that has been demonstrated in $^{133}Ba^{+}$ [18], which is even better than the best reported result in $^{171}Yb^{+}$ [72].

There are, however, additional considerations and possible disadvantages as well. Perhaps the most glaring is the issue of the radioactivity of this isotope. The half-life of ^{133}Ba is 10.5 years [179], so depletion of our atomic source is not much of a concern. However, for safety purposes, there would have to be considerable thought put into minimizing the quantities that would be used and thus the efficiency of loading ions. We would need to use an ablation source rather than a thermal source and operate in a regime releasing as few atoms as possible. Additionally, we may want to switch to one of the alternative photoionization schemes discussed in Sec. 3.2.1, which should be more efficient than the present scheme used for $^{138}Ba^{+}$. This consideration is certainly not a scientific limitation to this proposal, however.

Other considerations include how we will perform state readout in $^{133}Ba^{+}$ and, most importantly, if it is even feasible to use it as a memory qubit. The main concern

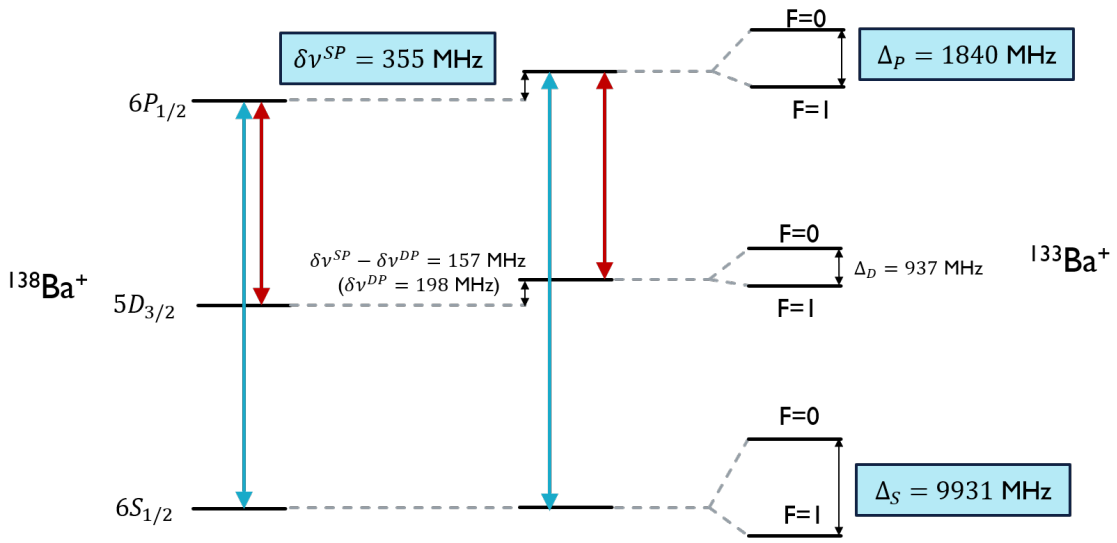

Figure 8.4: Comparison of the atomic structures of ^{138}Ba$^+$ and ^{133}Ba$^+$ showing isotope shifts and hyperfine splitting. Zeeman levels are not shown. All values are from [178].

for this second point is the relative proximity of its resonance to the resonance in ^{138}Ba$^+$ on the $S \leftrightarrow P$ transition and the resulting possibility of crosstalk between the ions during repeated remote entanglement attempts.

Unlike ^{171}Yb$^+$, ^{133}Ba$^+$ does not have a set of transitions that as closely approximate a cycling transition and that includes only one qubit state, assuming we define the qubit as in Yb as $|0\rangle \equiv \left|6S_{1/2}, F = 0, m_F = 0\right\rangle$ and $|1\rangle \equiv \left|6S_{1/2}, F = 1, m_F = 0\right\rangle$. As discussed in Sec. 8.1, in ^{138}Ba$^+$ we can transfer population in one or both of the qubit states to the $5D_{5/2}$ manifold using 1762 nm light. The same can be done in ^{133}Ba$^+$ using a similar approach or the non-coherent approach described in [18], which consists of optically pumping to the $5D_{5/2}$ manifold via the $6P_{3/2}$ manifold. This second scheme requires a 455 nm laser, a 585 nm laser, and a 614 nm laser in addition to the standard Ba lasers, but none of the lasers need to have a narrow linewidth since all of the transitions involved are electric dipole transitions. The

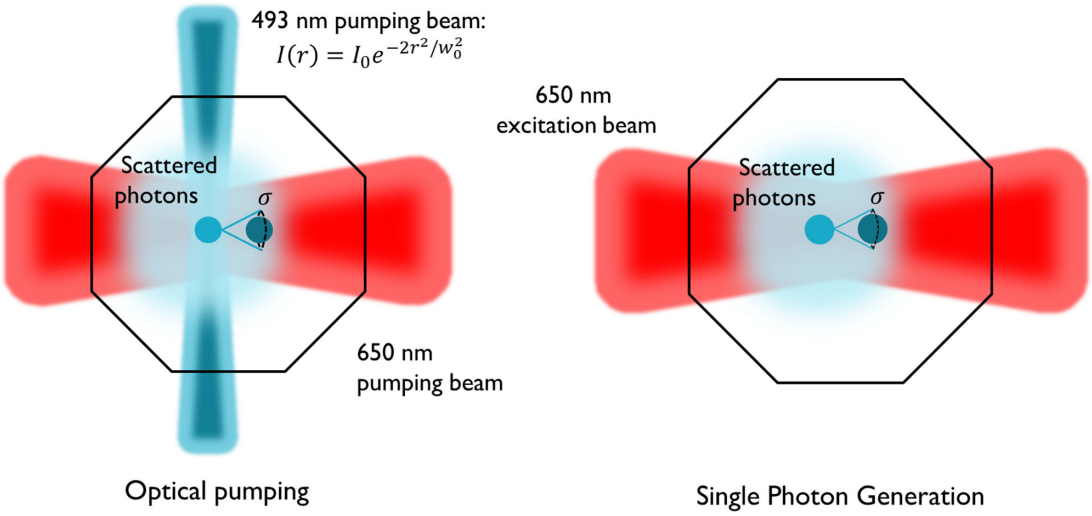

Figure 8.5: Operations with possible associated crosstalk. Optical pumping and single photon generation both could cause a neighboring memory qubit to decohere if enough slightly off-resonant photons interact with the memory qubit. These photons could come from the 493 nm pumping beam or photons that are scattered by the ion. σ represents the scattering cross-section of the neighboring memory ion.

1762 nm approach on the other hand requires only a 1762 nm laser and a 614 nm laser, but the 1762 nm laser must have a high finesse cavity lock to narrow its linewidth. Either way, we can then read out the qubit state as described in Sec. 8.1.

8.4.2.1 Crosstalk in an All-Barium Network

The resonance frequency of the $S \leftrightarrow P$ transition in $^{138}Ba^+$ is much closer to that in $^{133}Ba^+$ than the corresponding value in Yb. Therefore, there is an increased probability that photons from either the optical pumping beam or the communication ion itself could affect the memory qubit (Fig. 8.5). We now examine these probabilities to determine if they are acceptably small for an all-barium quantum network.

We first consider the probability of crosstalk due only to the pumping beam.

We assume the beam has a Gaussian intensity profile

$$I(r) = I_0 e^{-\frac{2r^2}{w_0^2}} \tag{8.7}$$

where I_0 is the peak intensity, r is the distance from the ion and w_0 is the beam waist at the focal plane, which we assume is the ion location. The crosstalk probability is the ratio of the scattering rate of the memory ion to that of the communication ion, where the scattering rate is given in Eq. 2.1 and the Doppler shift ω_D is of course 0. If the memory qubit is a distance r from the communication qubit, the probability of crosstalk is

$$P_{ct}(r) = \frac{\Gamma_{sc}(r,\Delta)}{\Gamma(r,0)} = \frac{s(r)/\left(1+s(r)+4\frac{\Delta^2}{\gamma^2}\right)}{s(0)/\left(1+s(0)\right)} \tag{8.8}$$

where $s(r)$ is the saturation parameter $\frac{I(r)}{I_{sat}}$. If we assume $s(0) = 1$, the crosstalk probability is

$$P_{ct}(r) = \frac{2e^{-\frac{2r^2}{w_0^2}}}{1+e^{-\frac{2r^2}{w_0^2}}+4\frac{\Delta^2}{\gamma^2}}. \tag{8.9}$$

The detuning will depend on the state of the memory qubit. For population in $|0\rangle$, only transitions to the $|F=1\rangle$ manifold can occur because of atomic selection rules. The detuning of these transitions from the $^{138}Ba^+$ resonance is 7.55 GHz [178]. Population in $|1\rangle$, on the other hand, can be driven to $\left|6P_{1/2}, F=0\right\rangle$ or $\left|6P_{1/2}, F=1, m_F=\pm 1\right\rangle$. The detuning of the first transition from the $^{138}Ba^+$ resonance is 4.21 GHz, and the detuning of the second set of transitions is 2.38 GHz [178]. The probability with which each transition occurs depends on the polarization of the pumping beam, but for simplicity, we will assume the chances of a transition

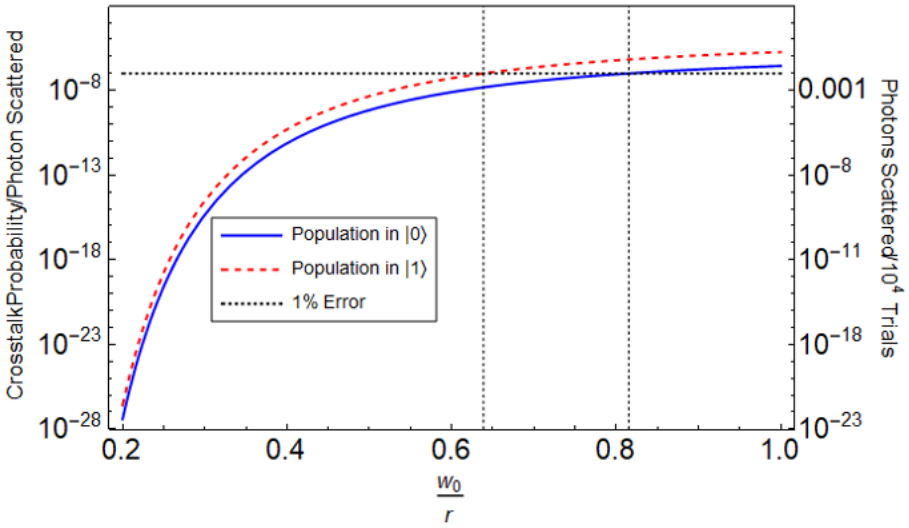

Figure 8.6: Crosstalk as a function of the ratio of beam waist to ion distance for population in both qubit states. The left vertical axis shows the probability of a photon being scattered by the memory qubit for each photon scattered from the communication qubit, and the right axis shows the total number of expected photons scattered for 10^4 repetitions with 10 photons scattered per repetition. The black dotted lines indicate an error of 1%.

to the $|F = 0\rangle$ state is equal to that for a transition to the $|F = 1\rangle$ manifold. We calculate the crosstalk for each memory qubit state separately, noting that there is only one allowed transition from $|0\rangle$ and two from $|1\rangle$. For $|1\rangle$, we take the average of the crosstalk from each possible transition, weighting them appropriately by transition probability. The results of this calculation are plotted in Fig. 8.6.

Our current probability of generating remote entanglement is approximately 10^{-4}, so we are interested in the probability of a photon being scattered in 10^4 entanglement attempts. To maintain an error of $< 1\%$ with population in $|0\rangle$ in the memory qubit, the optical pumping beam waist must be about 0.6 times the ion separation, which is typically about $\sim$5 μm. Since we cannot easily send this beam through our high numerical aperture lenses without blinding our single photon

detectors, the NA of this beam is likely limited to about 0.1. A Gaussian beam with this effective NA would have a waist of 1.5 μm, which would be sufficiently small. The effort to implement the optics for this would be significant but possible. If we can further improve our remote entanglement probability, the requirement for beam size can be relaxed. Additionally, if we pump with only π polarized 493 nm light, we will significantly suppress the probability of excitation of population in $|1\rangle$ since the detuning is smaller on the transitions to the $|F = 1, m_F = \pm 1\rangle$ states and these transitions can only be driven with σ polarization.

Errors due to photons scattered from the communication ion are determined by the fraction of the 4π total solid angle into which the ion emits subtended by the scattering cross section of the memory qubit. This fraction is given by [48]

$$\frac{\Omega}{4\pi} = \frac{2\pi \int_0^\theta \sin\theta' d\theta'}{4\pi} = \frac{1 - cos[\theta(r)]}{2} \tag{8.10}$$

where

$$\theta(r) = \arctan\left(\frac{\sqrt{3\lambda^2/(2\pi^2)}}{r}\right). \tag{8.11}$$

As discussed above, the detunings further decrease the probability of exciting the memory qubit by a factor of $\sim \left(\frac{\gamma}{\Delta}\right)^2$.

We must also consider the effect of the emitted photon polarization. Population in $|0\rangle$ is affected with equal probabilities by any polarization, since all of the Clebsch-Gordan coefficients are equal, and there are allowed transitions for each polarization. For population in $|1\rangle$, the detuning is larger for the allowed transi-

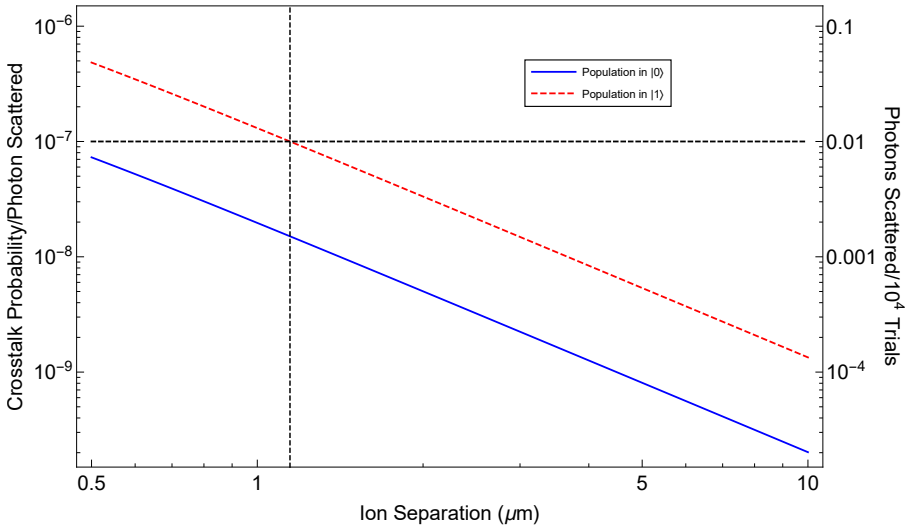

Figure 8.7: Probability of crosstalk due to light scattered from the communication qubit versus ion separation. Black dashed lines indicate 1% probability of a photon absorption event on the memory qubit. For population in $|0\rangle$, the distance corresponding to 1% error is shorter than the smallest distance shown on the plot, so that line is not shown.

tion with π polarized light than for the allowed transition with σ polarized light. However, the numbers of photons emitted that have π polarization and that have σ polarization will be, on average, approximately the same. At least for pumping, which scatters 10 times more photons than single photon generation, both excited states will be equally populated. We therefore conclude that the polarization of the emitted photons will have a small effect, if any. The probability of any excitation occurring is reduced by a factor of 0.54 because of the mismatch in the temporal profile between the exponentially decaying emitted photon and the desired temporal profile of a photon for exciting the ion [180].

From Fig. 8.7, we can see that for typical ion distances of 5 μm, the error due to scattering is very low ($< 10^{-3}$). Therefore, the error will primarily be a result of optical pumping. Overall, these calculations show that an all barium network is

certainly within the realm of possibility, although individual addressing for optical pumping beams will be needed. A further order of magnitude improvement in remote entanglement rate would also make such a network more feasible.

Appendix A: UHV Processing

A crucial component of any ion trapping system is the vacuum chamber. Collisions with background gas particles can cause ions to heat or even escape the trap and are a limiting factor for working with long chains of ions. During the course of this work, we have successfully constructed two vacuum chambers with pressures $\ll 10^{-10}$ Torr. In this appendix, we provide some technical details about the design and processing of these systems and vacuum systems in general.

A.1 Materials and Vacuum Pumping

Different materials will have different rates of outgassing and the gases they release will vary. It is therefore important to use only materials that outgas relatively slowly and only emit gases that can be adequately removed by the vacuum pumps we select. A long list of acceptable materials is available in [181]. We use only a small subset of these. The materials included in our chambers are:

- Stainless steel 304 and 316
- Aluminum
- Titanium

- Tungsten
- Macor (a ceramic)
- Beryllium copper alloy
- Alumel
- Kapton
- Copper
- Steatite (a ceramic)
- Gold
- Silver
- Indium
- Glass (fused silica and S-TIH53)

There may also be other materials in the ion pump, pressure gauge, TSP, vacuum windows, and piezo stages. In general, if parts are specified to pressures of 10^{-11} Torr especially by a company whose products we have previously used, we consider those parts acceptable.

Steel will outgas relatively large quantities of hydrogen. The other gases in a clean chamber containing only acceptable vacuum materials typically are the constituents of air. Water vapor is prevalent after first closing the chamber, and since we fill the chamber with argon, there are often significant quantities of that as well.

Parts that have not been air baked will also have residue from the solvents used for cleaning (Sec. A.2). Much of the pumping after first closing the chamber will use the pump station described in Sec. A.3, but the pumps on the chamber will need to work well for gases that remain after the bake. Additionally, the ion pump on the pump station is not one of the types of ion pumps that can pump noble gases [182]. Therefore, any pumping at UHV of argon must come from the chamber pumps.

As discussed in Sec. 5.2.2, we use a StarCell ion pump and titanium sublimation pump in Cleo for their complementary pumping properties. In Bob, the main chamber body was already constructed when we adapted it, and we chose not to modify the pumping, which consists of the same ion pump as Cleo and a non-evaporable getter (NEG).[1] We did not activate the NEG after opening the chamber, so the pumping is likely primarily from the ion pump.

A.2 Cleaning Procedure

With the exception of certain components that either cannot be cleaned or are from companies we trust to provide parts that have already been cleaned, all parts must be thoroughly cleaned to remove contaminants, especially organic substances. We did not clean parts from VAT, UC components, UKAEA, Smaract, and Agilent.

The standard cleaning procedure consists of the following steps. For each solvent, unless otherwise noted, the part must be placed in an ultrasonic bath for 15 minutes.

[1] SAES Getters

1. Alconox solution (10 g of soap/1 L of water) at 50 °C.

2. Rinse off soap either with running tap water for ∼3 minutes or sonicate in 50 °C deionized (DI) water for 15 minutes. For the second option, the water must then be changed and the step repeated.

3. Sonicate in DI water at 50 °C. This step is in addition to the rinsing in step 2, regardless of the method.

4. Allow parts to dry completely. This typically requires waiting overnight or blowing off the parts with clean, high-pressure air.

5. Sonicate in HPLC-grade hexane (room temperature).

6. Allow parts to dry.

7. Sonicate in ACS-grade acetone (room temperature)

8. Without allowing the acetone to evaporate, transfer parts to HPLC-grade methanol or HPLC-grade isopropyl alcohol (IPA) and sonicate.

If necessary, parts can subsequently be etched in an acid or base solution using distilled water to remove an oxide layer, smooth the surface, and possibly shape the part. We use this technique for the trap rods and needles.

In general, it is important that vacuum parts only come in contact with parts that are equally clean. Standard nitrile gloves are not sufficiently clean to handle vacuum parts, but cleanroom grade nitrile gloves are acceptable for dry parts. For transferring pieces into and out of beakers for cleaning, aluminum wire can be looped

around bigger parts and serve as a handle. Smaller parts can be handled with tools that are at least as far in the cleaning procedure. For example, a hemostat that has been cleaned with Alconox, DI water, and hexane may be used to remove a component from hexane after step 5.

The standard procedure leaves white residue on the surface of windows. We also worried that sonicating them would damage the quality of the optical surfaces, so we simply soaked the windows in HPLC-grade acetone and then HPLC-grade IPA for 15 minutes each. The window must not be allowed to dry in between the two solvents. After removing the window from the IPA, the window is tilted slightly to allow the IPA to peel off towards the edges. A cleanroom wipe or swab is used to wick residual IPA from the edges, and the window is left to dry with the glass surface vertical. Any residue on the glass surface can be removed using cleanroom swabs and a small quantity of solvent.

After cleaning the parts, any all-metal parts are baked in air at 400 °C for 1-3 days. This bake removes solvent residue that is left from the cleaning. On stainless steel parts, it also causes the formation of an oxide layer, which reduces the rate of hydrogen outgassing.

A.3 Baking the Chamber

The next step in preparing a chamber is to bake it under vacuum for at least 2 weeks to remove water vapor, hydrogen, solvent residue, and any other gases present. All of our chambers are built with a valve that can be opened to connect

to an external pumping system or closed off to seal the chamber.

We use an external pumping station that contains a turbo pump,[2] which can pump from atmospheric pressure down to about 10^{-8} Torr, and an ion pump,[3] which can be used at pressures $\lesssim 10^{-6}$ Torr. This ion pump has much higher pumping speeds than the turbo pump and the ion pumps on our chambers but cannot pump noble gases. Both the turbo pump and large ion pump have associated valves so we can control which is pumping the chamber. A bellows connects the pump station to the chamber through an opening in the side of the industrial oven in which the chamber is placed for the bake. The pump station also contains a residual gas analyzer (RGA) that measures the background gas partial pressures in the vacuum system.

At the beginning of the bake, the pump station must be exposed to air to connect it to the chamber. During this phase, the ion pump valve is closed so the pump is not exposed to air. The valve to the turbo pump is opened and the chamber valve is closed. At this point, we generally will have loaded the barium atoms into our chamber, and therefore, air must not enter the chamber to avoid oxidation of the barium. The turbo pump and bellows then pump down the system to $< 10^{-4}$ Torr, and we open the chamber valve. Once the pressure has reached $< 10^{-6}$ Torr we can leak check using helium and the RGA (see Sec. A.4). If no leaks are detected, we can proceed with the bake.

We increase the temperature of the chamber gradually (10 °C/hour) to en-

[2] Pfeiffer
[3] Duniway

sure minimal temperature gradients, which could lead to windows breaking due to different chamber components expanding at different rates. During this time, only the turbo pump should be used because the chamber pressure will increase dramatically. As long as the pressure remains $< 10^{-5}$, we monitor the system with the RGA. If the power supply to the turbo is shut off, the system will vent to air after a few minutes, which would be catastrophic at high temperatures. To avoid this possibility, the turbo is powered with a uninterruptible power supply (UPS) and a person remains in the building at all times.

After the temperature has reached its maximum value and the pressure has stabilized, we switch to the ion pump on the pump station by closing the valve to the turbo and opening the valve to the ion pump. This should immediately result in a large pressure drop because of the much greater pumping speed of the ion pump compared with the turbo pump. The ion pump will not vent to air in case of a power outage, so the chamber will be much safer at this point and will no longer require nearly constant observation. The system is monitored primarily using the RGA to ensure the partial pressures of all gases are decreasing and that no leaks appear for the remainder of the bake. A few days into the bake we attempt to turn on the chamber ion pump as well. On Cleo, however, the ion pump would have dramatic pressure spikes and shut itself off at temperatures $\gtrsim$130 °C, so we left it off at least until the temperature was below this limit.

The chamber is baked until the hydrogen partial pressure is no longer decreasing significantly on the timescale of days. We then cool down at 10 °C/hour. At some point during the cool down when the temperature is still $\gtrsim$ 100 °C the valve

to the chamber is closed, to minimize the flow of gases from the cooler pumping station into the chamber. For Bob, the maximum temperature we used was 200 °C and was limited by the windows and electrical feedthroughs. Bob was baked for about three weeks. For Cleo, the piezos could only be baked to 130 °C, which is too low to remove the hydrogen in a new chamber in a reasonable amount of time. We therefore first baked Cleo without the piezos to 200 °C for three weeks. We then reopened the chamber and added the piezos, aspheres, and atomic sources and performed a subsequent bake to 120 °C for a month.

After the first bake of Cleo, we fired the TSP for 5 minutes, which caused the pressure to drop from 2×10^{-10} Torr to 2.5×10^{-11} Torr over the course of a few days. After the second bake, we fired the TSP again, since it needs to be fired every time the chamber is opened. The second time we fired it for 12 minutes (4 minutes from each of the three filaments). The chamber was at a slightly elevated temperature when we first fired it ($\sim$ 35 °C), so the pressure was slightly higher than after the first bake (3.7×10^{-10} Torr). Several days after firing the TSP and with the chamber at room temperature, the final pressure was 2.1×10^{-11} Torr. The pressure gauge[4] readings must be multiplied by a factor of about 2 to obtain an accurate value for a pressure dominated by hydrogen. At pressures below 2×10^{-10} Torr, however, these readings are not accurate and are likely higher than the actual value. Regardless, these results indicate a chamber with a pressure well within the desired range.

[4] Agilent 9715007

A.4 Use of a Residual Gas Analyzer

An RGA is an important tool for characterizing vacuum systems because it can identify not only the overall pressure but also which gases are contributing. For example, we expect hydrogen to be prominent in our baked chambers but the presence of oxygen would strongly indicate a leak. It is also important to identify organic compounds since they are a primary contaminant and can be difficult to remove from the system. The RGA we use[5] can be operated either in a pressure versus mass mode, which scans across a range of mass to charge ratios and plots the result, or a pressure versus time mode for individual mass to charge ratios. Some fraction of the partial pressure reading at a certain mass may result from particles with twice the mass that have been doubly ionized.

RGAs can be operated with or without a continuous-dynode electron multiplier (CDEM), which allows detection of signals below 10^{-11} Torr. The CDEM can easily be destroyed by pressures over 10^{-6} Torr, however, so it is important to only use it when confident that the pressures will remain sufficiently low or when the risk of it breaking is acceptable.

Additionally, RGAs can be used to detect leaks in a vacuum system directly. Helium is sprayed around any possible sources of leaks on the chamber such as flange connections and electrical feedthroughs. Helium is the standard choice because the background is extremely low. The partial pressure of helium is then monitored in time. Using the CDEM for this function is highly preferable for detecting very small

[5] SRS RGA100 or SRS RGA200

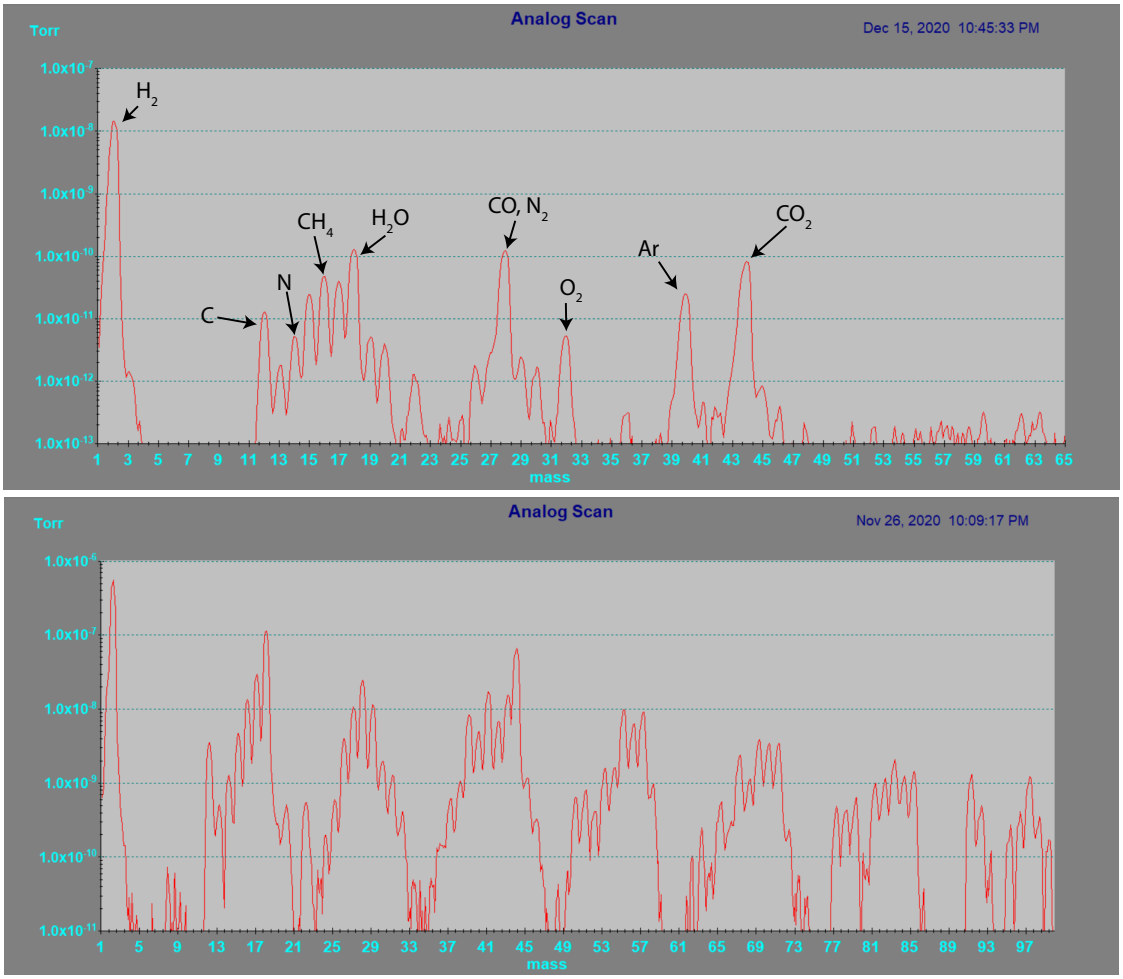

Figure A.1: RGA scans of partial pressure vs. mass. The top scan is in a clean system and has important peaks labeled. The bottom scan is of a dirtier system and shows prominent signatures of organics. The horizontal axis is the mass to charge ratio in atomic mass units (AMU) and the vertical axis is partial pressure in Torr.

leaks.

The other use of an RGA is to monitor the partial pressures of various gases. The discussion that follows is not meant to be a comprehensive review of interpreting RGA scans but does cover the most relevant information for our systems. Examples of scans across a range of masses are shown in Fig. A.1. The first scan is of Cleo and the pump station after Cleo was baked, so most of the contaminants were removed, and H_2 is by far the most prominent gas remaining. The fact that the pump station

had not been baked and had a small leak likely resulted in the presence of H_2O, O_2, N, N_2 CH_4 and Ar. In particular, the fact that there is a peak at 32 AMU is a strong indicator of a leak in the system since UHV systems should not contain any oxygen. The peak at 28 AMU can come from both N_2 and CO. We can determine the relative prevalence by comparing with the height of the peak at 14 AMU, which, for pure nitrogen, would be about 14 times lower than the peak at 28 AMU. In the top scan in this figure, it is about 24 times lower. This discrepancy indicates the presence of CO, which is produced by RGAs, the pressure gauge, and ion pumps, so it is not surprising that it is prevalent.

The bottom scan, on the other hand, was from the beginning of the bake of Cleo while the chamber was at 200 °C. The collections of peaks with one center tall peak and other surrounding smaller peaks are signatures of organic compounds, because some of the hydrogen atoms in the organic chain will be removed by the RGA ionizer and result in changes of 1 AMU. Some of this contamination is from residual solvents after the cleaning process, but the heaviest solvent we used was acetone, which has a peak at 58 AMU. All of the higher masses, therefore, were from other sources of contamination. While we did not determine what caused this, by the end of the bake this contamination had been removed nearly completely.

During the bake, we select prominent peaks and monitor the change in their pressures with time. A plateau in the partial pressure of hydrogen mostly determines when we stop the bake. An observed increase in oxygen indicates a leak, and corresponding increases in nitrogen and argon can confirm this assessment.

Bibliography

[1] P. Shor, in *Proceedings 35th Annual Symposium on Foundations of Computer Science* (1994) pp. 124–134.

[2] P. Benioff, Journal of Statistical Physics **29**, 515 (1982).

[3] R. P. Feynman, International Journal of Theoretical Physics **21**, 467 (1982).

[4] D. Deutsch and R. Penrose, Proceedings of the Royal Society of London. A. Mathematical and Physical Sciences **400**, 97 (1985).

[5] F. Arute *et al.*, Nature **574**, 505 (2019).

[6] E. Pednault, J. A. Gunnels, G. Nannicini, L. Horesh, T. Magerlein, E. Solomonik, E. W. Draeger, E. T. Holland, and R. Wisnieff, arXiv:1710.05867 [quant-ph] (2020).

[7] N. Moll, P. Barkoutsos, L. S. Bishop, J. M. Chow, A. Cross, D. J. Egger, S. Filipp, A. Fuhrer, J. M. Gambetta, M. Ganzhorn, A. Kandala, A. Mezzacapo, P. Müller, W. Riess, G. Salis, J. Smolin, I. Tavernelli, and K. Temme, Quantum Science and Technology **3**, 030503 (2018).

[8] Y. Cao, J. Romero, J. P. Olson, M. Degroote, P. D. Johnson, M. Kieferová, I. D. Kivlichan, T. Menke, B. Peropadre, N. P. D. Sawaya, S. Sim, L. Veis, and A. Aspuru-Guzik, Chemical Reviews **119**, 10856 (2019).

[9] K. L. Brown, W. J. Munro, and V. M. Kendon, Entropy **12**, 2268 (2010).

[10] Y. Nam, J.-S. Chen, N. C. Pisenti, K. Wright, C. Delaney, D. Maslov, K. R. Brown, S. Allen, J. M. Amini, J. Apisdorf, K. M. Beck, A. Blinov, V. Chaplin, M. Chmielewski, C. Collins, S. Debnath, K. M. Hudek, A. M. Ducore, M. Keesan, S. M. Kreikemeier, J. Mizrahi, P. Solomon, M. Williams, J. D. Wong-Campos, D. Moehring, C. Monroe, and J. Kim, npj Quantum Information **6**, 1 (2020).

[11] J. Zhang, G. Pagano, P. W. Hess, A. Kyprianidis, P. Becker, H. Kaplan, A. V. Gorshkov, Z.-X. Gong, and C. Monroe, Nature **551**, 601 (2017).

[12] Y. Alexeev, D. Bacon, K. R. Brown, R. Calderbank, L. D. Carr, F. T. Chong, B. DeMarco, D. Englund, E. Farhi, B. Fefferman, A. V. Gorshkov, A. Houck, J. Kim, S. Kimmel, M. Lange, S. Lloyd, M. D. Lukin, D. Maslov, P. Maunz, C. Monroe, J. Preskill, M. Roetteler, M. J. Savage, and J. Thompson, PRX Quantum **2**, 017001 (2021).

[13] T. D. Ladd, F. Jelezko, R. Laflamme, Y. Nakamura, C. Monroe, and J. L. O'Brien, Nature **464**, 45 (2010).

[14] P. Wang, C.-Y. Luan, M. Qiao, M. Um, J. Zhang, Y. Wang, X. Yuan, M. Gu, J. Zhang, and K. Kim, Nature Communications **12**, 233 (2021), number: 1 Publisher: Nature Publishing Group.

[15] T. Harty, D. Allcock, C. Ballance, L. Guidoni, H. Janacek, N. Linke, D. Stacey, and D. Lucas, Physical Review Letters **113**, 220501 (2014).

[16] J. Gaebler, T. Tan, Y. Lin, Y. Wan, R. Bowler, A. Keith, S. Glancy, K. Coakley, E. Knill, D. Leibfried, and D. Wineland, Physical Review Letters **117**, 060505 (2016).

[17] R. Barends, J. Kelly, A. Megrant, A. Veitia, D. Sank, E. Jeffrey, T. C. White, J. Mutus, A. G. Fowler, B. Campbell, Y. Chen, Z. Chen, B. Chiaro, A. Dunsworth, C. Neill, P. O'Malley, P. Roushan, A. Vainsencher, J. Wenner, A. N. Korotkov, A. N. Cleland, and J. M. Martinis, Nature **508**, 500 (2014).

[18] J. E. Christensen, D. Hucul, W. C. Campbell, and E. R. Hudson, npj Quantum Information **6**, 1 (2020).

[19] J. D. Wong-Campos, *Demonstration of a Quantum Gate with Ultrafast Laser Pulses*, Ph.D. thesis, University of Maryland, College Park (2017).

[20] C. Monroe and J. Kim, Science **339**, 1164 (2013).

[21] M. Cetina, L. N. Egan, C. A. Noel, M. L. Goldman, A. R. Risinger, D. Zhu, D. Biswas, and C. Monroe, arXiv:2007.06768 [quant-ph] (2020).

[22] D. P. DiVincenzo, Fortschritte der Physik **48**, 771 (2000).

[23] D. Maslov, New Journal of Physics **19**, 023035 (2017).

[24] D. Kielpinski, C. Monroe, and D. J. Wineland, Nature **417**, 709 (2002).

[25] J. M. Pino, J. M. Dreiling, C. Figgatt, J. P. Gaebler, S. A. Moses, M. S. Allman, C. H. Baldwin, M. Foss-Feig, D. Hayes, K. Mayer, C. Ryan-Anderson, and B. Neyenhuis, Nature **592**, 209 (2021).

[26] K. R. Brown, J. Kim, and C. Monroe, npj Quantum Information **2**, 1 (2016).

[27] C. Monroe, R. Raussendorf, A. Ruthven, K. R. Brown, P. Maunz, L.-M. Duan, and J. Kim, Phys. Rev. A **89**, 022317 (2014).

[28] N. M. Linke, D. Maslov, M. Roetteler, S. Debnath, C. Figgatt, K. A. Landsman, K. Wright, and C. Monroe, Proceedings of the National Academy of Sciences **114**, 3305 (2017).

[29] W. K. Wootters and W. H. Zurek, Nature **299**, 802 (1982).

[30] C. H. Bennett and G. Brassard, in *Proceedings of the IEEE International Conference on Computers, Systems and Signal Pricessing, Bangalore, India* (IEEE, New York, 1984) pp. 175–179.

[31] A. K. Ekert, Phys. Rev. Lett. **67**, 661 (1991).

[32] L. J. Stephenson, D. P. Nadlinger, B. C. Nichol, S. An, P. Drmota, T. G. Ballance, K. Thirumalai, J. F. Goodwin, D. M. Lucas, and C. J. Ballance, Phys. Rev. Lett. **124** (2020).

[33] D. Hucul, I. V. Inlek, G. Vittorini, C. Crocker, S. Debnath, S. M. Clark, and C. Monroe, Nature Physics **11** (2015).

[34] D. M. Greenberger, M. Horne, and A. Zeilinger, Fortschritte der Physik **48**, 243 (2000).

[35] W. Dür, G. Vidal, and J. I. Cirac, Phys. Rev. A **62**, 062314 (2000).

[36] A. Tavakoli, A. Pozas-Kerstjens, M.-X. Luo, and M.-O. Renou, arXiv:2104.10700 [quant-ph] (2021).

[37] M. Pompili, S. L. N. Hermans, S. Baier, H. K. C. Beukers, P. C. Humphreys, R. N. Schouten, R. F. L. Vermeulen, M. J. Tiggelman, L. dos Santos Martins, B. Dirkse, S. Wehner, and R. Hanson, Science **372**, 259 (2021).

[38] H. J. Metcalf and P. van der Straten, J. Opt. Soc. Am. B **20**, 887 (2003).

[39] C. J. Foot, *Atomic Physics* (Oxford University Press, 2005).

[40] W. M. Itano and D. J. Wineland, Phys. Rev. A **25**, 35 (1982).

[41] D. J. Wineland and W. M. Itano, Phys. Rev. A **20**, 1521 (1979).

[42] D. L. Hayes, *Remote and Local Entanglement of Ions Using Photons and Phonons*, Ph.D. thesis, University of Maryland, College Park (2012).

[43] J. A. Mizrahi, *Ultrafast Control of Spin and Motion in Trapped Ions*, Ph.D. thesis, University of Maryland, College Park (2013).

[44] J. J. Sakurai and J. Napolitano, *Modern Quantum Mechanics*, 2nd ed. (Addison-Wesley, 2010).

[45] D. Wineland, C. Monroe, W. Itano, D. Leibfried, B. King, and D. Meekhof, Journal of Research of the National Institute of Standards and Technology **103**, 259 (1998).

[46] A. Sørensen and K. Mølmer, Phys. Rev. A **62**, 022311 (2000).

[47] P. J. Lee, K.-A. Brickman, L. Deslauriers, P. C. Haljan, L.-M. Duan, and C. Monroe, Journal of Optics B: Quantum and Semiclassical Optics **7**, S371 (2005).

[48] I. V. Inlek, *Multispecies Trapped Atomic Ion Modules for Quantum Networks*, Ph.D. thesis, University of Maryland, College Park (2016).

[49] I. V. Inlek, C. Crocker, M. Lichtman, K. Sosnova, and C. Monroe, Phys. Rev. Lett. **118**, 250502 (2017).

[50] H. J. Metcalf and P. van der Straten, *Laser Cooling and Trapping* (Springer Science + Business Media, 1999).

[51] L. Luo, D. Hayes, T. Manning, D. Matsukevich, P. Maunz, S. Olmschenk, J. Sterk, and C. Monroe, Fortschritte der Physik **57**, 1133 (2009).

[52] C. Crocker, M. Lichtman, K. Sosnova, A. Carter, S. Scarano, and C. Monroe, Optics Express **27**, 28143 (2019).

[53] R. N. Zare, *Angular Momentum: Understanding Spatial Aspects in Chemistry and Physics* (Wiley-Interscience, 1988).

[54] D. Budker, D. F. Kimball, and D. P. DeMille, *Atomic Physics: An Exploration Through Problems and Solutions*, 2nd ed. (Oxford University Press, 2008).

[55] K. Sosnova, *Mixed-Species Ion Chains for Quantum Networks*, Ph.D. thesis, University of Maryland, College Park (2020).

[56] H. Oberst, *Resonance Fluorescence of Single Barium Ions*, *Diplomarbeit*, University of Innsbruck (1999).

[57] D. Rotter, *Quantum Feedback and Quantum Correlation Measurements with a Single Barium Ion*, Ph.D. thesis, University of Innsbruck (2008).

[58] D. A. Steck, Quantum and Atom Optics (2020), available online at `http://steck.us/teaching`.

[59] H.-P. Breuer and F. Petruccione, in *Irreversible Quantum Dynamics*, edited by F. Benatti and R. Floreanini (Springer Berlin Heidelberg, Berlin, Heidelberg, 2003) pp. 65–79.

[60] Y. Wang, M. Um, J. Zhang, S. An, M. Lyu, J.-N. Zhang, L.-M. Duan, D. Yum, and K. Kim, Nature Photonics **11** (2017).

[61] C. Balzer, A. Braun, T. Hannemann, C. Paape, M. Ettler, W. Neuhauser, and C. Wunderlich, Phys. Rev. A **73**, 041407 (2006).

[62] W. F. Meggers and C. H. Corliss, Journal of Research of the National Bureau of Standards. Section A, Physics and Chemistry **70A**, 63 (1966).

[63] W. C. Martin, R. Zalubas, and L. Hagan, in *Nat. Stand. Ref. Data Ser., NSRDS-NBS 60* (Nat. Bur. Stand., U.S., 1978).

[64] S. Olmschenk, D. Hayes, D. N. Matsukevich, P. Maunz, D. L. Moehring, K. C. Younge, and C. Monroe, Phys. Rev. A **80**, 022502 (2009).

[65] R. W. Berends, E. H. Pinnington, B. Guo, and Q. Ji, Journal of Physics B: Atomic, Molecular and Optical Physics **26**, L701 (1993).

[66] N. Yu and L. Maleki, Phys. Rev. A **61**, 022507 (2000).

[67] M. Roberts, P. Taylor, S. V. Gateva-Kostova, R. B. M. Clarke, W. R. C. Rowley, and P. Gill, Phys. Rev. A **60**, 2867 (1999).

[68] S. Olmschenk, *Quantum Teleportation between Distant Matter Qubits*, Ph.D. thesis, University of Michigan (2009).

[69] E. Biémont, J.-F. Dutrieux, I. Martin, and P. Quinet, Journal of Physics B: Atomic, Molecular and Optical Physics **31**, 3321 (1998).

[70] D. J. Berkeland and M. G. Boshier, Phys. Rev. A **65**, 033413 (2002).

[71] P. T. H. Fisk, M. J. Sellars, M. A. Lawn, and G. Coles, IEEE Transactions on Ultrasonics, Ferroelectrics, and Frequency Control **44**, 344 (1997).

[72] S. Crain, C. Cahall, G. Vrijsen, E. E. Wollman, M. D. Shaw, V. B. Verma, S. W. Nam, and J. Kim, Communications Physics **2**, 1 (2019).

[73] L. Egan, D. M. Debroy, C. Noel, A. Risinger, D. Zhu, D. Biswas, M. Newman, M. Li, K. R. Brown, M. Cetina, and C. Monroe, arXiv:2009.11482 [quant-ph] (2021).

[74] R. Islam, W. C. Campbell, T. Choi, S. M. Clark, C. W. S. Conover, S. Debnath, E. E. Edwards, B. Fields, D. Hayes, D. Hucul, I. V. Inlek, K. G. Johnson, S. Korenblit, A. Lee, K. W. Lee, T. A. Manning, D. N. Matsukevich, J. Mizrahi, Q. Quraishi, C. Senko, J. Smith, and C. Monroe, Optics Letters **39**, 3238 (2014).

[75] C. Crocker, *High Purity Single Photons Entangled with Barium Ions for Quantum Networking*, Ph.D. thesis, University of Maryland, College Park (2018).

[76] J. J. Curry, Journal of Physical and Chemical Reference Data **33**, 725 (2004).

[77] S. Niggli and M. C. E. Huber, Phys. Rev. A **35**, 2908 (1987).

[78] S. De, U. Dammalapati, K. Jungmann, and L. Willmann, Phys. Rev. A **79**, 041402 (2009).

[79] H. Karlsson and U. Litzén, Physica Scripta **60**, 321 (1999).

[80] K. J. Arnold, S. R. Chanu, R. Kaewuam, T. R. Tan, L. Yeo, Z. Zhang, M. S. Safronova, and M. D. Barrett, Phys. Rev. A **100**, 032503 (2019).

[81] P. Kuske, N. Kirchner, W. Wittmann, H. J. Andrä, and D. Kaiser, Physics Letters A **64**, 377 (1978).

[82] E. H. Pinnington, R. W. Berends, and M. Lumsden, Journal of Physics B: Atomic, Molecular and Optical Physics **28**, 2095 (1995).

[83] N. Yu, W. Nagourney, and H. Dehmelt, Phys. Rev. Lett. **78**, 4898 (1997).

[84] C. Auchter, T. W. Noel, M. R. Hoffman, S. R. Williams, and B. B. Blinov, Phys. Rev. A **90**, 060501 (2014).

[85] Z. Zhang, K. J. Arnold, S. R. Chanu, R. Kaewuam, M. S. Safronova, and M. D. Barrett, Phys. Rev. A **101**, 062515 (2020).

[86] D. Reiß, A. Lindner, and R. Blatt, Phys. Rev. A **54**, 5133 (1996).

[87] I. Siemers, M. Schubert, R. Blatt, W. Neuhauser, and P. E. Toschek, Europhysics Letters (EPL) **18**, 139 (1992).

[88] T. W. Noel, *Ion Photon Entanglement with Barium*, Ph.D. thesis, University of Washington (2014).

[89] J. D. Jackson, *Classical Electrodynamics*, 3rd ed. (Wiley, 1999).

[90] D. J. Griffiths, *Introduction to Electrodynamics*, 4th ed. (Cambridge University Press, 2017).

[91] H. Dehmelt, in *Advances in Atomic and Molecular Physics*, Vol. 3 (Elsevier, 1968) pp. 53–72.

[92] W. Paul, Reviews of Modern Physics **62**, 531 (1990).

[93] S. R. Jefferts, C. Monroe, E. W. Bell, and D. J. Wineland, Physical Review A **51** (1995).

[94] N. Yu, W. Nagourney, and H. Dehmelt, Journal of Applied Physics **69** (1991).

[95] R. G. Brewer, R. G. DeVoe, and R. Kallenbach, Physical Review A **46** (1992).

[96] P. L. W. Maunz, *High Optical Access Trap 2.0.*, Tech. Rep. SAND-2016-0796R (Sandia National Lab. (SNL-NM), Albuquerque, NM (United States), 2016).

[97] J. Chiaverini, R. B. Blakestad, J. Britton, J. D. Jost, C. Langer, D. Leibfried, R. Ozeri, and D. J. Wineland, Quantum Information & Computation **5** (2005).

[98] J. D. Prestage, G. J. Dick, and L. Maleki, Journal of Applied Physics **66** (1989).

[99] D. J. Berkeland, J. D. Miller, J. C. Bergquist, W. M. Itano, and D. J. Wineland, Journal of Applied Physics **83** (1998).

[100] F. G. Major and H. G. Dehmelt, Physical Review **170** (1968).

[101] M. Drewsen and A. Brøner, Phys. Rev. A **62**, 045401 (2000).

[102] S.-L. Zhu, C. Monroe, and L.-M. Duan, Phys. Rev. Lett. **97**, 050505 (2006).

[103] D. Szwer, *High Fidelity Readout and Protection of a* $^{43}Ca^{+}$ *Trapped Ion Qubit*, Ph.D. thesis, University of Oxford (2009).

[104] C. D. Bruzewicz, J. Chiaverini, R. McConnell, and J. M. Sage, Applied Physics Reviews **6** (2019).

[105] D. Hucul, *A Modular Quantum System of Trapped Atomic Ions*, Ph.D. thesis, University of Maryland, College Park (2015).

[106] L. Deslauriers, *Cooling and Heating of the Quantum Motion of Trapped Cadmium Ions*, Ph.D. thesis, University of Michigan (2006).

[107] G. H. Seward, *Optical Design of Microscopes* (Society of Photo-Optical Instrumentation Engineers, 2010).

[108] Ohara Corporation, Ohara Glass Catalog, available online at `http://www.oharacorp.com/catalog.html`.

[109] W. F. Gale and T. C. Totemeier, *Smithells Metals Reference Book*, eighth ed. (Butterworth-Heinemann, 2004).

[110] Corning, Macor: Machinable glass ceramic for industrial applications (2012), available online at `https://www.corning.com/worldwide/en/products/advanced-optics/product-materials/specialty-glass-and-glass-ceramics/glass-ceramics/macor.html`.

[111] M. Harlander, M. Brownnutt, W. Hänsel, and R. Blatt, New Journal of Physics **12**, 093035 (2010).

[112] H. Kim, J. S. Horwitz, G. Kushto, A. Piqué, Z. H. Kafafi, C. M. Gilmore, and D. B. Chrisey, Journal of Applied Physics **88** (2000).

[113] A. H. Turnbull, R. S. Barton, and J. C. Rivière, *An introduction to vacuum technique* (Wiley, 1963).

[114] C. Robens, S. Brakhane, W. Alt, F. Kleißler, D. Meschede, G. Moon, G. Ramola, and A. Alberti, Opt. Lett. **42**, 1043 (2017).

[115] A. Steffen, W. Alt, M. Genske, D. Meschede, C. Robens, and A. Alberti, Review of Scientific Instruments **84**, 126103 (2013).

[116] N. Solmeyer, K. Zhu, and D. S. Weiss, Review of Scientific Instruments **82**, 066105 (2011).

[117] J. Gil and E. Bernabeu, Optik **76**, 67 (1987).

[118] D. Stick, W. K. Hensinger, S. Olmschenk, M. J. Madsen, K. Schwab, and C. Monroe, Nature Physics **2**, 36 (2006).

[119] B. B. Blinov, D. L. Moehring, L.-M. Duan, and C. Monroe, Nature **428** (2004).

[120] S. Olmschenk, D. N. Matsukevich, P. Maunz, D. Hayes, L.-M. Duan, and C. Monroe, Science **323**, 486 (2009).

[121] J. M. Lukens and P. Lougovski, Optica **4**, 8 (2017).

[122] I. Marcikic, H. de Riedmatten, W. Tittel, V. Scarani, H. Zbinden, and N. Gisin, Phys. Rev. A **66**, 062308 (2002).

[123] P. C. Humphreys, B. J. Metcalf, J. B. Spring, M. Moore, X.-M. Jin, M. Barbieri, W. S. Kolthammer, and I. A. Walmsley, Phys. Rev. Lett. **111**, 150501 (2013).

[124] E. Nagali, F. Sciarrino, F. De Martini, L. Marrucci, B. Piccirillo, E. Karimi, and E. Santamato, Phys. Rev. Lett. **103**, 013601 (2009).

[125] W. Tittel and G. Weihs, arXiv:quant-ph/0107156 (2001).

[126] A. Treiber, A. Poppe, M. Hentschel, D. Ferrini, T. Lorünser, E. Querasser, T. Matyus, H. Hübel, and A. Zeilinger, New Journal of Physics **11**, 045013 (2009).

[127] V. Krutyanskiy, M. Meraner, J. Schupp, V. Krcmarsky, H. Hainzer, and B. P. Lanyon, npj Quantum Information **5** (2019).

[128] W. J. Munro, K. Azuma, K. Tamaki, and K. Nemoto, IEEE Journal of Selected Topics in Quantum Electronics **21**, 78 (2015).

[129] D. B. Higginbottom, L. Slodička, G. Araneda, L. Lachman, R. Filip, M. Hennrich, and R. Blatt, New Journal of Physics **18** (2016).

[130] J. D. Siverns, X. Li, and Q. Quraishi, Appl. Opt. **56**, B222 (2017).

[131] R. H. Brown and R. Q. Twiss, Nature **177**, 27 (1956).

[132] L. Schweickert, K. D. Jöns, K. D. Zeuner, S. F. Covre da Silva, H. Huang, T. Lettner, M. Reindl, J. Zichi, R. Trotta, A. Rastelli, and V. Zwiller, Applied Physics Letters **112**, 093106 (2018).

[133] C. Auchter, C.-K. Chou, T. W. Noel, and B. B. Blinov, J. Opt. Soc. Am. B **31**, 1568 (2014).

[134] D. P. Nadlinger, *Entanglement between Trapped Strontium Ions and Photons*, Master's thesis, ETH Zürich (2016).

[135] L. J. Stephenson, *Entanglement between nodes of a quantum network*, Ph.D. thesis, University of Oxford (2019).

[136] L. Slodička, G. Hétet, N. Röck, P. Schindler, M. Hennrich, and R. Blatt, Phys. Rev. Lett. **110**, 083603 (2013).

[137] C. K. Hong, Z. Y. Ou, and L. Mandel, Phys. Rev. Lett. **59**, 2044 (1987).

[138] Y. L. Lim and A. Beige, New Journal of Physics **7**, 155 (2005), publisher: IOP Publishing.

[139] N. Lütkenhaus, J. Calsamiglia, and K.-A. Suominen, Phys. Rev. A **59**, 3295 (1999).

[140] L. Zhou and Y.-B. Sheng, Scientific Reports **6**, 20901 (2016).

[141] E. A. Donley, T. P. Heavner, F. Levi, M. O. Tataw, and S. R. Jefferts, Review of Scientific Instruments **76**, 063112 (2005).

[142] D. L. Moehring, P. Maunz, S. Olmschenk, K. C. Younge, D. N. Matsukevich, L.-M. Duan, and C. Monroe, Nature **449**, 68 (2007).

[143] D. F. V. James, P. G. Kwiat, W. J. Munro, and A. G. White, Phys. Rev. A **64**, 052312 (2001).

[144] R. Nigmatullin, C. J. Ballance, N. d. Beaudrap, and S. C. Benjamin, New Journal of Physics **18**, 103028 (2016).

[145] M. Keller, B. Lange, K. Hayasaka, W. Lange, and H. Walther, Nature **431** (2004).

[146] J. D. Sterk, L. Luo, T. A. Manning, P. Maunz, and C. Monroe, Phys. Rev. A **85**, 062308 (2012).

[147] A. Stute, B. Casabone, B. Brandstätter, K. Friebe, T. E. Northup, and R. Blatt, Nature Photonics **7** (2013).

[148] M. Steiner, H. M. Meyer, C. Deutsch, J. Reichel, and M. Köhl, Phys. Rev. Lett. **110**, 043003 (2013).

[149] B. Casabone, K. Friebe, B. Brandstätter, K. Schüppert, R. Blatt, and T. E. Northup, Phys. Rev. Lett. **114**, 023602 (2015).

[150] B. Brandstätter, A. McClung, K. Schüppert, B. Casabone, K. Friebe, A. Stute, P. O. Schmidt, C. Deutsch, J. Reichel, R. Blatt, and T. E. Northup, Review of Scientific Instruments **84**, 123104 (2013).

[151] H. Takahashi, E. Kassa, C. Christoforou, and M. Keller, Phys. Rev. Lett. **124**, 013602 (2020).

[152] P. Kobel, M. Breyer, and M. Köhl, npj Quantum Information **7**, 1 (2021).

[153] M. Teller, D. A. Fioretto, P. C. Holz, P. Schindler, V. Messerer, K. Schüppert, Y. Zou, R. Blatt, J. Chiaverini, J. Sage, and T. E. Northup, Heating of a trapped ion induced by dielectric materials (2021), arXiv:2103.13846 [quant-ph] .

[154] G. S. Agarwal and S. Das, New Journal of Physics **10**, 013014 (2008).

[155] G. Vittorini, D. Hucul, I. V. Inlek, C. Crocker, and C. Monroe, Phys. Rev. A **90**, 040302 (2014).

[156] R. P. Khare, *Fiber Optics and Optoelectronics* (Oxford University Press, 2004).

[157] R. Paschotta, *Field Guide to Lasers*, SPIE Field Guides, Vol. FG12 (Society of Photo-Optical Instrumentation Engineers, 2008).

[158] G. Chartier, *Introduction to Optics* (Springer, 2005).

[159] J. C. Wyant and K. Creath, in *Applied Optics and Optical Engineering*, Vol. XI, edited by R. R. Shannon and J. C. Wyant (Academic Press, Inc., 1992).

[160] V. Lakshminarayanan and A. Fleck, Journal of Modern Optics **58** (2011).

[161] J. D. Wong-Campos, K. G. Johnson, B. Neyenhuis, J. Mizrahi, and C. Monroe, Nature Photonics **10** (2016).

[162] D. R. Neal, W. J. Alford, J. K. Gruetzner, and M. E. Warren, in *Proceedings of Society of Photo-Optical Instrumentation Engineers International Workshop on Laser Beam and Optics Characterization* (1996).

[163] T. Noel, M. R. Dietrich, N. Kurz, G. Shu, J. Wright, and B. B. Blinov, Phys. Rev. A **85**, 023401 (2012).

[164] M. M. T. Loy, Phys. Rev. Lett. **32**, 814 (1974).

[165] C. Wunderlich, T. Hannemann, T. Körber, H. Häffner, C. Roos, W. Hänsel, R. Blatt, and F. Schmidt-Kaler, Journal of Modern Optics **54** (2007).

[166] U. G. Poschinger, G. Huber, F. Ziesel, M. Deiß, M. Hettrich, S. A. Schulz, K. Singer, G. Poulsen, M. Drewsen, R. J. Hendricks, and F. Schmidt-Kaler, Journal of Physics B: Atomic, Molecular and Optical Physics **42**, 154013 (2009).

[167] T. Ruster, C. T. Schmiegelow, H. Kaufmann, C. Warschburger, F. Schmidt-Kaler, and U. G. Poschinger, Applied Physics B **122**, 254 (2016).

[168] C. H. Bennett, G. Brassard, S. Popescu, B. Schumacher, J. A. Smolin, and W. K. Wootters, Phys. Rev. Lett. **76**, 722 (1996).

[169] R. Reichle, D. Leibfried, E. Knill, J. Britton, R. B. Blakestad, J. D. Jost, C. Langer, R. Ozeri, S. Seidelin, and D. J. Wineland, Nature **443** (2006).

[170] N. Kalb, A. A. Reiserer, P. C. Humphreys, J. J. W. Bakermans, S. J. Kamerling, N. H. Nickerson, S. C. Benjamin, D. J. Twitchen, M. Markham, and R. Hanson, Science **356**, 928 (2017).

[171] S. Wehner, D. Elkouss, and R. Hanson, Science **362** (2018).

[172] T. R. Tan, J. P. Gaebler, Y. Lin, Y. Wan, R. Bowler, D. Leibfried, and D. J. Wineland, Nature **528** (2015).

[173] C. D. Bruzewicz, R. McConnell, J. Stuart, J. M. Sage, and J. Chiaverini, npj Quantum Information **5**, 1 (2019).

[174] A. C. Hughes, V. M. Schäfer, K. Thirumalai, D. P. Nadlinger, S. R. Woodrow, D. M. Lucas, and C. J. Ballance, Phys. Rev. Lett. **125**, 080504 (2020).

[175] D. Leibfried, B. DeMarco, V. Meyer, D. Lucas, M. Barrett, J. Britton, W. M. Itano, B. Jelenković, C. Langer, T. Rosenband, and D. J. Wineland, Nature **422**, 412 (2003).

[176] S. Debnath, N. M. Linke, C. Figgatt, K. A. Landsman, K. Wright, and C. Monroe, Nature **536**, 63 (2016).

[177] K. Sosnova, A. Carter, and C. Monroe, Phys. Rev. A **103**, 012610 (2021).

[178] D. Hucul, J. E. Christensen, E. R. Hudson, and W. C. Campbell, Phys. Rev. Lett. **119**, 100501 (2017).

[179] G. Audi, O. Bersillon, J. Blachot, and A. Wapstra, Nuclear Physics A **729**, 3 (2003).

[180] Y. Wang, J. c. v. Minář, L. Sheridan, and V. Scarani, Phys. Rev. A **83**, 063842 (2011).

[181] D.Coyne, Ligo vacuum compatible materials list (2014), available at `https://dcc.ligo.org/public/0003/E960050/013/E960050-v13%20Vacuum%20Compatible%20Materials%20List.pdf`.

[182] M. Audi, AIP Conference Proceedings **171**, 358 (1988).